Integrated Investigations of Lumbar Spine Biomechanics, Implant Fixation, and Design for Additive Manufacturing under Physiologic Loading

by

Martine Elizabeth McGregor

A thesis

presented to the University of Waterloo

in fulfillment of the

thesis requirement for the degree of

Doctor of Philosophy

in

Mechanical and Mechatronics Engineering

Waterloo, Ontario, Canada, 2024

© Martine Elizabeth McGregor 2024

Examining Committee Membership

The following served on the examining committee for this thesis. The decision of the examination committee is by majority vote.

External Examiner:	Sophia Sangiorgio, PhD Professor Dept. of Orthopaedic Surgery & Bioengineering Faculty of Engineering, University of California, Los Angeles
Internal-External Examiner:	Jack Callaghan, PhD Professor Dept. of Kinesiology and Health Sciences Faculty of Health, University of Waterloo
Internal Examiner:	Mihaela Vlasea, PhD, PEng Associate Professor Dept. of Mechanical & Mechatronics Engineering Faculty of Engineering, University of Waterloo
Internal Examiner:	Naveen Chandrashekar, PhD, PEng Associate Professor Dept. of Mechanical & Mechatronics Engineering Faculty of Engineering, University of Waterloo
Supervisor:	Stewart McLachlin, PhD, PEng Associate Professor Dept. of Mechanical & Mechatronics Engineering Faculty of Engineering, University of Waterloo

Author's Declaration

This thesis consists of material all of which I authored or co-authored: see Statement of Contributions included in the thesis. This is a true copy of the thesis, including any required final revisions, as accepted by my examiners.

Statements of Contributions

CHAPTER 1 *Sole Author* – Martine McGregor

CHAPTER 2 *Sole Author* – Martine McGregor

CHAPTER 3
Study Design – Martine McGregor, Stewart McLachlin, Parham Rasoulinejad
Specimen Preparation – Martine McGregor, Chloe Cadieux, Renan Fernandes
Data Collection – Martine McGregor, Jonah Leinwand
Data Analysis – Martine McGregor, Clare Thompson
Statistical Analysis – Martine McGregor
Manuscript Preparations – Martine McGregor
Manuscript Revisions – Martine McGregor, Parham Rasoulinejad, Stewart McLachlin

CHAPTER 4
Study Design – Martine McGregor, Stewart McLachlin
Specimen Preparation – Martine McGregor, Claire Thompson
Data Collection – Martine McGregor, Claire Thompson
Data Analysis – Martine McGregor
Statistical Analysis – Martine McGregor
Manuscript Preparations – Martine McGregor
Manuscript Revisions – Martine McGregor, Stewart McLachlin, Claire Thompson

CHAPTER 5
Study Design – Martine McGregor, Stewart McLachlin
Specimen Preparation – Martine McGregor, Claire Thompson
Data Collection – Martine McGregor, Claire Thompson
Data Analysis – Martine McGregor
Statistical Analysis – Martine McGregor
Manuscript Preparations – Martine McGregor
Manuscript Revisions – Martine McGregor, Stewart McLachlin, Claire Thompson

CHAPTER 6

Study Design – Martine McGregor, Mihaela Vlasea, Stewart McLachlin
Data Collection – Martine McGregor, Sagar Patel
Data Analysis – Martine McGregor, Sagar Patel
Manuscript Preparations – Martine McGregor, Sagar Patel
Manuscript Revisions – Martine McGregor, Mihaela Vlasea, Sagar Patel, Stewart McLachlin

CHAPTER 7

Study Design – Martine McGregor, Sagar Patel, Mihaela Vlasea, Stewart McLachlin
Data Collection – Martine McGregor, Adam Yu, Kevin Zhang
Data Analysis – Martine McGregor, Adam Yu, Kevin Zhang
Manuscript Preparations – Martine McGregor, Adam Yu, Sagar Patel
Manuscript Revisions – Martine McGregor, Sagar Patel, Mihaela Vlasea, Stewart McLachlin

CHAPTER 8

Sole Author – Martine McGregor

CHAPTER 9

Study Design – Martine McGregor, Stewart McLachlin, Parham Rasoulinejad
Specimen Preparation – Martine McGregor, Renan Fernandes, Claire Thompson
Data Collection – Martine McGregor, Claire Thompson
Data Analysis – Martine McGregor
Statistical Analysis – Martine McGregor
Manuscript Preparations – Martine McGregor
Manuscript Revisions – Martine McGregor, Claire Thompson, Renan Fernandes, Parham Rasoulinejad, Stewart McLachlin

CHAPTER 10

Sole Author – Martine McGregor

Abstract

Spinal implant loosening and migration are significant concerns following the surgical treatment of musculoskeletal spinal disorders because of the complex and highly variable loading experienced in the spine. During post-operative rehabilitation, the mechanical interface between the vertebral bone and metallic implant is subjected to variable, combined (multi-axial) loading modes during activities of daily living. However, most current methods for pre-clinical evaluations of spinal implants focus on application of simplified loading conditions (e.g. uniaxial toggle, static compression or pull-out tests) which do not fully represent physiologic multi-axial loading. As a result, there is a lack of biomechanical understanding in how spinal implants can fail following surgery. One of the goals of this thesis is to better understand mechanisms of clinical implant failures by improving pre-clinical spinal implant testing methodologies through the adoption of physiologically-derived loading conditions.

Spinal implants are often manufactured using titanium alloys like Ti6Al4V, beneficial for their superior osteogenic qualities. However, the mismatch in mechanical moduli between titanium and bone is a known cause of problematic stress shielding and failure of the bone-implant interface. To address this challenge, laser powder bed fusion (LPBF) additive manufacturing allows for the production of unique metamaterials that can act to reduce the bulk modulus of titanium implants, bringing mechanical properties closer to that of human bone. However, there is currently a disconnect between the understanding of additive manufacturing (AM) and the mechanical properties of bone. Therefore, a second goal of this

thesis was to develop design for additive manufacturing (DfAM) tools for selecting lattice properties to best match vertebral bone properties while ensuring manufacturability for LPBF.

Based on the two overall goals, the thesis research was defined based on the intersection of three themes: (1) multiaxial spinal loading, (2) spinal implant evaluation, and (3) LPBF AM. Within these themes, four *in vitro* biomechanical human cadaver investigations were completed to develop physiologically-derived, multi-axial loading test protocols for a commercially available joint motion simulator to evaluate the impact of multi-axial loading on implant loosening and migration. The first study examined the effect of uniaxial and multiaxial cyclic loading on pedicle screw loosening in osteoporotic human bone (n=7). It was found that multiaxial loading significantly accelerated pedicle screw loosening as well as increased deformation volume at the bone-implant interface. The second (n=8) and third (n=8) biomechanical studies focused on developing six degree-of-freedom (6DOF) test protocols for spinal loading simulation. Lumbar spine stability was compared between existing pure moment test methods against physiologically-derived 6DOF loading waveforms associated with activities of daily living. It was found that the commercial joint motion simulator was reliable for applying complex, physiologically-derived lumbar spinal loads. The loads associated with *in vivo* spinal movements resulted in reduced range of motion compared to application of pure moments. Longitudinal gait simulation also had little impact on lumbar spine segment biomechanics. The fourth *in vitro* investigation (n=8) was aimed at leveraging the developed protocols to evaluate implant migration of an LPBF additively manufactured spinal implant. It was found that cage penetration into the adjacent vertebra (failure of the bone-implant

interface) happened most often during simulated gait testing, while cage migration, towards the spinal cord, occurred primarily during flexion-extension.

Two additional DfAM investigations were undertaken to develop tools for selecting Ti6Al4V lattices for orthopaedic applications and evaluating manufacturability of lattice designs. A comprehensive literature review was undertaken to synthesize a dataset relating lattice parameters to compressive mechanical properties. Gibson-Ashby plots were generated to relate this dataset to human bone properties for selection of lattice parameters in orthopaedic implant designs. A manufacturability evaluation was also completed to determine which lattice structures were considered manufacturable based on geometric and defect analysis. It was found that surface-based lattice structures were the most manufacturable due to the high interconnectivity of the down-skin regions. Lastly, these DfAM tools were used to develop novel lumbar interbody cage implants, which were investigated under the physiologically-derived loading (described above).

Collectively, the research completed in this thesis provides new biomechanical understanding of the lumbar spine and spinal implants under multi-axial cyclic loading. With improved knowledge of how spinal implant failures can occur under multi-axial loading, pre-clinical testing standards can now be improved to help avoid these failure mechanisms, ultimately leading to the hope of improved clinical outcomes following spinal surgery. Further, new DfAM tools were created and evaluated providing new avenues for the use of emergent LPBF AM techniques for orthopaedic applications.

Acknowledgements

I would like to extend my sincerest thank you to my supervisor, mentor and friend Dr. Stewart McLachlin. Thank you for your expertise, curiosity, patience and kindness. It was an honour to learn and grow with you throughout my time as your first sole supervised PhD student. I feel supremely lucky to have had your guidance and am eternally grateful for all the opportunities you've provided me to learn and grow both as a researcher and as a person.

Thank you to my examination committee members, Drs. Mihaela Vlasea, Naveen Chandrashekar and Jack Callaghan for their time and thoughtful insights on my work. I also sincerely thank my external examiner, Dr. Sophia Sangiorgio, for attending my defence and for providing valuable feedback.

Thank you to my OrthoTron lab mates with whom this research would not be possible. It has been so special to see many of you grow from URAs to graduate students pursuing your own research goals. I would specifically like to thank Sagar Patel and Claire Thompson for being such wonderful friends both in and out of the research realm.

Thank you to our surgical partners at Western University, Drs. Chloe Cadieux, Renan Fernandes, Kingori Wangai, and Parham Rasoulinejad. Your assistance with instrumentation and clinical insights have been invaluable and positively impacted the quality of this work.

Thank you to the Natural Sciences and Engineering Research Council of Canada, the W.S. Rickert Fellowship in Science and the University of Waterloo President's Graduate Scholarship Program for providing me with the financial support to complete this work.

Finally, thank you to my family and friends. To my Zinnies, Jess (Eleanor), Emma, Megan (Quinn), Jen (Sophie) and Claire, I wouldn't be here today without your love, support and friendship. To my parents, Ian and Dolores, thank you for your unyielding support and encouragement. To my husband, Josh, a thank you will never be enough for what your love and support mean to me. To my daughter, Louise, thank you for providing me the motivation to continue. You are the very best detour this work could have taken.

Dedication

This thesis is dedicated to Margaret McGregor—my role model of lifelong learning—and to Louise Russell, my faith in the future.

Table of Contents

Examining Committee Membership ii
Author's Declaration iii
Statements of Contributions iv
Abstract vi
Acknowledgements ix
Dedication xi
List of Abbreviations xxxi
List of Publications from PhD Thesis xxxii
Chapter 1 – General Introduction 1
1.1 Global Thesis Objectives 5
1.2 Thesis Layout 5
1.3 Outline of Thesis Chapters 6
Chapter 2 - Background Literature 12
2.1 Anatomy of the Lumbosacral Spine 12
2.1.1 Bony Anatomy 13
2.1.2 Soft Tissue Anatomy of the Lumbar Spine 15
2.1.3 Joint Anatomy 16
2.1.4 Curvature of the Spine and Associated Pelvic Parameters 18
2.2 Biomechanics of the Lumbar Spine 18
2.2.1 Activities of Daily Living 18
2.2.2 Lumbar Spinal Loading 19
2.2.3 Biomechanical Properties of Vertebral Bone Tissues 22
2.3 Lumbar Spine Pathology 25
2.3.1 Spinal Deformities 25
2.3.2 Spinal Injuries 26
2.3.3 Degenerative Spinal Disorders 26

2.4 Orthopaedic Instrumentation 28
2.5 Design and Manufacture of Spinal Implants 30
2.5.1 Pedicle Screw Design 30
2.5.2 Interbody Cage Design 31
2.5.3 Design Opportunities through Additive Manufacturing 32
2.6 Experimental Evaluation of Spinal Implants 34
2.6.1 In Vitro Testing of Pedicle Screws 34
2.6.2 In Vitro Testing of Interbody Cages 37
2.6.3 Existing ASTM and ISO Spinal Implant Test Standards 37
2.6.4 Measurement of Implant Displacement 38
2.7 Spine Simulators 41
2.7.1 Pure Moment Load Simulation 41
2.7.2 Multiaxial Loading Simulation 43
Chapter 3 – A Biomechanical Investigation of Multiaxial Pedicle Screw Loosening in Osteoporotic Human Vertebral Bone 45
3.1 Introduction 46
3.2 Materials and Methods 47
3.2.1 Specimen Preparation 47
3.2.2 Biomechanical Test Setup 49
3.2.3 Measurement of Implant Loosening 51
3.2.4 Statistical Design 52
3.3 Results 52
3.4 Discussion 55
3.4.1 General Findings 55
3.4.2 Comparison to Prior Work 57
3.4.3 Comparison to Existing Test Standards 58
3.4.4 Limitations 59
3.5 Conclusions 60

3.6 References 61
Chapter 4 - Biomechanical comparison of human cadaveric lumbar motion segments under simple and physiologically-derived loading conditions 64
4.1 Introduction 65
4.2 Methods 67
4.2.1 Specimen Preparation 67
4.2.2 Six-degree of freedom Waveform Generation 68
4.2.3 Biomechanical Test Protocol 71
4.2.4 Post-hoc Analysis 74
4.3 Results 74
4.3.1 Pure Moment versus Physiologically-derived 6DOF Loading 74
4.3.2 Quasi-static versus Dynamic Test Rates 76
4.3.3 Pure Moment in Load versus Displacement Simulator Control 78
4.3.4 Neutral Zone Measurements 79
4.3.5 Summary of Previous Results 79
4.4 Discussion 80
4.4.1 Comparison of Pure Moment versus Physiologically Derived Applied Loads 81
4.4.2 Quasi-Static versus Dynamic Test Rates 81
4.4.3 Load Control versus Displacement Control 82
4.4.4 Comparison to Previous Literature 83
4.4.5 Limitations 83
4.5 Conclusions 84
4.6 References 85
Chapter 5 - Cyclic *in vitro* simulation of physiologically-derived gait and sit-to-stand loading on the lumbar spine 89
5.1 Introduction 90
5.2 Methods 91
5.2.1 Specimen Preparation 91

5.2.2 Six-degree of freedom waveform generation 92
5.2.3 Biomechanical Test Protocol 94
5.2.4 Statistical Analysis 96
5.3 Results 97
5.3.1 Lumbar Segment ROM Following 10,000 steps 97
5.3.2 6DOF Load Control Simulation 100
5.3.3 Cyclic Gait Simulation with ILC 100
5.4 Discussion 101
5.4.1 Lumbar Segment ROM Following 10,000 steps 101
5.4.2 6DOF Load Control Simulation 102
5.4.3 Cyclic Gait Simulation with ILC 102
5.4.4 Study Limitations 103
5.5 Conclusions 105
5.6 References 105
Chapter 6 – Architectural bone parameters and the relationship to titanium lattice design for powder bed fusion additive manufacturing 108
6.1 Introduction 109
6.2 Review of human bone properties relevant to lattice design 111
6.2.1 Review of human bone function 111
6.2.2 Trabecular bone 112
6.2.3 Cortical Bone 116
6.3 Additively Manufactured Lattices for Bone Replacement 117
6.3.1 Review of additive manufacturing for metals: powder bed fusion 118
6.3.2 Review of Lattice Designs 120
6.4 Review Methodology 127
6.5 Results and Discussion 129
6.5.1 Lattice Considerations 129
6.5.2 Manufacturability Considerations 135

6.6 Conclusions 146
6.7 References 148
Chapter 7 – A manufacturability evaluation of complex architectures by laser powder bed fusion additive manufacturing 162
7.1 Introduction 163
7.2 Methodology 167
7.2.1 Design and Evaluation of Lattice Structures 167
7.2.2 Evaluation of Down-skin 168
7.2.3 Manufacturing and Evaluation of Manufacturability 169
7.3 Results 172
7.3.2 Evaluation of Manufacturability 177
7.4 Discussion 182
7.5 Conclusions 186
7.6 References 187
Chapter 8 - Design and Manufacturability of Anatomically-Optimized Spinal Implants using Laser Powder Bed Fusion Additive Manufacturing 192
8.1 Background Rationale for Design 192
8.2 Decisions for Interbody Cage Design 193
8.3 Results of Manufacturability Investigation 196
8.4 Methodology for the Bench-Top Investigation for Implant Evaluation 197
8.5 Results of Bench-Top Investigation for Implant Evaluation 198
8.6 Conclusions on Interbody Cage Design Manufacturability and Preliminary Performance 201
8.7 References 202
Chapter 9 - An *in vitro* investigation of lumbar interbody cage migration under physiologically-derived loading conditions 204
9.1 Introduction 205
9.2 Methods 207

9.2.1 Specimen Preparation 207
9.2.2 Interbody Cage Design and Additive Manufacturing 208
9.2.3 Experimental Protocol and Biomechanical Testing 209
9.2.4 Posterior Element Resection and Cage Insertion 212
9.2.5 Simulated Cyclic Gait Loading 212
9.2.6 Statistical Analysis 213
9.3 Results 214
9.3.1 Cage Design Decisions 214
9.3.2 Lumbar Segment Range of Motion 214
9.3.3 Cage Migration and Subsidence 217
9.4 Discussion 220
9.4.1 Lumbar Segment Range of Motion 220
9.4.2 Cage Migration and Subsidence 220
9.4.3 Study Limitations 222
9.4.4 Clinical Significance 223
9.5 Conclusions 224
9.6 References 224
Chapter 10 – General Discussion and Conclusions 228
10.1 Summary and Global Research Contributions 228
10.2 Future Directions 233
10.3 Significance 235
References 236
Appendix A - Data related to architectural bone parameters and the relationship to Ti lattice design for powder bed fusion additive manufacturing 246
Table A0. Specifications Table 247
Appendix B – Standard Operating Procedures 295
Appendix C –Supplementary Material for Chapter 6 299

List of Figures

Figure 1.1 The human lumbar spine can be described in three columns: posterior column, middle column, and anterior column. 2

Figure 1.2: The three major themes of this thesis and the associated research studies conducted in each Chapter have been added to a Venn Diagram to highlight the interconnectivity of the thesis work. 6

Figure 2.1: Wilke et al., established test alignment recommendations allowing for the standardization of *in vitro* testing of spinal implants across research labs (Wilke et al., 1998). 13

Figure 2.2: Left: An axial top-down view of a lumbar vertebrae is shown to distinguish the vertebral body from the vertebral arch and indicate the location of the anatomical features. L and A indicate the lateral and anterior directions respectively. **Right:** A sagittal view of the two lumbar vertebrae is used to describe the location of the facet joint (red circle) formed between adjacent vertebrae. Orientation is described where S and A indicate the superior and anterior directions respectively. The spine can be divided into three columns: anterior, middle and posterior as described by Francis Denis (Denis, 1983). 14

Figure 2.4 The soft tissues of the lumbar spine include the (a) facet joint capsule, (b) intervertebral disc, (c) supraspinous ligament, (d) intertransverse ligament, (e) ligamentum flavum, (f) posterior longitudinal ligament, and (g) anterior longitudinal ligament. 16

Figure 2.5: Left: A sagittal view of the whole spine depicts the five regions: cervical, thoracic, lumbar sacral and coccygeal. **Right:** A sagittal view of the lumbosacral spine is used to describe a functional spinal unit (FSU), consisting of two adjacent vertebrae and their shared intervertebral disc. The lumbosacral joint or L5-S1 FSU is highlighted. Orientation is described where S and A indicate the superior and anterior directions respectively. 17

Figure 2.6: Three views of a lumbar vertebrae, axial (left), sagittal (centre), frontal (right) are used to describe the different loads experienced in the lumbar spine with reference to the local vertebral coordinate system. 20

Figure 2.7: The Orthoload group developed two telemeterized spinal implants, a vertebral body replacement (left) and an internal spinal fixator (right). Six degree of freedom loads were measured *in vivo* during activities of daily living and the data has been made open source (Dreischarf et al., 2015; Rohlmann et al., 1999) (www.orthoload.com). 22

Figure 2.8: Cortical bone exhibits transversely isotropic mechanical properties which are greatest in the longitudinal axis. In the longitudinal axis, the elastic modulus, compressive strength and tensile strength range from 15-20 GPa, 170-190 MPa and 120-130 MPa, respectively. In the transverse directions, the elastic modulus, compressive strength and tensile strength are 5-11.5 GPa, ~133 MPa and ~55 MPa, respectively (McGregor et al., 2021). 24

Figure 2.9: Left: Two functional spinal units (FSU) are used to show the changes to joint biomechanics that may occur due to degenerative disc disease. The superior FSU shows healthy loading about the vertebrae and facet while the red arrows on the inferior FSU depict increased compressive and shear loading at the facet joints with degeneration. **Right:** Spondylolisthesis causes anterior translation of the superior vertebrae (L5) with respect to the inferior vertebrae (S1). This misalignment alters joint biomechanics and may increase shear force between the vertebrae and compression in the nerve root foramen. 27

Figure 2.10: A visual step-by-step overview of the posterior lumbar interbody fusion (PLIF) procedure has been adapted from (Bohl et al., 2018). **(A)** Skin incision and distraction of the muscular tissues, with screws inserted in the pedicles. **(B)** A screw implant is placed in each pedicle for rigid fixation. Screws may be used to distract the disc space to improve decompression treatment. **(C)** The nucleus pulposus is removed and the endplates prepared for cage placement. **(D)** Interbody cage(s) are inserted in the disc space to restore disc height, provide anterior column support, and act as a scaffold for bone ingrowth. 29

Figure 2.11: Fixation of a functional spinal unit, L4-L5 above, can be achieved using of three implant types: pedicle screws, connecting rods and intervertebral (interbody) cages (McLachlin, 2008a). 30

Figure 2.12: Pedicle screws are implanted in the posterior elements to achieve posterior fixation (adapted from www.precisionspineinc.ccom). 31

Figure 2.13: Interbody cages are placed in the intervertebral disc space to provide anterior column stability and promote boney ingrowth. Cages are manufactured through traditional methods from Ti-alloys (left) and poly-ethylene ether ketone (centre). Additive manufacturing has been used to develop novel cages from Ti-alloys (right) (adapted from: www.stryker.com). 32

Figure 2.14: Uniaxial pull-out testing has been used historically to measure implant fixation. A screw is inserted in a foam or an animal or human vertebra (left). The implant-specimen construct is fixed to a mechanical test simulator and a tensile load is applied to the screw head along the axis of the screw (centre). Results are reported as a comparison of peak load to failure across effects (right) (Hashemi et al., 2009). 34

Figure 2.15. Uniaxial toggle testing has been introduced to replicate the fatigue failure seen clinically in spinal screw constructs. The American Society for Testing Materials has developed a standard for testing four-point posterior fixation constructs (left) and single screw implants (right) (ASTM F1717-15, 2021). 36

Figure 2.16. Liebsch et al. examined the effect of combined loading on implant loosening. The test set-up used geometry to induce cyclic multiaxial forces including shear and tension (Liebsch et al., 2018**).** 36

Figure 2.17: An example of a force by displacement curve for the pull-out strength of a pedicle screw from healthy adult vertebral trabecular bone (Varghese et al., 2017)..... 39

Figure 2.18: Left: Machine vision has been used to track real-time implant loosening (McLachlin, 2011). **Right:** Post-hoc 3D medical imaging can be utilized to quantify volumetric bone damage near the bone-implant interface. This method can be used to compare different implant types, surgical techniques and anatomical variations (McLachlin, 2008). 40

Figure 2.19 Early multiaxial spine simulator developed by Wilke et al., to apply pure moments to individual spinal segments (Wilke et al., 1994). 42

Figure 2.20 Stokes et al., developed a Stewart platform inspired force-control six-degree of freedom spine motion simulator (Stokes et al., 2002). 43

Figure 2.21 Holsgrove et al., have developed a spine simulator capable of applying complex multi-directional loading protocols at physiologic rates in displacement control (Holsgrove et al., 2014). 44

Figure 3.1: The six-degree of freedom test apparatus (left) was used to apply loads with respect to the defined local screw coordinate system (bottom right). Loads and displacements were resolved about the center of the pedicle screw head. 49

Figure 3.2: Uniaxial and multiaxial loads were applied along the x, y, and z screw axes. The x, y, and z were most similar to the anterior-posterior, medial-lateral, and cranial-caudal axes; however, there were differences based on the relative screw orientation. 50

Figure 3.3: Probability of survival with respect to the number of cycles required to reach 6 mm of screw head translation in any degree of freedom as measured by the joint motion simulator. Note there was an early failure of a single specimen. 53

Figure 3.4: The maximum screw displacement in the z-direction (~superior-inferior) and y-direction (~medial-lateral) for all screws tested (dotted) and the average (bold) as measured by the joint motion simulator. Failure occurred negative z-direction (~inferiorly) most often ($p=0.06$) for both uniaxial (blue) and multiaxial loading (red). Negative y-direction (~medial) ($p=0.12$) and positive y-direction (~lateral) screw displacement was greater in multiaxial loading (red) compared to uniaxial loading (blue) ($p=0.00$*)..... 54

Figure 3.5: Axial (left), posterior (top right), and sagittal (bottom right) computed tomography cross sections show the apparent differences in volumetric bone deformation from uniaxial (yellow) and multiaxial (green) screw loosening. With screws removed for scanning, only the distal 35mm of the empty screw volume was used for segmentation. 55

Figure 4.1. A physiologically-derived six-degree of freedom waveform for simulated flexion-extension was generated from *in vivo* flexion and extension load data obtained from an open-source database. A custom pipeline utilized dynamic time warping to develop average flexion and extension waveforms which were then concatenated to represent a cyclic spinal flexion-extension movement. Figure contains images obtained from www.orthoload.org. 70

Figure 4.2. A six-degree of freedom flexion-extension, lateral bending and axial rotation loading protocol was developed from the www.orthoload.org database through a dynamic time warping with peak matching approach (solid). The sinusoidal pure moment loading (+/- 4Nm with 250N of axial compression) waveforms (dashed) are shown for comparison. 70

Figure 4.3. Lumbar motion segments were mounted to a six-degree of freedom (6DOF) joint motion simulator. Actuators worked together in 6DOF load control to apply the translational and rotational displacements required to simulate spinal lateral bending (Mx), flexion-extension (My) and axial rotation (Mz). Inset: visual of the Aramis 3D optical motion tracking system identifying the marker locations for the L2 and L3 vertebrae relative to the reference tracker..... 72

Figure 4.4. Pure moment bending (blue) and physiologically derived (red) loading protocols were completed in quasi-static (solid) and dynamic (hashed) and compared for segmental range of motion across three linear translations and three rotations: Tx (anterior-posterior), Ty (medial-lateral), Tz (superior-inferior), Rx (lateral bending), Ry (flexion-extension), and Rz (axial rotation). Differences between pure moment and physiologically-derived were denoted with a # and a ^ for quasi-static and dynamic test rates, respectively. Differences between quasi-static and dynamic test rates for pure moment loading were denoted with a * and there were no differences between test rates under physiologically derived loading. 75

Figure 4.5. (a) Quasi-static (0.5 Nm/sec) and dynamic (5 Nm/sec) testing rates were compared. Lumbar segment range of motion was compared across three linear translations and three rotations: Tx (anterior-posterior), Ty (medial-lateral), Tz (superior-inferior), Rx (lateral bending), Ty (flexion-extension), and Tx (axial rotation). (b) Force-displacement curves for each spinal movement: flexion-extension, lateral bending and axial rotation. 77

Figure 4.6. (a) Load and displacement simulator control was compared. Lumbar segment range of motion was compared across three linear translations and three rotations: Tx (anterior-posterior), Ty (medial-lateral), Tz (superior-inferior), Rx (lateral bending), Ry (flexion-extension), and Rz (axial rotation). (b) Force-displacement curves for each spinal movement: flexion-extension, lateral bending and axial rotation. 78

Figure 5.1. Six degree-of-freedom (6DOF) waveforms were obtained from an open-source database (www.orthoload.org) and generalized 6DOF gait (shown above) and sit-to-stand

waveforms were generated using the shown data processing approach. Figure contains images obtained from www.orthoload.org. 93

Figure 5.2. The generalized six degree-of-freedom (Fx, Fy, Fz, Mx, My, Mz) loading waveforms for (a) gait and (b) sit-to-stand were developed from OrthoLoad datasets (www.orthoload.org) using a dynamic time warping with peak matching approach. The shown waveforms have been down-sampled to 1024 points to match the waveform input requirements for the AMTI VIVO joint motion simulator. The x-axis represents the percentage of total waveform length..... 94

Figure 5.3. Eight human cadaveric lumbar motion segments were mounted to a six-degree of freedom (6DOF) joint motion simulator. Actuators worked together in 6DOF force control to apply the translational and rotational displacements required to simulate pure moment flexion-extension (My), lateral bending (Mx), axial rotation (Mz), 6DOF gait and 6DOF sit-to-stand. Motion segment kinematics were quantified using an ARAMIS 12M optical 3D tracking system. 95

Figure 5.4. Lumbar segment range of motion was measured during (a) flexion-extension, (b) lateral bending, and (c) axial rotation before (blue) and after (red) the 10,000 step longitudinal cyclic loading protocol. Relevant segmental range of motion is reported across three linear translations and three rotations: Tx (anterior-posterior), Ty (medial-lateral), Tz (superior-inferior), Rx (lateral bending), Ry (flexion-extension), and Rz (axial rotation)..... 98

Figure 5.5. (b) Force-displacement curves for each spinal movement: (a) flexion-extension, (b) lateral bending and (c) axial rotation..... 99

Figure 5.6. Root mean square error for quasi-staic gait (QsGait), dynamic gait (DGait), quasi-static sit-to-stand (QsS2S) and dynamic sit-to-stand (DS2S) were compared to the simulator actuator resolution (SimRes) in three linear translations and three rotations: Tx (anterior-posterior), Ty (medial-lateral), Tz (superior-inferior), Rx (lateral bending), Ry (flexion-extension), and Rz (axial rotation)..... 100

Figure 5.7. Root mean square error for longitudinal gait testing for three linear translations and three rotations: Tx (anterior-posterior), Ty (medial-lateral), Tz (superior-inferior), Rx (lateral bending), Ry (flexion-extension), and Rz (axial rotation). The horizontal red line represents the actuator specific load resolution. Note: one specimen sustained a disc injury at 7200 steps..... 101

Figure 6.1 Human bone can be categorized into two main types: cortical and trabecular. Cortical bone is the stiffer, more dense bone which encapsulates short bones, the ends of long bones and comprises the shaft of long bones. Trabecular bone is the lattice like structure which makes up the majority of short bone structure as well as the ends of long bones. This

figure was adapted from the μCT work of Lui et al. and Gauthier et al. (Gauthier et al., 2019; X. S. Liu et al., 2010.) 112

Figure 6.2 Commonly reported measurements of trabecular bone microstructure (left) may be used to describe lattice parameters commonly used in additive manufacturing (right). (For interpretation of the references to colour in this figure legend, the reader is referred to the web version of this article.) 114

Figure 6.3 A comprehensive summary of two- and three-dimensional measurements of trabecular bone at the femoral head, illiac crest, calcaneal core, L2 vertebra and L4 vertebra as described by Hildebrand et al. 1999. The mean data reported by Hildebrand et al. was supplemented with Thomsen et al.'s report (Thomsen et al., 2005) of trabecular bone parameters at the proximal tibia to form an original visual representation*. Bone microstructure data is outlined in red and suggested translation to lattice design parameters is outlined in blue. The values listed represent the mean value of the each measurement. 115

Figure 6.4 Cortical bone exhibits transversely isotropic mechanical properties with nearly double the stiffness occurring along the axis of loading (Bartel and Davy, 2006; Burstein et al., 1976; Park and Lakes, 2007). Young's modulus, ultimate compressive strength, and ultimate tensile strength in the longitudinal direction are denoted Ez, σc,z, and σt,z respectively. The subscript "x,y" is given to denote mechanical properties in the transverse axes. 117

Figure 6.5 Classification chart for lattice designs. 121

Figure 6.6 Comparative images of a periodic (top row) and pseudo-periodic (bottom row) TPMS (surface-based) Schwarz diamond (D) lattice structure. 122

Figure 6.7 Comparative images of a homogeneous (top row) and heterogeneous (bottom row) strut-based body centered cubic lattice structure. 123

Figure 6.8 Comparative cross-sectional images of various TPMS Schoen gyroid lattice structures classified as periodic, pseudo-periodic, homogeneous, and heterogeneous. 124

Figure 6.9 Experimental data comparing the compressive strength (left) and Young's modulus (right) for common cellular lattice structures to those predicted by the Gibson-Ashby model. Cellular lattice structures examined include: BCC (A), BCCZ (B), FCC (C), FCCZ (D), cubic (E), Octet-truss (F), diamond (G), Schoen gyroid (H), Schwarz diamond (I), and Neovius (J). Original figures obtained from (Maconachie et al., 2019). 127

Figure 6.10 Porosity is the most common lattice parameter reported in literature. Compressive strength and Young's modulus of additively manufactured lattice structures were plotted over the Ashby plots of human trabecular and cortical bone. Lattice porosity

ranged from 15% to 97% and was plotted in a gradient to depict how best to design for material property matching. 130

Figure 6.11 Designed pore size of additively manufactured Ti and Ti-6Al-4 V lattice structures was plotted in a gradient over a compressive strength versus Young's modulus Ashby plot for human trabecular and cortical bone tissues to depict how best to design for material property matching. 131

Figure 6.12 Feature thickness was plotted in a gradient over a compressive strength versus Young's modulus Ashby plot for human trabecular and cortical bone tissues to depict how best to design for material property matching. 132

Figure 6.13 Lattice type, strut- vs surface-based, was plotted in a gradient over a compressive strength versus Young's modulus Ashby plot for human trabecular and cortical bone tissues to depict how best to design for material property matching. 133

Figure 6.14 Material type, Ti vs Ti-6Al-4V, was plotted in a gradient over a compressive strength versus Young's modulus Ashby plot for human trabecular and cortical bone tissues to depict how best to design for material property matching..... 134

Figure 6.15 A three-dimensional XCT visualization of the different types of surfaces observed in a laser powder bed fusion Ti-6Al-4V Voronoi lattice structure with respect to the build orientation along the Z-axis (left), a high resolution XCT image of a portion of the Voronoi lattice structure (center), visualization of the defects inside the printed lattice structure (right). 137

Figure 6.16 A 3D comparison of the XCT visual (shown in grey) and the original CAD (shown in blue) of a Ti-6Al-4V Voronoi lattice structure manufactured by laser powder bed fusion (left) and a 2D comparison of a slice along the XZ plane of the XCT visual (shown in grey) and the original CAD (shown in blue) of the lattice structure (right). 142

Figure 6.17 van Lenthe et al., used a micro computed tomographical (micro-CT) image of a human trabecular bone to develop a specimen-specific beam finite-element model. The process is shown above: (a) micro-CT reconstruction, (b) point cloud generation, (c) multi-colour dilation, and (d) assignment of element thickness and volume to finite element beams. Original figure obtained from (van Lenthe et al., 2006). 145

Figure 7.1 Seven unique homogenous lattice structures were printed using maraging steel through laser powder bed fusion (M290, EOS, Germany): (a) TPMS gyroid, (b) TPMS Schwarz, (c) TPMS diamond, (d) body-centered cubic, (e) face-centered cubic, (f) graphical diamond, and (g) octet (failed)..... 168

Figure 7.2 Seven unique homogeneous lattice structures were evaluated for down-skin regions ranging from 0 deg to 90 deg of down-skin in 15-deg increments: TPMS gyroid,

TPMS Schwarz, TPMS diamond, body-centered cubic, face-centered cubic (partially failed), graphical diamond, and octet (failed). 174

Figure 7.3 Down-skin distribution as determined using the custom 3D Slicer algorithm and discretized into 15o increments. Amongst the seven homogeneous lattice structures, FCC and octet lattices have the highest percentage of down-skin surfaces with an angle <30o at 11.07% and 11.47% respectively. 175

Figure 7.4 A bottom isometric view of the lattice down-skin is provided. Enlarged (1:3), discrete down-skin regions with an angle of 15 deg or less to the build plate (red) were isolated with the aim of better understanding the effect of down-skin area and interconnectivity of discrete down-skin features on printability challenges. Complete lattice structures with down-skin visualization were included for each lattice to provide context for the discrete down-skin regions. The discrete down-skin features for the TPMS gyroid (top left), TPMS diamond (top right), octet (bottom left), and face-centered cubic (bottom right) lattice structures are visualized above. 176

Figure 7.5 An X-ray computed tomography image of a maraging steel TPMS Schwarz lattice structure produced with laser powder bed fusion is visualized in frontal (left) and isometric (bottom right) views. An enlarged section (upper right) allows for visualization of irregular (blue) and round (red) porous defects to depict the prevalence and location. 178

Figure 7.6 Surface-based lattices TPMS gyroid (top), were found to be more printable than strut-based lattices, FCC (bottom). The TPMS gyroid had 5.3% and 21.6% volumetric over- and under-print respectively, while the FCC had 16.0% and 31.3% (left). When aligning quantitative values for over-print and under-print to X-ray computed tomography (XCT; middle) and surface angle (right), a clear association between down-skin surfaces and poor print quality becomes apparent. 179

Figure 7.7 Average and standard deviations for volumetric over-print and under-print from slice-by-slice comparisons of the CAD and XCT data of the eight successfully manufactured structures 180

Figure 7.8 Down-skin distribution within the complete orthopaedic implant parts was determined using a custom algorithm and discretized into 15-deg increments. Distribution for the TMPS gyroid and Voronoi cubic designs were included for comparison. The two lightweighted orthopaedic implants were then evaluated for down-skin regions ranging from 0 deg to 90 deg of down-skin in 15-deg increments 181

Figure 8.1. (a) A pre-established design tool was leveraged to determine which titanium lattice porosities would best match endplate compressive properties would best match endplate compressive properties while maintain manufacturability (McGregor et al., 2021).

(b) Titanium lattice porosity for lumbar cage designs varied from 40% at the posterior endplate to 70% at the central endplate. 194

Figure 8.2. Three different cage geometries were designed, including two variations (small and large) of tapered cages (top) and a straight cage design (bottom). 194

Figure 8.3. Six unique lumbar cages were manufactured (3 shapes x 2 lattice structures). The tapered cages have a greater height medially than laterally to account for the sagittal curvature of the endplate. The 9 mm to 7 mm tapered cage design with gyroid lattice structure is depicted in detail above. 195

Figure 8.4. Solid cages, as well as cages light-weighted with either a triply periodic minimal surface gyroid, or stochastic Voronoi lattice structures were manufactured in Ti6Al4V alloy through laser powder bed fusion additive manufacturing. 195

Figure 8.5. Down-skin distribution was measured in 15 degree increments for TPMS gyroid and Voronoi unit cells and interbody cages. Down-skin distribution ratio was determined for both cages, and they were considered manufacturable (down-skin ratio < 1). 196

Figure 8.6. Manufacturability of the anatomically-optimized lumbar spinal cages was evaluated using X-ray micro-computed tomography (mCT). mCT images were collected post-manufacture and final cage geometries were compared to CAD designs to quantify over- and under-printing. 197

Figure 8.7. (a) Two lumbar cages were tested: an endplate conforming cage and a traditional cage. (b) Implants were held in a fully constrained fixture and compressed into an engineered foam at 25 N/sec to 3.5 kN. (c) A force control joint motion simulator was used to apply unconstrained force with all off-axis actuators held at 0 N load. 198

Figure 8.8 An example (n=1) of the compression pattern in the Sawbones test substrate for the tapered (left) and straight (right) cage designs following compression testing to 3.5 kN at 25 N/sec. 199

Figure 8.9 Vertical cage subsidence was considered to have occurred at 2 mm of vertical displacement. Subsidence occurred for both the traditional (blue, shaded ± standard deviation) and endplate conforming implants (red ± standard deviation) at -643.4 ± 354.4 N and -900.8 ± 214.8 N. 200

Figure 8.10 Both lumbar cages rotated about the anterior-posterior axis throughout the unconstrained cage subsidence testing. Straight cages (blue, shaded ± standard deviation) rotated medially during the initial subsidence as they conformed to the sawbones and then rotated similarly to the tapered cages (red, shaded ± standard deviation) during post-yield subsidence. 200

Figure 9.1. (a) Two posterior lumbar interbody fusion cage designs were developed for (1) a straight endplate, and (2) a 2mm tapered endplate. (b) Gyroid lattice structures were incorporated to reduce the mechanical modulus of the Ti6Al4V implants to better match previously reported values for the lumbar vertebral endplate. 209

Figure 9.2. Lumbar motion segments were mounted to a six-degree of freedom joint motion simulator. Actuators worked together in force control to apply the translational and rotational displacements required to simulate spinal flexion-extension (My), lateral bedning (Mx), axial rotation (Mz) and a six-degree of freedom gait loading protocol. 210

Figure 9.3. The averaged six-degree of freedom (Fx, Fy, Fz, Mx, My, Mz) gait loading waveform was developed from five instrumented vertebral body replacement patient datasets (www.orthoload.org) using a dynamic time warping with peak matching approach for normalization to a 1s time period. 211

Figure 9.4. The average lumbar motion segment range of motion during simulated pure moment flexion-extension, lateral bending and axial rotation is shown with error bar representing standard deviations. Significant differences between intact, injured and repair states are shown with a * and $p < 0.05$ considered significant. 216

Figure 9.5. The average cage migration for straight and taper cage designs during simulated pure moment flexion-extension, lateral bending, axial rotation and six degree of freedom gait is shown with error bar representing ± standard deviations. There were no significant differences between cage designs, with $p > 0.05$. 218

Figure 9.6. Contributions towards cage migration differed between the simulated spinal motions. Significant differences between spinal flexion-extension, lateral bending, axial rotation and gait loading for 3000 steps are shown with a * and $p < 0.05$ considered significant. 219

Figure A1: A flowchart has been utilized to describe the review methodology with the search terms, inclusion and exclusion criteria outlined. 250

Figure C.1. A flowchart was developed to describe the process by which a custom python script was used to assign surface angle values to .stl files and visualize down-skin angle using 3D Slicer (v.4.11). 299

Figure C.2. Quantitative comparisons of the X-ray computed tomography and CAD datasets to understand slice-by-slice underprint and overprint of TPMS Schwarz, TPMS diamond, BCC and graphical diamond lattice structures. In the visualization on the right, grey is XCT and blue is the original CAD. 300

Figure C3. Quantitative comparisons of the X-ray computed tomography and CAD datasets to understand slice-by-slice underprint and overprint of the interbody cages with gyroid and Voronoi lattice structures. 301

List of Tables

Table 3.1. Specimen data for human vertebra specimens used for in vitro biomechanical testing. 48

Table 3.2. Uniaxial (1 degree of freedom) and multiaxial (6 degrees of freedom) loading was applied in three steps to human vertebra specimens relative to the screw loading axes, with the associated anatomical directions shown for reference. 51

Table 4.1. Comparison of quasi-static testing of load control and displacement control parameters 73

Table 4.2. A repeated measures test protocol was designed to compare (1) quasi-static vs dynamic test rates (*), (2) pure moment vs physiologically-derived (#), or (3) load vs displacement simulator control methods (^) for simulated spinal flexion-extension, lateral bending and axial rotation. 73

Table 4.3. The neutral zone for load control, displacement control, quasistatic, and dynamic test protocols for FE, LB, and AR 79

Table 4.4. Comparison of present study to previous literature examining in vitro lumbar segment range of motion including test rate, simulator control and load targets (Beaubien et al., 2005; Panjabi et al., 1985; Sawa et al., 2020; Tanaka et al., 2001; Wheeler et al., 2011; Wilke HJ et al., 1995; Zirbel et al., 2013). 80

Table 5.1. Data for gait and sit-to-stand waveforms was obtained from an open-source database (www.orthoload.com). The number of available subjects (n=4) and movement repetitions (20, 33) varied for each motion type. 93

Table 5.2. Neutral zone measurements for pre- and post-10,000 step in FE, LB, and AR 97

Table 6.1 The Hildebrand et al. method for calculating two dimensional trabecular measurements from known bone volume fractions (Hildebrand et al., 1999). 115

Table 6.2 Manufacturability comparisons between LPBF and EB-PBF (EBM) for fabricating titanium. 120

Table 7.1 Summary of the LPBF print parameters for the nine lattice structures using 18Ni-300 maraging steel on EOS M290 that include core, contour, down-skin, and up-skin parameters. 170

Table 7.2 Calculated values of the surface area of down-skin features, number of discrete down-skin features, and down-skin ratio for the seven homogeneous periodic lattice structures manufactured using LPBF in this study. 177

Table 7.3 Total volumetric over-print and under-print evaluation using the CAD and XCT data of the eight successfully manufactured structures..... 179

Table 7.4 Porosity fraction (of the CAD designs) and mass ratio (actual mass/CAD mass) for the six homogeneous periodic lattice structures manufactured to completion 180

List of Abbreviations

1DOF – One degree-of-freedom
6DOF – Six degrees-of-freedom
ADL – Activities of daily living
ALIF – Anterior lumbar interbody fusion
AM – Additive manufacturing
AR – axial rotation
ASTM - American Society for Testing Materials
BCC – Body centered cubic
BMD – Bone mineral density
BS – Total bone surface area
BV – Bone volume
CAD – Computer-aided design
CT – Computed tomography
DfAM – Design for additive manufacturing
DGait - Gait at dynamic test rate
DED – Direct energy deposition
DOF – Degrees of freedom
DS2S – Sit-to-stand at dynamic test rate
EB-PBF – Electron beam powder bed fusion
EDM – Electro discharge machining
FCC – Face centered cubic
FE – flexion-extension
FSU – Functional spinal unit
ISO – International Organization for Standardization
IVD – Intervertebral disc
LB – Lateral bending
LLIF – Lateral lumbar interbody fusion
LPBF - Laser powder bed fusion
L1, L2, L3, L4, L5 – Lumbar vertebrae 1-5 in descending order
mCT – Micro computed tomography
MSK – Musculoskeletal
NZ – Neutral zone
PBF – Powder bed fusion
PCF – Pounds per cubic foot
PEEK - Polyether-ether-ketone
PID – Proportional Integral Gain
PLIF – Posterior lumbar interbody fusion
QsGait – Gait at quasi-static test rate
QsS2S – Sit-to-stand at quasi-static test rate
RM-ANOVA – repeated measures analysis of variance
RMSE – Root mean square error
ROM – Range of motion
S1, S2, S3, S4, S5 – Sacral vertebrae 1-5 in descending order
S2S – Sit-to-stand
SimRes- Simulator resolution
SLM – Selective laser melting
STL - Stereolithography
TbTh – Trabecular thickness
TbSp – Trabecular spacing
TbN - Number of trabeculae that intersect with a given two-dimensional distance metric
Ti – Titanium
Ti6Al4V – A titanium alloy commonly used for manufacture of orthopaedic implants
TLIF – Transforaminal lumbar interbody fusion
TPMS - Triply period minimal surface
TV – Total volume of bone specimen
VTK – Visualization Toolkit
XCT – X-ray computed tomography

List of Publications from PhD Thesis

Published

1. McGregor, M; Patel, S; Zhang, K; Yu, A; McLachlin, S; Vlasea, M. (2024). A manufacturability evaluation of complex architectures by laser powder bed fusion additive manufacturing. Journal of Manufacturing Science and Engineering, 1-17.

2. McGregor, M; Patel, S; McLachlin, S; Vlasea, M. (2021). Architectural bone parameters and the relationship to titanium lattice design for powder bed fusion additive manufacturing. Additive Manufacturing, 47: 102273.

3. McGregor, M; Patel, S; McLachlin, S; Vlasea, M. (2021). Data related to architectural bone parameters and the relationship to Ti lattice design for powder bed fusion additive manufacturing. Data in Brief, 39: 107633.

Under Review

1. McGregor, M; Cadieux, C; Thompson, C; Fernandes, R; Lienwand, J; Rasoulinejad, P; McLachlin, S. (2024) A Biomechanical Investigation of Multiaxial Pedicle Screw Loosening in Osteoporotic Human Vertebral Bone. Under review for the The Spine Journal (SPINEE-D-24-01274)

2. McGregor, M; Thompson, C; Fernandes, R; Rasoulinejad, P; McLachlin, S. (2024) An in vitro investigation of lumbar interbody cage migration under physiologic loading conditions. Under review for The Spine Journal (SPINEE-D-24-01054)

3. McGregor, M; Thompson, C; McLachlin, S. (2024) Biomechanical comparison of human cadaveric lumbar motion segments under simple and physiologically-derived loading conditions. Under review for the Journal of Biomechanics (BM-D-24-01301).

In Preparation

1. McGregor, M; Thompson, C; McLachlin, S. (2024) Cyclic in vitro simulation of physiologically-derived gait and sit-to-stand loading on the lumbar spine. Proposed for submission to the Journal of Biomechanical Engineering.

Chapter 1 – General Introduction

Instrumented spinal fusion is a common surgical procedure used to treat various spinal pathologies including traumatic injuries, degenerative conditions and congenital deformities. In these surgeries, metallic implant constructs are used for reconstruction and stabilization of one or more spinal motion segments until long-term bony fusion occurs. Prior to the stability of bone-on-bone fusion, typically 3-6 months post-operation, the interface between the vertebral bone and the spinal implant is subjected to large cyclic multiaxial loads through regular activities of daily living (Bredow et al., 2016; Cho et al., 2011; Galbusera et al., 2015; Pearson et al., 2017). The strength of the bone-implant interface is integral in terms of maintaining rigidity of the spinal motion segments to promote fusion and is negatively affected by relative implant micromotion, such implant loosening, migration or subsidence (Puleo and Nanci, 1999).

Spinal fusion procedures typically require fixation through the three columns of the spine for stabilization, Figure 1.1. Posterior fixation is most commonly achieved with constructs formed by pedicle screws inserted into adjacent vertebrae and fixed together via metallic rods. In these posterior constructs, pedicle screw loosening remains a clinically relevant complication that occurs in up to 15% of instrumented spinal procedures performed on patients with healthy bone and 60% of patients with osteoporotic bone (Galbusera et al., 2015). For anterior spinal column reconstructions, interbody cage devices are inserted into the intervertebral disc space between vertebrae to restore spinal alignment; yet, up to 30% of patients will experience cage subsidence, penetration of the metallic implant into the vertebral body (Le et al., 2012; Malham et al., 2015; Marchi et al., 2013). As noted, implant loosening and subsidence are exacerbated by common bone diseases such as osteoporosis, that reduce bone density and lower the ability of bone to sustain

stresses without mechanical failure. Therefore, aging in populations increases both the risk of injury as well as the risk of failure modes like implant loosening and subsidence.

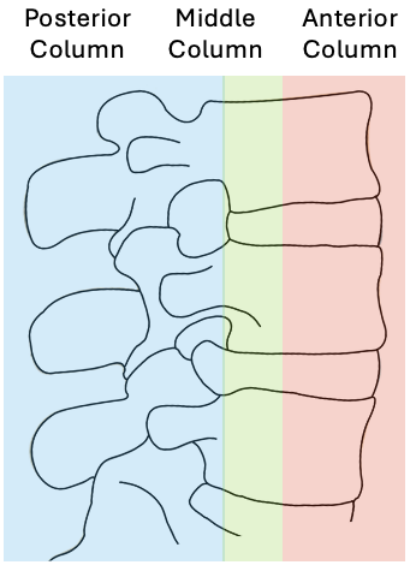


Figure 1.1 The human lumbar spine can be described in three columns: posterior column, middle column, and anterior column.

Improving understanding of the biomechanical factors that contribute to implant failure is a timely and pressing socioeconomic concern. In Ontario, Canada, the use of instrumented spinal surgeries as treatment for lumbosacral disorders steadily increased from 6.2 per 100,000 people of population in 1993 to 14.2 in 2012 (Xu et al., 2019). The direct cost of lumbar fixation procedures alone cost the Ontario single payer system $176 million cumulatively from 2002 to 2012, roughly $18 million dollars annually on average (Xu et al., 2019). The expenditure on spinal treatments has steadily grown in Canada and around the world (Martin et al., 2008). Spinal fusion surgeries are the sixth most common surgical procedure performed in the United States and the most expensive totaling $12.8 billion USD annually (Holsgrove et al., 2015; Weiss et al., 2014).

Spinal implant loosening or migration is typically associated with cyclic loading from activities of daily living causing relative movement or failure at the bone-implant interface (Esses

et al., 1993). Previous *in vitro* biomechanical studies examining fatigue failure of existing spinal fixation implants have typically simulated uniaxial fatigue testing (Law et al., 1993; Liebsch et al., 2018; McLachlin, 2008; Okuyama et al., 2000; Zindrick et al., 1986). A limitation with uniaxial loading is that damage to the bone-implant interface is biased to a single defined loading plane; when, in reality, bone-implant systems are subjected to multiaxial loading during spinal movements and activities. In the case of interbody cages, *in vitro* experimental investigations have been conducted to quantify the effect of implant material, placement, shape and size on implant subsidence (Jost et al., 1998; Suh et al., 2017; Tan et al., 2005; Yuan et al., 2020). However, a common limitation of these investigations is the use of simplified quasi-static compressive loading to induce cage subsidence, which is not representative of the multiaxial cyclic loading during activities of daily living (Rohlmann et al., 2014). As a result, there is a knowledge gap surrounding *how* cyclic multiaxial loading contributes to relative displacement and failure of spinal implants.

Loading of the bone-implant interface following surgical treatment of spinal disorders is complex and highly variable depending on activity (Galbusera et al., 2015). During post-operative rehabilitation prior to bone fusion, the mechanical interface between the vertebral bone and metallic implant (bone-implant interface) is subjected to variable combined loading modes (e.g. compression, bending, shear, torsion) during activities of daily living (i.e. standing, sitting, walking) (Rohlmann A, Graichen F, Weber U, 2000). Yet, there is limited understanding of how multiaxial loading contributes to risk of implant micromotion and/or bone damage, and the potential for costly failed surgeries (Figure 1.1). This problem remains a growing issue due to the aging population around the world (Martin et al., 2008). The proposed research seeks to better understand these mechanical phenomena using a novel experimental approach to simulate multiaxial implant loading associated with physiologic, activity-derived loading waveforms.

Additive manufacturing is a process by which a part is built layer by layer through material joining techniques. Laser powder bed fusion (LPBF), it an additive manufacturing technology that uses a laser heat source to melt powdered metal layer by layer as a recoater replaces powdered material. To address the issue of implant loosening or migration from an engineering design perspective, metal additive manufacturing has created new opportunities to generate implants that better reflect the mechanical environment of the spine. LPBF additive manufacturing allows for the integration of engineered lattice structures into titanium alloys implants (Ti6Al4V) to reduce modulus mismatch in an effort to reduce stress shielding. In the spine, this advantage has been shown to reduce interbody cage subsidence in some instances (Kumar et al., 2022; Liu et al., 2018; Moolman et al., 2023). Lattice selection in design for additive manufacturing (DfAM) and manufacturability considerations have been important areas of research in the recent years (Bari and Arjunan, 2019; El-Sayed et al., 2020; Wang et al., 2017). In orthopaedic surgery, the DfAM focus has remained on how to tailor mechanical properties of Ti6Al4V lattice structures to best match bone mechanics. While individual DfAM studies have focused on small subsets of lattice types, porosities, feature thicknesses and pore size, there remains a need for a consolidation of findings and the synthesis of a design tool for additive manufacturing in orthopaedics. Another important consideration often overlooked is the manufacturability of complex lattices designs; a DfAM tool is needed to identify manufacturability concerns with bone-matching lattice designs.

1.1 Global Thesis Objectives

This thesis brings together three distinct themes: (1) multiaxial spinal load simulation, (2) spinal implant evaluation and (3) metal additive manufacturing. Novel research across each of these themes seeks to address the following global thesis objectives:

1) Improving pre-clinical spinal implant testing methodologies by incorporating more physiologically representative loading conditions will allow us to better understand and prevent mechanisms of clinical implant failures; and
2) By developing new tools to better understand emergent LPBF additive manufacturing technologies we can best leverage AM for spinal implant design and manufacturing.

1.2 Thesis Layout

This thesis follows an integrated article format. The present chapter, Chapter 1, aims to provide an overview of the background, objectives and hypotheses, and need for the thesis work. Chapter 2 provides a more in-depth review of the literature surrounding the topics covered in the investigation chapters of the thesis. Chapters 3 – 9 are individual investigations towards one or more of the three thesis theme areas (Figure 1.2). It is of note that each Chapter abstract adheres to the format of the journal of publication, review or submission. Chapter 10 provides a summary of the thesis with focus on global research contributions, strengths and limitations, and future work.

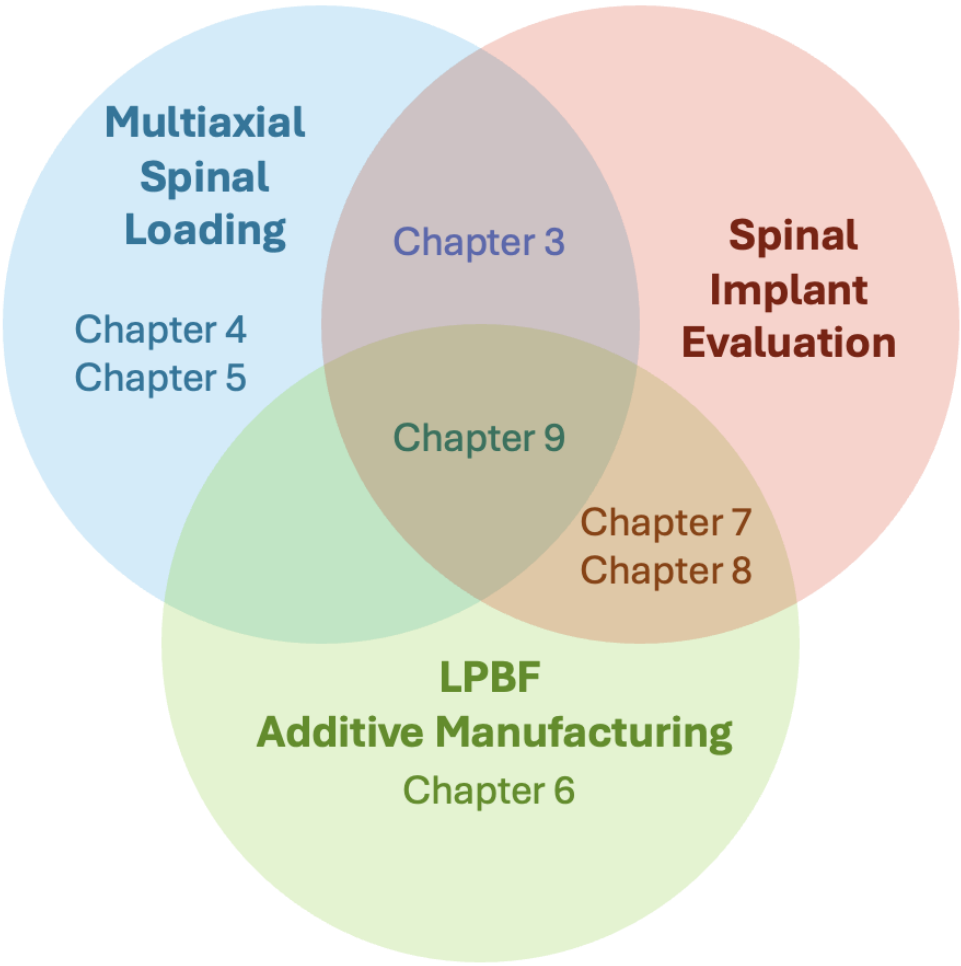


Figure 1.2: The three major themes of this thesis and the associated research studies conducted in each Chapter have been added to a Venn Diagram to highlight the interconnectivity of the thesis work.

1.3 Outline of Thesis Chapters

Each experimental chapter of the present thesis is outlined below. A brief overview of the chapter is included, along with the specific objectives and hypotheses. Any direct connections to other thesis chapters are stated.

Chapter 3: A Biomechanical Investigation of Multiaxial Pedicle Screw Loosening in Osteoporotic Human Vertebral Bone

Chapter 3 contains an *in vitro* human cadaveric investigation towards the impact of uniaxial vs. multiaxial loading on pedicle screw loosening. This chapter aimed to address the first global objective and includes research related to themes 1 and 2.

Specific Objectives (SO3): (SO3a) to develop and evaluate a biomechanical test method to simulate multiaxial loading of lumbar pedicle screw fixation, and (SO3b) assess screw loosening outcomes relative to traditional uniaxial toggle testing through a repeated measures study design.

Hypothesis (H3): multiaxial loading will accelerate pedicle screw loosening, resulting in decreased screw fixation and increased volumetric bone deformation.

Thesis Context: This chapter informed how multiaxial loading accelerates implant loosening when compared to uniaxial loading. This also provided the basis for further investigation of the impact of physiologically-derived loading on spinal implants such as those in Chapters 4 and 5.

Chapter 4: Biomechanical comparison of human cadaveric lumbar motion segments under simple and physiologically-derived loading conditions

Chapter 4 contains an *in vitro* human cadaveric investigation towards establishing a commercially available joint motion simulator as a spinal loading simulator. This chapter aimed to address the first global objective and includes research related to theme 1.

Specific Objectives (SO4): to assess the ability of a commercially available joint motion simulator to accurately replicate the complex physiological loads experienced by the human lumbar spine and investigate the effects of (SO4a) loading rate (quasi-static vs dynamic), (SO4b) control method

(force vs displacement control), and (SO4c) degrees-of-freedom of the loading waveform (pure moment vs physiologically derived) on lumbar spine biomechanics.

Hypotheses (H4): By comparing outlined parameters, this study will provide new data as steps towards validation of a six degree-of-freedom spine motion simulator. It is hypothesized lumbar segment ROM would be smaller under dynamic test rates than quasi-static test rates (H4a), ROM would not differ between force and displacement (H4b), and ROM would be smaller under physiologically-derived loads than pure moment loading (H5c).

Thesis Context: This chapter provides validation of a test protocol for existing test practices (pure moment bending), a novel physiologically derived test protocol and evaluation of test parameters such as test rate and control method. The findings of this study were used to evaluate a novel additively manufactured interbody cage in Chapter 9.

Chapter 5: Cyclic in vitro simulation of physiologically-derived gait and sit-to-stand loading on the lumbar spine

Chapter 5 contains an *in vitro* human cadaveric investigation towards establishing a test protocol for simulated activities of daily living, gait and sit-to-stand. This chapter aimed to address global thesis objective 1 and has research focused on thesis theme 1.

Specific Objectives (SO5): (SO5a) To develop a novel *in vitro* testing method to apply cyclic 6DOF loading waveforms associated with sit-to-stand and gait activities, and (SO5b) compare lumbar spine kinematics before and after simulation of 10,000 cycles of gait loading.

Hypotheses (H5): (H5a) by employing general PID controller tuning sit-to-stand and gait loading can be reliably simulated at quasi-static and dynamic rates and, (H5b) by employing iterative

learning control, a 6DOF complex loading protocol can be applied in force control at a physiologic rate with minimal error over longitudinal cyclic testing.

Thesis Context: This chapter evaluates the feasibility of applying complex 6DOF physiologically derived movements at physiologic frequencies in force-control. The findings of this study were used to evaluate a novel additively manufactured interbody cage in Chapter 9.

Chapter 6: Architectural bone parameters and the relationship to titanium lattice design for powder bed fusion additive manufacturing

Chapter 6 contains a literature review on the current state of titanium and titanium alloy lattice design for laser powder bed fusion additive manufacturing for bone repair and replacement applications in orthopaedics. This chapter aimed to address the second global objective and includes research related to thesis theme 3.

Specific Objective (SO6): To provide a comprehensive review of existing additive manufacturing literature to determine which titanium lattice parameters have been examined for bone replacement and repair implants.

Hypothesis (H6): Recommendations will be made on how to best use this information towards the design and additive manufacturing of improved titanium and Ti6Al4V lattice structures for bone replacement and repair.

Thesis Context: This chapter includes development of a design tool for lattice porosity selection for orthopaedic implants based on target bone mechanical properties which was used to develop a lumbar interbody cage in Chapter 8 which was used for evaluation in Chapter 9.

Chapter 7: A manufacturability evaluation of complex architectures by laser powder bed fusion additive manufacturing

Chapter 7 contains a manufacturability evaluation of the lattices reviewed in Chapter 6. Lattices were manufactured in maraging steel and surface geometry, and internal defects were measured to comment on manufacturability of each lattice through laser power bed fusion. A manufacturability tool was developed and validated on orthopaedic implants designs. This chapter aimed to address global thesis objective 2 and includes thesis themes 2 and 3.

Specific Objective (SO7): To examine the manufacturability of common lattice structures using laser powder bed fusion based on geometric and defect analysis.

Hypothesis (H7): Surface based lattices such as gyroid and Schwarz lattices will prove to be the most manufacturable based on the known challenges of printing down-skin surfaces with an angle of less than 45 degrees to build plate.

Thesis Context: The design tool generated in this chapter was used to develop a lumbar interbody cage in Chapter 8 which was used for evaluation in Chapter 9.

Chapter 8: Design and Manufacturability of Compliant and Anatomically Optimized Spinal Implants using Laser Powder Bed Fusion Additive Manufacturing

Chapter 8 includes a design overview of a lumbar interbody cage designed for manufacture through laser powder bed fusion additive manufacturing. This chapter aimed to address global thesis objective 2 and includes thesis themes 2 and 3.

Specific Objective (SO8): to utilize the design tools developed in Chapters 6 and 7 to design a lumbar interbody cage and assess manufacturability.

Hypothesis: As a design report, this chapter has no formal scientific hypotheses.

Thesis Context: The lumbar interbody cage described in this chapter was designed using the design tools established in Chapters 6 and 7 and evaluated in Chapter 9 using the protocols established in Chapters 4 and 5.

Chapter 9: An in vitro investigation of lumbar interbody cage migration under physiologically-derived loading conditions

Chapter 9 contains an *in vitro* human cadaveric investigation towards the performance of an additively manufactured, latticed, interbody cage under pure moment and physiologically derived gait loading protocols. This culminating study aimed to address global thesis objectives 1 and 2, and includes thesis themes 1, 2, and 3.

Specific Objective (SO9): To examine how loading conditions associated with different spinal movements impact lumbar interbody cage migration and subsidence.

Hypothesis (H9): Spinal movement, particularly flexion-extension, would exacerbate cage migration and subsidence when compared to other spinal movements.

Thesis Context: Findings from Chapter 3 encouraged the investigation of multiaxial loading on other spinal implants, such as interbody cages. The established pure moment protocol from Chapter 4 and physiologically derived gait protocol from Chapter 5 were used to evaluate the interbody designed in Chapter 8 using the tools established in Chapters 6 and 7.

Chapter 2- Background Literature

There are seven sub-sections of this Background Literature chapter, each focused on providing context for the clinical and engineering aspects of the research conducted: (1) spine anatomy, (2) spine biomechanics, (3) spine pathology, (4) orthopaedic instrumentation, (5) design and manufacturing of spinal implants, (6) spinal implant testing, and (7) spinal loading simulation. The background literature on powder bed fusion (PBF) additive manufacturing for applications in orthopaedic surgery is covered in detail in the review article forming Chapter 6 of this thesis. Therefore, background literature on additive manufacturing is not included in this Chapter.

2.1 Anatomy of the Lumbosacral Spine

The lumbosacral region of the human spinal column consists of five lumbar vertebrae, described as L1 to L5 in descending order, and the sacrum, the large, fused triangular bone at the base of the spine. The lumbosacral spine acts to support weight of the head and trunk and transfers loads from the upper body to the legs through the pelvis, as the upper body moves through flexion/extension, lateral bending and rotation during activities of daily living. The International Organization for Standardization (ISO) 2631 standard defines the three-dimensional (3D) coordinate system for the spine (Figure 2.1).

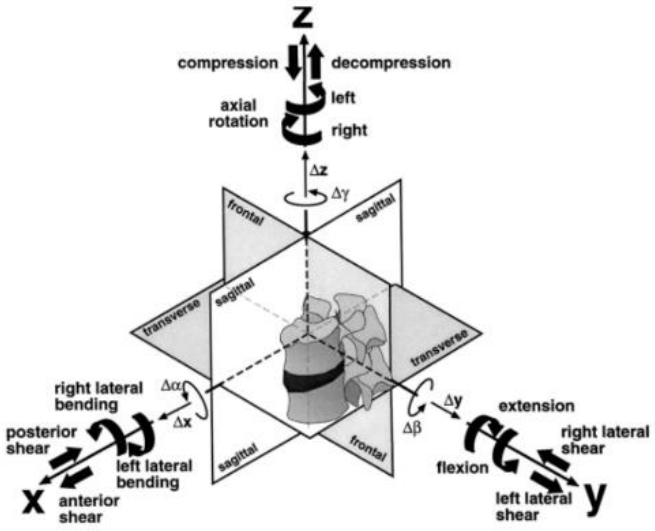


Figure 2.1: Wilke et al., established test alignment recommendations allowing for the standardization of *in vitro* testing of spinal implants across research labs (Wilke et al., 1998).

2.1.1 Bony Anatomy

Lumbar vertebrae consist of a vertebral body, two endplates, two pedicles and the vertebral arch including the spinous process, transverse processes, vertebral foramen and laminae (Figure 2.2). The vertebral body is primarily comprised of trabecular bone with a thin cortical shell which allows for lightweight, distributed load transfer. The posterior elements of the vertebral arch are mainly dense cortical bone, to support soft tissue attachments and protection of neural structures.

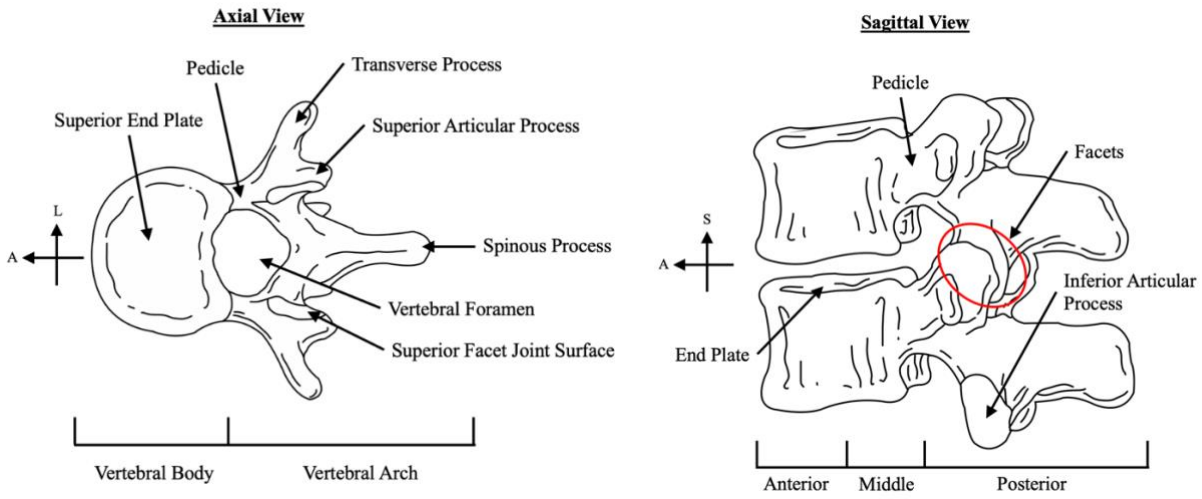


Figure 2.2: Left: An axial top-down view of a lumbar vertebrae is shown to distinguish the vertebral body from the vertebral arch and indicate the location of the anatomical features. L and A indicate the lateral and anterior directions respectively. **Right:** A sagittal view of the two lumbar vertebrae is used to describe the location of the facet joint (red circle) formed between adjacent vertebrae. Orientation is described where S and A indicate the superior and anterior directions respectively. The spine can be divided into three columns: anterior, middle and posterior as described by Francis Denis (Denis, 1983).

The sacrum is a triangular bone located inferior to the lumbar spine and superior to the coccyx made up of five fused segments described as S1-S5 in descending order (Figure 2.3). Segments 1-3 have transverse processes that are fused together to form the alae which articulate with the pelvis to form the sacroiliac joints. The sacrum has a bony process along its posterior surface called the median ridge that acts as an attachment point for ligaments. The sacrum has only one endplate, located at the superior S1 vertebra, which articulates with L5 of the lumbar spine.

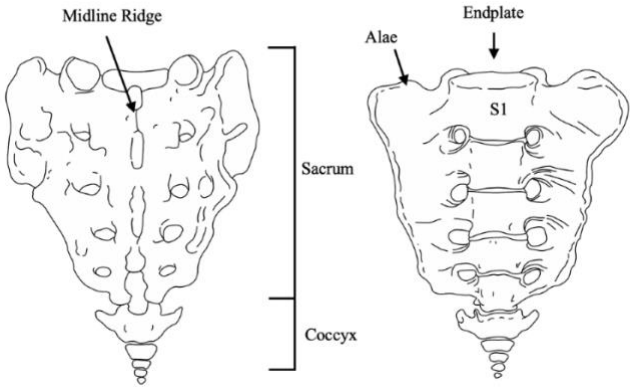


Figure 2.3: Left: A posterior view of the sacral spine (left) shows the location of the midline ridge and distinguishes between the sacrum and the coccyx. **Right:** An anterior view of the sacral spine shows the superior S1 endplates, and the fused transverse processed which make up the alae.

2.1.2 Soft Tissue Anatomy of the Lumbar Spine

The soft tissues of the lumbar spine play a critical role in providing stability, flexibility, and protection to the vertebral column (Figure 2.4). The intervertebral disc is composed of a tough outer ring, the annulus fibrosus, and a gel-like center called the nucleus pulposus. These discs act as shock absorbers and provide flexibility between the vertebrae. The ligamentum flavum is a strong elastic ligament that connects the laminae of adjacent vertebrae and aids in maintaining spinal alignment and flexibility. The anterior longitudinal ligament runs along the front of the vertebral bodies, providing stability and preventing excessive extension of the spine. In contrast, the posterior longitudinal ligament is located along the back of the vertebral bodies and helps to limit spinal flexion. The intertransverse ligaments connect the transverse processes of adjacent vertebrae and contribute to lateral stability. Similarly, the interspinous ligament connects the spinous processes and helps limit excessive spinal flexion. Extending over the top of the spinous processes is the supraspinous ligament, which plays a supportive role in maintaining the alignment of the vertebral column during movement. Finally, the facet capsular ligaments surround the facet joints, providing additional stability while allowing controlled movements between the vertebrae.

These soft tissues work together to protect the spine, allow complex movements, and maintain structural integrity and joint congruency.

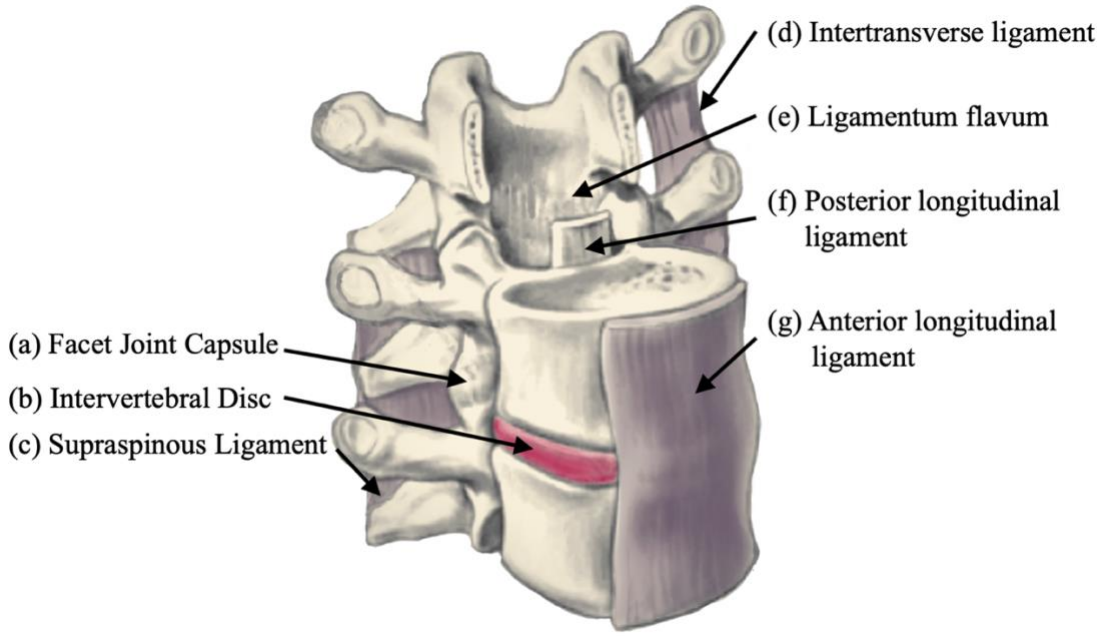


Figure 2.4 The soft tissues of the lumbar spine include the (a) facet joint capsule, (b) intervertebral disc, (c) supraspinous ligament, (d) intertransverse ligament, (e) ligamentum flavum, (f) posterior longitudinal ligament, and (g) anterior longitudinal ligament.

2.1.3 Joint Anatomy

Gross movements of the lumbosacral spine are achieved by compounded smaller movements at individual functional spinal units (FSU). An FSU consists of two adjacent vertebrae, a shared intervertebral disc (IVD), two facet joints and the surrounding ligaments and is capable of movement in six degrees-of-freedom (6DOF). Vertebrae articulate with one another in through the IVD and at the bilateral facet joints. The IVD is comprised of the ligamentous annulus fibrosus and the gel-like nucleus pulposus and forms a fibrocartilaginous joint between the vertebral endplates. Structurally, the IVD allows for movement between adjacent vertebral bodies while holding them together. The facet joint is a synovial joint located between superior and inferior

articular surfaces of adjacent vertebrae. In the lumbar spine, orientation of the facet joints protects against anterior shear forces and constrains rotational and flexural movements while allowing the posterior elements to articulate and glide past one another. Each FSU has two facet joints that, in addition of the IVD, comprise the articular triad. The lumbosacral joint exists between the most inferior lumbar vertebrae (L5) and the superior sacrum (S1) and can therefore be referred to as the L5-S1 FSU (Figure 2.5). The lumbosacral joint facilitates the transition in spinal curvature from the lordosis of the lumbar spine to the kyphosis of the sacrum. The unique anatomy and orientation of the L5-S1 joint induces a greater amount shear loading and biomechanical stress than in the superior FSUs, making the L5-S1 FSU more susceptible to injury and degeneration, and the need for repair through surgical intervention.

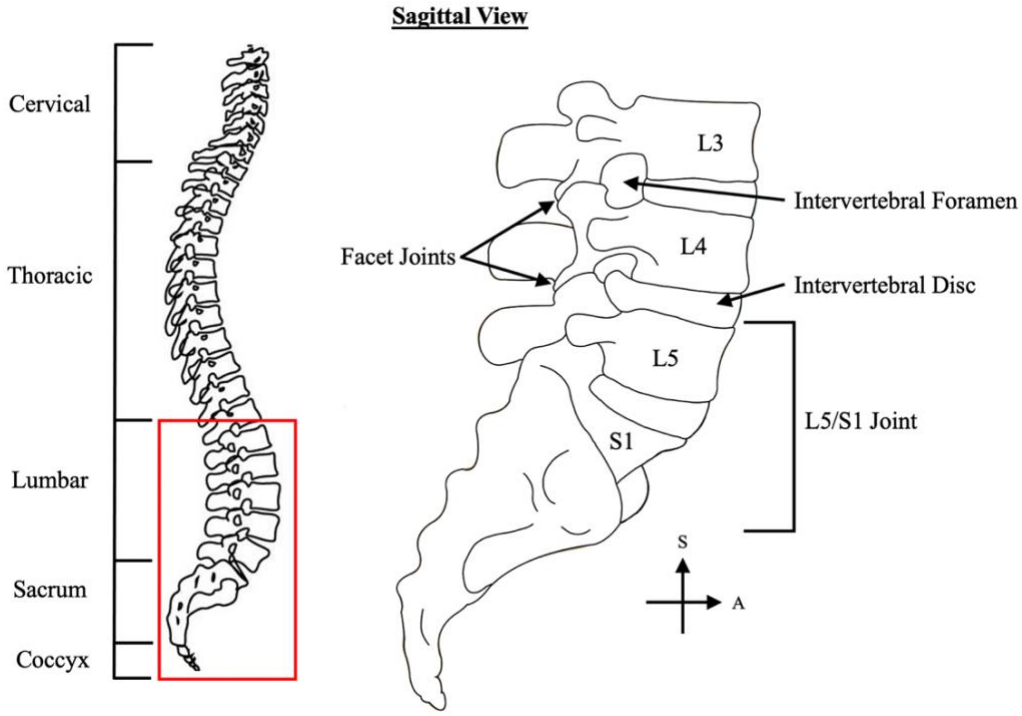


Figure 2.5: Left: A sagittal view of the whole spine depicts the five regions: cervical, thoracic, lumbar sacral and coccygeal. **Right:** A sagittal view of the lumbosacral spine is used to describe a functional spinal unit (FSU), consisting of two adjacent vertebrae and their shared intervertebral disc. The lumbosacral joint or L5-S1 FSU is highlighted. Orientation is described where S and A indicate the superior and anterior directions respectively.

2.1.4 Curvature of the Spine and Associated Pelvic Parameters

A healthy spine is aligned in the frontal and transverse planes with an S-shaped curve in the sagittal plane. Frontal and transverse alignment is often referred to as spinal balance and deviations in the frontal plane are often used to diagnose scoliosis. Spinal curves in the sagittal plane are described as lordosis (or backward curving) and kyphosis (or forward curving). Lordosis is found in the cervical and lumbar spine whereas kyphosis is present in the thoracic spine and sacrum. The normal sagittal curvature of the spine allows for a wide range of motion while withstanding the loads present during activities of daily living. Typical human aging results in a loss of lordosis in lumbar spine which significantly increases stress and loading.

2.2 Biomechanics of the Lumbar Spine

2.2.1 Activities of Daily Living

The lumbar spine undergoes a range of cyclic loading in 6DOF throughout activities of daily living (ADL). The three primary spinal movements are flexion/extension, lateral bending and axial rotation and can generally be described as the rotation about the sagittal, frontal, and transverse planes, respectively. The most common spinal movement is forward flexion in the sagittal plane (Rohlmann et al., 2014). In a study completed by Rohlmann et al., lumbar spine flexion was examined in 208 healthy volunteer participants over the course of 24 hours. Participants averaged 4,400 sagittal movements per day, with 66% of those being within 5-10 degrees of neutral lordosis. Female participants performed significantly more sagittal plane movements (29%) than male participants. Over the 24-hour period examined, the lumbar spine was in the 10-40 degrees of flexion for 15.1 hours and only 24 minutes in extension (Rohlmann et al., 2014). These results provide an estimation of the frequency of healthy sagittal movements of

the lumbar spine, an important consideration in the development of in vitro testing protocols. Yet, movement of the lumbar spine often involves combined rotation and translation to complete ADLs, such as walking, lifting, stair climbing and sit-to-stand movements. Therefore, in vitro testing should also attempt to include 6DOF loading modes to more closely replicate ADLs.

2.2.2 Lumbar Spinal Loading

The lumbar spine is capable of 6DOF movement and joint loading. Applied muscle loads and joint reaction forces have been measured and approximated through *in vivo* measurements, *in vitro* experiments and advanced musculoskeletal models. Loads attributed to lumbar flexion and extension movements are often described as bending moments occurring in the sagittal plane (M_y), in accordance with the ISO test standard developed by Wilke et al. (Wilke et al., 1998). Axial rotation and lateral bending loads are primarily described as rotational bending moments in the axial (M_z) and frontal (M_x) planes, respectively (Figure 2.1) (Wilke et al., 1998)(Seth et al., 2018). Translational forces can also occur along the x-, y- and z-axes and typically described as anterior/posterior shear (F_x), lateral shear (F_y) and compression (F_z), respectively (Wilke et al., 1998).

Biomechanical models have been developed to understand loading in the lumbar spine during various postures and activities, with a wide range of load values reported. Historically, loads in the lumbar spine were approximated experimentally by measuring *in vivo* intradiscal pressures and myoelectric signals, but this yielded limited information in terms of multiaxial loading (Schultz et al., 1982). Schultz et al. measured *in vivo* intradiscal pressure at the L3-L4 IVD to calculate compressive loads (F_z) during standing and seated spine movements. It was reported that compressive loads at the L3 disc averaged 1190 N, 710 N and 470 N for standing spinal flexion, lateral bending and axial rotation, respectively (Schultz et al., 1982). More recently,

advanced numerical finite element (FE) and rigid-body musculoskeletal (MSK) models have been developed to better estimate the resulting multiaxial loads on the lumbar spine during various postures and activities such as forward flexion, lateral bending, axial rotation, standing postures (Figure 2.6) (Arjmand and Shirazi-Adl, 2006; Shirazi-Adl et al., 2005). Shirazi-Adl et al. reported approximated loads for the lumbar spine with varying muscle contraction during static standing. Lumbar compression, shear and flexion moment were all greatest at L5 and ranged from 404-720 N (compression), 147-322 N (anterior), 0.8-1.3 Nm (flexion), respectively (Shirazi-Adl et al., 2005). Arjamand & Shirazi-Adl estimated lumbar loads during unweighted and weighted spinal flexion through musculoskeletal modelling. Loads were greatest at L5 and increased with flexion and measured 2332 N, 506 N and 31.5 Nm in compression, anterior shear and flexion moment (Arjmand and Shirazi-Adl, 2006).

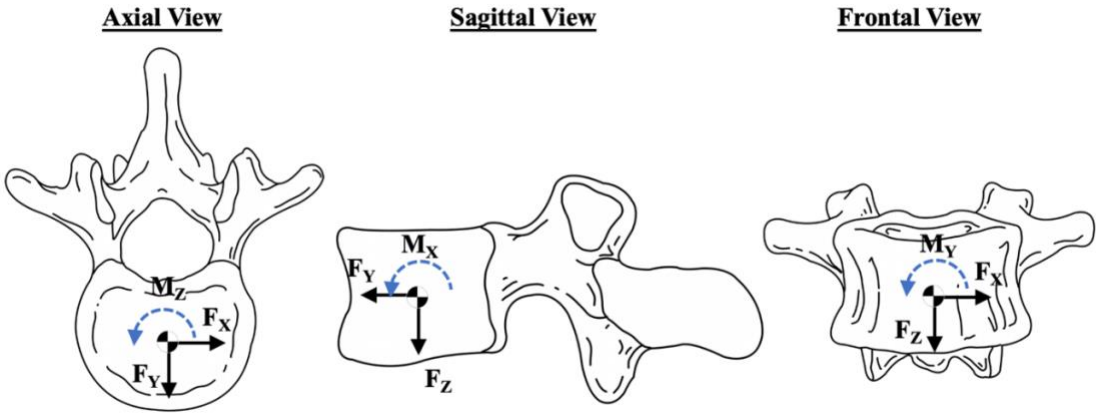


Figure 2.6: Three views of a lumbar vertebrae, axial (left), sagittal (centre), frontal (right) are used to describe the different loads experienced in the lumbar spine with reference to the local vertebral coordinate system.

MSK models are used to estimate joint reaction forces during discrete and combined movements of the spine. OpenSim (Stanford, CA, USA) is an advanced open source MSK modeling software for rigid body kinematic simulations and has been used recently approximate applied muscle loads in the spine (Seth et al., 2018). A musculoskeletal model for the lumbar spine

was initially developed by Christophy et al. to model muscle loads associated with the three major lumbar spine movements, flexion-extension, lateral bending and axial rotation (Christophy et al., 2012). This original work has been further developed and the current version includes a rigid pelvis and sacrum, five lumbar vertebrae with three rotational degrees of freedom, and thoracic spine and ribcage. While MSK models can provide insight into lumbar spine joint loads, the limitations of rigid body models prevent fully accurate representation of *in vivo* loading, especially following injury and repair.

While experiments and models can provide valuable insights into lumbar spinal loading, *in vivo* load measurement is the most accurate, yet invasive, method of determining spinal loads. The OrthoLoad group at The Julius Wolff Institute at the Charite Hospital in Berlin in Germany collected *in vivo* loading data from a variety of instrumented implants, providing an important physiologic benchmark for evaluating models of lumbar spine load magnitudes. Subsets of their original data have been made publicly available for research use including those measured from two different spinal implants, a vertebral body replacement and an internal spinal fixator (Figure 2.7) (Dreischarf et al., 2015; Rohlmann et al., 1999). Maximum compressive loads measured in the vertebral body replacements during standing flexion averaged 565 N, where standing loads average 330 N (Dreischarf et al., 2015). The *in vivo* compressive load and sagittal plane moment measured in the internal spinal fixator were 80N and 3.5 Nm in flexion, respectively. These datasets provide *in vivo* 6DOF loads measured in healthy participants in a wide range of positions and during activities of daily living. This unique data is invaluable for improving implant testing methods and biomechanical models; however, it is not without limitations. Due to the invasive nature of data collection, loads were only measured from a small set of the subjects (n=5 for vertebral body replacements, n=10 for internal spinal fixator) in only a few vertebral levels and

there was large intra-participant variability. Additionally, loads were measured post-operatively and using only a single design for each implant type. Therefore, these 6DOF load magnitudes must be carefully analyzed to accurately represent *in vivo* loading in computational modeling and implant testing.



Figure 2.7: The Orthoload group developed two telemeterized spinal implants, a vertebral body replacement (left) and an internal spinal fixator (right). Six degree of freedom loads were measured *in vivo* during activities of daily living and the data has been made open source (www.orthoload.org; Dreischarf et al., 2015; Rohlmann et al., 1999) (www.orthoload.com).

2.2.3 Biomechanical Properties of Vertebral Bone Tissues

Bone is a tough, elastic tissue that forms the structural foundation of the human body. As a living tissue, bone adapts to its mechanical environment and loading conditions through the breakdown of exiting bone by osteoclasts and the proliferation of new bone by osteoblasts. This process leads bone to exhibit mechanoresponsive behavior, wherein the more it is loaded the thicker and denser it becomes.

Bone tissues are categorized into two main types: cortical bone and trabecular bone. Trabecular bone, or cancellous bone, is a lattice-like structure that allows bones to maintain their strength while keeping them relatively lightweight. Trabecular bone is primarily located at the metaphysis of long bones and in the body of short bones, which allows for improved load transfer

through these structures. The exact configuration of trabecular bone micro-structure is still being discovered. The most established theory characterizes the trabeculae, or struts, by their thickness, spacing, number and configuration (Hildebrand et al., 1999). Measurement techniques for these parameters using micro-computed tomography are well established to comparatively describe trabecular bone quality, with more and thicker trabeculae indicating better bone health (Majumdar et al., 1997). However, emerging and more advanced geometric models consider the shape of trabecular surface and rod versus plate-like structures in greater detail (Callens et al., 2020; van Lenthe et al., 2006). Trabecular bone properties vary significantly with respect to bone density. The porosity of human trabecular bone ranges from 40-95% depending on skeletal location, bone region and population parameters. Stiffness and strength of trabecular bone is greatest in the axial direction, and similar in the transverse directions. The elastic modulus, or stiffness, of trabecular bone can range from 1-5 GPa in the axial direction and 50-700 MPa off-axis, transverse direction. The compressive and tensile strength of trabecular bone ranges from 0.1-30 MPa and 6-8 MPa, respectively (Long and Bartel, 2006; Park and Lakes, 2007; Velasco et al., 2015). The vertebral body consists primarily of trabecular bone and therefore trabecular bone strength and stiffness plays an important role in bone-implant mechanics.

Cortical bone, or compact bone, is much more dense than trabecular bone and acts as a stiff outer layer for short bones, joint surface in long bones and the sole composition of the hollow shafts in long bones. The outer cortical shell allows for a flat surface for ligamentous and tendonous attachment. Cortical bone improves the overall fracture toughness and also provides the required structural integrity and strength for spinal implant fixation in the pedicles. Cortical bone is transversely isotropic, where the mechanical properties along the axial direction are greater than those in the transverse axes. The mechanical properties of human cortical bone have been collated

and are illustrated in Figure 2.8 (Burstein et al., 1976; Long and Bartel, 2006; Park and Lakes, 2007). Due to the increased strength and density of cortical bone, improved spinal implant fixation may be achieved by maximizing the cortical bone contact.

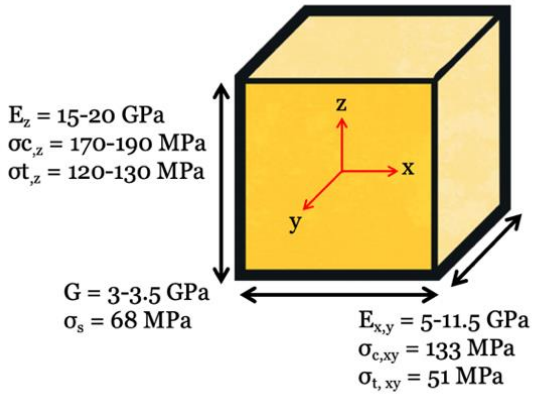


Figure 2.8: Cortical bone exhibits transversely isotropic mechanical properties which are greatest in the longitudinal axis. In the longitudinal axis, the elastic modulus, compressive strength and tensile strength range from 15-20 GPa, 170-190 MPa and 120-130 MPa, respectively. In the transverse directions, the elastic modulus, compressive strength and tensile strength are 5-11.5 GPa, ~133 MPa and ~55 MPa, respectively (McGregor et al., 2021).

Bone is a living tissue and has the ability to repair itself through osteogenic remodeling following mechanical damage, known as Wolfs LawClick or tap here to enter text.. However, fatigue failure of bone may occur when bone damage accumulates faster than remodeling can occur (Kaplan et al., 1994). The most common form of fatigue failure is known as a stress fracture, which are common in the lumbar spine, particularly in older adults (Hansson et al., 1987). Fatigue failure of bone may also be responsible for implant loosening and subsidence in spinal fixation constructs due to microstructural bone damage at bone-implant interface.

2.3 Lumbar Spine Pathology

The biomechanics of the lumbar spine change naturally with age; however, spinal deformity, injury and disease can accelerate this process. These conditions alter the functional mechanics of the spine by disruption to the soft tissues, changes in bone tissue and/or by loss of joint stability and mobility. A brief overview of spinal deformity, injury and disease and how each pathology alters lumbar spine mechanics is provided.

2.3.1 Spinal Deformities

Spinal deformities alter the natural alignment and/or curvature of the spine and can influence loading on the spine. A well-recognized spinal deformity is scoliosis, most commonly characterized by curvature in the frontal plane. Scoliosis is common, experienced by roughly 3% of the population (Hawes and O'brien, 2006). The severity of scoliosis is variable and also at risk of progression; therefore, patients must be monitored for changes in spinal curvature on an ongoing basis following diagnosis. This is thought to be due to the asymmetric loading of the spinal column. Progressive curvature of the spine can be minimized by re-alignment of the spine through bracing or surgical fixation to restore normal load patterns through the spine (Hawes and O'Brien, 2006). Surgical fixation of the scoliotic spine often requires long constructs that span the thoracic and lumbar spine with fixation extending to the sacrum or pelvis. In these long constructs, there is an increased risk of implant loosening at the ends of the construct due to the transfer of large bending loads (Kim et al., 2006; Weistroffer et al., 2008). Therefore, implant loosening in the lumbar spine following surgical correction of scoliosis is an unresolved problem of clinical need.

2.3.2 Spinal Injuries

Injuries to the lumbar spine may be acute or chronic. Traumatic bone fracture is an example of an acute injury that alters biomechanics, loading and integrity of the lumbar spine. Lumbar vertebrae are also susceptible to stress fractures, or spondylolysis, which can occur due to prolonged repetitive loading above the fatigue strength threshold of bone. Vertebral fractures can also lead to mechanical instability and the need for surgical stabilization (Stemper et al., 2015). With vertebral bone fractures, there is always a risk of disruption to adjacent neural tissues, which may lead to numbness, weakness or, in severe cases, paralysis. Therefore, re-establishing mechanical stability of lumbar fractures is imperative to the reinstating not only spinal function and mobility, but also for the protection of vulnerable neural tissues.

2.3.3 Degenerative Spinal Disorders

Various degenerative bone and joint diseases contribute to changes in spine biomechanics, often requiring surgical correction to restore normal joint loading and stability. For example, osteoporosis is the loss of bone density and mechanical strength that comes with age or other environment co-factors. The loss of mechanical strength due to osteoporosis increases the risk of vertebral fracture, implant loosening and the need for revision surgery following spinal fixation (Khalid et al., 2020; Myers and Wilson, 1997; Ponnusamy et al., 2011). The mechanical quality of bone tissue therefore needs to be considered in both design and testing of spinal implants.

Degenerative disc disease is the progressive degradation of the intervertebral disc between two vertebrae resulting in loss of disc height and stability (Figure 2.9). As the intervertebral disc space collapses compressive loads applied to the posterior vertebral elements may increase. This can cause compression of nerve roots and/or increased compressive and shear loading facet joints.

Increased loading in the facet joints can lead to joint arthritis, the painful loss of articular cartilage that supports normal joint function and mobility (Cornaz et al., 2021; Dunlop et al., 1984).

Spondylolisthesis is a degenerative spinal condition in which the superior vertebra translates anteriorly (forward) with respect to the vertebra below it (Figure 2.9). Spondylolisthesis can occur with degeneration of the intervertebral disc, bone fracture or congenital deformity that compromises the mechanical integrity of the FSU. The translation of the superior vertebra may cause narrowing of the foramen and compression of the nerve roots resulting in leg and low back pain. In this case, surgical correction may be required to restore spinal alignment and reduce pain.

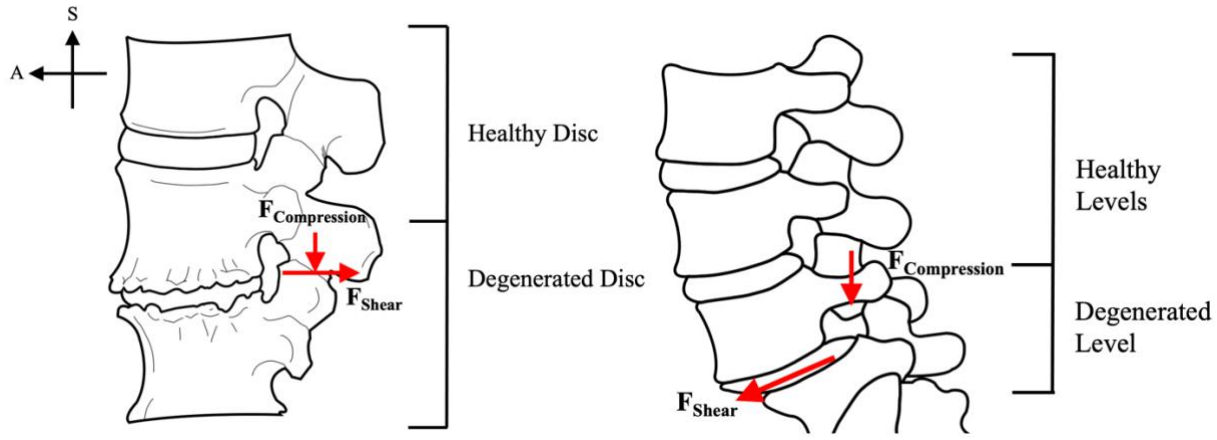


Figure 2.9: Left: Two functional spinal units (FSU) are used to show the changes to joint biomechanics that may occur due to degenerative disc disease. The superior FSU shows healthy loading about the vertebrae and facet while the red arrows on the inferior FSU depict increased compressive and shear loading at the facet joints with degeneration. **Right:** Spondylolisthesis causes anterior translation of the superior vertebrae (L5) with respect to the inferior vertebrae (S1). This misalignment alters joint biomechanics and may increase shear force between the vertebrae and compression in the nerve root foramen.

In stabilizing adjacent vertebrae with spinal instrumentation, a rigid construct is formed that can be considered to act as a single unit biomechanically. This loss of vertebral range of motion means the soft tissues from the adjacent vertebral levels (i.e., intervertebral discs and facet joints) must compensate to maintain mobility during activities of daily living. This may cause increased

wear and degeneration at the adjacent level tissues to a fusion construct (Ekman et al., 2009). This phenomenon is known as adjacent segment disease and is more prevalent with longer fusion constructs (Ghiselli et al., 2004; Kobayashi et al., 2018).

2.4 Orthopaedic Instrumentation

Lumbar fusion is a surgical approach used to restore spinal alignment and eliminate vertebral motion for treatment of a wide range of spinal disorders including deformities, traumatic injuries and degenerative diseases that cause debilitating low back pain and/or joint instability. Spinal implants are often used to immobilize the FSU while bone fusion occurs, typically across the intervertebral disc space. Surgical access to the lumbar spine is most commonly achieved through a posterior approach, known as posterior lumbar interbody fusion or PLIF, in which a low back incision and muscle retraction are used to gain access to the posterior elements of the L5 and S1 vertebrae (Figure 2.10). Lumbar interbody fusion may also be completed using different trajectories such as lateral (LLIF), transforaminal (TLIF) or anterior (ALIF) surgical approaches.

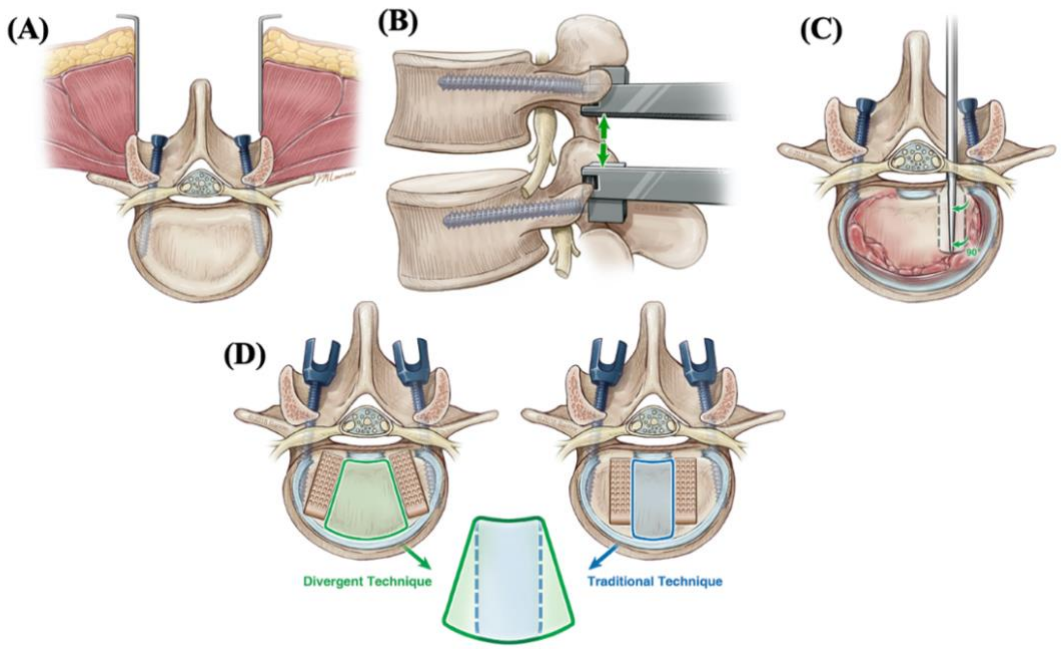


Figure 2.10: A visual step-by-step overview of the posterior lumbar interbody fusion (PLIF) procedure has been adapted from (Bohl et al., 2018). **(A)** Skin incision and distraction of the muscular tissues, with screws inserted in the pedicles. **(B)** A screw implant is placed in each pedicle for rigid fixation. Screws may be used to distract the disc space to improve decompression treatment. **(C)** The nucleus pulposus is removed and the endplates prepared for cage placement. **(D)** Interbody cage(s) are inserted in the disc space to restore disc height, provide anterior column support, and act as a scaffold for bone ingrowth.

In PLIF procedures screw implants are placed in both the left and right pedicles of the superior and interior vertebrae in order to maintain mechanical stability while fusion occurs. The nucleus pulposus is removed from the intervertebral disc and the endplates are lightly scraped to improve cage fixation and bone ingrowth. Interbody cages are inserted into the intervertebral disc space using cage specific tools. Interbody cages are often augmented with human bone allografts to encourage bone in-growth through the disc space and a stable fusion. Vertical rods connect the screws of the superior and inferior vertebrae, establishing a four-point fixation system (Figure 2.11). Together, the implant construct aims to provide rigid mechanical stability, which is most critical during the first six months post-operation, with bone fusion typically occurring between 3-6 months.

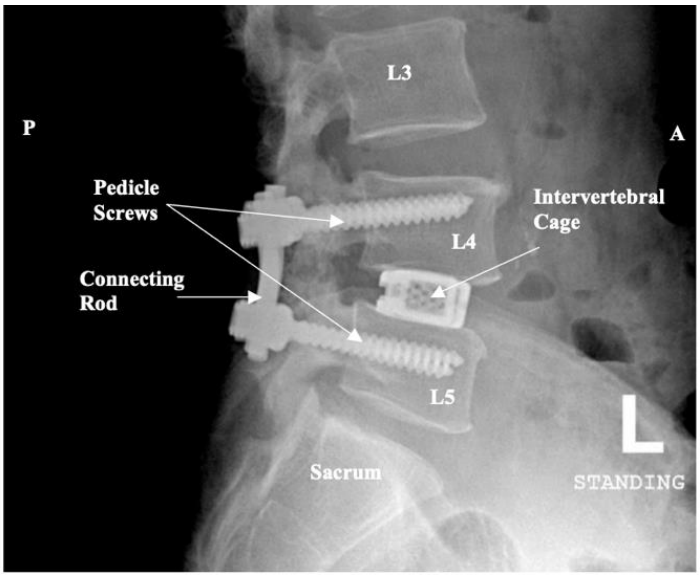


Figure 2.11: Fixation of a functional spinal unit, L4-L5 above, can be achieved using of three implant types: pedicle screws, connecting rods and intervertebral (interbody) cages (McLachlin, 2008a).

2.5 Design and Manufacture of Spinal Implants

2.5.1 Pedicle Screw Design

Pedicle screw implants are critical to posterior lumbar fixation systems as they provide rigid three-column fixation through the dense, cortical bone of the pedicle, enabling multi-level fusion constructs. Pedicle screws may be made of stainless steel; however, they are commonly titanium alloys due to demonstrated, superior boney adhesion (Figure 2.12). The design features of a traditional pedicle screw can be manipulated to improve bone fixation. Screw pitch can be controlled such that a coarser pitch interacts with the trabecular bone of the vertebral body and a finer pitch with dense cortical bone. Screw heads have a tulip design, either as a monoaxial body with the screw shaft, or as a polyaxial tulip that can freely rotate, allowing for easier rod placement and securement (Figure 2.12).

Augmentation of pedicle screws has been examined as a means to improve the strength at the bone-implant interface and therefore reduce the risk of implant loosening. Bone cement has

been proposed; however, its use remains high risk in the spine, due to concerns with leakage and the exothermic reaction (Cho et al., 2011). Expanding screw designs have also been recently proposed and compared to bone cement, may be a safer option for increasing bone purchase in the vertebral body and pedicle (Aycan et al., 2017; Demir and Örmeci, 2014).

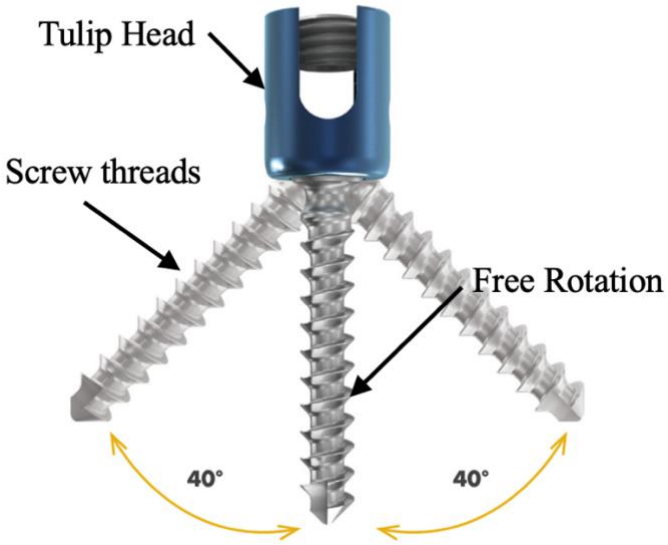


Figure 2.12: Pedicle screws are implanted in the posterior elements to achieve posterior fixation (adapted from www.precisionspineinc.ccom).

2.5.2 Interbody Cage Design

Interbody cages are an integral part of lumbar fusion systems. These devices are surgically implanted into the disc space to provide anterior column support while bone in-growth occurs through the intervertebral disc space, often through the assistance of bone allograft placed into the cage. There are many types of interbody cages aimed at facilitating fusion at different spinal levels and through a variety of surgical approaches (e.g. PLIF, TLIF, etc.). The most common materials for interbody cages are polyether-ether-ketone (PEEK), carbon fibre, and titanium/titanium alloys (Figure 2.13). Metallic interbody cage designs are often porous to reduce the implant stiffness to more closely match the mechanical properties of the vertebral bone. Yet, implant subsidence due

to the stiffness mismatch remains an unresolved clinical problem. However, the porous nature of interbody cages introduces the potential for advances in design through the use of additive manufacturing techniques.



Figure 2.13: Interbody cages are placed in the intervertebral disc space to provide anterior column stability and promote boney ingrowth. Cages are manufactured through traditional methods from Ti-alloys (left) and poly-ethylene ether ketone (centre). Additive manufacturing has been used to develop novel cages from Ti-alloys (right) (adapted from: www.stryker.com).

2.5.3 Design Opportunities through Additive Manufacturing

Additive manufacturing (AM) allows for the design and manufacturing of complicated geometries that are not attainable through more traditional manufacturing techniques. AM expands the design space for spinal implants and allows for rapid prototyping and testing. With respect to interbody cage designs, AM allows for complex latticing of titanium that may improve the known issue of implant subsidence by better matching the mechanical stiffness of vertebral bone. Despite the widespread use of titanium and titanium alloys in the orthopaedic industry, these metals do not have mechanical properties similar to bone. Titanium and titanium alloys are roughly twice as stiff as human cortical bone and up to seven times the compressive strength (du Plessis et al., 2018; Emmelmann et al., 2011; Murr et al., 2011). With the mechanoresponsive nature of bone, this stiffness mismatch can lead to stress shielding at the bone-implant interface and may ultimately lead to implant loosening and failure due to resorption of the surrounding bone (Tonino et al.,

1976). Therefore, it is imperative that implant designs be revisited with emerging technologies like AM in order to improve upon existing titanium and titanium alloy solutions.

One approach to reducing the mismatch in mechanical properties between bone and current implant materials is through design light-weighting with lattice structures in an effort to reduce mechanical properties from those of the bulk material modulus. AM allows for unique design approaches that maximize strength while minimizing weight through unique geometries and graded material properties. This technique is of particular use in the medical device industry where parts are made for specific applications with weight and mechanical performance being integral to function. Production of titanium and titanium-alloy lattice structures through AM for biomedical applications was reviewed, concluding that optimal guidelines for lattice design in biological environments have not yet been established and that the AM field is rapidly and continually evolving (Tan et al., 2017). Many studies have successfully manipulated titanium lattice parameters such as porosity, pore size and strut thickness in order to produce unit cells that exhibit stiffness, compressive strength and fatigue strength more closely to human bone. Yet, the lattice parameters vary widely across the literature and while general recommendations have been made, it is currently not clear as to which lattice structure produces the optimal structure for osseointegration and reduction of stress shielding through mechanical property optimization. Further, the manufacturability of these lattice structures at the porosities required to replicate bone properties remain challenging to quantify.

2.6 Experimental Evaluation of Spinal Implants

2.6.1 In Vitro Testing of Pedicle Screws

Historically, pedicle screw fixation has been examined through destructive *in vitro* pull-out tests in which screws are inserted into the pedicles of animal or human cadaveric specimens and removed along the screw axis (Figure 2.14) (Boos and Webb, 1997; Weinstein et al., 1992; Zindrick et al., 1986). The pull-out test has proven to be a valuable tool for comparing various biological, technique and implant design factors on pedicle screw fixation strength (Chen et al., 2014; Fölsch et al., 2012; Lotz et al., 1997). Axial pull-out testing allows for quick and reliable comparisons of factors affecting screw fixation and is still the predominant test used today (Shibasaki et al., 2020; Sumiya et al., 2021). However, pedicle screws are rarely exposed to the extreme, destructive axial loading used in pull-out testing and therefore results from these studies cannot be considered representative of the clinical failure mechanisms for pedicle screws.

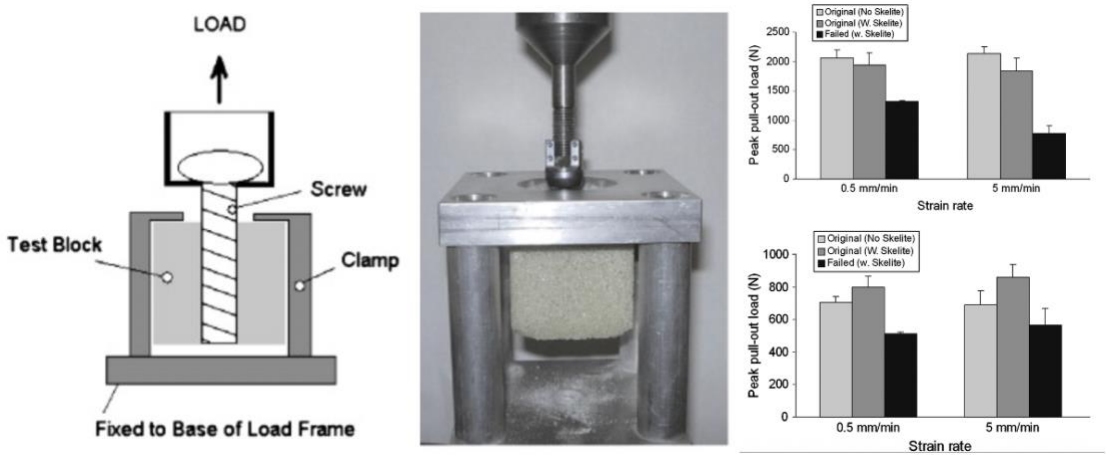


Figure 2.14: Uniaxial pull-out testing has been used historically to measure implant fixation. A screw is inserted in a foam or an animal or human vertebra (left). The implant-specimen construct is fixed to a mechanical test simulator and a tensile load is applied to the screw head along the axis of the screw (centre). Results are reported as a comparison of peak load to failure across effects (right) (Hashemi et al., 2009).

Clinically, pedicle screw failure is most often due to loosening associated with the cyclic loading of the spine causing fatigue failure at the bone-implant interface (Esses et al., 1993). Previous studies examining fatigue failure of existing spinal fixation implants have typically simulated uniaxial cyclic loading in the cranial-caudal direction (Law et al., 1993; Liebsch et al., 2018; McLachlin, 2008b; Okuyama et al., 2000; Zindrick et al., 1986) (Figure 2.14). The limitation with uniaxial loading is that damage to the bone-implant interface occurs in only a single plane, when in reality the spinal column is subjected to multiaxial stresses which cause *in vivo* implant loosening. Yet, there is currently a lack of knowledge surrounding *how, when and where* spinal implants loosen under physiologically derived, multiaxial loads.

Liebsch et al. aimed to generate a more physiologically relevant spinal implant loading scenario by increasing the sagittal angle of the specimen to induce both shear and tension forces (Liebsch et al., 2018). This study confirmed the feasibility of applying multiaxial loads at the bone implant interface (Figure 2.16), including loading modes derived from the Orthoload data set. Yet, there was no direct comparison between uniaxial and multiaxial loading with respect to quantifying implant fixation. Additionally, the loads used in the Liebsch study were solely aimed at replicating spinal flexion-extension; however, this does not consider the 6DOF spinal motions and loads associated with other movements and tasks. Therefore, it is unknown how implant loosening under physiologic multiaxial loading is accelerated in comparison to uniaxial “toggle” tests.

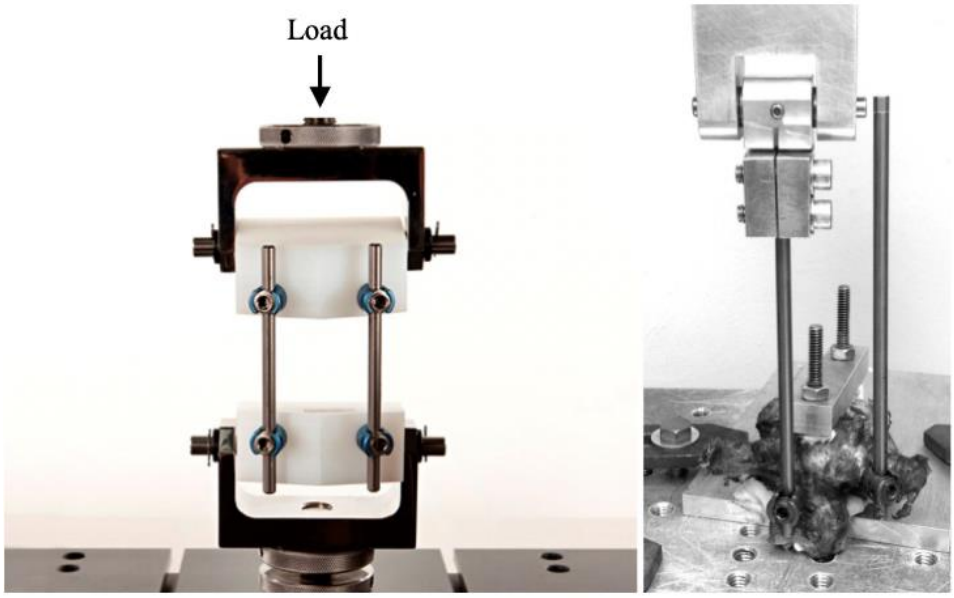


Figure 2.15. Uniaxial toggle testing has been introduced to replicate the fatigue failure seen clinically in spinal screw constructs. The American Society for Testing Materials has developed a standard for testing four-point posterior fixation constructs (left) and single screw implants (right) (ASTM F1717-15, 2021).

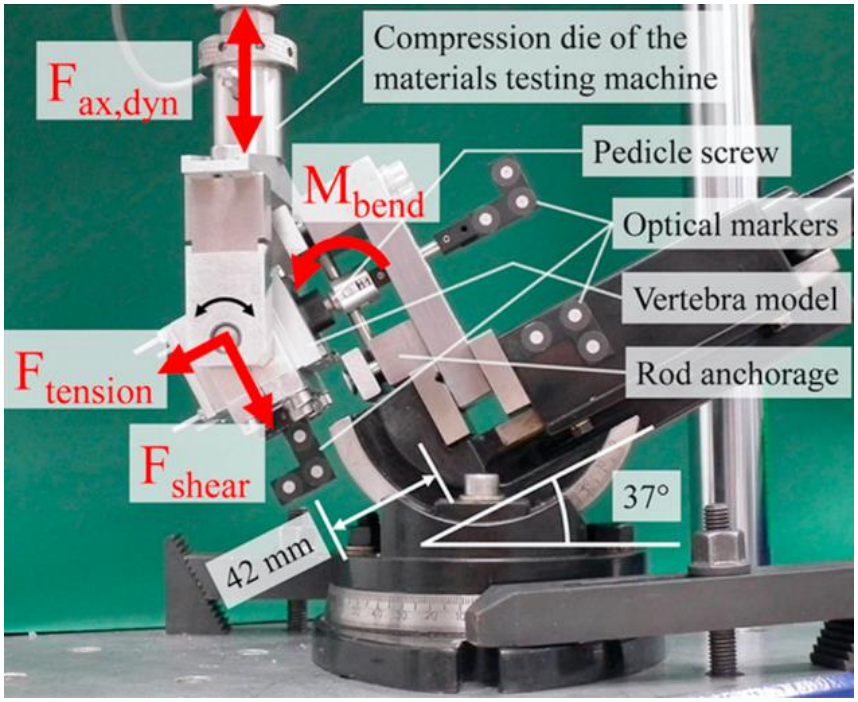


Figure 2.16. Liebsch et al. examined the effect of combined loading on implant loosening. The test set-up used geometry to induce cyclic multiaxial forces including shear and tension (Liebsch et al., 2018)**.**

2.6.2 In Vitro Testing of Interbody Cages

In vitro pre-clinical testing of lumbar interbody cages is commonly performed using cadaveric spine specimens or synthetic models such as Sawbones (Sawbones, Vashon, WA). Risk factors towards cage subsidence include low bone mineral density (Formby et al., 2016; Mi et al., 2017), poorly positioned cages (Tokuhashi et al., 2009), used of posterior fixation (Grant et al., 2001; Polikeit et al., 2003), and excessive endplate resection (Marchi et al., 2013; Park et al., 2019). Typically, uniaxial compressive loads are applied to measure the force required to penetrate the cage into the adjacent vertebra (Andriamifidy et al., 2024; Briski et al., 2017; Fernandes et al., 2024). Evaluating the risk of subsidence through maximum static load testing, may not fully replicate the repetitive, lower-magnitude physiological loads encountered during activities of daily living. Recent studies have aimed at including pure moment loads to static testing to represent spinal movements such as flexion-extension, lateral bending and axial rotation into their lumbar cage subsidence investigations (Deviren et al., 2012; Freeman et al., 2016; Kiapour et al., 2022). Additionally, biomechanical studies are incorporating fatigue testing to better simulate long-term functional loading conditions, helping to predict how interbody cages will perform *in vivo* (Deviren et al., 2012; Freeman et al., 2016; Orías et al., 2023). However, these longitudinal fatigue tests continue to employ uniaxial compression as the loading mode.

2.6.3 Existing ASTM and ISO Spinal Implant Test Standards

The American Society for Testing Materials (ASTM) has developed standard test methods for spinal implant constructs in a vertebrectomy model (ASTM F1717-15, 2021). The ASTM-F1717 standard covers three static and one fatigue-type test methods and aims to provide a basis for mechanical comparison of implant types, placements and surgical techniques. The test methods included in ASTM-F1717 provide the type and magnitudes of loads that should be applied to

sufficiently compare mechanical performance of spinal fixation systems. The ASTM-F1717 standard has been successfully used in literature to examine the effect of bone quality, insertion trajectory and novel implant designs on screw loosening in spinal fixation systems (Amirouche et al., 2016; Kwon et al., 2020; Nowak, 2019). The International Organization for Standardization (ISO) has also developed a test standard for mechanical test methods focused on fatigue failure of semi-rigid or flexible spinal systems (ISO 12189, 2008). The ISO 12189 standard defines failure of the spinal fixation construct (not the interface) as the permanent deformation resulting from fracture and state that fatigue testing is only complete once implant fracture, or five million cycles has been met. Currently, there are no accepted standards for fatigue testing of the bone-implant interface (Aycan and Demir, 2020).

2.6.4 Measurement of Implant Displacement

Spinal implant loosening is characterized by micromotion at the bone-implant interface under mechanical loading. Once initiated, loosening can accelerate bone deformation and/or damage (Puleo and Nanci, 1999). It is thought that micromotion as small as 100-150 μm can impede osseointegration, critical to spinal fusion, and lead to implant loosening (Engh et al., 1992; Pilliar et al., 1986; Hosein et al., 2014; Puleo and Nanci, 1999). Some have reported that micromotions as small as 20-30 microns is necessary to ensure stable growth (Jasty et al., 1997; Pilliar et al., 1986). Therefore, it is important to accurately and reliably determine *when* loosening has occurred to mitigate associated implant failure. Clinically, damage at the bone-implant interface is only found when a clinical complication is also present: pain, implant failure, loss of surgical correction. Even when bone damage has occurred at the bone-implant interface it is difficult to characterize because damage may have progressed to implant loosening by the time that it is detectable on medical images. Beyond X-ray and computed tomography (CT) imaging

there are no established tools available for measuring implant loosening *in vivo.* Others have proposed sensor-based tools to measure implant vibrations and impedances; however, they have yet been tested for spinal implant loosening or used in a clinical model (Arami et al., 2018).

Experimentally, as the ISO and ASTM test standards show, force-displacement curves from materials testing machines can be used to examine implant loosening (Figure 2.17). Implant fixation can be measured directly, through axial pull-out testing, and indirectly through fatigue testing followed by pull-out testing. In indirect fatigue testing, the final pull-out strength of an implant is correlated to the degree of fatigue failure (Aycan et al., 2018). The results from axial pull-out tests are limited because bone failure is only considered in a single direction, which does not represent the *in vivo* loading scenario.

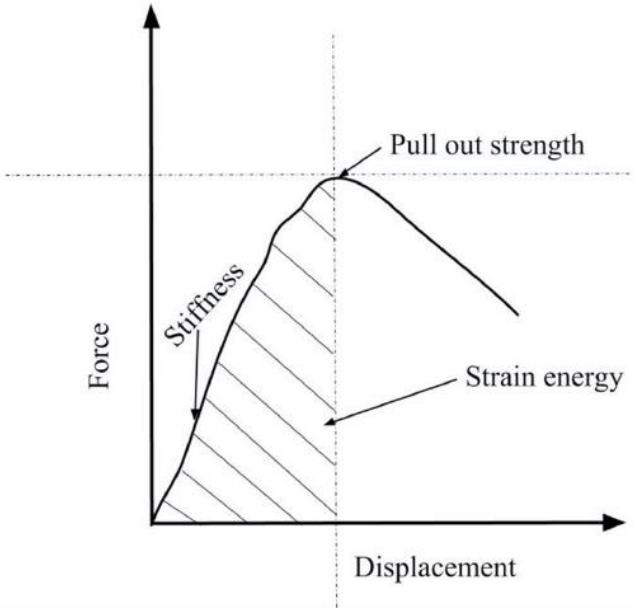


Figure 2.17: An example of a force by displacement curve for the pull-out strength of a pedicle screw from healthy adult vertebral trabecular bone (Varghese et al., 2017).

Real-time implant tracking during *in vitro* cyclic fatigue tests can more precisely identify *when* implant loosening has occurred. State-of-the-art optical tracking systems can measure implant micromotion at 500 µm resolution (Schmidt et al., 2009). Yet, to measure implant

micromotion within the reported threshold for implant stability, 100-150 μm, higher resolution machine vision under magnification is required. Previous work has shown an ability to quantify implant micromotion (Hosein et al., 2014; McLachlin, 2011) (Figure 2.18). More recently, high-resolution optical 3D measuring systems have improved image acquisition and processing techniques, like digital image correlation, to better track 3D implant micromotion (Morosato et al., 2019; Yang et al., 2020).

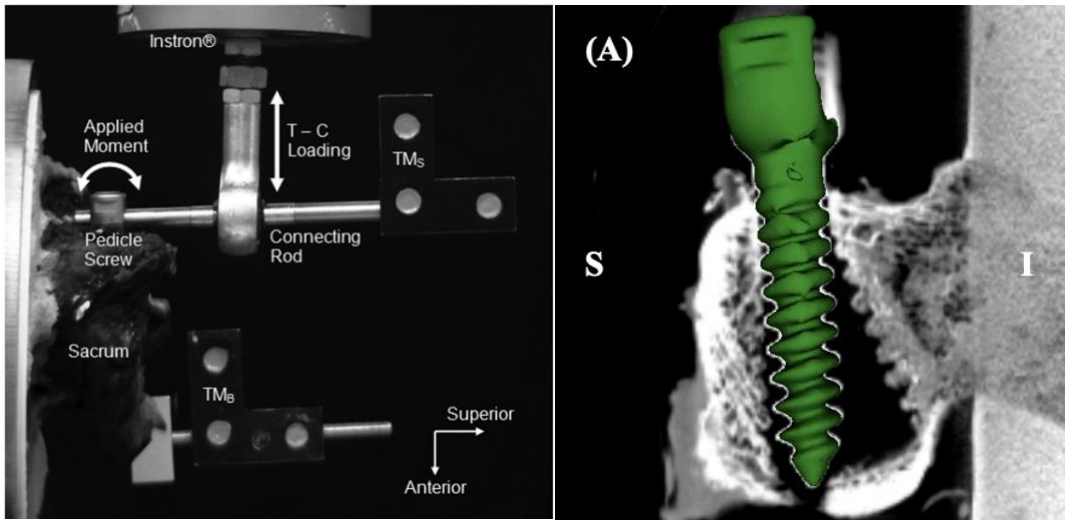


Figure 2.18: Left: Machine vision has been used to track real-time implant loosening (McLachlin, 2011). **Right:** Post-hoc 3D medical imaging can be utilized to quantify volumetric bone damage near the bone-implant interface. This method can be used to compare different implant types, surgical techniques and anatomical variations (McLachlin, 2008).

Post-hoc medical imaging may also be used to assess implant loosening following *in vitro* experiments. Much like techniques employed clinically, X-Ray and CT images may be taken following fatigue testing and implant removal to quantify volumetric bone damage surrounding the implant cavity. This method has been successful employed previously in assessing how and where implant damage occurs following cyclic loading protocols (McLachlin, 2008). Yet, to date, no study has quantified volumetric bone damage following multiaxial implant loosening.

2.7 Spine Simulators

In vitro biomechanical testing is an important tool for advancing our understanding of spinal mechanics and assessing the efficacy of innovative treatments, surgical methods, and spinal implants. By simulating spinal movements and loading scenarios in a controlled laboratory setting, these experiments offer valuable insights into joint and tissue responses that are difficult to achieve in clinical or *in vivo* studies. Spine motion simulators follow three main designs: (1) a custom gantry, (2) mobile Stewart-gough type manipulators, and (3) adaptation of commercially available multiaxial and uniaxial test frames.

2.7.1 Pure Moment Load Simulation

Wilke et al., described one of the first custom multiaxial spine simulators (Wilke et al., 2001, 1994). A gimbal design allowed for three-axes rotations and translations occurred along a gantry system (Figure 2.19). Load capacities were 500 N in medial-lateral and anterior posterior shear, 1500 N in compression and all moment directions had a capacity of 40 Nm. Limitations of this system are a lack of force control and inability to actuate multiple moments at once. This multiaxial simulator was capable of applying pure moments in three directions to simulate flexion/extension, lateral bending and axial rotation in cadaveric FSU. The *in vitro* loads observed were comparable to *in vivo* data; however, the lack of applied muscle forces presented a notable challenge when implant and surgical procedure testing was considered. The use of a multiaxial force control system may address these challenges.

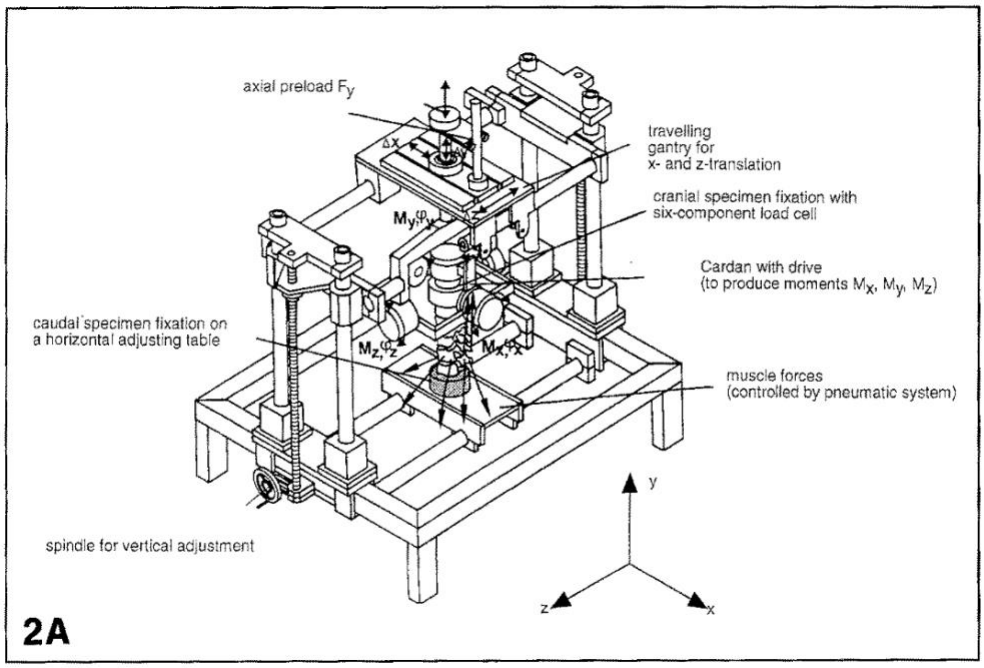


Figure 2.19 Early multiaxial spine simulator developed by Wilke et al., to apply pure moments to individual spinal segments (Wilke et al., 1994).

Other custom multiaxial spinal simulators capable of pure moment test include linear actuator systems developed by Lysack et al. and Gay et al., and a gimbal system developed by Cunningham et al., (Cunningham et al., 2003; Gay et al., 2008; Lysack et al., 2000). Limitations of these systems include low test frequencies, requirement of displacement control and inability to apply multi-directional moment testing.

The use of commercially available linear actuating test frames is common for simulating pure moment bending in the spine (Cadieux et al., 2024; Zehr and Callaghan, 2022). In some instances, these simulators will have an additional rotational actuator attached to simulate axial rotation of the spine. The inferior most vertebra is left often free to move to reduce shear forces generated from applied moment simulation. The commercially available 8DOF MTS Mini-Bionix has also been used for spine testing and it allows for multiaxial load and kinematic control (Borkowski et al., 2017).

2.7.2 Multiaxial Loading Simulation

Stokes et al., developed a Stewart platform inspired system with the capacity to simulate multi-directional load protocols (Stokes et al., 2002). This simulator employs force control but limited to quasi-static test rates. This system able to achieve beyond physiologic loads with shear, force capacity of 350 N, a compressive force capacity of 1100 N, an axial moment capacity of 10 Nm and flexion-extension and lateral bending moment capacity of 35 Nm (Figure 2.20).

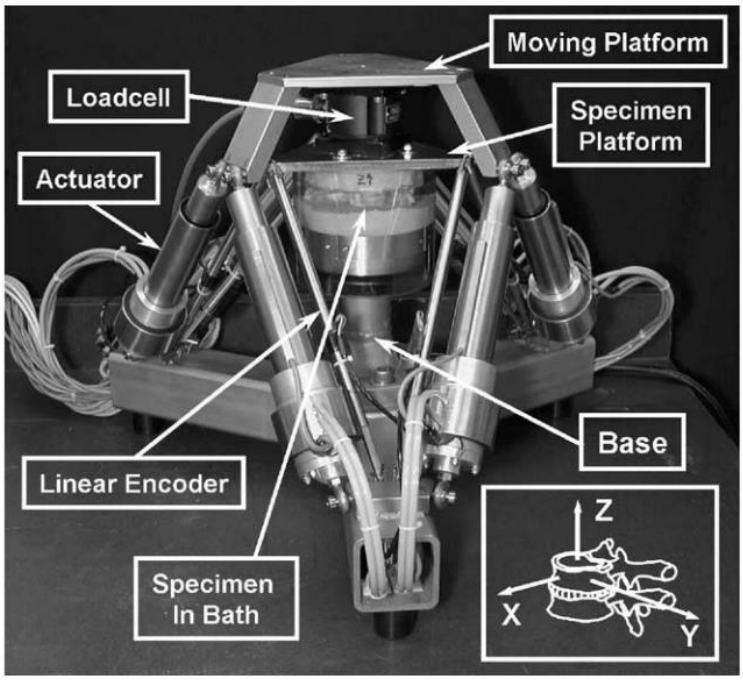


Figure 2.20 Stokes et al., developed a Stewart platform inspired force-control six-degree of freedom spine motion simulator (Stokes et al., 2002).

Most recently, Holsgrove et al., have developed a custom multi-axial spine simulator capable of applying complex multidirectional loads and physiologic rates, Figure 2.21 (Ebisch et al., 2024; Holsgrove et al., 2014; Lazaro-Pacheco et al., 2024). They employ a gantry system with brushless motors and zero-backlash couplings to generate loads. The system capacities of ±25 kN

and ±500 N in compression and shear respectively, and ±200 Nm, ±31 Nm and ±31 Nm in axial rotation, flexion-extension and lateral bending respectively. The Holsgrove et al., simulator is capable of simulating high complexity multiaxial movements (Ebisch et al., 2024). A limitation of the system is the reliance on displacement control at physiologic test rates (Lazaro-Pacheco et al., 2024).

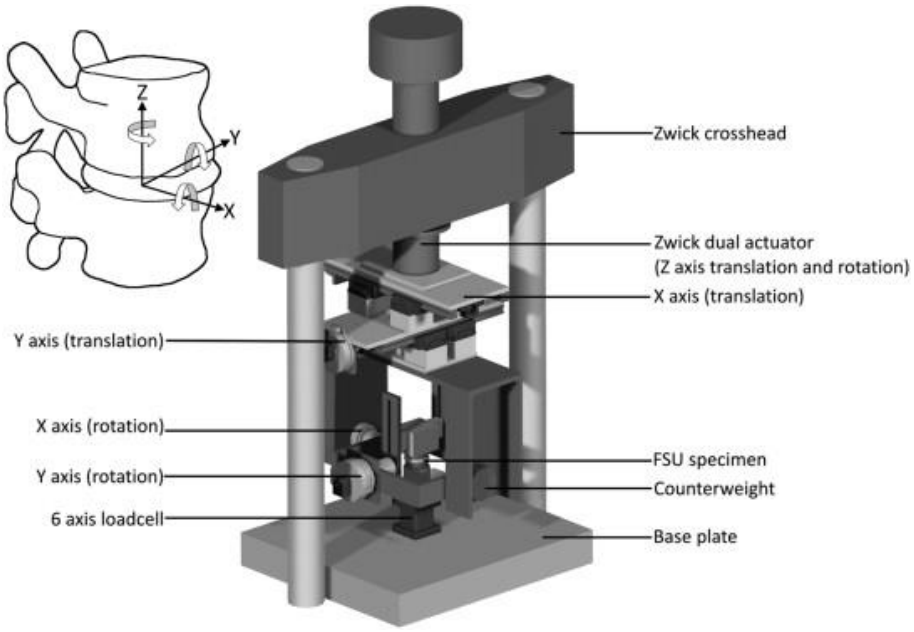


Figure 2.21 Holsgrove et al., have developed a spine simulator capable of applying complex multi-directional loading protocols at physiologic rates in displacement control (Holsgrove et al., 2014).

Despite the availability of 6DOF simulators, pure moment testing continues to dominate spine testing due to the complexities involved in generating multi-axis force and moment inputs and the sophisticated control systems required for six-degree-of-freedom simulation, particularly in force control. Force control is particularly important in longitudinal and high rate testing as soft tissues, such as the intervertebral disc and spinal ligaments, display viscoelastic properties and are therefore subject to rate-dependent behavior, creep and hysteresis.

Chapter 3– A Biomechanical Investigation of Multiaxial Pedicle Screw Loosening in Osteoporotic Human Vertebral Bone [1]

Abstract

Pedicle screw loosening is a clinically significant complication in spinal surgeries, especially for osteoporotic patients. Traditional *in vitro* tests for screw loosening use single degree-of-freedom (DOF) methods (axial pullout or uniaxial craniocaudal toggle testing), which do not replicate physiologic multiaxial spine loading. This study aimed to develop and assess a method for inducing spinal implant loosening under six degree-of-freedom loading conditions, comparing it to uniaxial toggle testing in osteoporotic lumbar vertebrae. Eight osteoporotic human lumbar vertebrae (L2-L4, 70.1 ± 5.5 years old, all male) underwent testing to compare screw loosening under uniaxial and multiaxial loading. Load magnitudes were incrementally increased after 1000 and 2000 cycles, with the final load step continuing until the screw head displaced more than 6 mm. After screw loosening, axial pullout tests were conducted. Post-test computed tomography (CT) imaging was used to quantify bone damage. Multiaxial loading accelerated implant loosening compared to uniaxial loading (p=0.00*). Pullout strength was similar between uniaxial and multiaxial loading (p=0.38). Failure predominantly occurred in the inferior direction (p=0.06). Medial (p=0.07) and lateral (p=0.00*) loosening were greater under multiaxial loading. CT imaging showed greater volumetric bone deformation with multiaxial than uniaxial loading (p=0.01*). Multiaxial loading accelerates pedicle screw loosening, increases lateral implant displacement, and increases volumetric bone deformation in osteoporotic vertebrae. This study developed a novel approach to improve the relevance of pedicle screw loosening mechanisms achieved through *in vitro* testing of spinal implants through the application of physiologic multiaxial cyclic loading.

[1] A version of this chapter is under peer-review: McGregor, M; Cadieux, C; Thompson, C; Fernandes, R; Leinwand, J; Rasoulinejad, P; McLachlin, S. (2024) A Biomechanical Investigation of Multiaxial Pedicle Screw Loosening in Osteoporotic Human Vertebral Bone. Under review for The Spine Journal (SPINEE-D-24-01274)

3.1 Introduction

Posterior fixation is often required for stabilizing the spine following trauma, deformity correction and for degenerative spine conditions (Dickman et al., 1992). Posterior spinal fixation is comprised of screws placed in the pedicles of adjacent vertebrae and rods which connect the pedicle screws to form a four-point fixation construct per spine level. Despite the wide scale usage of pedicle screws in spinal fixation procedures, failure due to loosening at the screw-bone interface remains a clinically relevant complication (Galbusera et al., 2015). Pedicle screw loosening is thought to result from cyclic loading of the spinal column during activities of daily living which causes fatigue loading and eventual failure at the screw-bone interface (Galbusera et al., 2015; Halvorson et al., 1994; Puleo et al., 1999; Soshi et al., 1991).

Accelerated pedicle screw loosening has been associated with osteoporosis, advanced age, and disease state (Bredow et al., 2016; Cho et al., 2011; Pearson et al., 2017). Osteoporosis results in fewer and thinner trabeculae and is characterized by bone mineral density (BMD) less than 80mg/cm^3 in the trabecular bone region (American College Radiology, 2021; Goldstein et al., 1993). Osteoporosis is a well-established risk factor for pedicle screw loosening with up to 60% of osteoporotic patients experiencing pedicle screw loosening when compared to only 15% of patients with healthy bone (El Saman et al., 2013). Previous experimental investigations found that pedicle screw loosening becomes more prevalent and adequate stabilization cannot be achieved in vertebrae with BMD values of <90 mg/cm^3 (Wittenberg et al., 1991; Okuyama et al., 1993).

Biomechanical investigations of pedicle screw fixation have typically been conducted through uniaxial posterior pull-out tests. Despite prevalence in historical literature, posterior pull-out failure is not indicative of *in vivo* failure modes (Bostelmann et al., 2017; Kueny et al., 2014;

Schulze et al., 2017; Weiser et al., 2016). Therefore, in recent years cranio-caudal toggle tests have been completed to simulate cyclic bending loads associated with flexion-extension motion of the spine (Holsgrove et al., 2015; Song et al., 2023; Weber et al., 2024; Weiser et al., 2021; Weiss et al., 2014). However, these uniaxial toggle tests do not account for the multiaxial loads the spine experiences during lateral bending, axial rotation, and translational spinal movements (Galbusera et al., 2015). Therefore, the mechanistic understanding of the activities and loading conditions that result in pedicle screw loosening in osteoporotic bone remains limited. As a result, there is a need for an evaluation method to simulate cyclic, multiaxial loading of pedicle screw fixation.

The purpose of this study was to develop and evaluate a biomechanical test method to simulate multiaxial loading of lumbar pedicle screw fixation and assess screw loosening outcomes relative to traditional uniaxial toggle testing through a repeated measures study design. It was hypothesized that multiaxial loading would accelerate pedicle screw loosening, resulting in decreased screw fixation and increased volumetric bone deformation.

3.2 Materials and Methods

3.2.1 Specimen Preparation

Lumbar vertebrae from four donor specimens ranging from 65 to 78 years (73 ± 3 years of age, male) were sectioned from the spinal column and surrounding soft tissues were removed. Eight human cadaveric lumbar vertebrae, L2(1) L3 (4), and L4 (2), were used for biomechanical testing (Table 3.1). Pre-test clinical computed tomography (CT) scans and medical history were reviewed to ensure no previous fractures, spinal deformities or musculoskeletal diseases. A phantom with a density of 0.182 g/cm^3 was included during CT imaging to calculate BMD to ensure osteoporosis was present and for comparison with loosening measurement outcomes. Pedicle screws were inserted bi-laterally by a fellowship-trained orthopaedic spine surgeon to

allow for intra-specimen normalization. Pedicle screws were selected based on pedicle size, and all had a diameter of 6.5 mm and lengths ranging from 40 to 50 mm (Medtronic, Minneapolis, MN, USA). Following instrumentation, specimens were stored at -40°C until testing.

Table 3.1. Specimen data for human vertebra specimens used for in vitro biomechanical testing.

				Pedicle Width (mm)		Pedicle Height (mm)	
Specimen	Age	Level	BMD (mg/cm^3)	Uniaxial Loading	Multiaxial Loading	Uniaxial Loading	Multiaxial Loading
1	78	L3	82.3	11.8	11.7	18.5	19.2
	---	L4	84.1	13.1	11.4	19.6	19.0
2	71	L3	75.1	10.0	9.9	18.3	17.7
	---	L4	79.6	13.1	12.8	21.6	23.3
3	68	L3	84.8	13.6	10.9	20.2	20.1
4	65	L2	81.1	8.7	9.7	17.5	17.4
	---	L3	74.4	12.4	11.2	15.9	17.1
	---	L4	74.3	13.6	12.6	22.5	21.9
Av. ± St. Dev.	70.1 ± 5.5	--	79.1 ± 4.2	12.0 ± 1.8	11.3 ± 1.1	19.3 ± 2.2	19.5 ± 2.2

Specimens were thawed at room temperature overnight for 14 hours prior to testing day. Lumbar vertebrae were potted in a custom fixation device using a low exothermic reaction cement (Denstone, Kulzer Mitsui Medical Group, South Bend, IN, USA). The potted specimens were mounted on a six-degree of freedom joint motion simulator (AMTI VIVO, AMTI, Watertown, MA, USA) (Figure 3.1). The screw head and long axis were positioned in-line with the simulator's Grood-Suntay axis (Grood and Suntay, 1983), allowing for the six degree of freedom (6DOF) force control features to be used.

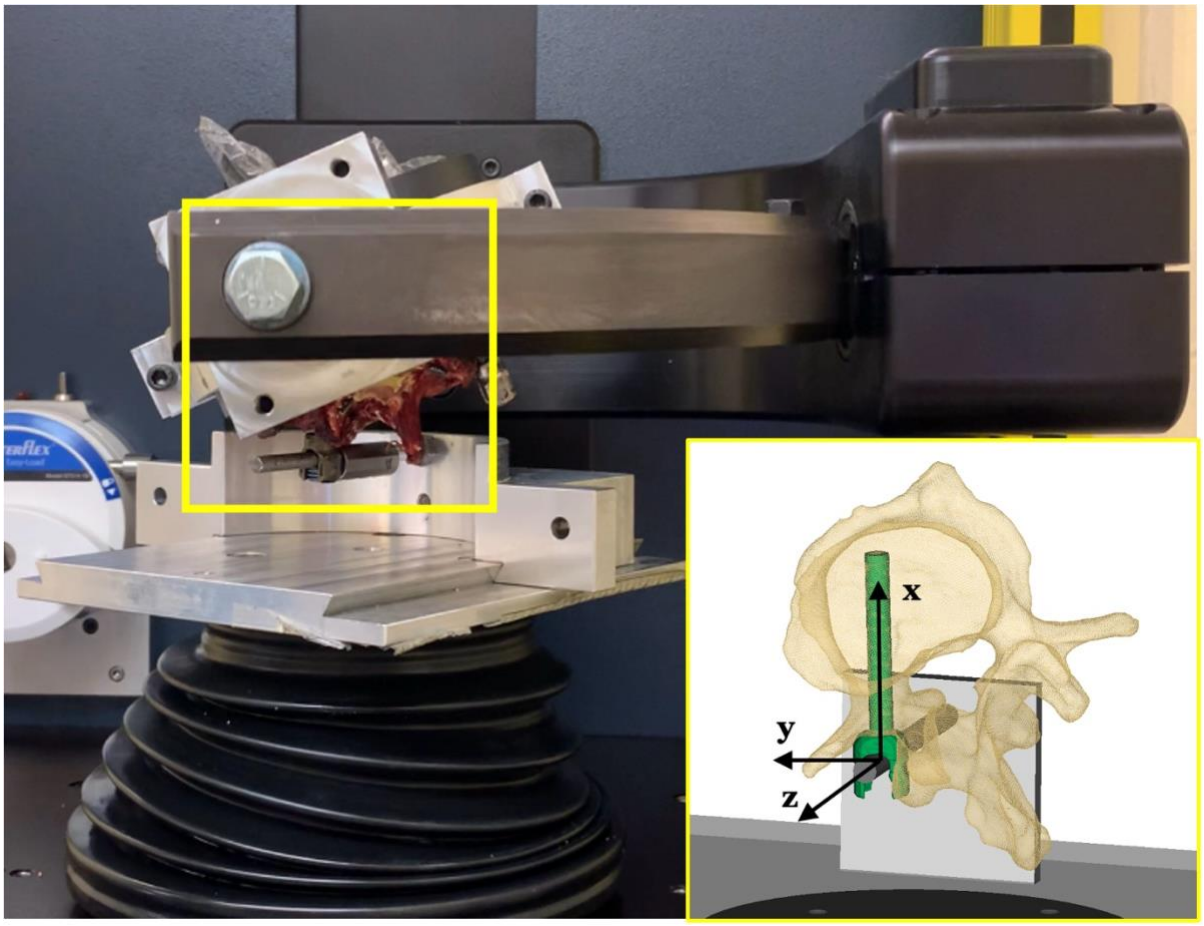


Figure 3.1: The six-degree of freedom test apparatus (left) was used to apply loads with respect to the defined local screw coordinate system (bottom right). Loads and displacements were resolved about the center of the pedicle screw head.

3.2.2 Biomechanical Test Setup

Uniaxial and multiaxial cyclic loading conditions were applied using the joint motion simulator (Figure 1). The potted end of each specimen was secured to the upper actuators with a custom fixation device. A 5.5 mm rod was used to rigidly secure the pedicle screw head to the base platen of the simulator. A laser level was used to align the pedicle screw perpendicular to the simulator base. A screw coordinate system was determined using a digital stylus, and the origin for force and displacement resolution was placed at the centre of the screw head (Figure 3.1). Loads were defined relative to the screw axes, similar to the Orthoload definition for internal spinal

fixators (Figure 3.2) (Rohlmann et al., 1999). The x, y and z screw axes were defined as most similar to anatomic anterior-posterior, medial-lateral, and superior-inferior spinal axes, respectively.

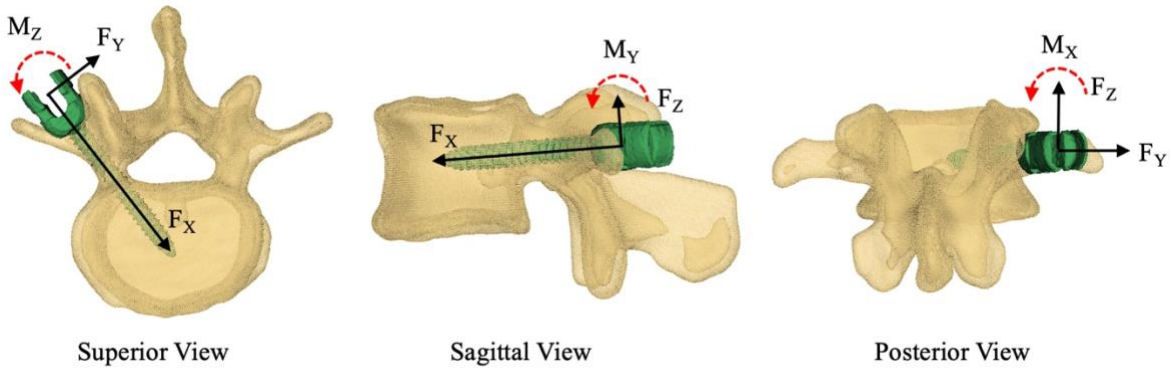


Figure 3.2: Uniaxial and multiaxial loads were applied along the x, y, and z screw axes. The x, y, and z were most similar to the anterior-posterior, medial-lateral, and cranial-caudal axes; however, there were differences based on the relative screw orientation.

Applied multiaxial load magnitudes were approximated from *in vivo* loads measured in internal spinal fixators during three major gross movements of the whole spine: flexion-extension, lateral bending, and axial rotation (Rohlmann et al., 1999). Uniaxial loads were also applied, representing existing toggle-test standards representative of spinal flexion-extension (ASTM F1717, 2021). Loading profiles were applied to bi-laterally placed pedicle screws to compare posterior spinal implant loosening under applied multiaxial loading and uniaxial toggle testing using force-control curves within the same vertebra. Uniaxial loading was applied to either the left or right pedicle screw in a randomized fashion to account for possible handedness differences in BMD and cortical shell thickness. Following uniaxial loading, the specimen was rotated, realigned, and multiaxial loading was applied to the contralateral side. Loads were applied in three steps to ensure initial failure was captured (Table 3.2). Loads were increased following 1000 and 2000 cycles and then sustained until failure. Failure was considered to have occurred when screw

position deviated 6 mm in any direction, as measured by the actuator displacement relative to the screw coordinate system (Liebsch et al., 2018). The iterative learning control capabilities of the joint motion simulator enabled consistent loading, cycle to cycle, despite potential changes in implant position and relative motion due to progressive loosening. Following fatigue testing, ultimate failure pull-out tests were completed. Pull-out tests were completed under displacement control at a 20 mm/min rate, and maximum pullout strength was recorded.

Table 3.2. Uniaxial (1 degree of freedom) and multiaxial (6 degrees of freedom) loading was applied in three steps to human vertebra specimens relative to the screw loading axes, with the associated anatomical directions shown for reference.

	Uniaxial			Multiaxial		
Screw Loading Axis (~anatomic direction)	0-1000 cycles	1001-2000 cycles	2001+ cycles	0-1000 cycles	1001-2000 cycles	2001+ cycles
Fx (~anterior-posterior)	0 N	0 N	0 N	± 12.5 N	± 12.5 N	± 50 N
Fy (~medial-lateral)	0 N	0 N	0 N	± 25 N	± 50 N	± 100 N
Fz (~superior-inferior)	0 N	0 N	0 N	± 50 N	± 100 N	± 200 N
Mx (~lateral bending)	0 Nm	0 Nm	0 Nm	± 0.75 Nm	± 1.5 Nm	± 3 Nm
My (~flexion/extension)	± 2 Nm	± 4 Nm	± 8 Nm	± 0.2 Nm	± 4 Nm	± 8 Nm
Mz (~axial rotation)	0 Nm	0 Nm	0 Nm	± 0.75 Nm	± 1.5 Nm	± 3 Nm

3.2.3 Measurement of Implant Loosening

Loads and position of the screw head were measured in real-time throughout the test using the joint motion simulator's 6DOF load cell and actuator position, respectively. An event was set to stop the test when the screw head had translated more than 6 mm in any direction. The maximum displacement for each axis was saved at the end of the uniaxial and multiaxial fatigue tests.

Following pull-out tests, screws were removed, and each vertebra was imaged using clinical 3D computed tomography (CT) imaging, with the scanner resolution set to 0.693x0.693x0.625mm, to examine volumetric deformation of the vertebral bone. Volumetric deformation was calculated using 3DSlicer (v.4.11) by manual 3D segmentation of the empty screw volume in each vertebra using a consistent image segmentation workflow. To account for variability in the screw length and position, only the distal 35 mm of the empty screw volume was used for calculating volumetric bone deformation using the Segment Statistics module.

3.2.4 Statistical Design

A repeated measures analysis of variance (RM-ANOVA) was performed to determine differences between number of cycles to failure, pull-out strength, volumetric deformation and deformation in each loading direction using RStudio (RStudio Team (2024), PBC, Boston, MA, USA). Statistical significance was considered at $p<0.05$.

3.3 Results

All specimens had some degree of osteoporosis, with an average BMD of 79.1 ± 4.2 mg/cm3, based on established criteria for osteoporotic vertebral bone mineral density (<80 mg/cm3) (American College of Radiology, 2021). All pedicle screws (16) in each of the eight vertebrae tested reached at least 6 mm of screw head displacement during both uniaxial or multiaxial tests. Multiaxial loading (1977.5 ± 276.5 cycles) resulted in accelerated implant loosening when compared to uniaxial toggle loads (3271.2 ± 628.9 cycles) (p=0.00*). A survivability plot was generated to visualize this phenomenon (Figure 3.3).

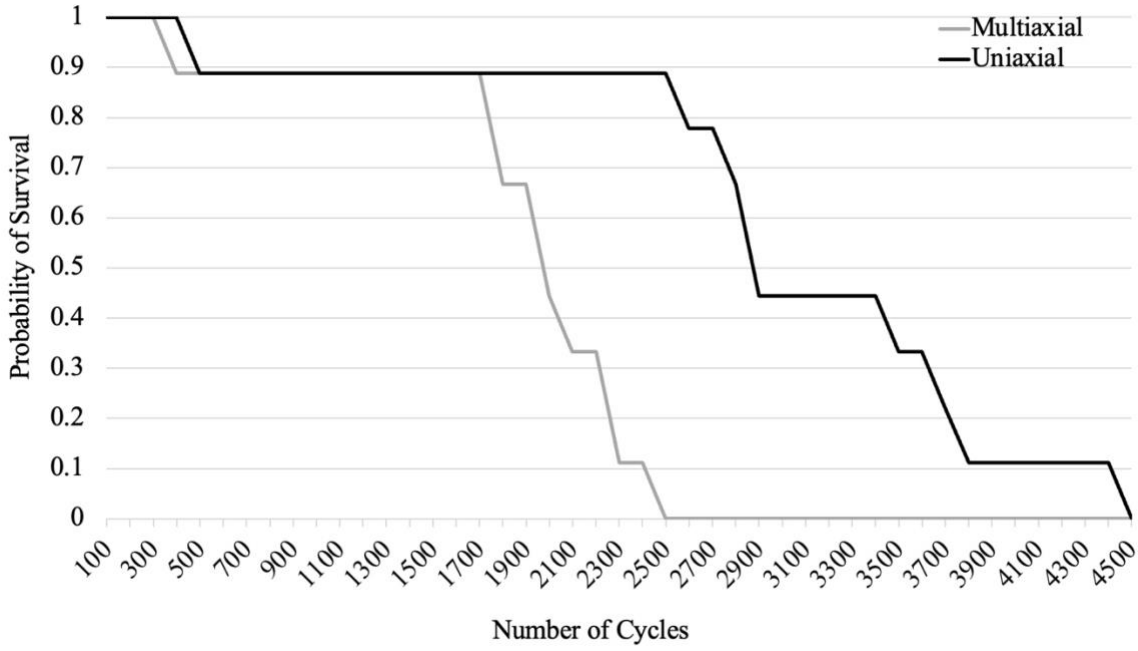


Figure 3.3: Probability of survival with respect to the number of cycles required to reach 6 mm of screw head translation in any degree of freedom as measured by the joint motion simulator. Note there was an early failure of a single specimen.

Independent of the applied loading protocol, failure occurred most often in the inferior direction when compared to superior (p=0.06). Pedicle screws that underwent multiaxial loading saw greater loosening in the medial (p=0.120) and lateral (p=0.00*) directions (Figure 3.4). There were no significant differences in displacement caused by shear along the long axis of the screw, push-in displacement (p=0.145) and pull-out displacement (p=0.512).

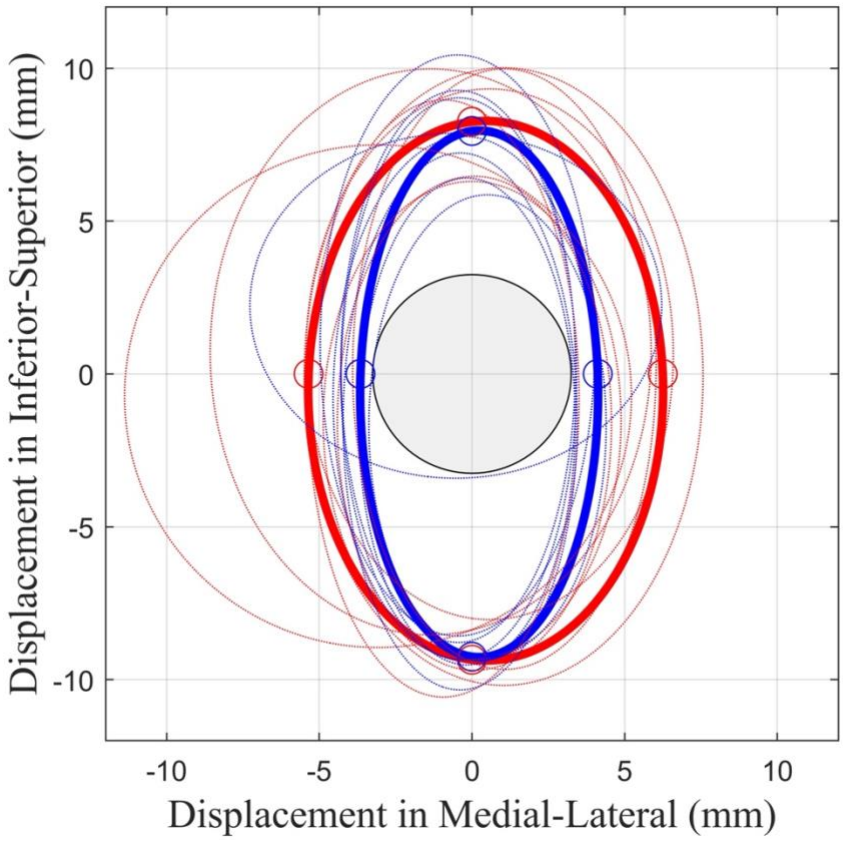


Figure 3.4: The maximum screw displacement in the z-direction (~superior-inferior) and y-direction (~medial-lateral) for all screws tested (dotted) and the average (bold) as measured by the joint motion simulator. Failure occurred negative z-direction (~inferiorly) most often (p=0.06) for both uniaxial (blue) and multiaxial loading (red). Negative y-direction (~medial) (p=0.12) and positive y-direction (~lateral) screw displacement was greater in multiaxial loading (red) compared to uniaxial loading (blue) (p=0.00*).

Following cyclic fatigue testing, one specimen sustained bone damage resulting in fracture of the transverse process. This specimen was therefore excluded from pull-out testing. There was no significant difference in pullout strength between the pedicle screws in the seven remaining vertebrae receiving the uniaxial loading (343.5 ± 120.6 N) and multiaxial loading (309.7 ± 84.6 N) (p=0.38).

Multiaxial loading (1293.6 ± 156.8 mm^3) resulted in a greater volume of bone deformation than uniaxial loading (1196.6 ± 151.3 mm^3) (p=0.01*). Increased bone deformation was apparent

in the axial and anterior-posterior cross-sections and less so in the sagittal plane corresponding to the additional loading along in the M_z and F_y screw axes present in the multiaxial loading protocol when compared to the uniaxial protocol (Figure 3.5).

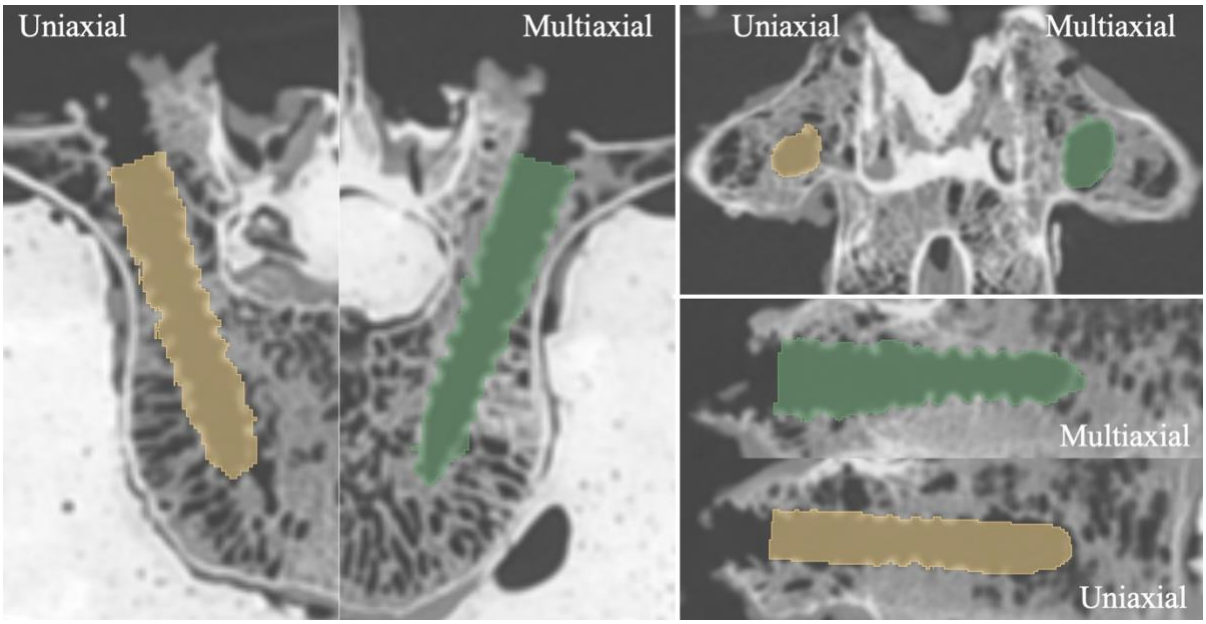


Figure 3.5: Axial (left), posterior (top right), and sagittal (bottom right) computed tomography cross sections show the apparent differences in volumetric bone deformation from uniaxial (yellow) and multiaxial (green) screw loosening. With screws removed for scanning, only the distal 35mm of the empty screw volume was used for segmentation.

3.4 Discussion

3.4.1 General Findings

Previous studies examining fatigue failure of pedicle screw implants have typically simulated uniaxial cyclic loading in the cranial-caudal direction (Esses et al., 1993; McLachlin, 2008; Okuyama et al., 2000; Zindrick et al., 1986). A limitation with uniaxial loading is that damage to the screw-bone interface occurs in a single, pre-determined plane, when *in vivo*, the spinal column is subjected to variable, multiaxial loads. In the present study, physiologically derived, multiaxial loading significantly accelerated pedicle screw loosening in osteoporotic

vertebral bone when compared to traditional uniaxial toggle testing methods. These findings indicate a clear need to better understand how multiaxial loading conditions associated with activities of daily living can impact surgical outcomes related to posterior fixation instrumentation failure.

The addition of transverse (side-to-side) loading in the multiaxial condition increased screw loosening in the medial-lateral direction as expected. Human bone is transversely isotropic and is stronger in the superior-inferior direction than the transverse directions. Osteoporosis results in fewer and thinner trabeculae which weakens bone in all directions (Goldstein et al., 1993). Therefore, the increased screw displacement in the medial-lateral direction under multiaxial loading aligns with our understanding of osteoporotic bone mechanics. There was a significant increase in lateral displacement in the multiaxial relative to the uniaxial condition, but not in the medial direction despite equivalent load magnitudes in each direction. This may be due to the underlying bony anatomy, where the pedicle is largely unsupported laterally and supported medially by the facet joint. This was further evidenced by the total failure of the transverse process during multiaxial fatigue test for one specimen.

Post-test CT images showed deformation volumes were significantly larger for multiaxial loading when compared to uniaxial loading. However, there were some minor differences between screw deformation recorded during testing and volumetric bone deformation measured from the post-hoc CT images. Screw pull-out tests completed following multiaxial and uniaxial loading may have altered bone deformation profile and volume between cyclic testing and post-test CT imaging. This difference may also be partially explained by the manual segmentation process, but also potentially by the delay between testing and scanning. Following mechanical testing, specimens were re-frozen and stored until there was CT scanner availability (3+ months). It could

be hypothesized that during testing, the screw loosening measurement is a combination of both elastic and plastic bone deformation. During the rest period between testing and post-test imaging, the elastic deformation may have relaxed, resulting in smaller hole magnitudes when compared to the testing measurements of screw loosening.

3.4.2 Comparison to Prior Work

Despite accelerated loosening with multiaxial loading, pull-out forces remained similar between uniaxial and multiaxial loading. Historically, pedicle screw fixation has been examined through destructive *in vitro* pull-out tests in which screws are removed along the screw axis (Law et al., 1993; McLachlin, 2008; Weinstein et al., 1992). The pull-out test has proven to be a valuable tool for comparing various biological, technique and implant design factors on pedicle screw fixation strength, such as cement augmentation, cortical threaded screws and screw trajectory (Boos and Webb, 1997; Fölsch et al., 2012; Lotz et al., 1997). Axial pull-out testing allows for quick and reliable comparisons of factors affecting screw fixation and is still the predominant test used today (Chen et al., 2014; Shibasaki et al., 2020). However, pedicle screws are rarely exposed to the extreme, destructive axial loading used in pull-out testing and therefore results from these studies cannot be considered representative of the clinical failure mechanisms for pedicle screws. In this study, all pedicle screws were failed to the same loosening threshold, 6 mm of screw head displacement, before pull-out testing was conducted. Therefore, similar pull-out strength for both loading protocols is consistent with amount of screw loosening induced.

Previous studies have examined pedicle screw loosening under uniaxial cyclic loading with cycles to failure as the reported metric. Weiser et al. reported screw loosening (5.4 mm of displacement) occurring between 1682 and 2285 cycles under applied uniaxial loading for osteoporotic and normal bone, respectively (Weiser et al., 2021). Further, Weber et al. examined

the effect of cement volume augmentation on screw fixation found loosening to 5mm occurred between 1074 and 2377 cycles (Weber et al., 2024).

Previously, Liebsch et al., aimed to generate a more physiologically relevant spinal implant loading scenario by increasing the sagittal angle of the specimen to induce both shear and tensile forces (Liebsch et al., 2018). Liebsch et al., confirmed the feasibility of applying multiaxial loads at the bone implant interface, including loading modes derived from the Orthoload data set; yet there was no direct comparison of how multiaxial loading compares to uniaxial toggle tests and pull-out tests with respect to measuring implant fixation. Therefore, the present study builds off previous advancements and provides new information regarding different loosening mechanisms between common uniaxial cyclic testing and physiologically derived multiaxial cyclic loading conditions.

Volumetric bone deformation as a metric of measuring screw loosening is a new technique. Zhan et al. used volumetric deformation to evaluate the effect of pedicle screw insertion trajectory on loosening under cyclic uniaxial cranio-caudal loading. This was completed in foam bone surrogate, and we believe that the present study is the first presentation of this measurement technique in human vertebral bone (Zhan et al., 2024).

3.4.3 Comparison to Existing Test Standards

The American Society for Testing Materials (ASTM) has developed standard test methods for spinal implant constructs in a vertebrectomy model (ASTM F1717, 2021). ASTM F1717 includes three static and one uniaxial fatigue-type test methods that aim to provide a basis for mechanical comparison of implant types, placements, and surgical techniques. The ASTM-F1717 standard has been successfully used in literature to examine the effect of bone quality, insertion trajectory and novel implant designs on screw loosening in spinal fixation systems (Amirouche et

al., 2016; Nowak, 2019; Sumiya et al., 2021). The International Organization for Standardization (ISO) has also developed a test standard for mechanical test methods focused on fatigue failure of semi-rigid or flexible spinal systems (ISO 12189, 2008). The ISO 12189 standard defines failure of the spinal fixation construct (not the interface) as the permanent deformation resulting from fracture and states that fatigue testing is only complete once implant fracture, or five million cycles has been met. Currently, there are no accepted standards for fatigue testing of the screw-bone interface under multiaxial loading (Kwon et al., 2020).

3.4.4 Limitations

The present study is not without limitations. Aggressive loading protocols were selected from the peak loads seen previously from instrumented posterior fixators during activity of daily living (Rohlmann et al., 1999)]. Therefore, the cyclic failure seen in this study does not perfectly represent the daily loading of a spine implant, like that of a gait cycle applied during pre-clinical evaluation total knee and total hip replacement implants. There are also known limitations of cadaveric implant testing, mainly inter-specimen variability and unreliable tissue quality. A repeated measures study design was selected for this reason and uniaxial versus multiaxial loading was randomized from left to right to limit the effect of handedness on fixation. Further, only male specimens were included in the present study. Shu et al., recently reported that sex was not a predictor in pedicle screw loosening and that BMD was the primary driver in any perceived sex differences (Shu et al., 2023). Therefore, we aimed to account for the exclusion of female specimens by controlling for the BMD. Pre-test CT scans were used to ensure viable bone for testing and age, BMD, level, pedicle width and pedicle length were all accounted for to limit any effect of the results. Finally, screw displacements were measured by actuator displacement with respect to the screw coordinate system; more accurate measurement of 3D screw loosening at

smaller (micro-motion) displacements would likely have required an external optical tracking system, which was not available at the time of this study.

3.5 Conclusions

The present study provides a new understanding of pedicle screw loosening under multiaxial loading. This includes new data on the role of anatomical torsion and lateral bending directions on accelerating implant loosening, which has not previously been examined in implant fixation testing. Further, the development of a new test method to apply physiologically derived, multiaxial loading waveforms provides a more realistic simulation of how spinal implant loosening may occur in osteoporotic patients during activities of daily living.

3.6 References

American College of Radiology. ACR practice guideline for the performance of quantitative computed tomography (QCT) bone densitometry. Published online 2021.

Amirouche F, Solitro GF, Magnan BP. Stability and spine pedicle screws fixation strength—A comparative study of bone density and insertion angle. Spine Deform. 2016; 4:261-267.

ASTM Standard F1717-21. Standard Test Methods for Spinal Implant Constructs in a Vertebrectomy Model. ASTM International; 2021.

Boos N, Webb JK. Pedicle screw fixation in spinal disorders: a European view. Eur Spine J. 1997; 6:2-18.

Bostelmann R, Keiler A, Steiger HJ, Scholz A, Cornelius JF, Schmoelz W. Effect of augmentation techniques on the failure of pedicle screws under cranio-caudal cyclic loading. Eur Spine J. 2017; 26:181-188.

Bredow J, Boese CK, Werner CML, et al. Predictive validity of preoperative CT scans and the risk of pedicle screw loosening in spinal surgery. Arch Orthop Trauma Surg. 2016; 136:1063-1067.

Chen YL, Chen WC, Chou CW, et al. Biomechanical study of expandable pedicle screw fixation in severe osteoporotic bone comparing with conventional and cement-augmented pedicle screws. Med Eng Phys. 2014; 36(11):1416-1420.

Cho W, Shimer AL, Shen FH. Complications associated with posterior lumbar surgery. In: Seminars in Spine Surgery. Vol 23. WB Saunders; 2011:101-113.

Dickman CA, Fessler RG, MacMillan M, Haid RW. Transpedicular screw-rod fixation of the lumbar spine: operative technique and outcome in 104 cases. J Neurosurg. 1992; 77(6):860-870.

El Saman A, Meier S, Sander A, et al. Reduced loosening rate and loss of correction following posterior stabilization with or without PMMA augmentation of pedicle screws in vertebral fractures in the elderly. Eur J Trauma Emerg Surg. 2013; 39:455-460.

Esses SI, Sachs BL, Dreyzin V. Complications associated with the technique of pedicle screw fixation a selected survey of ABS members. Spine. 1993; 18(15):2231-2239.

Fölsch C, Goost H, Figiel J, et al. Correlation of pull-out strength of cement-augmented pedicle screws with CT-volumetric measurement of cement. Biomed Tech (Berl). 2012; 57(6):473-480.

Galbusera F, Volkheimer D, Reitmaier S, Berger-Roscher N, Kienle A, Wilke HJ. Pedicle screw loosening: a clinically relevant complication? Eur Spine J. 2015; 24:1005-1016.

Goldstein SA, Goulet R, McCubbrey D. Measurement and significance of three-dimensional architecture to the mechanical integrity of trabecular bone. Calcif Tissue Int. 1993;53

Grood ES, Suntay WJ. A joint coordinate system for the clinical description of three-dimensional motions: application to the knee. Published online 1983.

Halvorson TL, Kelley LA, Thomas KA, Whitecloud TS III, Cook SD. Effects of bone mineral density on pedicle screw fixation. Spine. 1994; 19(21):2415-2420.

Holsgrove TP, Nayak NR, Welch WC, Winkelstein BA. Advanced multi-Axis spine testing: clinical relevance and research recommendations. Int J Spine Surg. 2015; 9.

Kueny RA, Kolb JP, Lehmann W, et al. Influence of the screw augmentation technique and a diameter increase on pedicle screw fixation in the osteoporotic spine: pullout versus fatigue testing. Eur Spine J. 2014; 23:2196-2202.

Kwon J, Ha MH, Lee MG. Alternative pedicle screw design via biomechanical evaluation. Appl Sci. 2020;10(14):4746.

Law M, Tencer AF, Anderson PA. Caudo-cephalad loading of pedicle screws: mechanisms of loosening and methods of augmentation. Spine. 1993; 18(16):2438-2443.

Liebsch C, Zimmermann J, Graf N, Schilling C, Wilke HJ, Kienle A. In vitro validation of a novel mechanical model for testing the anchorage capacity of pedicle screws using physiological load application. J Mech Behav Biomed Mater. 2018; 77:578-585.

Lotz JC, Hu SS, Chiu DF, et al. Carbonated apatite cement augmentation of pedicle screw fixation in the lumbar spine. Spine. 1997; 22(23):2716-2723.

McLachlin SD, Beaton BJ, Sabo MT, et al. Comparing the fixation of a novel hollow screw versus a conventional solid screw in human sacra under cyclic loading. Spine. 2008; 33(17):1870-1875.

Nowak B. Experimental study on the loosening of pedicle screws implanted to synthetic bone vertebra models and under non-pull-out mechanical loads. J Mech Behav Biomed Mater. 2019; 98:200-204.

Okuyama K, Abe E, Suzuki T, et al. Can Insertional Torque Predict Screw Loosening and Related Failures?: An: In Vivo: Study of Pedicle Screw Fixation Augmenting Posterior Lumbar Interbody Fusion. Spine. 2000; 25(7):858-864.

Okuyama K, Sato K, Abe E, et al. Stability of Transpedicle Screwing for the Osteoporotic Spine: An: In Vitro: Study of the Mechanical Stability. Spine. 1993; 18(15):2240-2245.

Pearson HB, Dobbs CJ, Grantham E, et al. Intraoperative biomechanics of lumbar pedicle screw loosening following successful arthrodesis. J Orthop Res. 2017; 35(12):2673-2681.

Puleo DA, Nanci A. Understanding and controlling the bone–implant interface. Biomaterials. 1999; 20(23-24):2311-2321.

Rohlmann A, Bergmann G, Graichen F. Loads on internal spinal fixators measured in different body positions. Eur Spine J. 1999; 8(5):354-359.

Schulze M, Gehweiler D, Riesenbeck O, et al. Biomechanical characteristics of pedicle screws in osteoporotic vertebrae—comparing a new cadaver corpectomy model and pure pull-out testing. J Orthop Res. 2017; 35(1):167-174.

Shibasaki Y, Tsutsui S, Yamamoto E, et al. A bicortical pedicle screw in the caudad trajectory is the best option for the fixation of an osteoporotic vertebra: An in-vitro experimental study using synthetic lumbar osteoporotic bone models. Clin Biomech. 2020; 72:150-154.

Shu L, Wang X, Li L, et al. Computed tomography-based prediction of lumbar pedicle screw loosening. Biomed Res Int. 2023; 2023:107625.

Sumiya S, Fukushima K, Kurosa Y, et al. Comparative analysis of clinical factors associated with pedicle screw pull-out during or immediately after surgery between intraoperative cone-beam computed tomography and postoperative computed tomography. BMC Musculoskelet Disord. 2022; 23(1):1-10.

Song F, Liu Y, Fu R, et al. Craniocaudal toggling increases the risk of screw loosening in osteoporotic vertebrae. Comput Methods Programs Biomed. 2023; 238:107625.

Soshi S, Shiba R, Kondo H, Murota K. An experimental study on transpedicular screw fixation in relation to osteoporosis of the lumbar spine. Spine. 1991; 16(11):1335-1341.

Weiser L, Dreimann M, Huber G, et al. Cement augmentation versus extended dorsal instrumentation in the treatment of osteoporotic vertebral fractures: a biomechanical comparison. Bone Joint J. 2016; 98(8):1099-1105.

Weber M, Lenz M, Egenolf P, et al. Increased stability due to symmetric cement volume in augmented pedicle screws? A biomechanical study. J Biomed Mater Res B Appl Biomater. 2024; 112(1).

Weinstein JN, Rydevik BL, Rauschning W. Anatomic and technical considerations of pedicle screw fixation. Clin Orthop Relat Res. 1992; (284):34-46.

Weiss AJ, Elixhauser A, Andrews RM. Characteristics of operating room procedures in US hospitals, 2011. Published online 2014.

Weiser L, Sellenschloh K, Püschel K, et al. Cortical threaded pedicle screw improves fatigue strength in decreased bone quality. Eur Spine J. 2021; 30:128-135.

Wittenberg RH, Shea M, Swartz DE, Lee KS, White AA III, Hayes WC. Importance of bone mineral density in instrumented spine fusions. Spine. 1991; 16(6):647-652.

Zhan X, Gao F, Yang Y, et al. Effect of Insertional Direction of Pedicle Screw on Screw Loosening: A Biomechanical Study on Synthetic Bone Vertebra under a Physiology-like Load. Orthop Surg. 2024.

Zindrick MR, Wiltse LL, Widell EH, et al. A biomechanical study of intrapeduncular screw fixation in the lumbosacral spine. Clin Orthop Relat Res. 1986;(203):99-112.

Chapter 4 - Biomechanical comparison of human cadaveric lumbar motion segments under simple and physiologically-derived loading conditions[2]

Abstract:

In vitro biomechanical spine testing is an important tool for understanding spinal mechanics and evaluating the effectiveness of treatments, surgical techniques, and spinal devices. Yet, the majority of current *in vitro* test methods for spinal loading simulation fail to replicate the complex physiological loads and degrees-of-freedom (DOF) of the lumbar spinal motion segments in the low back. This goal of this study was to compare the application of simple (1DOF) and physiologically-derived (6DOF) loading conditions using a commercially available joint motion simulator for *in vitro* lumbar spinal motion segment testing. Comparison of the simple and more complex, physiologically-derived loading conditions included investigating the effects of loading rate (quasi-static vs. dynamic), actuator control method (load vs. displacement), and waveform type (1DOF vs. 6DOF waveforms). Eight fresh-frozen cadaveric lumbar spine segments (four L2/L3, four L4/L5) from four donors (69 ± 4.7 years; 3 female, 1 male) were used. Results indicated significant differences between simple 1DOF and physiologically-derived 6DOF loading protocols, with 1DOF producing larger ROM, albeit with a larger applied moment magnitude based on previous literature recommendations. Dynamic loading also led to reduced ROM in lateral bending compared to quasi-static rates, while neutral zone characteristics remained similar across rates. The findings from this study highlight some limitations of current literature recommendations for pure moment testing protocols for accurately simulating lumbar motion segment characteristics and emphasize the importance of incorporating 6DOF loading in future studies. Ultimately, the comparison of the different spinal loading conditions conducted in this study contributes to the growing body of research advocating for more comprehensive *in vitro* testing to better reflect the true mechanical loading environment of the human spine.

[2] A version of this chapter in preparations for submission to the Journal of Biomechanics: McGregor, M; Thompson, C; McLachlin, S. (2024) Biomechanical comparison of human cadaveric lumbar motion segments under simple and physiologically-derived loading conditions.

4.1 Introduction

In vitro testing plays an important role in understanding the biomechanics of the spine and evaluating the effectiveness of new treatments, surgical techniques, and spinal devices. By replicating spinal motions and loading conditions in a controlled environment, *in vitro* experiments using spinal loading simulators can obtain deeper insights into the joint and tissue-level response that would not be feasible in clinical or other *in vivo* settings. However, the majority of spinal loading simulators have a limited ability to reproduce complex spinal loading. Cyclic application of quasi-static pure moments in a single plane has been widely adopted for *in vitro* simulation of flexion-extension, lateral bending, and axial rotation type movements (Cadieux et al., 2024; Cunningham et al., 2003; Gay et al., 2008; Lysack et al., 2000; Wilke et al., 1994; Zehr and Callaghan, 2022). Yet, these single-axis loading protocols do not fully capture the dynamic and multi-directional nature of spinal movements (Costi et al., 2021; Holsgrove et al., 2018; Stokes et al., 2002).

The three-dimensional (3D) flexibility of the human spine naturally allows for a wide variety of daily activities to be performed with six degrees-of-freedom (6DOF). The extent of these activities can be quantified kinematically using 3D motion analysis to measure the spine's range of motion. However, the 6DOF loads applied to spinal motion segments during activities of daily living have been more difficult to elucidate. 6DOF loading of instrumented lumbar spinal motion segments in living subjects has been documented through the open-source Orthoload database for various activities of daily living (Rohlmann et al., 2000, 2007). These Orthoload datasets provide rich detail regarding 6DOF loading for individual patients following lumbar spine surgery; however, the surgical instrumentation is likely to alter spinal loading patterns compared to healthy individuals. As a less invasive alternative, computational human body musculoskeletal models,

such as those available on OpenSim and the Twente Spine Model, can use knowledge of muscle optimization to relate measured spinal kinematics during activities of daily living to multi-axial spinal loading (Bayoglu et al., 2019; Beaucage-Gauvreau et al., 2021, 2019; Lerchl et al., 2022). These detailed models and databases can provide valuable information for *in vitro* testing with regards to the 6DOF spinal loading associated with activities of daily living; yet, to date, there have been few advances in spinal loading simulators that incorporate this knowledge (Lazaro-Pacheco et al., 2024).

For more sophisticated *in vitro* testing, several six-axis spinal loading simulators have been developed, each varying in design and control capabilities, to assess the biomechanics of both single and multi-level spinal motion segments (Holsgrove et al., 2018, 2014; Stokes et al., 2002). These systems enable testing under more realistic, physiologically-derived loading conditions, but present their own challenges, such as reliance on displacement control and test standardization (Ebisch et al., 2024; Holsgrove et al., 2015; Wilke et al., 2016). As a result of the complexities associated with simulating physiologically-derived loading, use of reduced DOF loading, like the application of pure moments, remains the most common form of *in vitro* spinal loading simulation. This is largely due to challenges in determining accurate multi-axis force and moment inputs combined with the complex control systems required for six-axis load simulation. Additionally, an important consideration for spinal loading simulations is test method reproducibility across industrial and academic research labs. Custom-developed simulators can be difficult to reproduce, maintain and translate to large multi-centre or industrial studies. To date, there have been only a few commercial spinal loading simulators (e.g. MTS Bionix, Bose Spine Tester) with limited capabilities of applying physiologically-derived 6DOF loads associated with spinal movements and activities. For commercial joint simulation outside of spine applications, the VIVO joint

simulator (AMTI, Watertown, MA, USA) has been recently shown to be capable of applying physiologically-derived 6DOF loading for studies of the hip and knee; however, no one has yet examined the VIVO joint simulator for applying 6DOF spinal loads (Donnelly et al., 2022; Fitzpatrick et al., 2016).

The objective of the present study was to investigate the VIVO joint simulator for *in vitro* spine testing to accurately replicate physiologically-derived 6DOF loading of the lumbar spine. This investigation was interested in answering questions related to the relative effect of simulator loading rate (quasi-static vs. dynamic), control method (load vs. displacement control) and applied waveforms (pure moment vs. physiologically-derived loading) on lumbar spine biomechanics. By comparing the outlined parameters, the present study aimed to validate the VIVO joint simulator for spinal testing. A comparison of the lumbar spinal motion segment response to existing literature is included to further the discussion surrounding the reliability and comparability of biomechanical evaluations of the lumbar spine across different research settings (Costi et al., 2021; Holsgrove et al., 2018).

4.2 Methods

4.2.1 Specimen Preparation

Institutional ethics approval was obtained for the present study to include eight lumbar spinal segments comprised of four L2-L3 and four L4-L5 segments extracted from four fresh frozen cadavers (Science Care, Phoenix, AZ, USA). The mean age of the specimens was 69 ± 4.7 years, from 3 female and 1 male donor. Prior to dissection, the full intact spine specimens (occiput to coccyx) were scanned using clinical resolution computed tomography (CT) with a 0.182 g/cm³ phantom to exclude any specimens with bone abnormalities and to measure bone mineral density (average 82.7 ± 3.8 mg/cm³). The specimens were then sectioned and preserved at -40 °C until

biomechanical testing. Prior to testing, lumbar spinal segments were thawed overnight at room temperature (20 – 22 °C) and carefully further dissected by an orthopaedic surgeon to ensure preservation of the intervertebral discs and spinal ligaments. The cranial and caudal ends of each specimen were attached to custom 3D-printed endplate fixtures (PLA, Original Prusa MK4S, Prague, Czech Republic) and mounted onto the VIVO joint simulator. Specimens were sprayed with saline throughout testing to limit tissue dehydration.

4.2.2 Six-degree of freedom Waveform Generation

The VIVO joint simulator allows for 6DOF waveform inputs, with each DOF capable of operating in either displacement or load control. For simulating pure moment loading, the 6DOF input waveform was setup to independently produce LB, FE and AR by applying a sinusoidal wave of ±4 Nm for each of the respective loading axes (Mx, My, or Mz) based on recommendations for osteoporotic lumbar spine specimens (Costi et al., 2021; Wilke et al., 1998). Additionally, a compressive axial load (Fz) of 250 N was held constant throughout each loading cycle, while all other DOFs were set to hold zero load during the pure moment waveform (Figure 4.2).

Physiologically-derived 6DOF load waveforms were generated from an open-source repository collected from *in vivo* telemeterized vertebral body replacements from patients performing various physical movements of the spine (www.orthoload.org) (Rohlmann et al., 2007). A custom Python script was generated to import Orthoload 6DOF waveforms for each subject performing the desired movement types: flexion, extension, left lateral bending, and left axial rotation. For each of the respective movement types, dynamic time warping with peak matching was used to align and resample each waveform by the global shape of the respective loading degree of freedoms (Fx, Fy, Fz, Mx, My, Mz). This ensured that each waveform was

aligned by the movement performed and resampled to the same number of data points. A mean waveform was then generated from the peak matched data. Following averaging, the waveform was subjected to a 4th order low-pass Butterworth filter with a cutoff of 5 Hz, effectively smoothing the data by attenuating frequencies above 5 Hz while preserving the general shape of the signal. Movement waveforms were then concatenated to produce a full range of motion profile for each of the respective planar movement directions. Flexion (n=5, discrete movements=17) and extension (n=3, discrete movements=8) waveforms were added together. The inverse of left lateral bend (representing right lateral bend) was added to the left lateral bend (n=3, discrete movements=5) data to produce the left-right bending waveform. The same process as left-right bending was completed for clockwise-counterclockwise axial rotation (n=3, discrete movements=8). Linear ramp adjustments at the end of each waveform were then added to ensure that the start position, and end position were identical, necessary for the cyclic simulator control. Lastly, waveform data was down-sampled to 1024 data points, to meet the input waveform requirements of the VIVO joint simulator (Figure 4.1). The final 6DOF waveforms generated for physiologically-derived FE, LB, and AR are depicted in Figure 4.2.

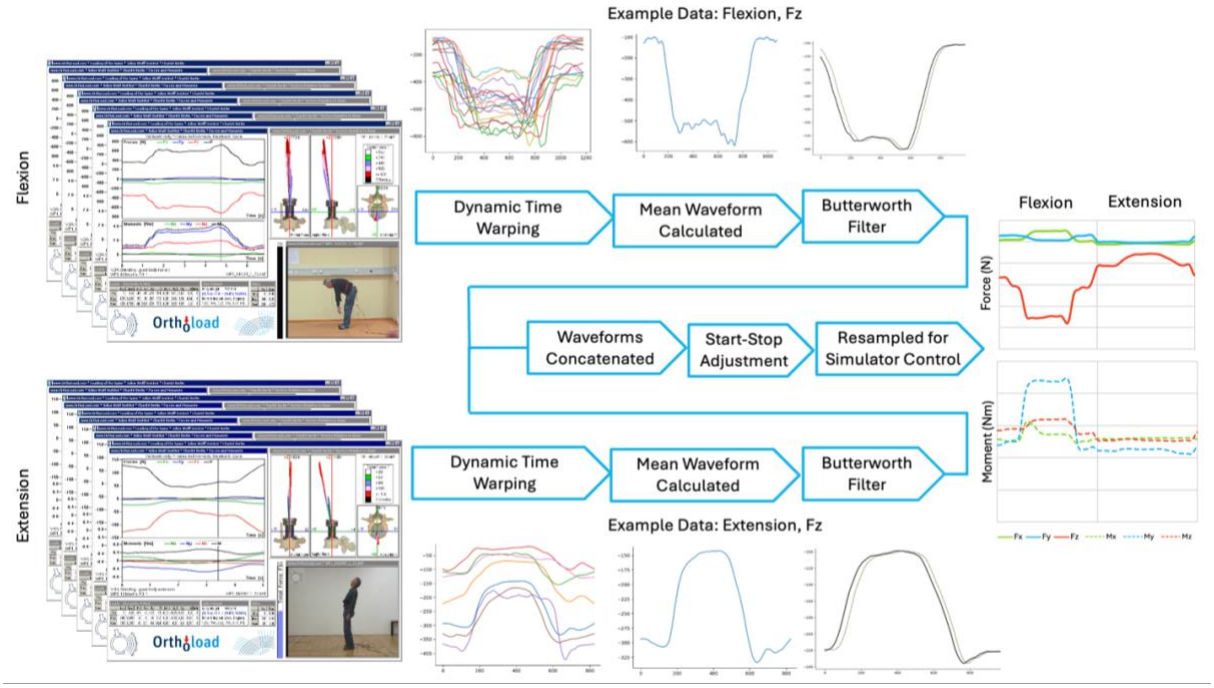


Figure 4.1. A physiologically-derived six-degree of freedom waveform for simulated flexion-extension was generated from *in vivo* flexion and extension load data obtained from an open-source database. A custom pipeline utilized dynamic time warping to develop average flexion and extension waveforms which were then concatenated to represent a cyclic spinal flexion-extension movement. Figure contains images obtained from www.orthoload.org.

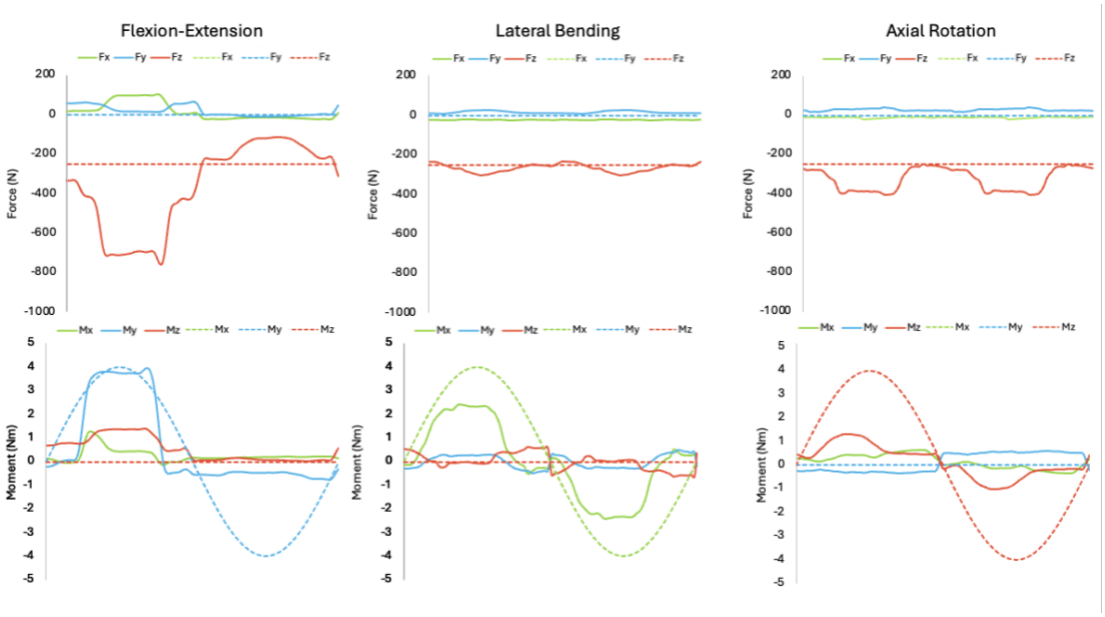


Figure 4.2. A six-degree of freedom flexion-extension, lateral bending and axial rotation loading protocol was developed from the www.orthoload.org database through a dynamic time warping with peak matching approach (solid). The sinusoidal pure moment loading (+/- 4Nm with 250N of axial compression) waveforms (dashed) are shown for comparison.

4.2.3 Biomechanical Test Protocol

Biomechanical testing was conducted using custom fixtures to adapt the VIVO joint simulator for spinal loading simulation (Figure 4.3). The superior vertebra was connected to the actuators controlling the LB and FE loading directions (Mx and My), while the inferior vertebra was secured to the actuators managing the three force directions (Fx, Fy, Fz) and AR loading (Mz). Loads were applied and resolved around the center of the superior vertebra, which was positioned at the joint simulator origin. Five cycles were completed for each test condition: the first three cycles were used for specimen pre-conditioning, the fourth cycle was designated for data collection, and the fifth cycle allowed for the spine segment to return to its neutral loaded state.

First, the pure moment loading tests for each simulated movement (FE, LB, and AR) were completed at quasi-static and dynamic loading rates. The quasi-static waveform had a cycle frequency of 0.033Hz, which corresponds to loading rate of 0.5 Nm/sec, whereas the dynamic frequency was 0.3Hz, equivalent to loading at 5 Nm/s. Next, the physiologically-derived 6DOF waveform was run in load control again for each movement (FE, LB, and AR) to match the quasi-static and dynamic cycle frequencies from the pure moment tests. For displacement control testing, the actuator range of motion (ROM) for each of the three simulated movements for each specimen from the quasi-static pure moment tests were calculated based on the difference between the actuator joint angles at the maximum and minimum peak loads (+4 Nm and -4 Nm). For conversion to displacement control with sinusoidal waveform testing, the zero displacement value was defined as mid-point of the corresponding load control ROM. The sinusoidal target displacements were then used as waveform inputs to match the specimen-specific ROM peaks from the load control tests. The quasi-static waveform frequency was held constant between the tests; however, the

rotation rate (deg/second) varied based on individual specimen ROM, Table 4.1. In summary, the entire testing protocol for each specimen is outlined in Table 4.2.

In addition to actuator displacement measurements for the VIVO joint simulator, relative 3D vertebral motions were recorded using digital 3D optical motion tracking (ARAMIS Adjustable 12M, GOM Metrology, Braunschweig, Germany). Each vertebra was tracked with respect to a fixed tracker, with post-hoc analysis of the relative motion of the superior vertebra to the inferior vertebra. Lumbar segment ROM was considered as the difference between the minimum and maximum values for each DOF.

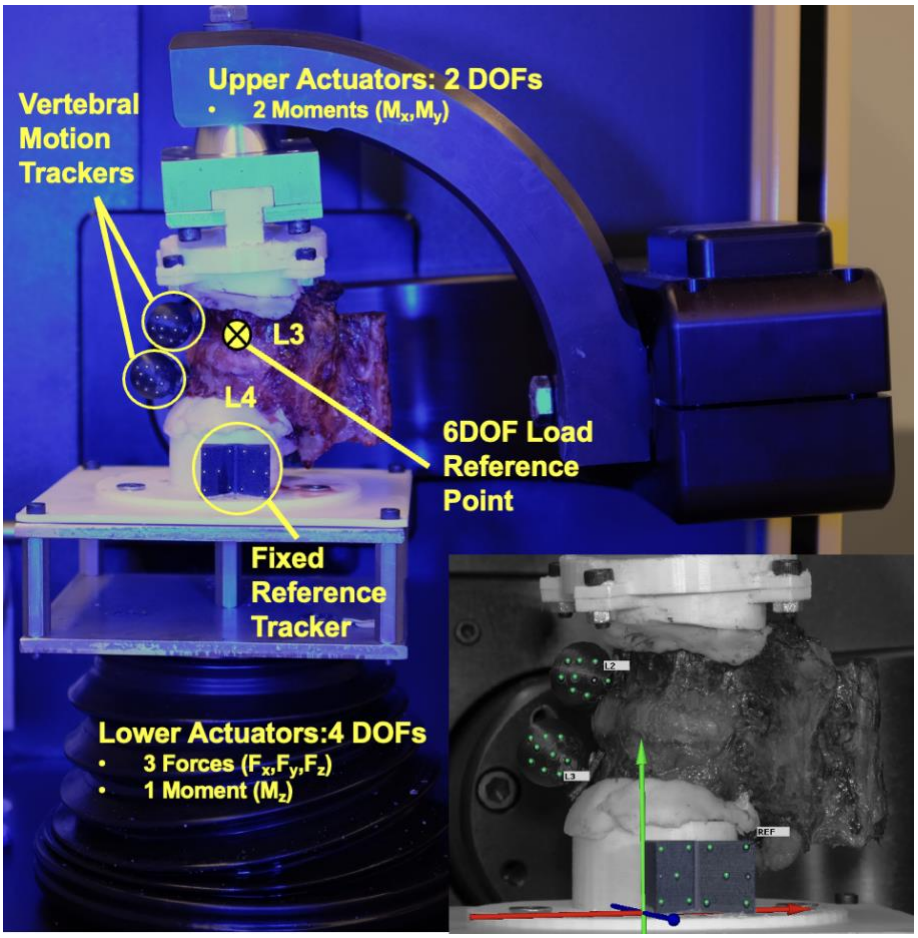


Figure 4.3. Lumbar motion segments were mounted to a six-degree of freedom (6DOF) joint motion simulator. Actuators worked together in 6DOF load control to apply the translational and rotational displacements required to simulate spinal lateral bending (Mx), flexion-extension (My) and axial rotation (Mz). Inset: visual of the Aramis 3D optical motion tracking system identifying the marker locations for the L2 and L3 vertebrae relative to the reference tracker.

Table 4.1. Comparison of quasi-static testing of load control and displacement control parameters.

	Load Control	**Displacement Control**
Waveform Shape	Sinusoid	Sinusoid
Target	± 4 Nm	Specimen Specific ROM (deg)
Waveform Frequency	0.03 Hz	0.03 Hz
Rate	0.5 Nm/sec	0.07- 0.2 deg/sec
Off-axes Target	0 N, 0 Nm	0 mm, 0 deg

Table 4.2. A repeated measures test protocol was designed to compare (1) quasi-static vs dynamic test rates (*), (2) pure moment vs physiologically-derived (#), or (3) load vs displacement simulator control methods (^) for simulated spinal flexion-extension, lateral bending and axial rotation.

Movement	**Test Rate**	**Waveform**	**Simulator Control**
Flexion-Extension	0.5 Nm/sec*	Pure moment#	Load^
	5 Nm/ sec*	Pure moment	Load
	0.5 Nm/sec*	Physiologically-Derived#	Load
	5 Nm/sec*	Physiologically-Derived	Load
	0.5 Nm/sec	Pure moment	Displacement^
Lateral Bending	0.5 Nm/sec*	Pure moment #	Load ^
	5 Nm/ sec*	Pure moment	Load
	0.5 Nm/sec*	Physiologically-Derived#	Load
	5 Nm/sec*	Physiologically-Derived	Load
	0.5 Nm/sec	Pure moment	Displacement^
Axial Rotation	0.5 Nm/sec*	Pure moment #	Load ^
	5 Nm/ sec*	Pure moment	Load
	0.5 Nm/sec*	Physiologically-Derived#	Load
	5 Nm/sec*	Physiologically-Derived	Load
	0.5 Nm/sec	Pure moment	Displacement^

4.2.4 Post-hoc Analysis

The total lumbar segment ROM for FE, LB and AR were compared to draw conclusions towards overall joint motion between the different test parameters: applied load degrees of freedom (pure moment vs. physiologically-derived), simulator control (load vs. displacement) and test rate (quasi-static vs. dynamic). Additionally, neutral zone measurements were calculated from the VIVO joint simulator based on the load-displacement curves. The neutral zone was determined as the height of vertical space between the loading and unloading curves at 0 N (Panjabi, 1992).

For statistical analysis of the repeated measures study design, a Bartlett's test for homogeneity of variance was used to determine if variance between parameters were equal. If they were, a one-way analysis of variance was used to test the differences between parameters. If not, a Welch's F-Test was used for comparison. A Holm's step-down post hoc test was conducted to account for family-wise error rate and provide a more conservative assessment of significance. For all parameters, significance was established as $p<0.05$.

4.3 Results

4.3.1 Pure Moment versus Physiologically-derived 6DOF Loading

Lumbar segment ROM varied significantly between the pure moment and physiologically-derived loading protocols at both quasi-static and dynamic test rates (Figure 4.4). At the quasi-static test rate, the pure moment loading protocol resulted in a larger ROM in FE ($p=0.000$), LB ($p=0.000$) and AR ($p=0.02$) when compared to the physiologically-derived 6DOF loading protocol. With the dynamic test, the pure moment loading protocol resulted in a larger ROM in FE ($p=0.000$), LB ($p=0.000$) and AR ($p=0.01$) when compared to the physiologically-derived 6DOF loading protocol.

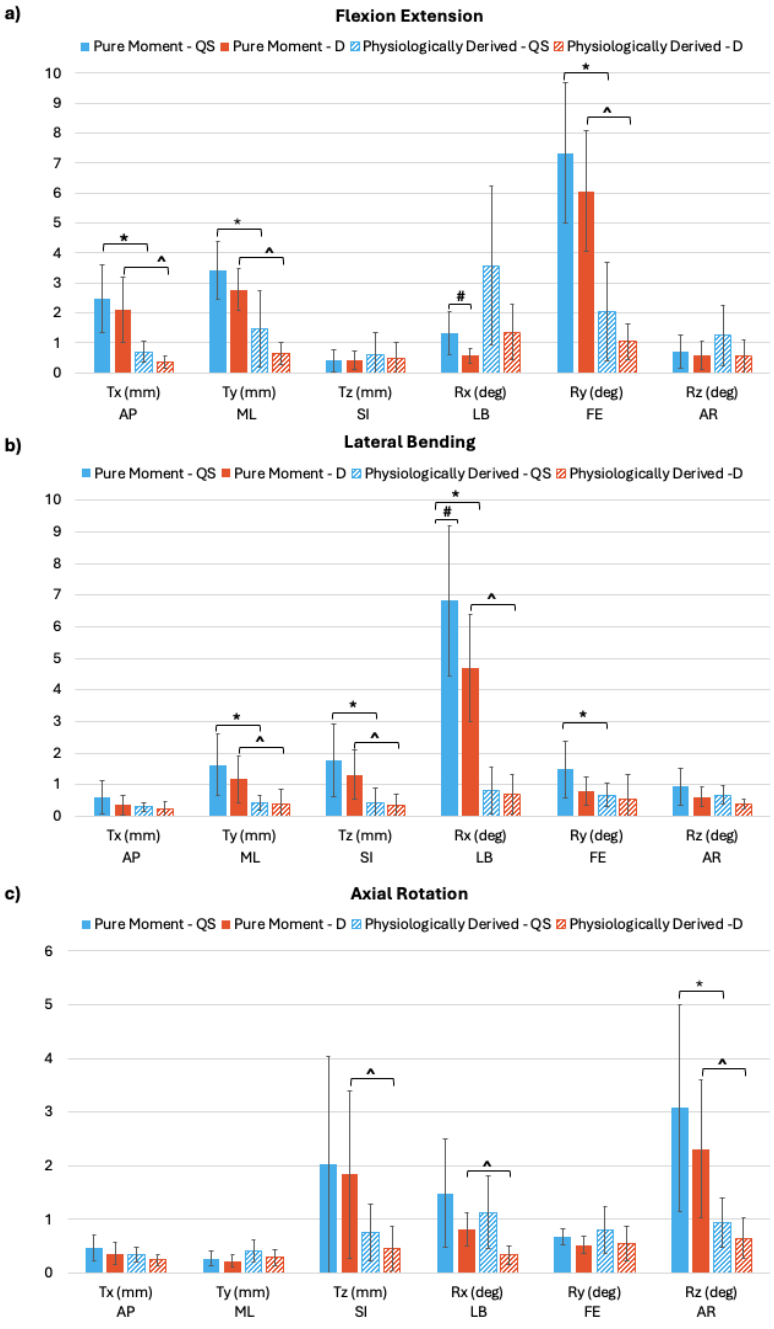


Figure 4.4. Pure moment bending (blue) and physiologically derived (red) loading protocols were completed in quasi-static (solid) and dynamic (hashed) and compared for segmental range of motion across three linear translations and three rotations: Tx (anterior-posterior), Ty (medial-lateral), Tz (superior-inferior), Rx (lateral bending), Ry (flexion-extension), and Rz (axial rotation). Differences between pure moment and physiologically-derived were denoted with a # and a ^ for quasi-static and dynamic test rates, respectively. Differences between quasi-static and dynamic test rates for pure moment loading were denoted with a * and there were no differences between test rates under physiologically derived loading.

4.3.2 Quasi-static versus Dynamic Test Rates

In pure moment loading, lumbar segment ROM in LB was smaller for the dynamic test rate ($p=0.05$) (Figure 4). There was no difference in lumbar segment ROM in FE and AR between the quasi-static and dynamic test rates ($p>0.05$). In physiologically-derived loading, there were no differences in ROM for FE, LB, and AR ($p>0.05$). Force-displacement curves for pure moment data in quasi-static and dynamic test rates are displayed in Figure 4.5.

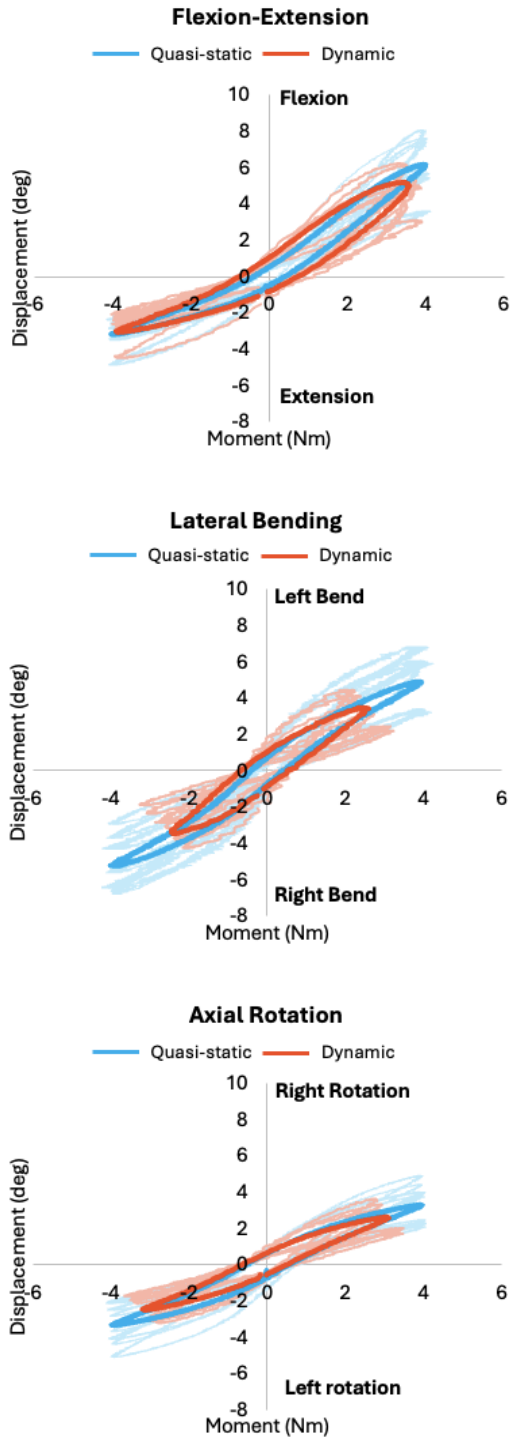


Figure 4.5. (a) Quasi-static (0.5 Nm/sec) and dynamic (5 Nm/sec) testing rates were compared. Lumbar segment range of motion was compared across three linear translations and three rotations: Tx (anterior-posterior), Ty (medial-lateral), Tz (superior-inferior), Rx (lateral bending), Ty (flexion-extension), and Tx (axial rotation). (b) Force-displacement curves for each spinal movement: flexion-extension, lateral bending and axial rotation.

4.3.3 Pure Moment in Load versus Displacement Simulator Control

Lumbar segment ROM did not change between the load control and displacement control, as the load control ROM matched the set targets for displacement control, Figure 4.6(a). Force-displacement curves, Figure 4.6(b), highlight any minor differences between the directional ROM between load and displacement control ($p > 0.05$)

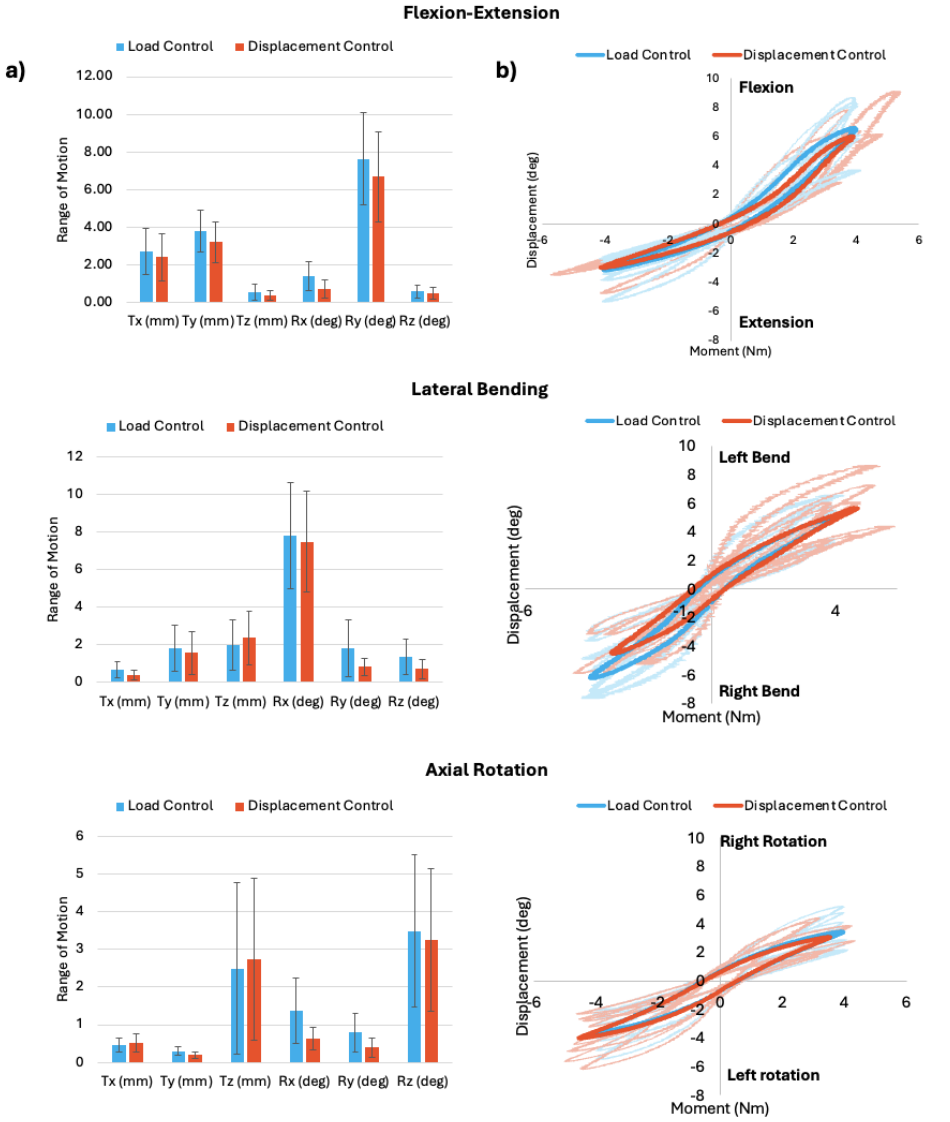


Figure 4.6. (a) Load and displacement simulator control was compared. Lumbar segment range of motion was compared across three linear translations and three rotations: Tx (anterior-posterior), Ty (medial-lateral), Tz (superior-inferior), Rx (lateral bending), Ry (flexion-extension), and Rz (axial rotation). (b) Force-displacement curves for each spinal movement: flexion-extension, lateral bending and axial rotation.

4.3.4 Neutral Zone Measurements

The neutral zone was measured from the force-displacement curves for the pure moment loading conditions, Figure 4.5, Figure 4.6b, and Table 4.3. The neutral zone for load control vs. displacement control tests were similar for FE, LB, and AR ($p>0.05$). Additionally, the neutral zone remained unchanged between the quasi-static vs dynamic tests for FE, LB, and AR ($p>0.05$).

Table 4.3. The neutral zone for load control, displacement control, quasistatic, and dynamic test protocols for FE, LB, and AR

	Load	**Displacement**	**Quasi-Static**	**Dynamic**
Flexion-Extension	1.0 ± 0.4 deg	0.8 ± 0.3 deg	1.1 ± 0.3 deg	1.5 ± 0.5 deg
Lateral Bending	1.9 ± 1.3 deg	1.4 ± 0.8 deg	1.7 ± 0.9 deg	1.7 ± 1.0 deg
Axial Rotation	1.3 ± 0.4 deg	1.3 ± 0.6 deg	1.4 ± 0.7 deg	1.1 ± 0.4 deg

4.3.5 Summary of Previous Results

Previous studies reporting ROM for *in vitro* spine biomechanics investigations using human cadaver tissues were compiled in Table 4.4. The presence of pure moment and physiologically-derived loading, quasi-static and dynamic test rates, and load and displacement control in each study was included for comparison to the present study.

Table 4.4. Comparison of present study to previous literature examining *in vitro* lumbar segment range of motion including test rate, simulator control and load targets (Beaubien et al., 2005; Panjabi et al., 1985; Sawa et al., 2020; Tanaka et al., 2001; Wheeler et al., 2011; Wilke HJ et al., 1995; Zirbel et al., 2013).

Study	Flexion-Extension (deg)	Lateral Bending (deg)	Axial Rotation (deg)	Degrees of Freedom	Testing Rate	Load Targets	Axial Pre-load	Control Mode
Present study	7.6 ± 2.5	7.8 ± 2.8	3.5 ± 2.0	1 DOF, pure moment	0.5 Nm/s	±4 Nm	250 N	Force
	6.6 ± 2.0	6.8 ± 2.4	3.1 ± 1.9	1 DOF, pure moment	5 Nm/s	±4 Nm	250 N	Force
	6.7 ± 2.4	7.5 ± 2.7	3.3 ± 1.9	1 DOF, pure moment	0.5 Nm/s	N/A*	250 N	Displacement
Wilke et al. (1995)	1.9-5.3 (F), 0.9-4.1 (E)	4.1-10.6	0.9-6.4	1 DOF, pure moment	1.7 deg/s	±3.75 Nm	No	Force
Zirbel et al., (2013)	11.8 ± 0.6	11.5 ± 6.9	2.0 ± 0.6	1 DOF, pure moment	1 deg/s	±7.5 Nm	440 N	Displacement
Beaubien et al., (2005)	10.0 ± 2.0	7.0 ± 1.5	2.0 ± 0.8	1 DOF, pure moment	0.32 Nm/s	±7.5 Nm	100 N	Force
Sawa et al., (2020)	8.9 ± 3.5	4.7 ± 1.6	2.2 ± 1.2	1 DOF, pure moment	0.03 Nm/s	±7.5 Nm	Yes, variable	Force
Wheeler et al., (2011)	7.0 ± 1.7	7.5 ± 2.7	2.6 ± 0.9	1 DOF, pure moment	0.45 Nm/s	±7.5 Nm	No	Force
Tanaka et al., (2001)	3.6 ± 2 (F), 2.4 ± 1 (E)	9.5 ± 4.0	2.2 ± 1	1 DOF, pure moment	Quasi-static	± 5.7 Nm	No	Force
Panjabi et al., (1998)	5.8-10.0 (F), 2.3-4.8 (E)	9.9-14.0	2.8-5.2	1 DOF, pure moment	Quasi-static	± 10.0 Nm	No	Displacement

4.4 Discussion

The present study compared lumbar spinal segment ROM under various testing conditions, including pure moment versus physiologically-derived 6DOF loading. Both loading profiles were also compared in quasi-static versus dynamic test rates, as well as pure moment testing in load control versus displacement control. Findings from this study provide new insights into how these factors influence lumbar segment ROM, with a brief comparison to existing literature also provided.

4.4.1 Comparison of Pure Moment versus Physiologically Derived Applied Loads

Results of the current study demonstrate significant differences in ROM between pure moment and physiologically-derived tests at both quasi-static and dynamic test rates, which is consistent with previous findings (Ebisch et al., 2024). Specifically, pure moment loading resulted in larger ROM values than physiologically-derived 6DOF testing in the primary direction of loading. This indicates that pure moment tests might not fully reflect the physiological loading conditions or magnitudes experienced by the spine *in vivo*. Lumbar spine ROM measured *in vivo* are consistently lower than those reported in cadaveric pure moment studies (Beaubien et al., 2005; Ochia et al., 2006; Sawa et al., 2020; Zirbel et al., 2013). Previous studies have also discussed that pure moment testing conditions can impose large unphysiological loads on spinal segments, potentially leading to ROM measurements that do not align with the normal functional spine kinematics observed in everyday activities (Holsgrove et al., 2014; Stokes et al., 2002). This highlights the necessity of incorporating multi-axis loading conditions in biomechanical testing to avoid overestimating ROM and to provide a more realistic simulation of spinal function.

4.4.2 Quasi-Static versus Dynamic Test Rates

The present study also compared pure moment and physiologically-derived loading at quasi-static (0.033 Hz) and dynamic (0.3 Hz) test rates, finding that dynamic loading generally resulted in slightly reduced ROM, although the differences were not statistically significant. This observation aligns with previous findings, where higher loading rates were associated with decreased ROM and increased stiffness (Newell et al., 2020; Stolworthy et al., 2014). Our study found that significant differences were observed only in ROM associated with the left-right LB actuator during FE and LB in pure moment loading. This may have been due to the generalized proportional–integral–derivative (PID) controller tuning approach taken. Specimen-specific or

movement-specific PID control parameter tuning could improve dynamic performance; however, this was not done in the present study. Interestingly, the size of the neutral zone—an indicator of the spine's flexibility and stability—remained consistent across both loading rates for pure moment loading. This suggests that despite the variations in loading rates, the overall spinal stability properties remain relatively unchanged, further supporting the robustness of the neutral zone as a critical metric in spine biomechanics. To the author's knowledge, the dynamic loading rate testing in the current study is the highest rate of physiologically-derived, 6DOF load-control spine simulation reported in literature.

4.4.3 Load Control versus Displacement Control

Our comparison of load versus displacement control testing revealed little difference in ROM. Similarly, displacement control resulted to a similar neutral zone, a finding that suggests joint stiffness does not change between load and displacement control at low cycle quasi-static rates. Load control testing has been widely favored in following the Panjabi et al., 1998 works on spine testing due to its ability to establish neutral and elastic zones reliably between specimens without overloading tissues to failure, based on an unknown ROM for each specimen (Panjabi et al., 1985). In recent years however, complex 6DOF spine simulators have favored displacement control as it is easier to apply these types of waveforms at physiological loading (Bell et al., 2013; Ebisch et al., 2024; Lazaro-Pacheco et al., 2024). However, the similar neutral zones observed under load and displacement control in the present work highlights that at quasi-static rates, simulator control mode has little effect.

4.4.4 Comparison to Previous Literature

Overall, the ROM values reported in the present study are similar those previously reported in literature as seen in Table 2, (Beaubien et al., 2005; Panjabi et al., 1985; Sawa et al., 2020; Tanaka et al., 2001; Wheeler et al., 2011; Wilke HJ et al., 1995; Zirbel et al., 2013). The FE and LB ROM in the present study are at the lower end of reported values. This is to be expected as load targets (± 4 Nm) were lower than many of the studies compared (range: ± 3.75 Nm to ± 10 Nm). Lower load targets were selected based on current recommendations for cadaveric spine testing of low density, osteoporotic bone. Further, the specimens included in the present study were of advanced age, a parameter known to increase spine stiffness and reduce range of motion (Arshad et al., 2019).

4.4.5 Limitations

The present study is not without limitations. There are known limitations of cadaveric testing, primarily inter-specimen variability and small sample sizes. A repeated measures study design was selected for this reason. Specimens used were predominantly female and of advanced age. While female spine specimens have been shown to have a larger ROM in some instances (Cook et al., 2015; Nachemson et al., 1979), these differences minimize with age (Ochia et al., 2006). Despite specimens being of advanced age (Mimura et al., 1994), the ROM similar to published literature were achieved and therefore, age-related decreases in ROM were not overwhelming. The FE, LB, and AR load waveforms were developed using data obtained from telemeterized vertebral body replacements. This dataset has certain limitations, as it was derived from a small cohort (n=3-5, movements=5-17) where participants had additional posterior instrumentation, likely resulting in partial shielding of the telemeterized implants from full spinal loading. Yet, by using directly measured *in vivo* loads, approximation errors associated with 6DOF

loading derived from computational musculoskeletal models, such as skin motion artifact, are removed (Johnson et al., 2024). However, the magnitudes of the 6DOF spinal loads applied in this study are lower compared to other computational modeling estimates, such as those generated using OpenSim (Beaucage-Gauvreau et al., 2021, 2019; Lerchl et al., 2022). With this context, it is important to recognize that a key contribution of this work is establishing a framework for creating and implementing generalized 6DOF spinal loading waveforms using the VIVO joint simulator. However, uncertainty remains with respect to the appropriate 6DOF load magnitudes that should be applied in representing spinal diversity. The use of a single commercially available joint simulator addresses challenges typically faced with custom-built joint simulators, such as maintenance, user knowledge transfer, and translating results between labs. However, the limitations related to the cost and accessibility of such commercial equipment are acknowledged by the authors.

4.5 Conclusions

Overall, the findings from this study underscore the importance of using physiologically-derived 6DOF testing with load control and appropriate pre-load conditions to best replicate *in vivo* spinal loading environments. The significant differences observed between pure moment and physiologically-derived testing highlight the potential limitations of pure moment protocols, which may not accurately represent the complex, multi-directional loading experienced by the spine in real-world conditions. By carefully selecting the appropriate testing conditions, researchers can ensure that biomechanical assessments of spinal motion segments more closely reflect the true functional behavior of the human spine.

4.6 References

Arshad, R., Pan, F., Reitmaier, S., Schmidt, H., 2019. Effect of age and sex on lumbar lordosis and the range of motion. A systematic review and meta-analysis. J Biomech. https://doi.org/10.1016/j.jbiomech.2018.11.022

Bayoglu, R., Galibarov, P.E., Verdonschot, N., Koopman, B., Homminga, J., 2019. Twente Spine Model: A thorough investigation of the spinal loads in a complete and coherent musculoskeletal model of the human spine. Med Eng Phys 68, 35–45. https://doi.org/10.1016/j.medengphy.2019.03.015

Beaubien, B.P., Derincek, A., Lew, W.D., Wood, K.B., 2005. In Vitro, Biomechanical Comparison of an Anterior Lumbar Interbody Fusion with an Anteriorly Placed, Low-Profile Lumbar Plate and Posteriorly Placed Pedicle Screws or Translaminar Screws, SPINE.

Beaucage-Gauvreau, E., Brandon, S.C.E., Robertson, W.S.P., Fraser, R., Freeman, B.J.C., Graham, R.B., Thewlis, D., Jones, C.F., 2021. Lumbar spine loads are reduced for activities of daily living when using a braced arm-to-thigh technique. European Spine Journal 30, 1035–1042. https://doi.org/10.1007/s00586-020-06631-0

Beaucage-Gauvreau, E., Robertson, W.S.P., Brandon, S.C.E., Fraser, R., Freeman, B.J.C., Graham, R.B., Thewlis, D., Jones, C.F., 2019. Validation of an OpenSim full-body model with detailed lumbar spine for estimating lower lumbar spine loads during symmetric and asymmetric lifting tasks. Comput Methods Biomech Biomed Engin 22, 451–464. https://doi.org/10.1080/10255842.2018.1564819

Bell, K.M., Hartman, R.A., Gilbertson, L.G., Kang, J.D., 2013. In vitro spine testing using a robot-based testing system: Comparison of displacement control and “hybrid control.” J Biomech 46, 1663–1669. https://doi.org/10.1016/j.jbiomech.2013.04.007

Cadieux, C., Brzozowski, P., Fernandes, R.J.R., McGregor, M.E., Zdero, R., Bailey, C.S., McLachlin, S.D., Rasoulinejad, P., 2024. Topping-Off a Long Thoracic Stabilization With Semi-Rigid Constructs May Have Favorable Biomechanical Effects to Prevent Proximal Junctional Kyphosis: A Biomechanical Comparison. Global Spine J. https://doi.org/10.1177/21925682241259695

Cook, D.J., Yeager, M.S., Cheng, B.C., 2015. Range of motion of the intact lumbar segment: A multivariate study of 42 lumbar spines. Int J Spine Surg 9. https://doi.org/10.14444/2005

Costi, J.J., Ledet, E.H., O’Connell, G.D., 2021. Spine biomechanical testing methodologies: The controversy of consensus vs scientific evidence. JOR Spine. https://doi.org/10.1002/jsp2.1138

Cunningham, B.W., Gordon, J.D., Dmitriev, A.E., Hu, N., Mcafee, P.C., 2003. Biomechanical Evaluation of Total Disc Replacement Arthroplasty: An In Vitro Human Cadaveric Model. Number 20S 28, 110–117.

Donnelly, E., Vakili, S., Getgood, A., Willing, R., Degen, R.M., 2022. Cadaveric Biomechanical Evaluation of Capsular Constraint and Microinstability After Hip Capsulotomy and Repair. Orthop J Sports Med 10. https://doi.org/10.1177/23259671221128348

Ebisch, I., Lazaro-Pacheco, D., Farris, D.J., Holsgrove, T.P., 2024. Replicating spine loading during functional and daily activities: An in vivo, in silico, in vitro research pipeline. J Biomech 163. https://doi.org/10.1016/j.jbiomech.2023.111916

Fitzpatrick, C.K., Maag, C., Clary, C.W., Metcalfe, A., Langhorn, J., Rullkoetter, P.J., 2016. Validation of a new computational 6-DOF knee simulator during dynamic activities. J Biomech 49, 3177–3184. https://doi.org/10.1016/j.jbiomech.2016.07.040

Gay, R.E., Ilharreborde, B., Zhao, K., Boumediene, E., An, K.N., 2008. The effect of loading rate and degeneration on neutral region motion in human cadaveric lumbar motion segments. Clinical Biomechanics 23, 1–7. https://doi.org/10.1016/j.clinbiomech.2007.08.006

Holsgrove, T.P., Amin, D.B., Pascual, S.R., Ding, B., Welch, W.C., Gheduzzi, S., Miles, A.W., Winkelstein, B.A., Costi, J.J., 2018. The equivalence of multi-axis spine systems: Recommended stiffness limits using a standardized testing protocol. J Biomech 70, 59–66. https://doi.org/10.1016/j.jbiomech.2017.09.010

Holsgrove, T.P., Gheduzzi, S., Gill, H.S., Miles, A.W., 2014. The development of a dynamic, six-axis spine simulator. Spine Journal 14, 1308–1317. https://doi.org/10.1016/j.spinee.2013.11.045

Holsgrove, T.P., Nayak, N.R., Welch, W.C., Winkelstein, B.A., 2015. Advanced multi-axis spine testing: Clinical relevance and research recommendations. Int J Spine Surg 9, 1–21. https://doi.org/10.14444/2034

Johnson, M.E., LeVasseur, C., Gale, T., Megherhi, S., Shoemaker, J., Pellegrini, C., Gray, E.C., Smith, P., Anderst, W.J., 2024. Lumbar spine marker placement errors and soft tissue artifact during dynamic flexion/extension and lateral bending in individuals with chronic low back pain. J Biomech 176. https://doi.org/10.1016/j.jbiomech.2024.112356

Lazaro-Pacheco, D., Ebisch, I., Holsgrove, T.P., 2024. The physiological, in-vitro simulation of daily activities in the intervertebral disc using a load Informed kinematic evaluation (LIKE) protocol. J Biomech 163. https://doi.org/10.1016/j.jbiomech.2023.111919

Lerchl, T., El Husseini, M., Bayat, A., Sekuboyina, A., Hermann, L., Nispel, K., Baum, T., Löffler, M.T., Senner, V., Kirschke, J.S., 2022. Validation of a Patient-Specific Musculoskeletal Model for Lumbar Load Estimation Generated by an Automated Pipeline From Whole Body CT. Front Bioeng Biotechnol 10. https://doi.org/10.3389/fbioe.2022.862804

Lysack, J.T., Dickey, J.P., Dumas, G.A., Yen, D., 2000. A continuous pure moment loading apparatus for biomechanical testing of multi-segment spine specimens, Journal of Biomechanics.

Mimura, M., Panjabi, M.M., Oxland, T.R., Crisco, J.J., Yamamoto, I., Vasavada, A., 1994. Disc Degeneration Affects the Multidirectional Flexibility of the Lumbar Spin. Spine (Phila Pa 1976) 19, 1371–1380.

Nachemson, A., Schultz, A., Berkson, M., 1979. Mechanical Properties of Hyman Lumbar Spine Motion Segments. Spine (Phila Pa 1976) 4, 1–8.

Newell, N., Rivera Tapia, D., Rahman, T., Lim, S., O'Connell, G.D., Holsgrove, T.P., 2020. Influence of testing environment and loading rate on intervertebral disc compressive mechanics: An assessment of repeatability at three different laboratories. JOR Spine 3. https://doi.org/10.1002/jsp2.1110

Ochia, R.S., Inoue, N., Renner, S.M., Lorenz, E.P., Lim, T.-H., Andersson, G.B.J., An, H.S., 2006. Three-Dimensional In Vivo Measurement of Lumbar Spine Segmental Motion. Spine (Phila Pa 1976) 31, 2073–2078.

Panjabi, M.M., 1992. The Stabilizing System of the Spine. Part II. Neutral Zone and Instability Hypothesis. Journal of Spine Disorders 5, 390–397.

Panjabi, M.M., Krag, M., Summers, D., Videman, T., 1985. Biomechanical time-tolerance of fresh cadaveric human spine specimens. Journal of Orthopaedic Research 3, 292–300. https://doi.org/10.1002/jor.1100030305

Rohlmann, A., Gabel, U., Graichen, F., Bender, A., Bergmann, G., 2007. An instrumented implant for vertebral body replacement that measures loads in the anterior spinal column. Med Eng Phys 29, 580–585.

Sawa, A.G.U., Lehrman, J.N., Crawford, N.R., Kelly, B.P., 2020. Variations among human lumbar spine segments and their relationships to in vitro biomechanics: A retrospective analysis of 281 motion segments from 85 cadaveric spines. Int J Spine Surg 14, 140–150. https://doi.org/10.14444/7021

Stokes, I.A., Gardner-Morse, M., Churchill, D., Laible, J.P., 2002. Measurement of a spinal motion segment stiffness matrix, Journal of Biomechanics.

Stolworthy, D.K., Zirbel, S.A., Howell, L.L., Samuels, M., Bowden, A.E., 2014. Characterization and prediction of rate-dependent flexibility in lumbar spine biomechanics at room and body temperature. Spine Journal 14, 789–798. https://doi.org/10.1016/j.spinee.2013.08.043

Tanaka, N., An, H.S., Lim, T.-H., Fujiwara, A., Jeon, C.-H., Haughton, V.M., 2001. The relationship between disc degeneration and flexibility of the lumbar spine, The Spine Journal.

Wheeler, D.J., Freeman, A.L., Ellingson, A.M., Nuckley, D.J., Buckley, J.M., Scheer, J.K., Crawford, N.R., Bechtold, J.E., 2011. Inter-laboratory variability in in vitro spinal segment flexibility testing. J Biomech 44, 2383–2387. https://doi.org/10.1016/j.jbiomech.2011.06.034

Wilke, H.-J., Claes, L., Schmitt, H., Wolf, S., 1994. A universal spine tester for in vitro experiments with muscle force simulation. Eur Spine J 3, 91–97.

Wilke, H.J., Kienle, A., Maile, S., Rasche, V., Berger-Roscher, N., 2016. A new dynamic six degrees of freedom disc-loading simulator allows to provoke disc damage and herniation. European Spine Journal 25, 1363–1372. https://doi.org/10.1007/s00586-016-4416-5

Wilke, H.-J., Wenger, K., Claes, L., 1998. Testing criteria for spinal implants: recommendations for the standardization of in vitro stability testing of spinal implants. European spine journal 7, 148–154.

Wilke HJ, Wolf S, Claes LE, Arand M, Wiesend A, 1995. Stability Increase of the Lumbar Spine With Different Muscle Groups. Spine (Phila Pa 1976) 20, 192–198.

Zehr, J.D., Callaghan, J.P., 2022. Reaction Forces and Flexion-Extension Moments Imposed on Functional Spinal Units With Constrained and Unconstrained In Vitro Testing Systems. J Biomech Eng 144. https://doi.org/10.1115/1.4053208

Zirbel, S.A., Stolworthy, D.K., Howell, L.L., Bowden, A.E., 2013. Intervertebral disc degeneration alters lumbar spine segmental stiffness in all modes of loading under a compressive follower load. Spine Journal 13, 1134–1147. https://doi.org/10.1016/j.spinee.2013.02.010

Chapter 5 - Cyclic *in vitro* simulation of physiologically-derived gait and sit-to-stand loading on the lumbar spine

Abstract:

In vitro spinal load simulation is a critical tool for understanding the biomechanics of the spine and pre-clinical evaluation of spinal implants. However, cyclic loading for *in vitro* experiments is commonly confined to application of forces or moments in only one or two degrees-of-freedom (DOF), based on limitations of most experimental test frames. While these methods can be easily adopted, 1DOF testing does not capture the true complexity of the six degree-of-freedom (6DOF) loading associated with spinal movements and activities. This study aimed to develop a more comprehensive testing method for cyclic *in vitro* spinal loading simulation of the lumbar spine by incorporating 6DOF gait and sit-to-stand (S2S) loading profiles. Eight lumbar segments from cadaveric specimens were initially subjected to 1DOF pure moment testing in load control for simulated flexion-extension, lateral bending, and axial rotation, followed by 6DOF gait and S2S simulations for 5 cycles each. Gait and S2S tests were compared at quasi-static (0.03Hz) and dynamic (0.33Hz) loading rates. 6DOF gait simulations were also simulated over a longer-duration test (10,000 steps), with comparison of the pre- and post-cycle movement response examined. Load control testing with iterative learning control (ILC) was employed to ensure load accuracy during longer-duration gait simulations. Following 10,000 steps, no significant changes in spinal range of motion were observed. Root mean square error remained below simulator load cell resolution, except for dynamic gait and sit-to-stand in compression and dynamic gait in lateral bending. During longitudinal gait testing convergence was reached at 4-10% of total test length in all actuators. One specimen experienced disc herniation mid-test, though convergence was quickly re-established. This study highlights the feasibility of simulating real-world loading conditions, such as walking and sit-to-stand motions, to better evaluate spinal implants and treatments under physiologically-derived loading conditions.

5.1 Introduction

Sit-to-stand and walking are fundamental activities of daily living that exert significant and repetitive loads on the lumbar spine. The five-repetition sit-to-stand test has become an effective clinical tool for assessing functional spine impairment (Staartjes and Schröder, 2018). During the sit-to-stand motion, the lumbar region experiences increased compressive and shear forces due to the transition from a flexed seated posture to an upright position (Nowakowska et al., 2017; Pourahmadi et al., 2019; Antonius Rohlmann et al., 2014). Similarly, walking involves continuous cyclic loading with the spine enduring smaller loads compared to sit-to-stand but more repetitions (Dreischarf, et al., 2014). Research has shown that these repetitive loading scenarios, rather than peak loads, may contribute more to conditions like disc degeneration or cage subsidence following spinal surgeries (Alkalay et al., 2018; Parkinson and Callaghan, 2009).

Simulating the loads associated with these activities in pre-clinical and biomechanical investigations is important to better understand spinal biomechanics under real-world loading conditions associated with activities of daily living. Including sit-to-stand and walking motions in testing protocols helps simulate the dynamic loading conditions that implants and treatments will experience *in vivo*, allowing for a more comprehensive evaluation and better determination of implant efficacy and potential post-operative rehabilitation guidelines. Human gait typically occurs at 1-2 Hz, with the common recommendation of 10,000 steps approximately being completed daily adults (Donelan et al., 2002; Tudor-Locke and Bassett, 2004). Dynamic frequency and duration makes accurate simulation of human gait challenging in load control. Therefore, there have been few *in vitro* investigations that have effectively simulated these types of loading conditions experimentally. Ebisch et al., used kinetic data from healthy participants in a computational OpenSim model using static optimization to generate 6DOF loading waveforms

associated with flexion-extension, lateral bending and axial rotation movements (Ebisch et al., 2024). The computed 6DOF loading waveforms were then applied experimentally to bovine motion segments at a quasi-static rate for a single cycle. Subsequently, Lazarao-Pacheco et al., expanded on this work by developing an experimental method for simulating loading conditions associated with a larger number of movements, including gait, in quasi-static load control testing, followed by applying the measured kinematics from load control in displacement control at dynamic rates. However, this study did not investigate simulation of sit-to-stand, and rate of load control was limited to very slow, quasi-static testing. To date, there has not been a spinal motion - loading simulator that can effectively simulate physiologically-derived loading conditions associated with sit-to-stand and gait activities at physiologically-derived loading rates in load control.

The objectives of the present study were to (1) develop a novel *in vitro* testing method to apply cyclic 6DOF loading waveforms associated with sit-to-stand and gait activities, and (2) compare lumbar spine kinematics before and after simulation of 10,000 cycles of gait loading. It was hypothesized that (1) by employing general PID controller tuning sit-to-stand and gait loading can be reliably simulated at quasi-static and dynamic rates and, (2) by employing iterative learning control, a 6DOF complex loading protocol can be applied in force control at a physiologic rate with minimal error over longitudinal cyclic testing.

5.2 Methods

5.2.1 Specimen Preparation

Institutional ethics approval was obtained for the use of eight lumbar spinal segments, four L2/L3 and four L4/L5, harvested from four fresh frozen cadavers (mean age: 69 ± 4.7 years; 3 females, 1 male) sourced from Science Care, Phoenix, AZ, USA. Intact spine specimens (from the

occiput to the coccyx) were first scanned via computed tomography (CT) at clinical resolution, using a 0.182 g/cm³ phantom to exclude specimens with injuries, bone abnormalities and to assess bone mineral density (average: 82.7 ± 3.8 mg/cm³). After CT scanning, the spines were sectioned and stored at -40°C until the time of biomechanical testing. Before testing, the spinal segments were thawed overnight at room temperature (20–22°C) and further dissected with care to preserve intervertebral discs and spinal ligaments. Custom 3D-printed fixtures were then used to mount the specimens onto a six-degree-of-freedom (6DOF) joint motion simulator for testing. Lumbar spinal segment specimens were sprayed with saline throughout testing to ensure tissue hydration.

5.2.2 Six-degree of freedom waveform generation

6DOF load waveforms were developed using data obtained from an open-access repository, which features *in vivo* telemetrized vertebral body replacement data (www.orthoload.org) (Rohlmann et al., 2007). Sit-to-stand and gait data, detailed in Table 5.1, were retrieved from this repository. A custom Python script was created to process the dataset. Sit-to-stand data was taken directly from the open-source repository, while gait data was sectioned to a two-step sequence (right heel strike to right heel strike). The script imported the gait and sit-to-stand 6DOF load data from each trial and applied dynamic time warping combined with peak matching to align each waveform based on the overall shape of each DOF (Fx, Fy, Fz, Mx, My, Mz). After alignment, a mean waveform was generated using the peak-matched data. This averaged waveform was subsequently filtered with a 4th order low-pass Butterworth filter at a 5 Hz cutoff, effectively smoothing the signal by removing frequencies above 5 Hz while maintaining its essential shape. A linear ramp was applied at the dataset's end to ensure identical starting and ending positions, required for cyclic operation of the joint motion simulator. Finally, the data were down sampled to 1024 points, as required by the control system of the joint motion simulator,

Figure 5.1. The resulting six-degree-of-freedom waveforms for both sit-to-stand and gait are illustrated in Figure 5.2.

Table 5.1. Data for gait and sit-to-stand waveforms was obtained from an open-source database (www.orthoload.com). The number of available subjects (n=4) and movement repetitions (20, 33) varied for each motion type.

Movement	Number of Subjects	Number of Movements
Gait	4	20
Sit-to-stand	4	33

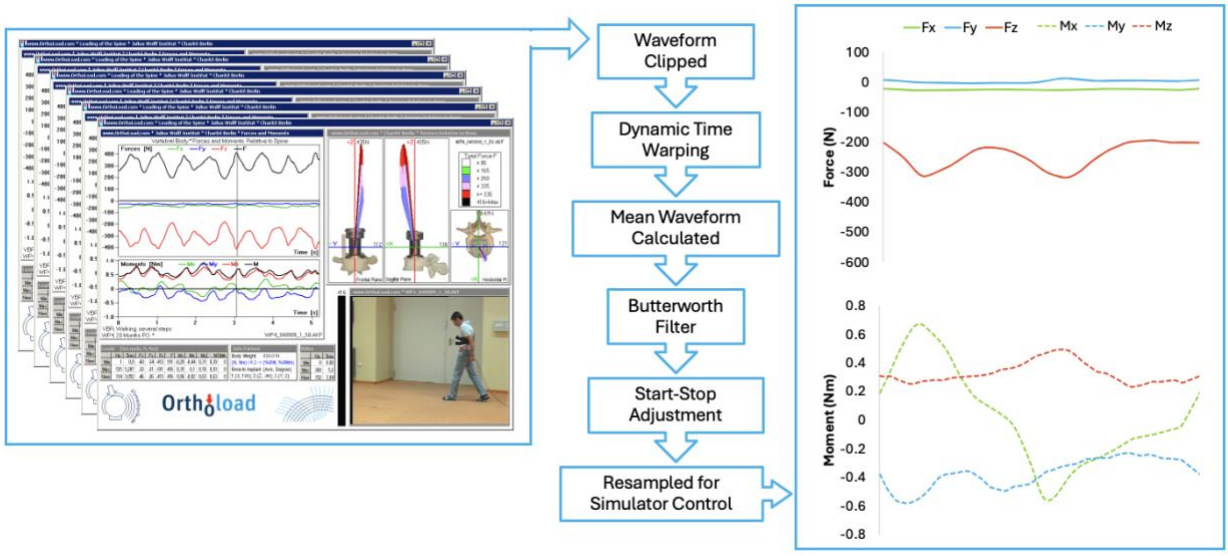


Figure 5.1. Six degree-of-freedom (6DOF) waveforms were obtained from an open-source database (www.orthoload.org) and generalized 6DOF gait (shown above) and sit-to-stand waveforms were generated using the shown data processing approach. Figure contains images obtained from www.orthoload.org.

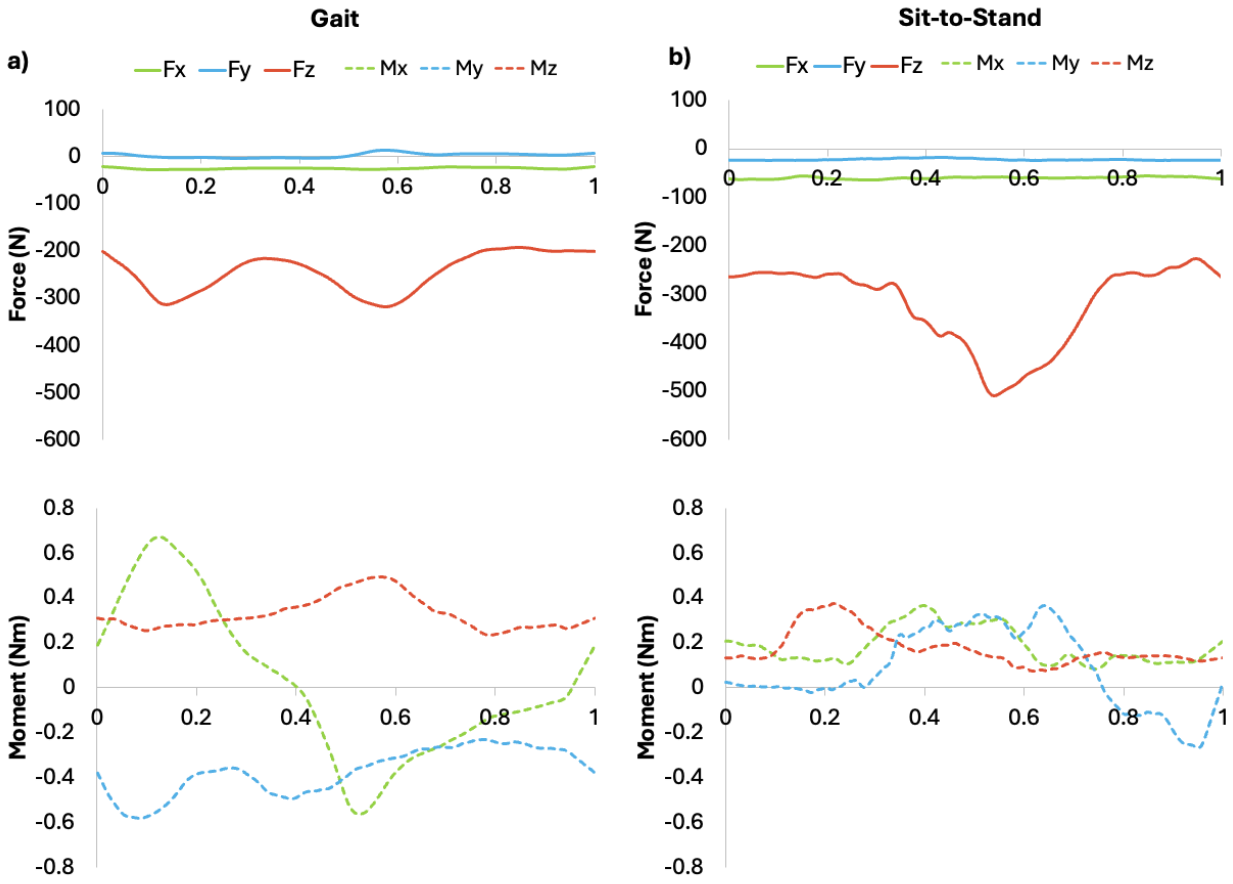


Figure 5.2. The generalized six degree-of-freedom (Fx, Fy, Fz, Mx, My, Mz) loading waveforms for (a) gait and (b) sit-to-stand were developed from OrthoLoad datasets (www.orthoload.org) using a dynamic time warping with peak matching approach. The shown waveforms have been down-sampled to 1024 points to match the waveform input requirements for the AMTI VIVO joint motion simulator. The x-axis represents the percentage of total waveform length.

5.2.3 Biomechanical Test Protocol

Biomechanical testing was completed using a commercially-available 6DOF joint motion simulator, Figure 5.3 (AMTI VIVO, AMTI, Watertown, MA, USA). Prior to fixing the specimen in place, the actuator load values were set to zero. The superior vertebra was then attached to the simulator actuators responsible for applying FE and LB loads (My and Mx respectively) and the inferior vertebra was fixed to the actuators responsible for AR (Mz) and translational forces, anterior-posterior shear (Fx), medial-lateral shear (Fy), and tension-compression (Fz). 6DOF actuator loads were resolved about the approximated centre of the superior vertebra.

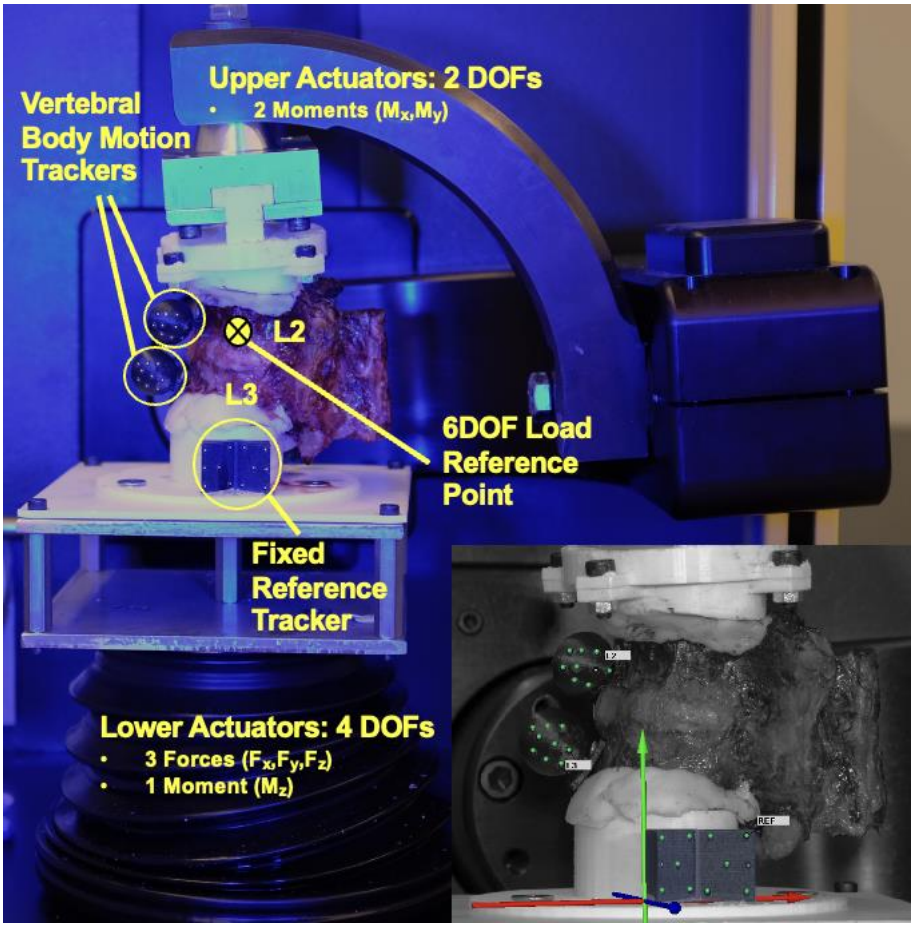


Figure 5.3. Eight human cadaveric lumbar motion segments were mounted to a six-degree of freedom (6DOF) joint motion simulator. Actuators worked together in 6DOF force control to apply the translational and rotational displacements required to simulate pure moment flexion-extension (My), lateral bending (Mx), axial rotation (Mz), 6DOF gait and 6DOF sit-to-stand. Motion segment kinematics were quantified using an ARAMIS 12M optical 3D tracking system.

The testing protocol first loaded each lumbar motion segment under pure moment loading in 6DOF force control to simulate FE, LB, and AR, following previously established spine testing protocols (Costi et al., 2021; Wilke et al., 1998). A compressive pre-load of 250 N was applied followed by five cycles of pure moment loading (±4 Nm) and a quasi-static rate (0.03 Hz). Physiologically-derived gait and sit-to-stand load profiles were then applied at both quasi-static (0.03 Hz) and dynamic (0.33 Hz) test rates for five cycles each. Dynamic rate was selected based on the duration of the sit-to-stand task from the OrthoLoad database. Error was measured between the input and applied waveforms throughout testing. The first three cycles of each movement were

used for pre-conditioning, the fourth cycle for data analysis and the fifth cycle for the simulator to return to start position. Applied load, error, and actuator motion data was collected from the joint motion simulator continuously at 50 Hz. Relative vertebral body positions were measured throughout tests using digital 3D optical motion tracking (ARAMIS Adjustable 12M, GOM Metrology, Braunschweig, Germany) using attached rigid body motion flags containing between 7-9 tracking markers (0.4mm diameter) (Figure 3). 3D motion of each vertebra were tracked relative to a fixed reference tracker, with post-hoc determination of the vertebral motion based on the superior vertebra relative to the inferior vertebra. The range of motion (ROM) of the individual motion segments was calculated from the difference between the minimum and maximum values for each of the 6DOF from the ARAMIS camera data.

5.2.4 Statistical Analysis

The total lumbar segment ROM and neutral zone for FE, LB and AR were compared before and after the 10,000 steps gait loading protocol to draw conclusions towards specimen degradation during longitudinal testing. A Bartlett's test for homogeneity of variance was used to determine if variance between parameters were equal. All variance between parameters were equal and therefore a one-way analysis of variance was used to test the differences between parameters. A Holm's step-down post hoc test was conducted to account for family-wise error rate and provide a more conservative assessment of significance. For all parameters, significance was established as $p<0.05$. Root mean square error (RMSE) was calculated and reported for discrete gait and sit-to-stand movements at quasi-static and dynamic test rates. RMSE was calculated every 200 steps and reported for longitudinal gait testing to visualize the waveform convergence over time.

5.3 Results

5.3.1 Lumbar Segment ROM Following 10,000 steps

Lumbar segment ROM was slightly larger in FE, LB, and AR following 10,000 steps; however, there was no significant difference in the pre- and post-10,000 step ROM in any DOF for FE, LB, or AR ($p > 0.05$), Figure 5.4. The force-displacement curves between pre- and post-10,000 steps pure moment data were similar ($p > 0.05$), Table 5.2, indicating no changes in elastic response of the lumbar motion segments after longitudinal cyclic testing, Figure 5.5.

Table 5.2. Neutral zone measurements for pre- and post-10,000 step in FE, LB, and AR

	Pre-10,000 steps	**Post-10,000 steps**
Flexion-Extension	1.1 ± 0.3 deg	1.0 ± 0.4 deg
Lateral Bending	1.7 ± 0.9 deg	1.8 ± 1.3 deg
Axial Rotation	1.4 ± 0.5 deg	1.3 ± 0.4 deg

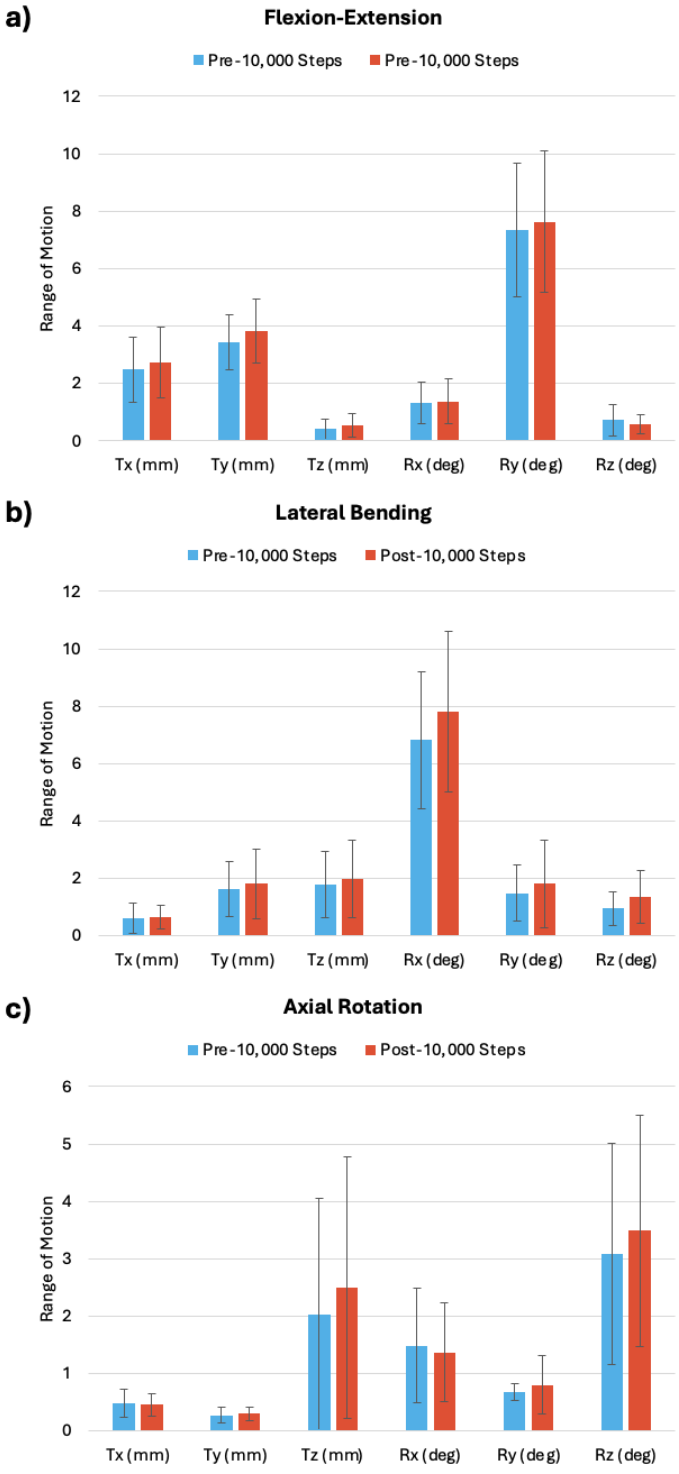


Figure 5.4. Lumbar segment range of motion was measured during (a) flexion-extension, (b) lateral bending, and (c) axial rotation before (blue) and after (red) the 10,000 step longitudinal cyclic loading protocol. Relevant segmental range of motion is reported across three linear translations and three rotations: Tx (anterior-posterior), Ty (medial-lateral), Tz (superior-inferior), Rx (lateral bending), Ry (flexion-extension), and Rz (axial rotation).

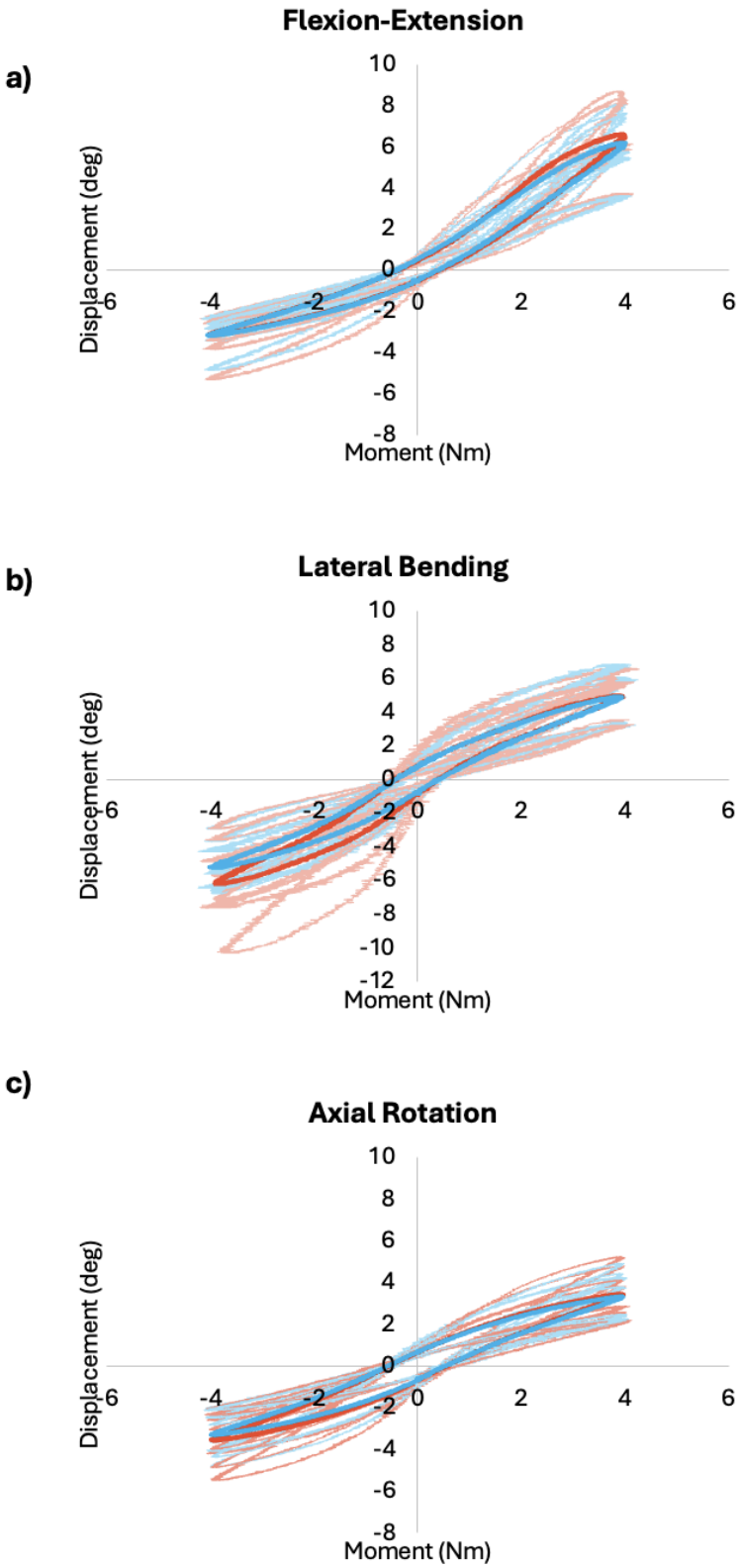


Figure 5.5. (b) Force-displacement curves for each spinal movement: (a) flexion-extension, (b) lateral bending and (c) axial rotation.

5.3.2 6DOF Load Control Simulation

The RMSE for both quasi-static and dynamic simulation of the gait and sit-to-stand waveforms was less than the load cell resolution for the majority of DOF with specific exceptions, Figure 5.6. RMSE was greater than load cell uncertainty error for dynamic gait and sit-to-stand in the Fz direction (superior-inferior) and dynamic gait in the My direction (lateral-bending).

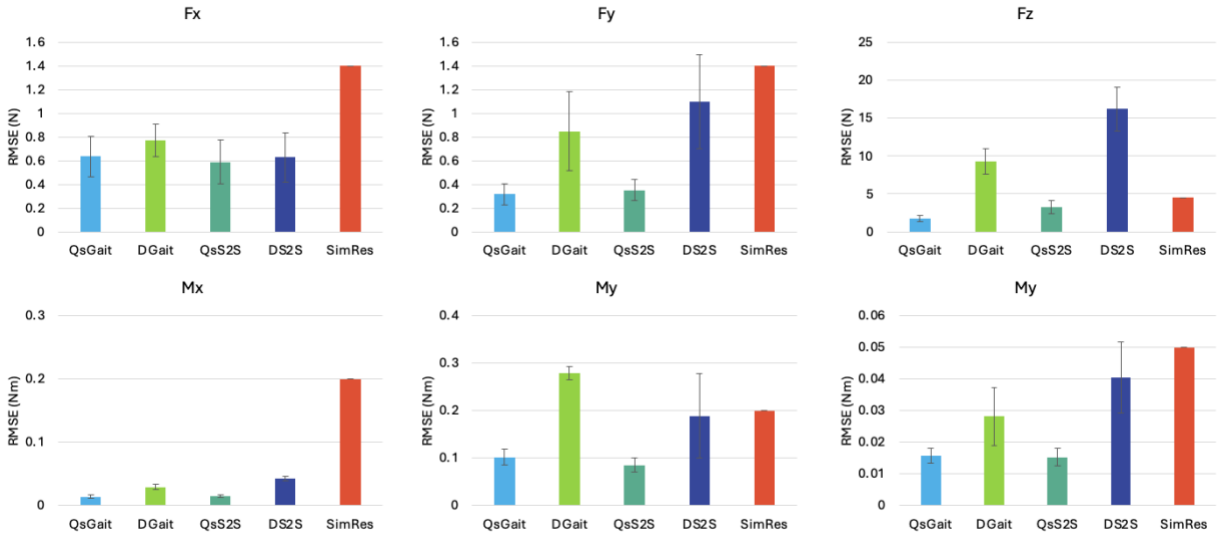


Figure 5.6. Root mean square error for quasi-staic gait (QsGait), dynamic gait (DGait), quasi-static sit-to-stand (QsS2S) and dynamic sit-to-stand (DS2S) were compared to the simulator actuator resolution (SimRes) in three linear translations and three rotations: Tx (anterior-posterior), Ty (medial-lateral), Tz (superior-inferior), Rx (lateral bending), Ry (flexion-extension), and Rz (axial rotation).

5.3.3 Cyclic Gait Simulation with ILC

Waveform convergence was reached when RMSE was below the level of the actuator specific resolution. Under the cyclic gait loading waveform convergence was reached at 10%, 6%, 4%, 8% and 6% of the total test length for Fx, Fy, Fz, My, and Mz actuators, respectively (Figure 5.7). Mx convergence occurred at 4% of total test duration; however, an upwards drift was noted in all specimens. One specimen sustained an anterior disc herniation at approximately 7200 steps,

which resulted in a brief RMSE deviation which quickly re-converged with continued testing to 10000 cycles.

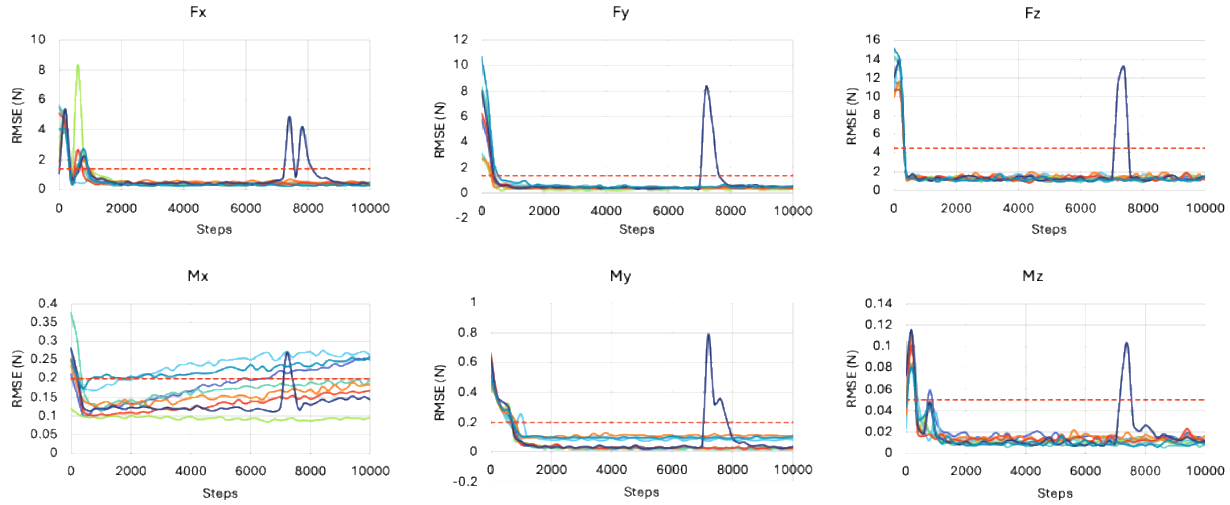


Figure 5.7. Root mean square error for longitudinal gait testing for three linear translations and three rotations: Tx (anterior-posterior), Ty (medial-lateral), Tz (superior-inferior), Rx (lateral bending), Ry (flexion-extension), and Rz (axial rotation). The horizontal red line represents the actuator specific load resolution. Note: one specimen sustained a disc injury at 7200 steps.

5.4 Discussion

5.4.1 Lumbar Segment ROM Following 10,000 steps

While small increases were noted, there were no significant differences in lumbar segment range of motion following 10,000 steps for simulated FE, LB, or AR movements. At a gait frequency of 2 Hz (1 Hz simulator frequency for the two-step waveform), the 10,000 step protocol duration was approximately 83.3 minutes of continuous, uninterrupted testing. The present study results are consistent with previous literature. Panjabi et al. reported that freeze thaw cycles and test duration have little impact on biomechanical behaviour of lumbar spine segments (Panjabi et al., 1985). Wilke et al. found similar results stating that long-duration has limited impact on spine biomechanics when tissue hydration is maintained (Wilke et al., 1998). Compressive mechanics of the intervertebral disc have been shown to be resilient to test environment during short-term

testing, < 90 minutes (Newell et al., 2020). Therefore, the test protocol provided in the present study provides a reasonable longitudinal test protocol for examining the effect of injury and surgical interventions.

5.4.2 6DOF Load Control Simulation

The present study was successful in simulating complex 6DOF spine loading at quasi-static rates. General PID control parameters were used for both gait and sit-to-stand movements at both quasi-static and dynamic test rates. This resulted in RMSE larger than the actuator specific resolution in Fz and My for dynamic gait and sit-to-stand. Therefore, specimen specific and movement specific PID controls may improve simulator performance but at the cost of increased test length.

5.4.3 Cyclic Gait Simulation with ILC

The ten-thousand steps value as a targeted number of cycles holds relevance for cyclic load simulation in spine biomechanics and implant testing. Ten-thousand steps per day is commonly used as the reasonable expectation of daily activity for healthy adults (Tudor-Locke and Bassett, 2004). Physiologic gait occurs a step frequency of 1-2Hz and, as such, the test frequency of 2 steps per second (2 Hz) was selected to simulate lumbar segment loading in a medium to fast walking pace (Donelan et al., 2002). Simulating complex 6DOF movements at physiologic rates in load control has proven difficult in the past. To achieve physiologic rates for activities of daily living, protocols have recorded kinematics in load control at quasistatic rates and implemented displacement control at higher dynamic or physiologic rates (Lazaro-Pacheco et al., 2024). While this approach may mitigate simulator control issues, soft tissues are known to be viscoelastic and have rate-dependent responses, including hysteresis and creep. By employing an ILC approach,

the present study was successful in simulating complex 6DOF spinal loading at physiologic rates in load control. This allowed for load magnitudes to remain static while lumbar segment kinematics could change to account for time-dependent changes in soft tissue mechanics. Further, simulator convergence was reached at 4-10% of total test duration. Therefore, highly accurate simulation of 6DOF spine loading under load control can be achieved without the need for specimen or movement-specific PID tuning.

Of note, one specimen did experience an anterior intervertebral disc herniation during the 10,000 step protocol. This is believed to have occurred as a result of an injury sustained during tissue preparation and dissection, rather than as a result of the load protocol itself. This occurrence did highlight the ILC capability to compensate with changes to PID control settings following an injury mid-test. The potential of this feature could be investigated in further studies aimed at identifying the ILC capabilities.

5.4.4 Study Limitations

There are recognized limitations to this study. *In vitro* cadaveric testing has known limitations such as inter-specimen variability, small sample sizes, and tissue degradation in older specimens. Therefore, a repeated measures study design was selected to help mitigate these challenges. Additionally, the sample set was primarily made up of female specimens and sex differences were not included in study outcomes. Past studies have suggested that female specimens have larger ROM of the lumbar spine; however, these differences are less prominent in older specimens and Ochia et al., 2006 showed there were no significant differences between male and female cadaveric spine specimens. The gait and sit-to-stand load waveforms were generated from data recorded in telemeterized vertebral body replacements. This data is limited due to the small number of participants in the original study (n=4) and the fact that subjects had additional

posterior implant fixation, which did not include any load sensing instrumentation so the degree of load sharing between the anterior and posterior implants is unknown. In any case, the posterior implants would have likely shared some degree of the lumbar segment loading with the telemeterized vertebral body replacement implants in the anterior column. Therefore, the loads used in the current study are lower than those from other estimations, such as from the use of computational musculoskeletal modeling software like OpenSim and SIMPACK (Beaucage-Gauvreau et al., 2021, 2019; Lerchl et al., 2022). However, the current study does provide a framework for generating and applying generalized complex 6DOF loading waveforms, even if there is larger variations in the expected load magnitudes. This study was also completed in a single laboratory using one type of commercially-available joint motion simulator. Inter-laboratory testing with a variety of custom spinal motion-loading simulators has been used recently to show important variations in spine biomechanics testing; however, these studies are very costly and require significant coordination between labs. As an alternative, use of a commercially-available joint motion simulator more easily allows for this methodology to be adopted by other labs with similar equipment; however, the authors acknowledge the limitations associated with the cost and acquisition of such resources. Lastly, only two activities of daily living were examined. These were selected for their relevance and frequency in daily life; however, two activities alone do not cover the well documented breadth of complex loading conditions in the lumbar spine and low back (Ignasiak et al., 2018). Previous groups have examined as many as 20 complex movements in longitudinal spine testing and therefore expanding the scope of this work should be a future aim (Lazaro-Pacheco et al., 2024).

5.5 Conclusions

The present study provides a valuable 6DOF test protocol that has potential for improving biomechanical testing methods to better represent the complex loading experienced in the lumbar spine. To the best of the authors knowledge, this is the first study to successfully employ complex 6DOF load control lumbar spine motion simulation at a physiologic loading rate over extended duration cyclic testing, an important step towards the goal of representing the physiologic environment in laboratory testing. This work provides the basis for future studies aimed at expanding the magnitude of loads applied and the number of activities of daily living that can be simulated. Future work should focus on the further investigating the impact of physiologically-derived loading on spinal implant performance as well as quantifying tissue mechanics at a more granular level with extended 6DOF cyclic testing.

5.6 References

Alkalay, R.N., Adamson, R., Groff, M.W., 2018. The effect of interbody fusion cage design on the stability of the instrumented spine in response to cyclic loading: an experimental study. Spine Journal 18, 1867–1876. https://doi.org/10.1016/j.spinee.2018.03.003

Beaucage-Gauvreau, E., Brandon, S.C.E., Robertson, W.S.P., Fraser, R., Freeman, B.J.C., Graham, R.B., Thewlis, D., Jones, C.F., 2021. Lumbar spine loads are reduced for activities of daily living when using a braced arm-to-thigh technique. European Spine Journal 30, 1035–1042. https://doi.org/10.1007/s00586-020-06631-0

Beaucage-Gauvreau, E., Robertson, W.S.P., Brandon, S.C.E., Fraser, R., Freeman, B.J.C., Graham, R.B., Thewlis, D., Jones, C.F., 2019. Validation of an OpenSim full-body model with detailed lumbar spine for estimating lower lumbar spine loads during symmetric and asymmetric lifting tasks. Comput Methods Biomech Biomed Engin 22, 451–464. https://doi.org/10.1080/10255842.2018.1564819

Costi, J.J., Ledet, E.H., O'Connell, G.D., 2021. Spine biomechanical testing methodologies: The controversy of consensus vs scientific evidence. JOR Spine. https://doi.org/10.1002/jsp2.1138

Delp, S.L., Anderson, F.C., Arnold, A.S., Loan, P., Habib, A., John, C.T., Guendelman, E., Thelen, D.G., 2007. OpenSim: Open-source software to create and analyze dynamic simulations

of movement. IEEE Trans Biomed Eng 54, 1940–1950. https://doi.org/10.1109/TBME.2007.901024

Donelan, J.M., Kram, R., Kuo, A., 2002. Mechanical work for step-to-step transitions is a major determinant of the metabolic cost of human walking 3717–3727.

Ebisch, I., Lazaro-Pacheco, D., Farris, D.J., Holsgrove, T.P., 2024. Replicating spine loading during functional and daily activities: An in vivo, in silico, in vitro research pipeline. J Biomech 163. https://doi.org/10.1016/j.jbiomech.2023.111916

Ignasiak, D., Rüeger, A., Sperr, R., Ferguson, S.J., 2018. Thoracolumbar spine loading associated with kinematics of the young and the elderly during activities of daily living. J Biomech 70, 175–184. https://doi.org/10.1016/j.jbiomech.2017.11.033

Lazaro-Pacheco, D., Ebisch, I., Holsgrove, T.P., 2024. The physiological, in-vitro simulation of daily activities in the intervertebral disc using a load Informed kinematic evaluation (LIKE) protocol. J Biomech 163. https://doi.org/10.1016/j.jbiomech.2023.111919

Lerchl, T., El Husseini, M., Bayat, A., Sekuboyina, A., Hermann, L., Nispel, K., Baum, T., Löffler, M.T., Senner, V., Kirschke, J.S., 2022. Validation of a Patient-Specific Musculoskeletal Model for Lumbar Load Estimation Generated by an Automated Pipeline From Whole Body CT. Front Bioeng Biotechnol 10. https://doi.org/10.3389/fbioe.2022.862804

Newell, N., Rivera Tapia, D., Rahman, T., Lim, S., O'Connell, G.D., Holsgrove, T.P., 2020. Influence of testing environment and loading rate on intervertebral disc compressive mechanics: An assessment of repeatability at three different laboratories. JOR Spine 3. https://doi.org/10.1002/jsp2.1110

Nowakowska, K., Gzik, M., Michnik, R., Myśliwiec, A., Jurkojć, J., Suchoń, S., Burkacki, M., 2017. The Loads Acting on Lumbar Spine During Sitting Down and Standing Up, in: Innovations in Biomedical Engineering. Springer International Publishing, pp. 169–176.

Panjabi, M.M., Krag, M., Summers, D., Videman, T., 1985. Biomechanical time-tolerance of fresh cadaveric human spine specimens. Journal of Orthopaedic Research 3, 292–300. https://doi.org/10.1002/jor.1100030305

Parkinson, R.J., Callaghan, J.P., 2009. The role of dynamic flexion in spine injury is altered by increasing dynamic load magnitude. Clinical Biomechanics 24, 148–154. https://doi.org/10.1016/j.clinbiomech.2008.11.007

Pourahmadi, M.R., Takamjani, I.E., Jaberzadeh, S., Sarrafzadeh, J., Sanjari, M.A., Bagheri, R., Taghipour, M., 2019. Kinematics of the spine during sit-to-stand movement using motion analysis systems: A systematic review of literature. J Sport Rehabil. https://doi.org/10.1123/jsr.2017-0147

Rohlmann, A., Dreischarf, M., Zander, T., Graichen, F., Bergmann, G., 2014. Loads on a vertebral body replacement during locomotion measured in vivo. Gait Posture 39, 750–755. https://doi.org/10.1016/j.gaitpost.2013.10.010

Rohlmann, A., Gabel, U., Graichen, F., Bender, A., Bergmann, G., 2007. An instrumented implant for vertebral body replacement that measures loads in the anterior spinal column. Med Eng Phys 29, 580–585.

Rohlmann, Antonius, Pohl, D., Bender, A., Graichen, F., Dymke, J., Schmidt, H., Bergmann, G., 2014. Activities of everyday life with high spinal loads. PLoS One 9, 1–9. https://doi.org/10.1371/journal.pone.0098510

Seth, A., Hicks, J.L., Uchida, T.K., Habib, A., Dembia, C.L., Dunne, J.J., Ong, C.F., DeMers, M.S., Rajagopal, A., Millard, M., others, 2018. OpenSim: Simulating musculoskeletal dynamics and neuromuscular control to study human and animal movement. PLoS Comput Biol 14, e1006223.

Staartjes, V.E., Schröder, M.L., 2018. The five-repetition sit-to-stand test: Evaluation of a simple and objective tool for the assessment of degenerative pathologies of the lumbar spine. J Neurosurg Spine 29, 380–387. https://doi.org/10.3171/2018.2.SPINE171416

Tudor-Locke, C., Bassett, D.R., 2004. CURRENT OPINION How Many Steps/Day Are Enough? Preliminary Pedometer Indices for Public Health, Sports Med.

Wilke, H.J., Jungkunz, B., Wenger, K., Claes, L.E., 1998. Spinal segment range of motion as a function of in vitro test conditions: Effects of exposure period, accumulated cycles, angular-deformation rate, and moisture condition. Anatomical Record 251, 15–19. https://doi.org/10.1002/(SICI)1097-0185(199805)251:1<15::AID-AR4>3.0.CO;2-D

Wilke, H.-J., Wenger, K., Claes, L., 1998. Testing criteria for spinal implants: recommendations for the standardization of in vitro stability testing of spinal implants. European spine journal 7, 148–154.

Chapter 6– Architectural bone parameters and the relationship to titanium lattice design for powder bed fusion additive manufacturing [3]

Abstract

Additive manufacturing (AM) of titanium (Ti) and Ti-6Al-4V lattices has been proposed for bone implants and augmentation devices. Ti and Ti-6Al-4V have favorable biocompatibility, corrosion resistance and fatigue strength for bone applications; yet, the optimal parameters for Ti-6Al-4V lattice designs corresponding to the natural micro- and meso-scale architecture of human trabecular and cortical bone are not well understood. A comprehensive review was completed to compare the natural lattice architecture properties in human bone to Ti and Ti-6Al-4V lattice structures for bone replacement and repair. Ti and Ti-6Al-4V lattice porosity has varied from 15% to 97% with most studies reporting a porosity between 50% and 70%. Cortical bone is roughly 5–15% porous and lattices with 50–70% porosity are able to achieve comparable stiffness, compressive strength, and yield strength. Trabecular bone has a reported porosity range from 70% to 90%, with trabecular thickness varying from 120 to 200 μm. Existing powder bed fusion technologies have produced strut and wall thicknesses ranging from 200 to 1669 μm. This suggests limited overlap between current AM of Ti and Ti-6Al-4V lattice structures and trabecular bone architecture, indicating that replicating natural trabecular bone parameters with latticing is prohibitively challenging. This review contributes to the body of knowledge by identifying the correspondence of Ti and Ti-6Al-4V lattices to the natural parameters of bone microarchitectures and provides further guidance on the design and AM recommendations towards addressing recognized performance gaps with powder bed fusion technologies.

[3] A version of this chapter has been published in peer-reviewed journal and has been modified to fit the current thesis style: McGregor, M; Patel, S; McLachlin, S; Vlasea, M. (2021). Architectural bone parameters and the relationship to titanium lattice design for powder bed fusion additive manufacturing. Additive Manufacturing, 47: 102273.

6.1 Introduction

The use of Ti-6Al-4V is well established in the medical device industry (Oshia, 2010). Titanium and titanium alloys are ideal for replacing hard tissues, such as bone, due to their biocompatibility and excellent strength-to-weight ratio (Lin et al., 2013; Song et al., 2017). Ti-6Al-4V also exhibits excellent fatigue strength and corrosion resistance allowing implants to withstand the cyclic loading in high ion environments present *in vivo* during activities of daily living (Ong et al., 2014). These properties of titanium and Ti-6Al-4V have led such alloys to become some of the most widely used metal materials for bone replacement and fixation procedures in the orthopaedic industry.

Despite their widespread use in the medical device industry for the replacement and repair of bone, pure titanium and Ti-6Al-4V do not have material properties similar to those of bone. Ti-6Al-4V is roughly twice as stiff as human cortical bone with up to seven times the compressive strength (u Plessis et al., 2019; Emmelmann et al., 2011; Murr et al., 2011). Bone is mechanoresponsive and requires regular loading in order to proliferate new bone. Implanting a stiffer material like titanium adjacent to bone can cause stress shielding of bone, resorption of the surrounding bone tissue which can lead to implant loosening and failure (Tonino et al., 1976). Therefore, it is imperative that designs of titanium and titanium alloy implants are tailored to more closely match the natural mechanical response of bone tissue.

One approach to reducing stress shielding near the bone-implant interface is by light-weighting implants through latticing in an effort to reduce mechanical properties from those of the bulk modulus of the material. Additive manufacturing allows for unique design approaches thereby allowing for control of mechanical properties, while minimizing weight through unique geometries and graded material properties. Additive manufacturing technologies are of particular use in the

orthopaedic device industry where implants are made for specific applications in which weight and mechanical properties are integral to implant function. Some examples of orthopaedic applications for latticed titanium structures include light-weighting femoral stems for total hip replacement, optimized lattice structure for spinal interbody fusion cages and bone repair scaffolds following tumor resection procedures (Arabnejad et al., 2017; Choy et al., 2017; Kim et al., 2017; Mobbs et al., 2017; Phan et al., 2016; Xu et al., 2016).

Production of Ti-6Al-4V lattice structures through additive manufacturing for biomedical applications was thoroughly reviewed by Tan et al. in 2017. They concluded that optimal guidelines for lattice design in biological environments has not yet been established and that the field is rapidly and continually evolving (Tan et al., 2017). Since the review by Tan et al. in 2017 was completed, many additional studies have successfully progressed toward this goal by manipulating lattice parameters such as porosity, pore size, and strut thickness in order to produce unit cells that more closely exhibit stiffness, compressive strength and fatigue strength of human bone. Lattice parameters vary widely across the literature and while general recommendations have been made, there remain questions as to which lattice design produces the optimal structure for implant fixation and reduction of stress shielding through mechanical property optimization.

A consideration that is notably overlooked in developing lattice structures for bone replacement is how to best model the architectural parameters of human bone. Therefore, a comprehensive literature review is needed to examine the parameters of bone micro-architecture in correspondence with lattice design parameters used in additive manufacturing. A review of existing additive manufacturing literature was completed to determine which titanium lattice parameters have been examined for bone replacement and repair implants. Lastly, recommendations are made on how to best use this information towards the design and additive

manufacturing of improved titanium and Ti-6Al-4V lattice structures for bone replacement and repair.

6.2 Review of human bone properties relevant to lattice design

6.2.1 Review of human bone function

Bone is a tough, elastic tissue that gives structural support to the human body. As a living tissue, bone adapts to its environment and loading conditions through the breakdown of existing bone by osteoclasts and the proliferation of new bone by osteoblasts. This process leads bone to exhibit mechanoresponsive behavior, wherein the more it is loaded, the thicker and denser it becomes. Bone can be categorized into two main types: cortical bone and trabecular bone, see Fig. 6.1. Different bones in the human body consist of different amounts and configurations of cortical and trabecular bone. Long bones, such as the femur, tibia, radius, and humerus, have a long shaft made up of primarily cortical bone. The metaphysis of long bones are made of primarily trabecular bone contained by a thin shell of cortical bone. Short bones, such as vertebrae, carpals, and tarsals, are made primarily of trabecular bone with a thin cortical shell making them strong and compact. Cortical bone density and trabecular bone density are important indicators of bone strength, and decrease with age, for instance by approximately 0.41% and 0.65% per year, respectively, for women ages 70–87 years old (Boonen et al., 1997). However, studies have demonstrated that trabecular bone has a higher correlation to bone strength than cortical bone (Spadaro et al., 1994).

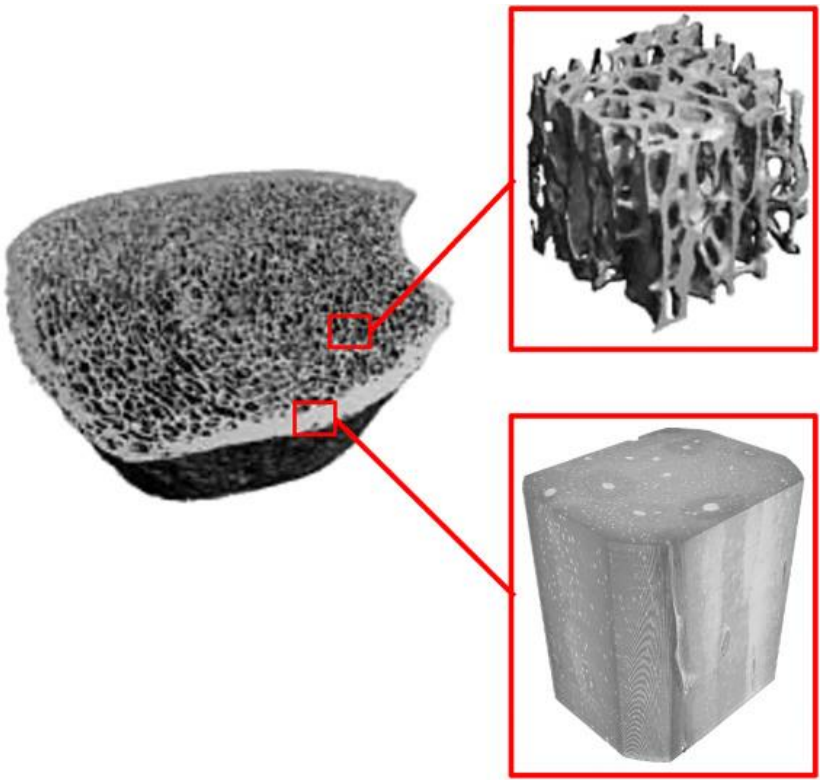


Figure 6.1 Human bone can be categorized into two main types: cortical and trabecular. Cortical bone is the stiffer, more dense bone which encapsulates short bones, the ends of long bones and comprises the shaft of long bones. Trabecular bone is the lattice like structure which makes up the majority of short bone structure as well as the ends of long bones. This figure was adapted from the μCT work of Lui et al. and Gauthier et al. (Gauthier et al., 2019; X. S. Liu et al., 2010.)

6.2.2 Trabecular bone

Trabecular bone, or cancellous bone, is a lattice-like structure that allows bone to maintain its strength, while being relatively lightweight. Trabecular bone is primarily located at the metaphysis of long bones and in the body of short bones, which allows for improved load transfer through these structures. The exact configuration of trabecular bone micro-structure is still being discovered. The most established theory characterizes the trabeculae, or struts, by their thickness, spacing, number and spatial configuration. Measurement techniques for these parameters are well established and widely published to comparatively describe trabecular bone quality, with more and thicker trabeculae suggesting better bone health (Majumdar et al., 1997). However, emerging and

more advanced geometric models consider the shape of trabecular surface and the rod vs plate-like structures of trabecular architecture in greater detail (Callens et al., 2020; van Lenthe et al., 2006).

The integrity of trabecular bone microstructure is often used as an indicator for overall bone health. At any given age, men have a higher trabecular bone mass than women but decreases in trabecular bone density due to aging are similar in women and men (Chen et al., 2013; Khosla et al., 2006; Macdonald et al., 2011; Nicks et al., 2012; Riggs et al., 2004). Age-related changes cause buckling of trabeculae due to a decrease in the number and thickness of trabeculae, and an increase in trabeculae length (Majumdar et al., 1997). Collectively, these changes result in a decreased trabecular density; however, the pathology of this reduction differs in men and women (Majumdar et al., 1997). In women, the decrease in bone volume occurs primarily due to a decrease in the number of trabeculae, whereas in men, it may be predominantly attributed to the thinning of trabeculae (Aaron et al., 1987; Chen et al., 2013). The decrease in trabeculae in women is related to menopause, where less estrogen is produced, which increases bone reabsorption (Seeman et al., 2002). Therefore, in making design considerations for orthopaedic medical devices, the patient population, age and sex should be carefully considered. Changes may be made to lattices designs to model the reduction in bone density with age. Lattice structures with fewer shorter features may better represent aging female bone and lengthening features may better model aging male bone. Lower density lattice designs should also be considered for older adults and post-menopausal women.

6.2.2.1 Micro-architecture of trabecular bone

The micro-structure of trabecular bone can be characterized by the individual trabeculae and the spaces between them. To determine bone porosity, the volume of bone (BV) is divided by the total volume (TV) for a given sample (BV/TV). Other groups have also compared total bone

surface area (BS) with respect to bone volume (BS/BV) or total specimen volume (BS/TV) as another form of trabecular quality indicator. Trabeculae are further characterized by thickness of individual vertical trabeculae (TbTh), the distance between trabeculae (TbSp), and the number of trabeculae that intersect with a given two-dimensional distance metric (TbN), typically 1 cm, as shown in Fig. 6.2.

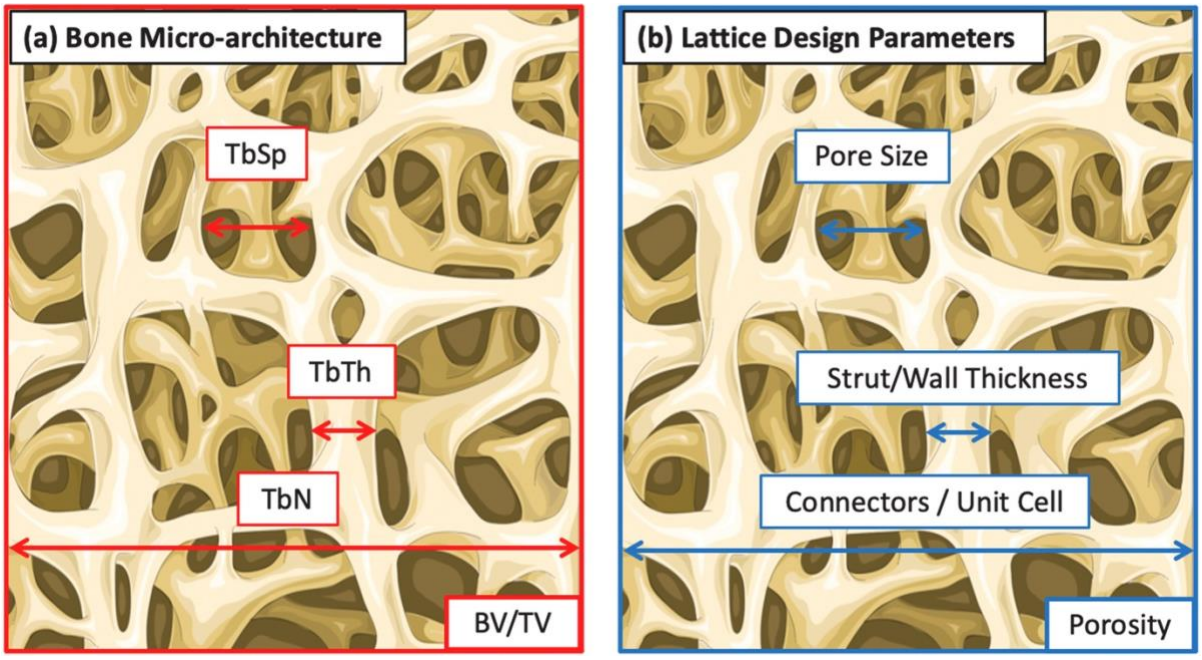


Figure 6.2 Commonly reported measurements of trabecular bone microstructure (left) may be used to describe lattice parameters commonly used in additive manufacturing (right). (For interpretation of the references to colour in this figure legend, the reader is referred to the web version of this article.)

Methods of calculating bone architectural parameters may vary between studies; however, the technique proposed by Hildebrand et al. is the most widely accepted in general literature, as shown in Table 6.1. Hildebrand et al. proposed a two-dimensional (2D) plate model that allows for calculation of 2D parameters such as TbTh, TbSp and TbN (Hildebrand et al., 1999).

Table 6.1 The Hildebrand et al. method for calculating two dimensional trabecular measurements from known bone volume fractions (Hildebrand et al., 1999).

Trabecular Bone Parameter	Measurement/Calculation
Apparent bone density	BV/TV
Porosity	1 - BV/TV
Bone surface fraction	BS/BV or BS/TV
Trabecular thickness	TbTh = 2 BV/BSs
Trabecular spacing	TbSp = 2 (TV-BV)/BS
Trabecular number	TbN = 0.5 BS/TV

Trabecular bone density and parameters vary greatly with anatomical location, as shown in Fig. 6.3. When determining design considerations for bone replacing implants, anatomical location and device function should be considered. Hildebrand et al. undertook an in-depth *in vitro* study comparing the micro-architecture of trabecular bone at different sites across the skeleton (Hildebrand et al., 1999).

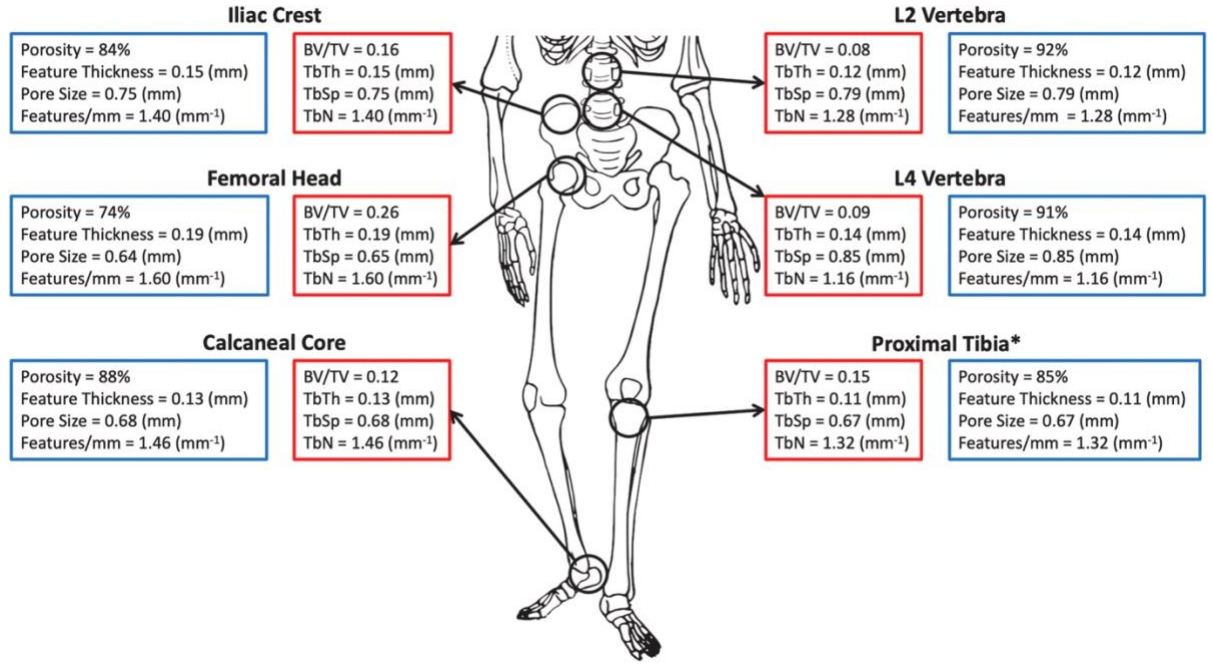


Figure 6.3 A comprehensive summary of two- and three-dimensional measurements of trabecular bone at the femoral head, illiac crest, calcaneal core, L2 vertebra and L4 vertebra as described by Hildebrand et al. 1999. The mean data reported by Hildebrand et al. was supplemented with Thomsen et al.'s report (Thomsen et al., 2005) of trabecular bone parameters at the proximal tibia to form an original visual representation*. Bone microstructure data is outlined in red and suggested translation to lattice design parameters is outlined in blue. The values listed represent the mean value of the each measurement.

6.2.2.2 Mechanical properties of trabecular bone

The mechanical properties of trabecular bone vary significantly with respect to bone density. For instance, trabecular bone density predicts 81% of axial strength variation in the human tibia (Munford et al., 2020). The porosity of human trabecular bone ranges from 40% to 95%, dependent on skeletal location, bone region, and population parameters (Morgan et al., 2018). Trabecular bone is anisotropic with stiffness and strength differing along the z-, x- and y-axis (Liu et al., 2008). Young's modulus of trabecular bone can range from 1 to 5 GPa along the axis of loading and 50–700 MPa off-axis. As such, the compressive and tensile strength of trabecular bone ranges from 0.1 to 30 MPa and 6 to 8 MPa, respectively (Bartel and Davy, 2006; Park and Lakes, 2007; Velasco et al., 2015).

6.2.3 Cortical Bone

Cortical bone, or compact bone, is much more dense than trabecular bone and acts as a stiff outer layer for short bones, joints in long bones and the sole composition of the hollow shafts of long bones. Cortical shells allow for a continuous surface at the joints for ligamentous and tendonous attachment. Cortical bone improves the overall fracture toughness and provides structural integrity to limbs allowing for gross movement.

6.2.3.1 Micro-architecture of cortical bone

Cortical bone is much more dense than trabecular and exhibits only 5–15% porosity (Morgan et al., 2018). It is well documented that cortical bone density and thickness decrease with age (Chen et al., 2013). Interestingly, micro-structural analysis has shown that the cortical bone stiffness, fatigue strength and fracture toughness decrease with age (McCalden et al., 1993). It

should also be noted that studies have indicated that the decrease in cortical bone density is significant in women, but insignificant in men (Chen et al., 2013).

6.2.3.2 Mechanical properties of cortical bone

Cortical bone is widely considered to be transversely isotropic, with mechanical properties along the axis of loading, or the z-axis, being significantly greater than those in the x- and y- axis. The transversely isotropic mechanical properties of human cortical bone have been collated from literature to provide a holistic visual representation, see Fig. 6.4 (Bartel and Davy, 2006; Burstein et al., 1976; Park and Lakes, 2007).

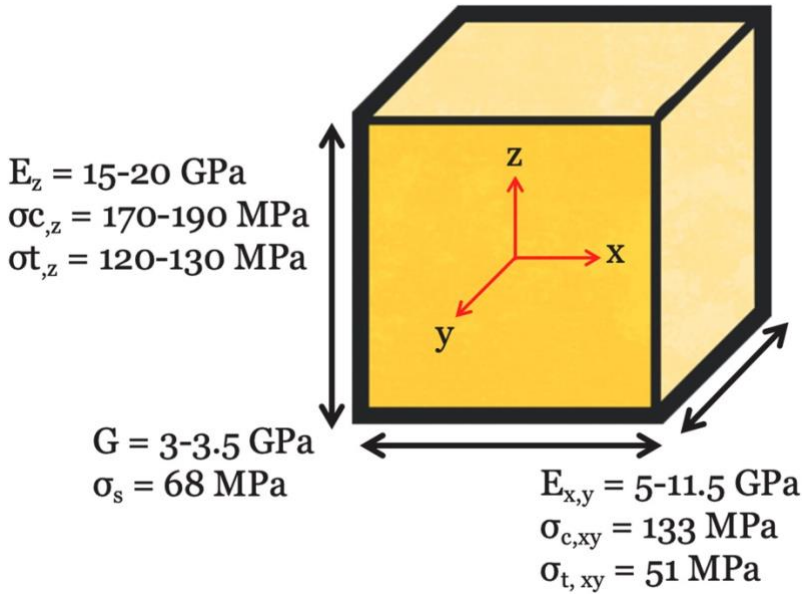


Figure 6.4 Cortical bone exhibits transversely isotropic mechanical properties with nearly double the stiffness occurring along the axis of loading (Bartel and Davy, 2006; Burstein et al., 1976; Park and Lakes, 2007). Young's modulus, ultimate compressive strength, and ultimate tensile strength in the longitudinal direction are denoted Ez, σc,z, and σt,z respectively. The subscript "x,y" is given to denote mechanical properties in the transverse axes.

6.3 Additively Manufactured Lattices for Bone Replacement

The production of three-dimensional (3D) parts in AM technologies is digitally controlled, from a computer-aided design (CAD) model, to layer-by-layer customization of process parameters, to monitoring and controlling the process while parts are being manufactured. The

digitization of AM opens up exciting avenues in areas of medical device design, AM process planning for device production, and advanced monitoring and control during production. The advances in CAD fueled by the maturity of AM enable both technologies to have advanced technological readiness, enabling the regulatory pathways and component mechanical performance to be ready for wide-scale application in the medical device industry (Burton et al., 2018; Peel and Eggbeer, 2016). Existing literature on additively manufactured medical devices for bone replacement or augmentation is widely spread based on target audience, research background, and study type. Research on additively manufactured medical devices can be found in surgical, tissue, biomedical engineering, additive manufacturing and/or material science journals. Collating the existing body of research into a cohesive overview proves challenging, as the focus of research covers a wide array of topics from AM process parameters, material properties, and biocompatibility, all the way to medical function and clinical outcomes. In order to review metal additive manufacturing as a technology for bone replacement an overview of metal AM and lattice design approaches has been included below

6.3.1 Review of additive manufacturing for metals: powder bed fusion

Metal powder bed fusion (PBF) technologies such as laser powder bed fusion (LPBF) and electron beam powder bed fusion (EB-PBF) are currently the leading metal AM technologies for industrial part production for biomedical, aerospace, and automotive applications. The faster fusion of metal possible by these two technologies alongside better process automation has resulted in a forecasted dominance of LPBF and EB-PBF until 2025 (Küpper et al., 2017).

LPBF (also known as selective laser melting (SLM)) and EB-PBF (also known as electron beam melting (EBM) are AM processes in which a heat source is directed towards a powdered material to micro-weld the material together, layer-by-layer. During the LPBF process, a fine laser

beam (with beam spot sizes (σ) generally between 50 and 100 μm) is generally directed through a series of lenses towards an X-Y plane via scanning mirrors which direct the beam towards the build platform. In EB-PBF (beam spot sizes (σ) generally greater than 200 μm) the same phenomenon is achieved through a directed high energy electron beam rather than a laser. In both cases, the build platform contains a bed of powdered material. As each layer is micro-welded together, the build platform lowers and a new layer of powder is deposited over the build platform with a blade or rake. This process is repeated layer-by-layer until the part is complete. Post-processing may be required to ensure certain material properties, part geometry and/or surface finish.

LPBF and EB-PBF do not necessarily compete with each and rather offer different advantages for a given application, as summarized in Table 6.2. Some of the major advantages of LPBF when compared to other metal AM processes are its fine resolution (Sames et al., 2016), wide range of materials available for the technology (Sing et al., 2016), and the potential to obtain performance superior to conventional manufacturing processes (Wang et al., 2018). The superior resolution of LPBF when compared to direct energy deposition (DED) and EB-PBF makes it an ideal candidate for manufacturing intricate lattices used in light-weighting parts, as well as for manufacturing complex lattice structures with fine feature sizes. LPBF also has the largest range of metal material options of any metal AM technologies. One such material is Ti-6Al-4V, a widely used biomaterial in the medical device industry. There are some benefits to considering EB-PBF for the fabrication of biomedical devices: a higher build speed and reduction in residual stresses resulting in reduced part distortion. The reduction in residual stress is due to the elevated environment temperature during EB-PBF production, where the powder layer is pre-heated into a powder cake which serves as a thermal dissipation pathway, reducing the need for extensive

support structures except for part substrate anchoring requirements. As such, both LPBF and EB-PBF will be considered in this work, with a focus on lattice structure design, performance, and manufacturability for orthopaedic bone replacement and augmentation devices.

Table 6.2 Manufacturability comparisons between LPBF and EB-PBF (EBM) for fabricating titanium.

Metric	LPBF	EB-PBF
Feature resolution	+	–
Manufacturing (build) speed	–	+
Residual stresses & distortion	–	+
Need for support structures	–	+
Feature accuracy	+	–
Material choices	+	–

6.3.2 Review of Lattice Designs

Lattice structures are a form of hierarchical design structures used to minimize unnecessary material with respect to design function. Lattices are typically designed for a specific application or function such as reducing weight while maintaining mechanical strength or improving energy absorption characteristics of a design component (Broda, et al., 2007; Mines et al., 2013). Lattice structures can be categorized into two main structure types: cellular lattices and stochastic (random) lattices (Gibson et al., 2014). A visualization of the types of lattice structures is provided by a classification chart in Fig. 6.5.

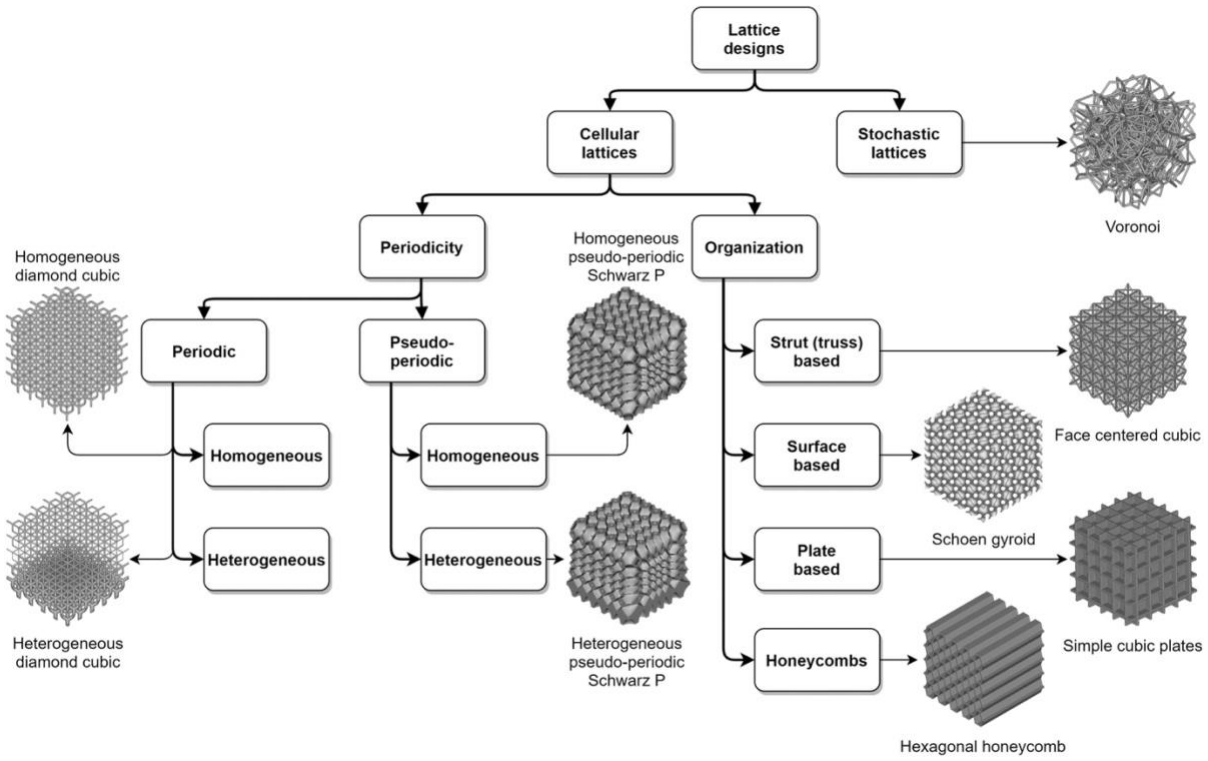


Figure 6.5 Classification chart for lattice designs.

6.3.2.1 Cellular lattices

The majority of lattice structures can be categorized as cellular structures that are made up of unit cells with distinct, repeatable features. Cellular lattice structures are made up of struts, walls, and/or plates that are repeatedly interconnected in 3D-space by nodes, as shown in Fig. 6.5.

Periodicity driven classification

Cellular lattices can then be further categorized into periodic and pseudo-periodic lattices that are of homogeneous or heterogeneous organizations (Fig. 6.5) (Dong et al., 2017). The periodicity of a lattice refers to the size of the unit-cells throughout the structure and homogeneity refers to the thickness of the unit-cell elements such as struts and walls. Therefore, a periodic lattice would have a uniform unit-cell size throughout its structure and a pseudo-periodic structure would have variable unit cell size, as shown in Fig. 6.6 for a triply period minimal surface (TPMS)

Schwarz diamond (D) lattice structure. Both periodic and pseudo-periodic lattices can be further categorized into homogeneous or heterogeneous lattices. Homogeneous lattice structures have a uniform strut and/or wall thickness, and heterogeneous lattice structures have gradients in the strut and/or wall thickness, as shown in Fig. 6.7 for a strut-based body centered cubic lattice structure. A visual comparison between periodic and pseudo-periodic lattice structures with a homogeneous and heterogeneous organization is given in Fig. 6.8 for TPMS Schoen gyroid lattices.

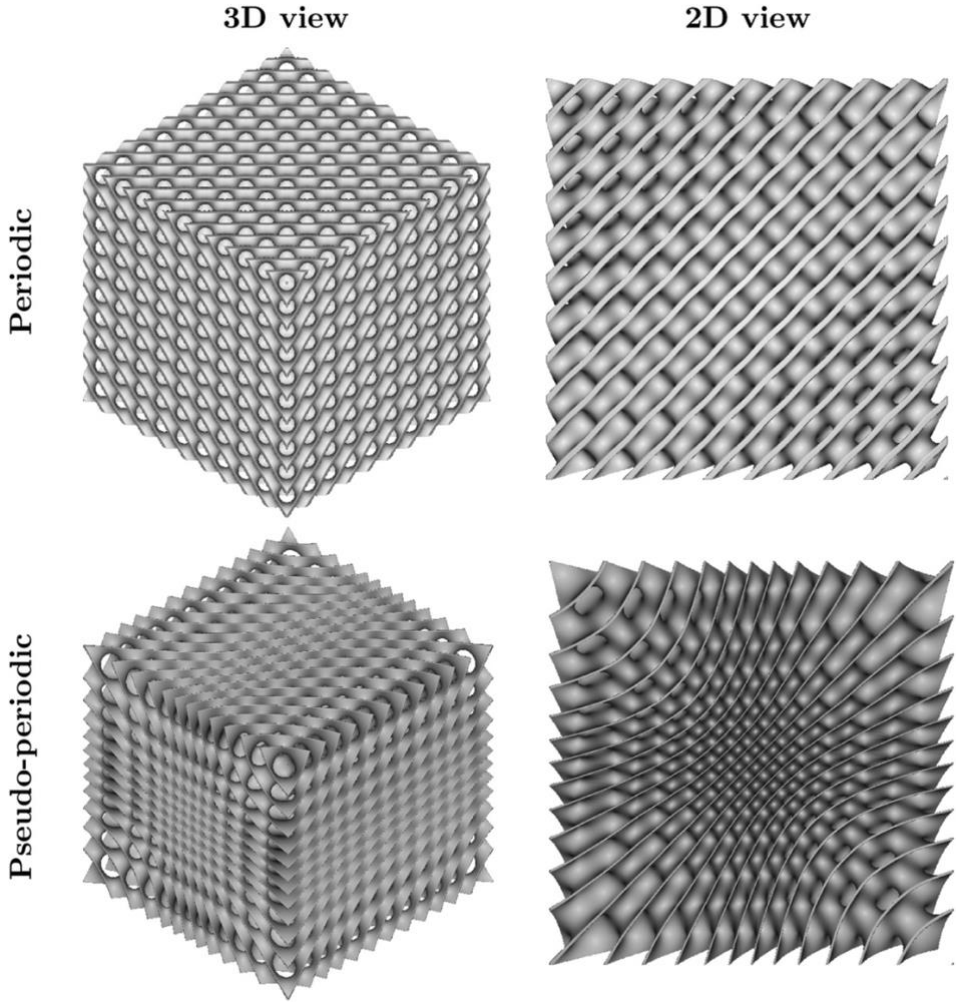


Figure 6.6 Comparative images of a periodic (top row) and pseudo-periodic (bottom row) TPMS (surface-based) Schwarz diamond (D) lattice structure.

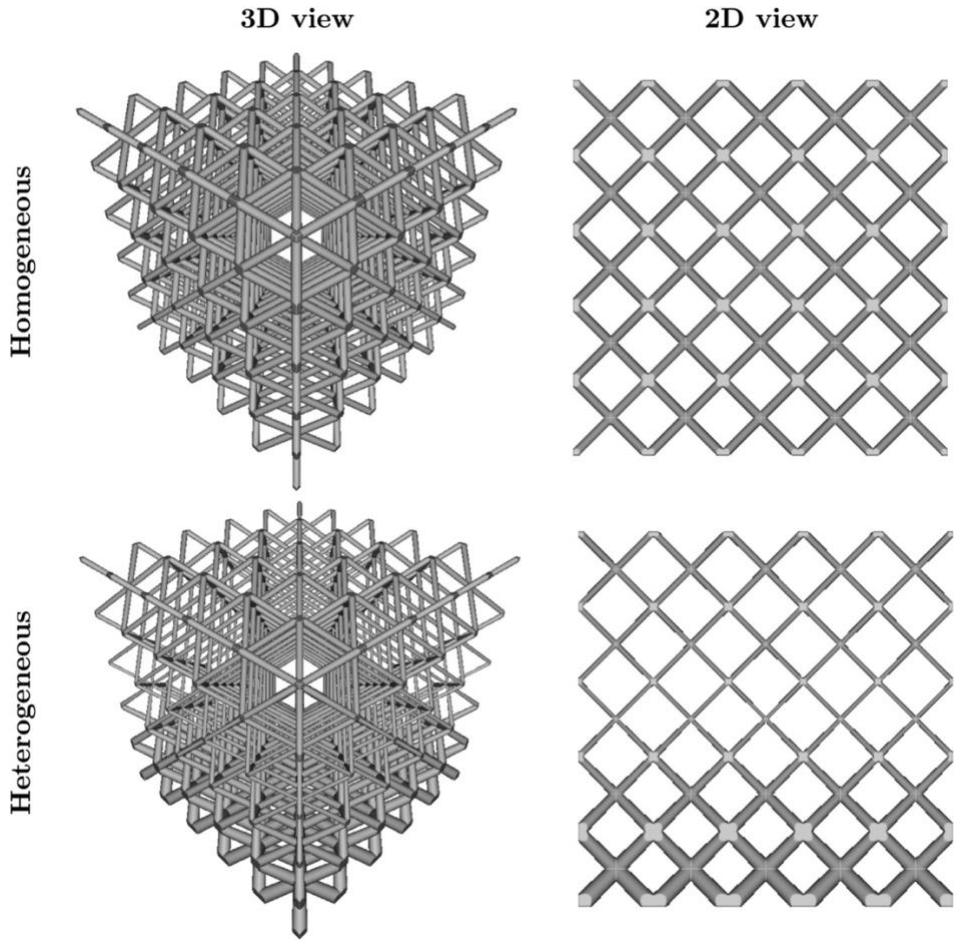


Figure 6.7 Comparative images of a homogeneous (top row) and heterogeneous (bottom row) strut-based body centered cubic lattice structure.

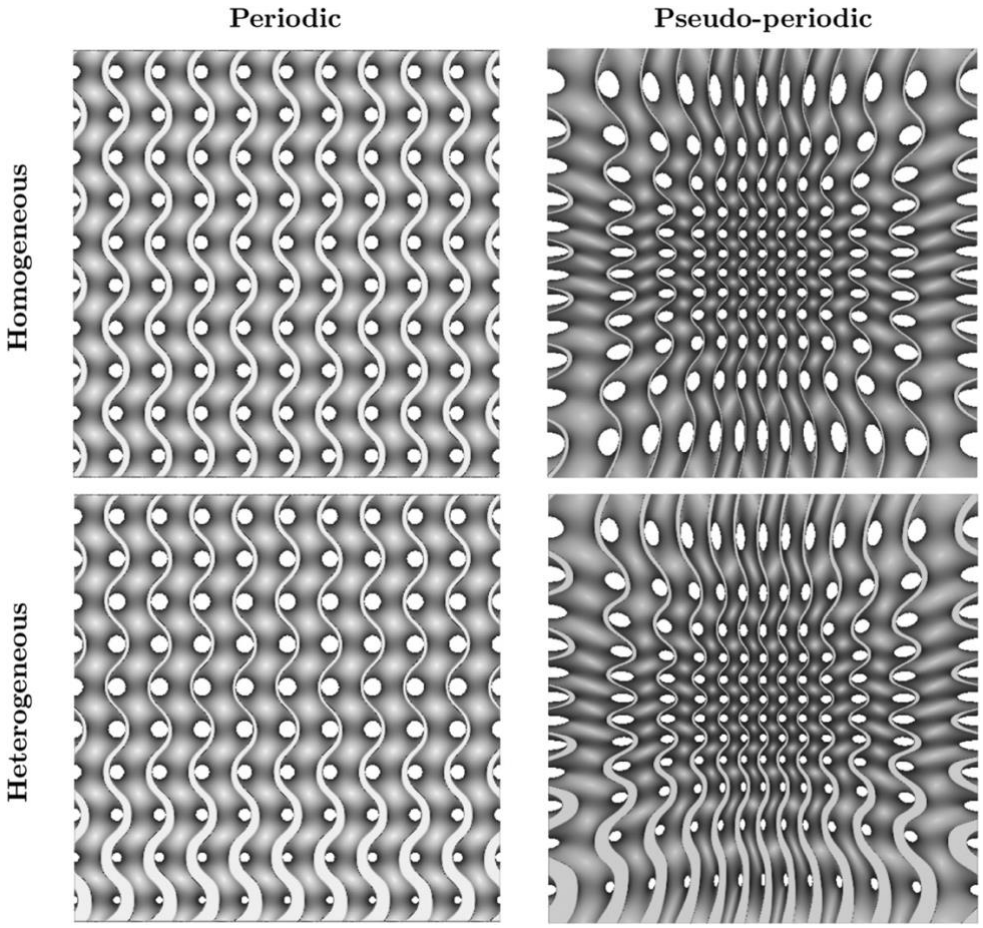


Figure 6.8 Comparative cross-sectional images of various TPMS Schoen gyroid lattice structures classified as periodic, pseudo-periodic, homogeneous, and heterogeneous.

Organization driven classification

Another form of categorization for lattice structures is by their cellular organization, as shown in Fig. 6.5. The four commonly known cellular organizations of lattice structures are strut-based, surface-based, plate-based, and honeycomb lattices (Al-Ketan and Al-Rub, 2019; Bauer et al., 2017; Tancogne-Dejean et al., 2018; Wadley, 2006; Zheng et al., 2016), as shown in Fig. 6.5. Strut-based lattices are generated by determining unit cell size, the number nodes located throughout the unit cell, and the number and configuration of connectors linking nodes to each other. Porosity of the lattice may be controlled directly, or strut thickness may be selected as the control variable for lattice density. Surface-based lattices consist of a locus of points defined by a

function. The most commonly used and discussed surface lattice family are triply period minimal surface (TPMS) lattices. TPMS lattices are defined by implicit functions for which the function has a constant value. Plate-based lattices can be derived either from strut-based lattices by placing plates between two adjacent trusses (Lui et al., 2021), or by placing plates on the closest packed planes of lattices derived from crystal structures (Berger et al., 2017; Crook et al., 2020; Tancogne-Dejean et al., 2018). Plate-based lattices are known to have significantly higher stiffness when compared to truss-based lattices (Andrew et al., 2021; Berger et al., 2017; Tancogne-Dejean et al., 2019). Honeycomb lattices consist of plates that form the edges of unit cells. The unit cells for honeycomb lattices can have either a triangular, hexagonal (Fig. 6.5), square, or related shapes forming the 2D cross-section. These unit cells are then repeated in a 2D space to obtain a cellular solid, and then extruded in a 3D space to obtain a lattice structure, such as the hexagonal honeycomb structure shown in Fig. 6.5 (Wadley et al., 2006). All types of lattice structures may be periodic or pseudo-periodic and heterogeneous or homogeneous.

6.3.2.2 Stochastic lattices

Stochastic, or random, lattice structures consist of irregular and non-periodic cells resulting in a network of interconnected struts, surfaces, and/or plates. Unlike other lattice structures there are no distinct cellular features that are repeated in 3D space and each cell contains a unique configuration of struts and nodes. Stochastic lattices have superior performance under both compressive and shear loading when compared to regular lattice structures (Maliaris and Sarafis, 2017). However, due to their complex design, there are not as many readily available tools for the design and implementation and therefore they are not as commonly examined in literature. The final lattice type to be examined are spinodoid lattices (Kumar et al., 2020), which are a subset of stochastic lattices and surface lattices. The major differentiating characteristic of spinodal lattices

is that they are non-periodic. This allows for a larger design space and more achievable control of the directional mechanical properties. The benefit of spinodal surfaces is that they are immune to the symmetry-breaking defects present in cellular lattices, thus improving their mechanical properties (Kumar et al., 2020).

6.3.2.3 Mechanical properties of PBF lattice structures

Mechanical properties of lattice structures, such as compressive strength and elastic modulus, typically refer to the macroscopic properties of a unit cell or group of units cells which differs from the mechanical properties of the bulk modulus for a given material (Zadpoor, 2019). Typically, the relationship between the mechanical properties of lattice structures and those of the bulk modulus can be described using a ratio which relates apparent density of a cellular lattice to the density of the structure's material. Therefore, as apparent density of the lattice structure decreases, or designed lattice porosity increases, mechanical properties of the lattice structure decrease. The Gibson-Ashby model is the most widely accepted model used for predicting the mechanical properties of cellular-lattice structures (Gibson, 2003). Maconachie et al. conducted a detailed review of mechanical properties of lattice structures produced by LPBF (Maconachie et al., 2019). They used the Gibson-Ashby model to predict mechanical properties of common cellular lattice structures and compared the findings to experimental data (Fig. 6.9). They found that the Gibson-Ashby model was useful in predicting mechanical properties of cellular lattice structures produced trough LPBF.

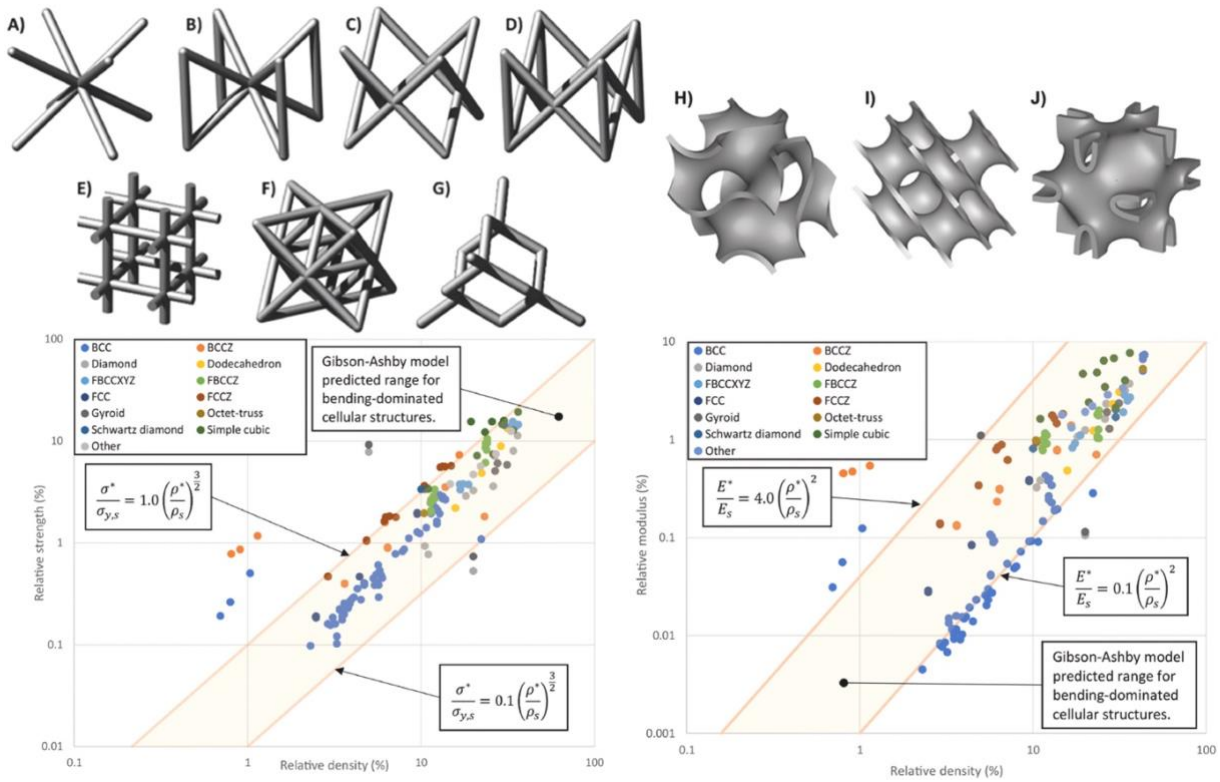


Figure 6.9 Experimental data comparing the compressive strength (left) and Young's modulus (right) for common cellular lattice structures to those predicted by the Gibson-Ashby model. Cellular lattice structures examined include: BCC (A), BCCZ (B), FCC (C), FCCZ (D), cubic (E), Octet-truss (F), diamond (G), Schoen gyroid (H), Schwarz diamond (I), and Neovius (J). Original figures obtained from (Maconachie et al., 2019).

6.4 Review Methodology

A comprehensive literature review was completed to better understand how lattice parameters are controlled in additively manufactured titanium and titanium alloy parts aimed at replacing or augmenting bone. In order to collect the most relevant data, all powder bed additive manufacturing processes were considered, pure titanium and titanium alloys were considered, and all study types were considered; however, studies were only included when bone was the target tissue for replacement, repair and/or augmentation, to enhance the relevant scope of the designed architectures. A total of 50 journal articles fit the above criteria and the effect of lattice design parameters on mechanical properties was extracted and examined.

Existing literature describing additive manufactured titanium implants for bone replacement fits into two main categories of critical design focus: studies focused on improving osseointegration and studies focused on targeted mechanical properties. Osseointegration refers to bone's ability to grow on the surface of the implants and infiltrate the porous implant to improve implant fixation. In general, literature focused on osseointegration was found to have fewer reported AM and lattice parameters provided and often focused on *in vivo* results in animals or human case studies. The primary target audience for this category seems to be medical and academic researchers interested in bone tissue mechanics, growth and healing and secondarily, the additive manufacturing community. The other category of literature aims at matching the mechanical properties of bone by controlling the lattice design parameters and by controlling the printing process parameters of the respective technologies. Literature focused on matching mechanical properties of lattice structures to bone, primarily targets the additive manufacturing community with implications for bone tissue and device design being secondary suggestions. It is noteworthy to highlight this lack of apparent synergy between the two categories; such synergy is required to ensure advancements in this field.

A wide cross-section of lattice design information was collected from the bone and AM focused journals and was collated in the associated Data in Brief. Key parameters collected include: Young's modulus, compressive strength, lattice porosity, pore size, feature thickness, lattice type and material used. When studies compared more than one lattice design parameter, all relevant data points were collected in order to make the most robust comparison possible. Data points were then plotted on alongside Ashby plots for trabecular and cortical bone to assist in making recommendations for future lattice designs focused on titanium implant designs for bone repair and replacement (CES EduPack software, Granta Design Limited, Cambridge, UK, 2009).

6.5 Results and Discussion

6.5.1 Lattice Considerations

6.5.1.1 Porosity

The exercise of understanding trabecular and cortical bone porosity provides insight into the porosity required to match the structural properties of bone through titanium and Ti-6Al-4V latticing. The most common lattice parameter reported in literature focused on additively manufactured titanium and titanium-alloy lattice structures was macro-scale porosity or void fraction. Designed lattice porosity varied from 15% to 97% with the majority of studies reporting a designed porosity between 50% and 70%. Titanium and titanium alloy lattices within this designed porosity range were successful in matching the stiffness of cortical bone which is known to be 5–15% porous. However, few were successful in matching mechanical properties of trabecular bone, as depicted in Fig. 6.10. Trabecular bone is 70–90% porous, and through this review, it was determined that titanium and Ti-6Al-4V lattices must have a designed porosity of >80% to replicate mechanical properties of trabecular bone. These findings indicate that matching material properties of titanium and Ti-6Al-4V via latticing may be challenging with existing AM technologies.

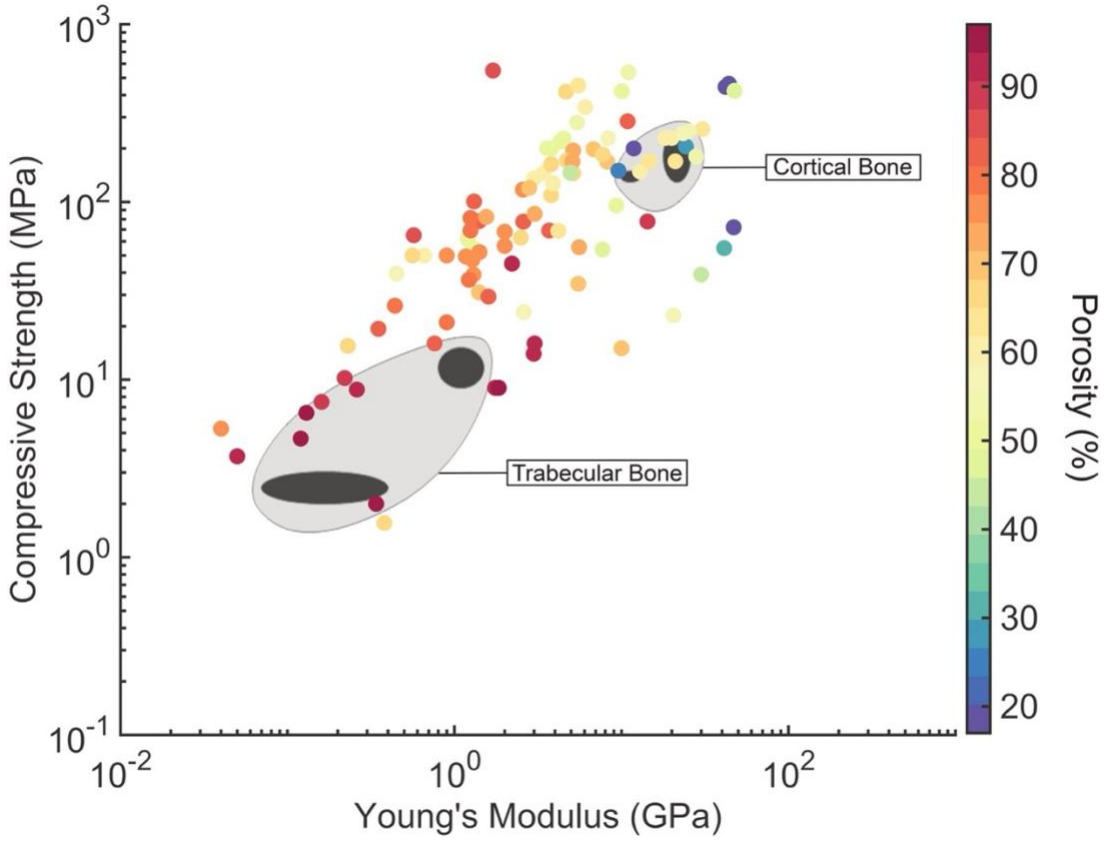


Figure 6.10 Porosity is the most common lattice parameter reported in literature. Compressive strength and Young's modulus of additively manufactured lattice structures were plotted over the Ashby plots of human trabecular and cortical bone. Lattice porosity ranged from 15% to 97% and was plotted in a gradient to depict how best to design for material property matching.

6.5.1.2 Pore size

Two-dimensional micro-architecture measurements of bone can also be described in terms of lattice parameters. When considering TbSp as a surrogate bone pore size, Hildebrand et al. reported a range from 638 μ m in the femoral head to 854 μ m in the lumbar spine (Hildebrand et al., 1999). In the literature focused on osseointegration for additively manufactured titanium lattice designs, the lattice parameter most commonly reported was pore size. The pore sizes reported ranged from 100 to 1500 μ m. Recommendations for tailoring pore size to optimize bone in-growth or osseointegration were consistent and conclusions were drawn surrounding an acceptable range for optimal boney ingrowth. A minimum pore size of 200 μ m should be considered to allow for

initial cell adhesion (Xue et al., 2007). However, to maximize cell proliferation and limit cell occlusion, large pore sizes > 1000 μ m are recommended (Zhao et al., 2018). Therefore, a functionally graded lattice which combines small pores for initial cell attachment and large pores to avoid cell occlusion would account for both recommendations (Van Bael et al., 2012; Yadroitsava et al., 2019). Pore size did not exhibit a trend with respect to compressive strength and Young's modulus as seen in Fig. 6.11. Therefore, pore size should be viewed as a design parameter for biological reaction rather than mechanical function.

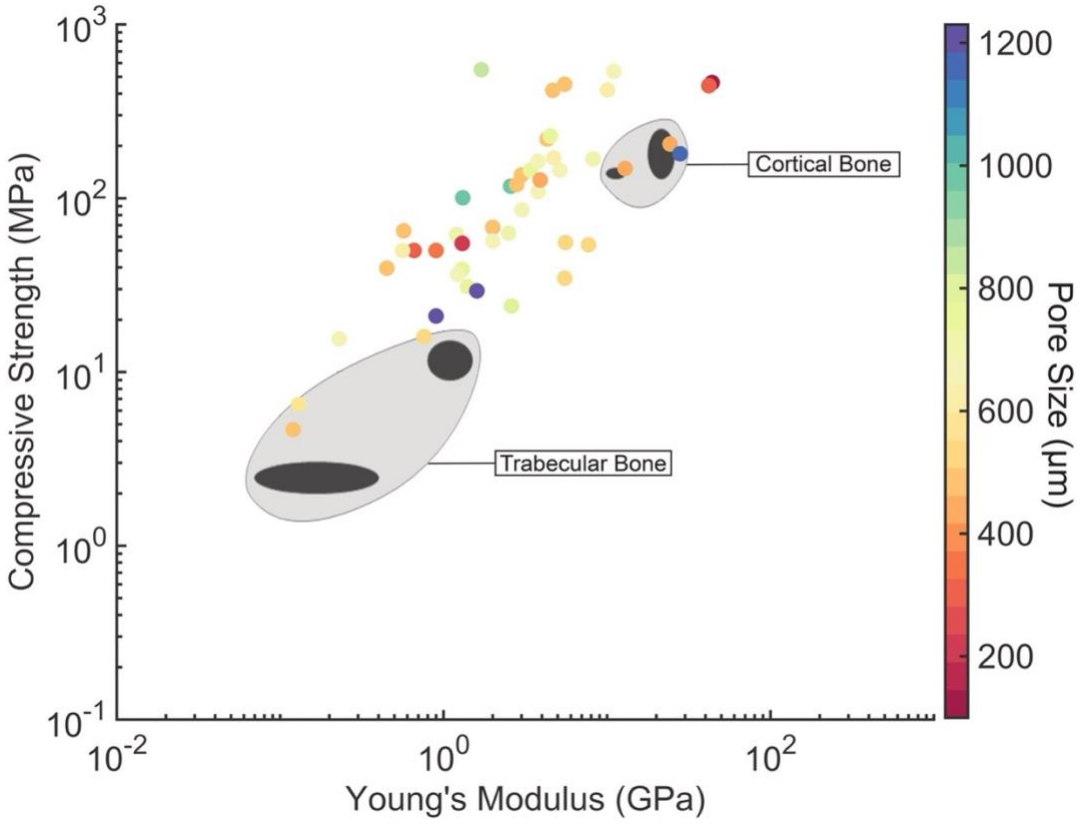


Figure 6.11 Designed pore size of additively manufactured Ti and Ti-6Al-4 V lattice structures was plotted in a gradient over a compressive strength versus Young's modulus Ashby plot for human trabecular and cortical bone tissues to depict how best to design for material property matching.

6.5.1.3 Feature thickness

Trabecular thickness can be related to feature, strut or wall thickness. Across the human skeleton, trabecular thickness varies from roughly 120–200 μm (Hildebrand et al., 1999). This is lower than 400 μm, or the minimum feature thicknesses typically recommended for powder bed fusion. This is most likely due to the part resolution that can be obtained through current additive manufacturing technologies. While there were no strong trends in the effect of feature thickness on compressive strength and Young's modulus for the feature size range captured in these studies, decreasing feature thickness is one way to control lattice porosity, which is critical to manipulating mechanical properties, as seen in Fig. 6.12.

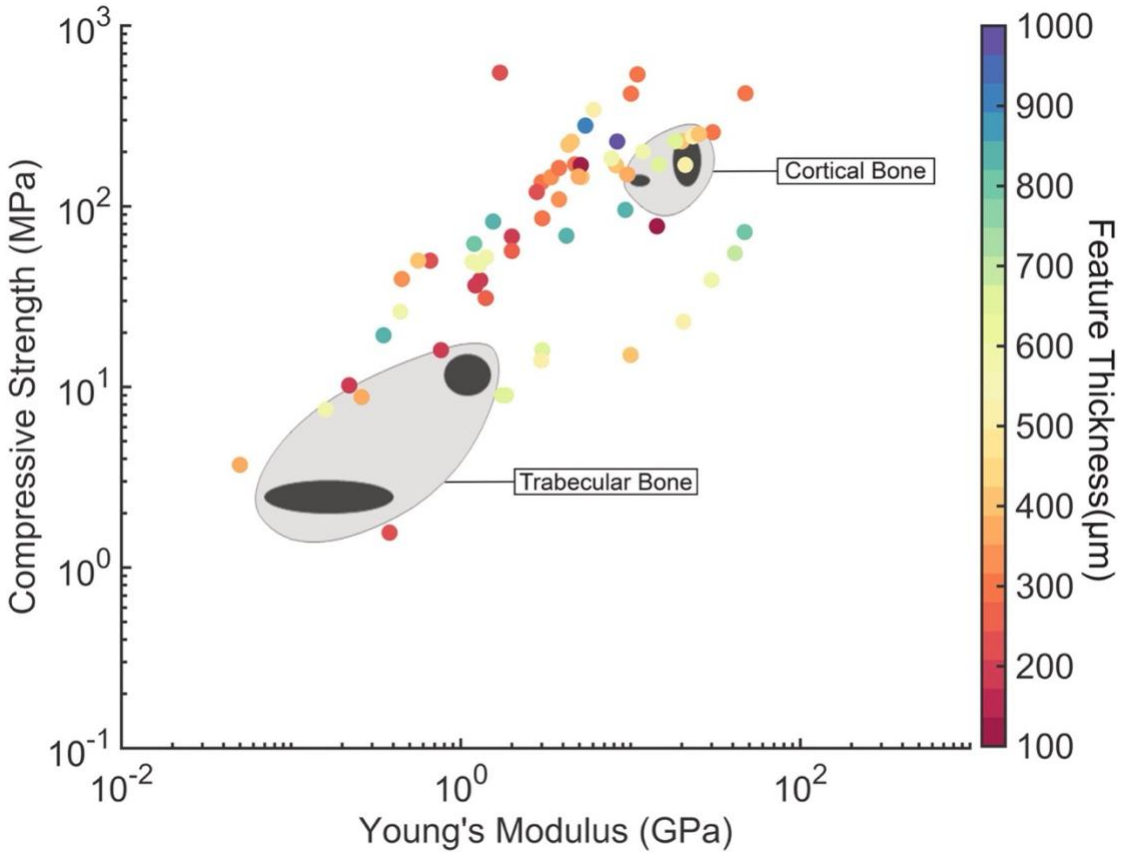


Figure 6.12 Feature thickness was plotted in a gradient over a compressive strength versus Young's modulus Ashby plot for human trabecular and cortical bone tissues to depict how best to design for material property matching.

6.5.1.4 Lattice type

When compared to strut-based lattices, surface-based lattices, such as TPMS structures, allow for better osseointegration (Yadroitsava et al., 2019). This is thought to be due to the increased surface area available in surface-based lattices for cellular adhesion. However, the designed lattice porosity needed to match the mechanical properties of trabecular bone requires very thin wall thickness. Surface lattices also have lower stress concentrations under angular load simulation, which may make them further suitable for bone implants (Yadroitsava et al., 2019). A recent study from Alabort et al. showed promising results for reaching the mechanical properties of trabecular bone through the use of TPMS surface lattices, specifically Schwartz's diamond surface structures (Alabort et al., 2019). In this review, lattice type had no noticeable influence on compressive strength nor Young's modulus of titanium and Ti-6Al-4V lattice structures aimed at human bone replacement, see Fig. 6.13.

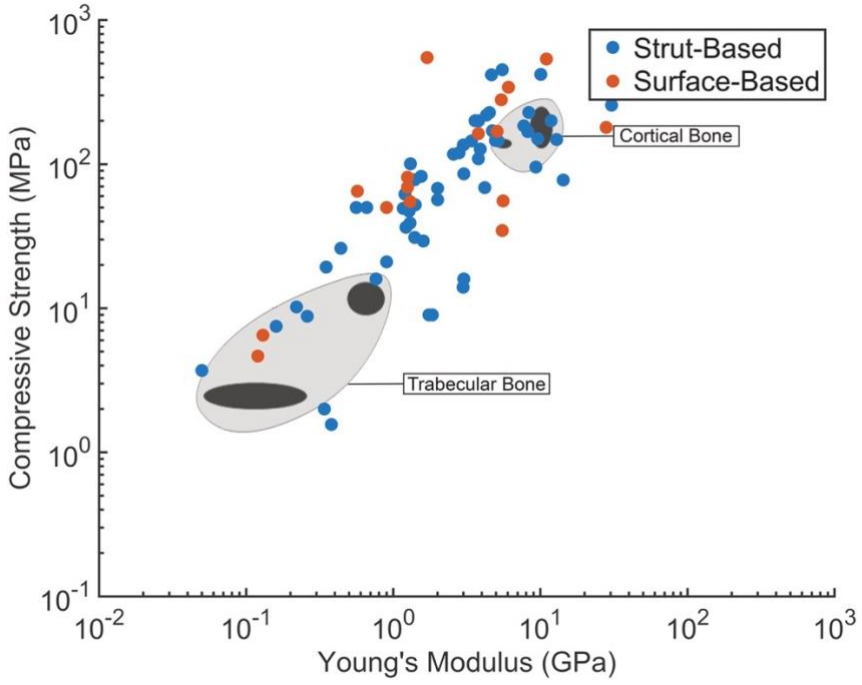


Figure 6.13 Lattice type, strut- vs surface-based, was plotted in a gradient over a compressive strength versus Young's modulus Ashby plot for human trabecular and cortical bone tissues to depict how best to design for material property matching.

6.5.1.5 Material selection

Finally, material choice was examined and Ti and Ti-6Al-4V lattices were compared for their ability to achieve comparable Young's Modulus and compressive strength to human bone tissues. Despite having slightly different bulk modulii, Ti and Ti-6Al-4V lattices did not differ in ability to reach bone properties, see Fig. 6.14. This may be due to other lattice design decisions, such as porosity, pore size and feature thickness, that were made to tailor overall mechanical properties

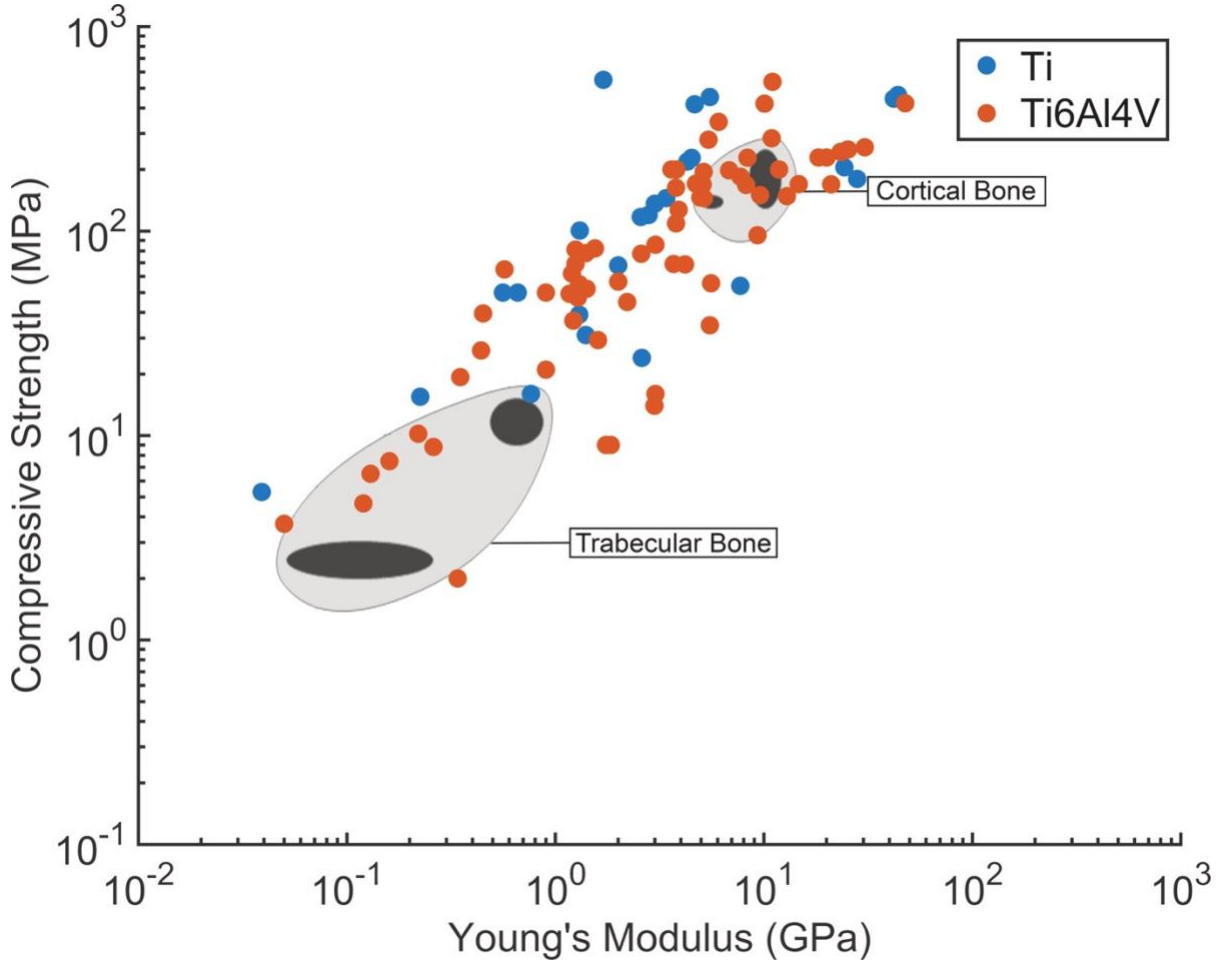


Figure 6.14 Material type, Ti vs Ti-6Al-4V, was plotted in a gradient over a compressive strength versus Young's modulus Ashby plot for human trabecular and cortical bone tissues to depict how best to design for material property matching.

6.5.1.6 Considerations for fatigue strength

Fatigue strength is another mechanical property that is important to characterize for bone replacement and repair applications due to the cyclic nature of *in vivo* implant loading. Fatigue strength of additively manufactured lattice structures have been examined with manufacturing defects, bulk material modulus, designed lattice porosity, and lattice geometry all playing key roles (Zargarian et al., 2016). To date, there has been limited investigations into fatigue strength of titanium lattice structures for bone replacement and repair specifically. Dallago et al. examined the effects of unit-cell size and strut orientation on fatigue strength of Ti-6Al-4V lattice structures produced through laser powder bed fusion (Dallago et al., 2021). They found that fatigue strength of lattice structures can be improved for bone replacement by optimizing build direction and junction geometry. They suggest that to improve fatigue strength load bearing struts should be printed perpendicular to the build plate and unit cell size should be up-scaled to decrease manufacturing defects associated with reduced fatigue strength (Dallago et al., 2021). These recommendations should be taken into account when designing for titanium lattices aimed at human bone replacement and repair, particularly when the fatigue life requirements for certain implants are to withstand loads without failure for over 5 million cycles, as noted in ISO 7206–4 for hip implants (ISO 7206-4, 2010.).

6.5.2 Manufacturability Considerations

The potential of powder bed fusion AM technologies such as LPBF and EB-PBF to manufacture parts with higher geometric complexity compared to traditional manufacturing, makes them well suited for fabricating lattice structures mimicking bone properties. The complex features involved in the design of most lattice structures tests the manufacturability limits of LPBF and EB-PBF. This is mainly because most lattice structures used for bone replacements require

fine feature sizes, particularly to replace trabecular bone. The minimum feature size strongly depends upon the beam spot size used which is generally between 50 and 100 μ m for LPBF and >200 μm for EB-PBF. Additionally, lattice structure designs generally incorporate numerous overhanging features within a unit cell, which are challenging to produce by both LPBF (Charles et al., 2020; Druzgalski et al., 2020) and EB-PBF (Cooper et al., 2018; Newton et al., 2020; X. Wang and Chou, 2018). For LPBF in particular, surfaces with an overhang angle of <30∘ (with respect to the PBF build plate) are considered non-self-supporting leading to print failures or significant distortion in the manufactured lattice structures (Maconachie et al., 2019). Pushing the design boundaries in LPBF and EB-PBF to achieve lattice architectures tailored for bone replacement and augmentation necessitates an understanding of the three main categories of manufacturability challenges which arise in these AM technologies - defects (micro-porosity within the manufactured lattice structure), surface roughness, and geometric fidelity.

6.5.2.1 Porous defects

Due to the fatigue strength and stiffness requirements associated with manufacturing titanium-based bone replacements, understanding defects is important, as they directly impact both stiffness and fatigue life of a given AM part. It is well documented in AM literature that defects are particularly deleterious for fatigue properties (Du Plessis et al., 2020; Echeta et al., 2020; Soro et al., 2021). In most of the articles reviewed in this work, stiffness values and lattice design details were commonly reported for titanium alloy lattice structures used for bone replacements, but studies into the defects within the lattice structures and their effects on fatigue life were less frequently reported.

The number of defects and their typical morphology observed in powder bed fusion (PBF) AM depends on the process parameters used for manufacturing a given lattice structure. A low

energy input is typically associated with the formation of irregularly shaped lack of fusion defects (Patel and Vlasea, 2020), with a high aspect ratio (width/depth) which are known to be more detrimental to the fatigue strength of lattice structures (Du Plessis et al., 2020), when compared to rounded keyhole defects typically associated with high energy inputs (Patel and Vlasea, 2020). It is important to note that the presence of rounded or irregularly shaped defects is not only dependent upon the energy input, but rather requires an understanding of PBF process parameters, particularly power, beam velocity, beam spot size, powder layer thickness, and hatching distance. It is quite possible to obtain irregularly shaped, lack of fusion defects within a lattice structure that uses high energy keyhole mode parameters, as shown by an X-ray computed tomography visualization of the defect space within a Ti-6Al-4V Voronoi lattice structure manufactured by LPBF in Fig. 6.15. A summary of the LPBF processing details and XCT measurements of the lattice structure are provided in the associated Data in Brief.

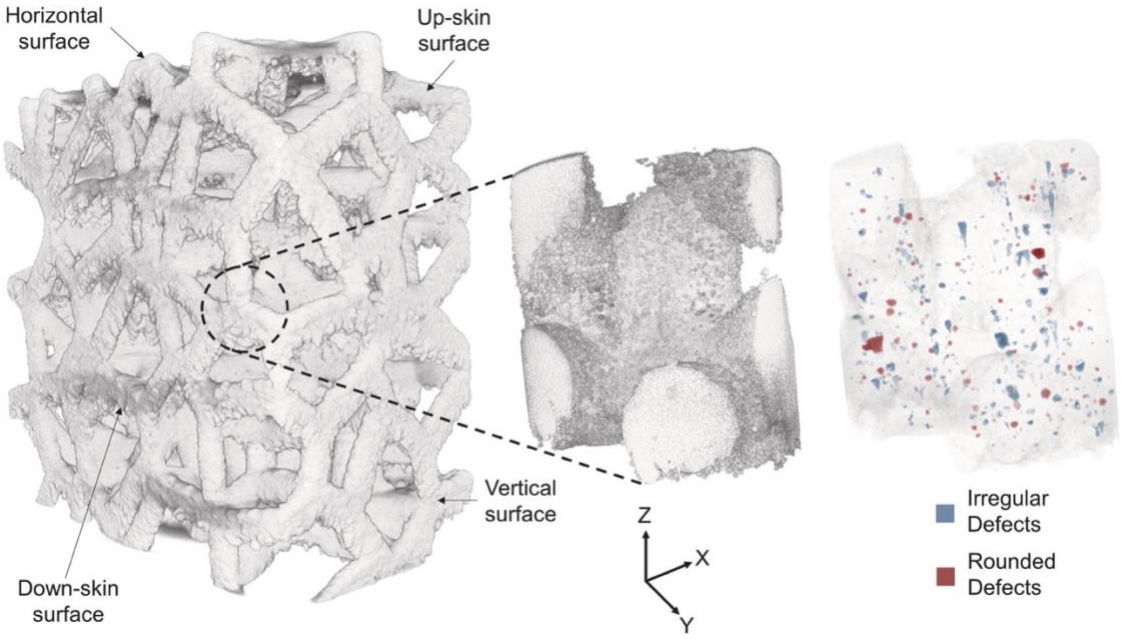


Figure 6.15 A three-dimensional XCT visualization of the different types of surfaces observed in a laser powder bed fusion Ti-6Al-4V Voronoi lattice structure with respect to the build orientation along the Z-axis (left), a high resolution XCT image of a portion of the Voronoi lattice structure (center), visualization of the defects inside the printed lattice structure (right).

6.5.2.2 Surface roughness

Surfaces in PBF parts are generally identified with their orientation with respect to the build plate used for manufacturing as shown by the left image in Fig. 6.15. The four type of surfaces shown in Fig. 15 include - horizontal up-facing surfaces that are parallel to the build plate (along the XY plane), vertical surfaces that are perpendicular to build plate (along the Z axis and also known as side-skin surfaces), upward facing surfaces (known as up-skin surfaces) which are typically on an incline, but facing upwards, and downward facing surfaces (known as down-skin surfaces) (Patel et al., 2020). Since most lattices used for bone replacement are comprised of a combination of all four surface types, these surfaces are distinctly different contributors towards the final surface roughness in the printed lattice structures. Side-skin (vertical) surfaces (Abele and Kniepkamp, 2015; Patel et al., 2020) and down-skin surfaces (Chen et al., 2018; Echeta et al., 2020; Tian et al., 2017) are associated with a higher number of challenges when trying to obtain lower surface roughness values in as-printed PBF lattices, when compared to horizontal up-facing and up-skin surfaces.

In PBF AM processes, an interplay between process parameters, build file characteristics, machine characteristics, and powder characteristics drive the final surface topography of a given lattice structure. More precisely, processing parameters such as power, scan speed and layer thickness, build file characteristics such as feature geometry, feature orientation, feature location on the build plate, and beam path strategy, machine and energy source characteristics such as beam spot size, laser beam quality, and gas flow (for LPBF), and powder morphology and size distribution are some of the primary drivers for roughness of a given lattice structure.

Out of the four influencing factors, PBF process parameters are known to have the greatest effect on roughness and are also the most readily controllable for a given lattice. Horizontal and

up-skin surface roughness possibly depend upon the overall size of the melt pools (Snyder and Thole, 2020; Tian et al., 2019), where the roughness on these surface features generally includes visibility of the melt pool tracks alongside partially fused adhered powder, particularly for the up-skin surfaces. Down-skin surface features include partially fused adhered powder as sources of coarse roughness and dross (at higher energy inputs); overall, the down-skin roughness strongly depends on the melt pool depth (Snyder and Thole, 2020; Tian et al., 2019). A melt pool depth close to the powder layer thickness is generally considered to be useful for lowering down-skin surface roughness values (Tian et al., 2019). Remelting scans of horizontal, up-skin, and down-skin surfaces are known to improve the roughness values of these surfaces (Snyder and Thole, 2020). Side-skin (vertical) surfaces are an exception, wherein remelting would generally not help further improve surface roughness, when compared to a well-executed first side-skin scan (Calignano, 2018). Side-skin surfaces are generally dominated by partially fused adhered powder in PBF, but the effects of powder can be reduced by an appropriate energy input selection which enables a dominance of melt pool track features on the side-skin that are associated with lower surface roughness values (Abele and Kniepkamp, 2015; Patel and Vlasea, 2020).

Surface roughness of AM titanium lattices for bone replacement applications has been previously examined in literature. Webster and Ejiofor examined osteoblast proliferation on 90–95% dense Ti and Ti-6Al-4V structures. They reported that osteoblasts prefer titanium surfaces with nanometer topology features (Webster and Ejiofor, 2004). Conversely, Zhang et al. reported that a surface roughness of 1–2 μm improved osteogenic properties of titanium bone implants (Zhang et al., 2010). There is still no consensus on optimal surface topology and roughness for osseointegration and adhesion, as changes in the microstructure and nanostructure of lattice surfaces both influence the cell response in bone tissues (Gui et al., 2018).

6.5.2.3 Geometric fidelity of lattice features

The fine and complex features involved in the CAD of most lattices used for bone replacements test the manufacturability limits of both LPBF and EB-PBF. This implies that a lattice structure with a fine feature size might print successfully, but not conform to the original CAD, leading to dimensional inaccuracies. Inaccuracies in additively manufactured lattices would directly impact their performance as bone replacements, since the reality of the AM structure would differ from the modelling efforts and design decisions used to determine the feature size and morphology of the lattice. Attempts at reporting the geometric fidelity of AM lattices, however, have been scarce.

In literature where dimensional inaccuracies have been reported, significant under-sizing and over-sizing of additively manufactured lattices compared to the original CAD are observed, sometimes over 100%, as reviewed by Echeta et al., 2020. Dimensional inaccuracies in AM lattices depend on numerous factors, including build file setup (location, orientation, recoater offset angle, etc.) (Moylanet al., 2013), PBF process parameters (Patel et al., 2020; Yasa et al., 2009), CAD file resolution (Chougrani et al., 2017), powder size and morphology (Sames et al., 2016; Shanbhag and Vlasea, 2020), and beam properties such as wavelength, operating mode, shape and quality (Gong et al., 2012; Lee et al., 2017).

All types of lattice structures including strut-based, surface-based, plate-based, honeycombs, and stochastic lattices present their own unique setting of challenges for PBF manufacturing. When it comes to strut-based lattices, higher dimensional inaccuracies are reported for diagonal and horizontal struts, when compared to vertically printed struts (Cuadrado et al., 2017; L. Liu et al., 2017; Melancon et al., 2017). This is because horizontal and diagonal struts contain the highest proportion of overhanging features which are known to have the highest surface roughness-related concerns, as noted in Section 6.5.2.2. Additionally, distortion and excessive

material accumulation has been previously reported at the nodes of strut-based lattices (Gümrük et al., 2013; Leary et al., 2016; Tancogne-Dejean et al., 2016), with comparatively smoother nodes observed in surface-based lattices (Al-Ketan et al., 2018). Plate-based lattices also have issues during production using PBF such as overhanging features with zero inclination angle (Liu et al., 2021), and closed-cell topologies (Crook et al., 2020) making the removal of powder from the lattices challenging after PBF. Honeycomb lattices are a class of lattice structures which would not have the same challenges as strut or surface based lattices during PBF manufacturing due to the extrusion of a 2D unit cell into a 3D lattice structure. As long as the 2D unit cell dimensions are within the feature resolution possible by PBF, honeycomb lattices should be relatively simple to manufacture. Lastly, stochastic lattices are the most challenging lattice type to manufacture using PBF. Stochastic lattice structures such as the Voronoi lattice structures shown in Figures 6.15 and 6.16 provide control only over the strut thickness and the spacing between the centroids of the Voronoi cells. This leads to numerous overhanging struts, many of which could have non self-supporting overhanging angles <30° (with respect to the PBF build plate) thereby leading to the large deviation from CAD as shown in Figures 6.16 and could lead to print failures at greater length scales. The spinodoid type of lattice structures developed by Kumar et al., 2020 provide additional control in the creation of stochastic lattice structures and might provide more opportunities in the area of printable stochastic lattice structures.

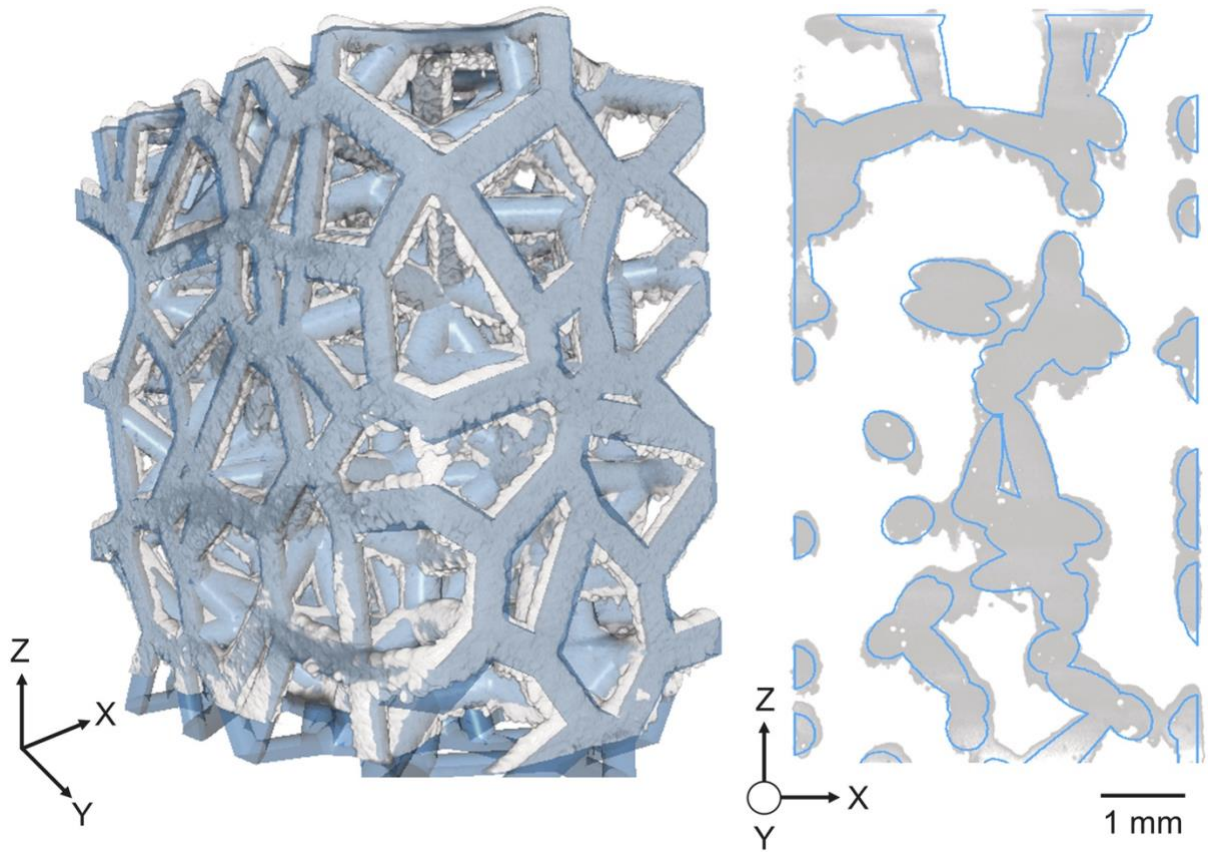


Figure 6.16 A 3D comparison of the XCT visual (shown in grey) and the original CAD (shown in blue) of a Ti-6Al-4V Voronoi lattice structure manufactured by laser powder bed fusion (left) and a 2D comparison of a slice along the XZ plane of the XCT visual (shown in grey) and the original CAD (shown in blue) of the lattice structure (right).

For inclined up-skin surfaces in diagonal struts, a 'stair step' effect is commonly observed, wherein the edges of individual layers during PBF manufacturing are visible alongside effects of partially fused adhered powder (Strano et al., 2013; Townsend et al., 2016). This is caused primarily due to the stepped approximation of curves in inclined surfaces by layers for PBF, which further adds to dimensional inaccuracies of a manufactured lattice structure. In 2D and 3D comparison of a Voronoi lattice structure manufactured using LPBF shown in Fig. 16, numerous dimensional anomalies of the printed lattice structure (compared to original CAD) can be observed, especially for the horizontal and diagonal struts which consist of down-skin surface areas. Additionally, nodes within strut based lattices are known to be regions with highest

dimensional inaccuracies and defects (Echeta et al., 2020), especially when compared to surface based lattices (Al-Ketan et al., 2018). Nodes in strut based lattices are complex surfaces which involve a combination of up-skin, down-skin, and vertical surfaces. This complexity adds to the 'stair step' effect (Al-Ketan et al., 2018) alongside effects of partially fused adhered powder (Li et al., 2016). Additionally, there could a compounded effect of joining multiple struts together in the subsequent layers, wherein due to residual stresses caused by large areas, the struts may not converge to a single point in space as observed in the CAD. These issues of geometric fidelity in AM lattices would be deleterious for bone replacement applications, and hence must be evaluated well before use.

X-ray computed tomography (XCT) of AM lattices is the most common method currently used to evaluate the geometric fidelity of printed lattices by comparison of the XCT scanned model with the original CAD model (u Plessis et al., 2018; Echeta et al., 2020; Vilardell et al., 2019), as also demonstrated in Fig. 16. Other methods include scanning electron microscopy (SEM), optical microscopy, and vernier caliper based comparisons of the AM lattice with the original CAD dimensions (Echeta et al., 2020).

6.5.2.4 Advances considerations for surface modifications

Porous titanium is unable to simulate organic components of bone. Surface modifications to porous titanium structures in post processing have shown to improve the biological performance and osseointegration (Asri et al., 2017; Chouirfa et al., 2019; Deering et al., 2020; Deering and Grandfield, 2021; de Wild et al., 2013; Park et al., 2011; Wang et al., 2016; Wang et al., 2008; Wang et al., 2017; Xiu et al., 2016; Yan et al., 1997; Yavari et al., 2014.). Surface modifications may include mechanical, chemical or physical methods (Liu et al., 2004). Mechanical methods such as machining, grinding, polishing and blasting aim to smooth or roughen surface topography

to improve osteoblast adhesion (de Wild et al., 2013). Chemical surface modification methods such as alkaline treatments, hydrogen peroxide treatment, and biochemical modifications are typically aimed at improving biocompatibility, bioactivity or to induce a specific cell and tissue response (Deering et al., 2020; de Wild et al., 2013; Park et al., 2011; Xiu et al., 2016). Physical modifications such as sprays, vapour and ion deposition modify surfaces to improve wear and corrosion resistance (Liu et al., 2004). One surface modification that has proven to improve osseointegration and increase osteogenesis is hydroxyapatite coatings (Park et al., 2011; Yadroitsava et al., 2019).

Surface modifications may also reduce the risk of surface-bonded powder releasing into the body and causing tissue inflammation possibly due to macrophage activation (Hollander et al., 2006). Surface-bonded powder particles are also deleterious to an implants fatigue life as they act as stress concentrators (Hrabe et al., 2011). There have been notably few *in vivo* investigations into the effects of surface modification on titanium lattice structures produced the PBF AM technologies (Deering and Grandfield, 2021). Future experimental work and systemic reviews should aim to quantify and discuss the effect of surface modification made to titanium lattice structures produced through PBF AM on osseointegration, osteogenesis and inflammatory tissue response.

6.5.2.5 Advances considerations for trabecular geometry

This review compared trabecular bone micro-architecture to lattice parameters that can be deployed in additive manufacturing. A simplistic model of trabeculae thickness and spacing was used to relate to the lattice parameters of strut thickness and pore size, respectively. However, trabecular bone has a more complex micro-architecture than traditional strut-based lattices and therefore surface-based lattices should be considered more closely in this application. Furthermore,

van Lenthe et al recognized that trabecular bone exhibits both rod and plate-like behaviour and suggested that a combined strut- and surface-based lattice configuration may best represent the trabecular bone micro-structure, see Fig. 6.17 (van Lenthe et al., 2006); such structures can now be closer to attainable from a manufacturability standpoint.

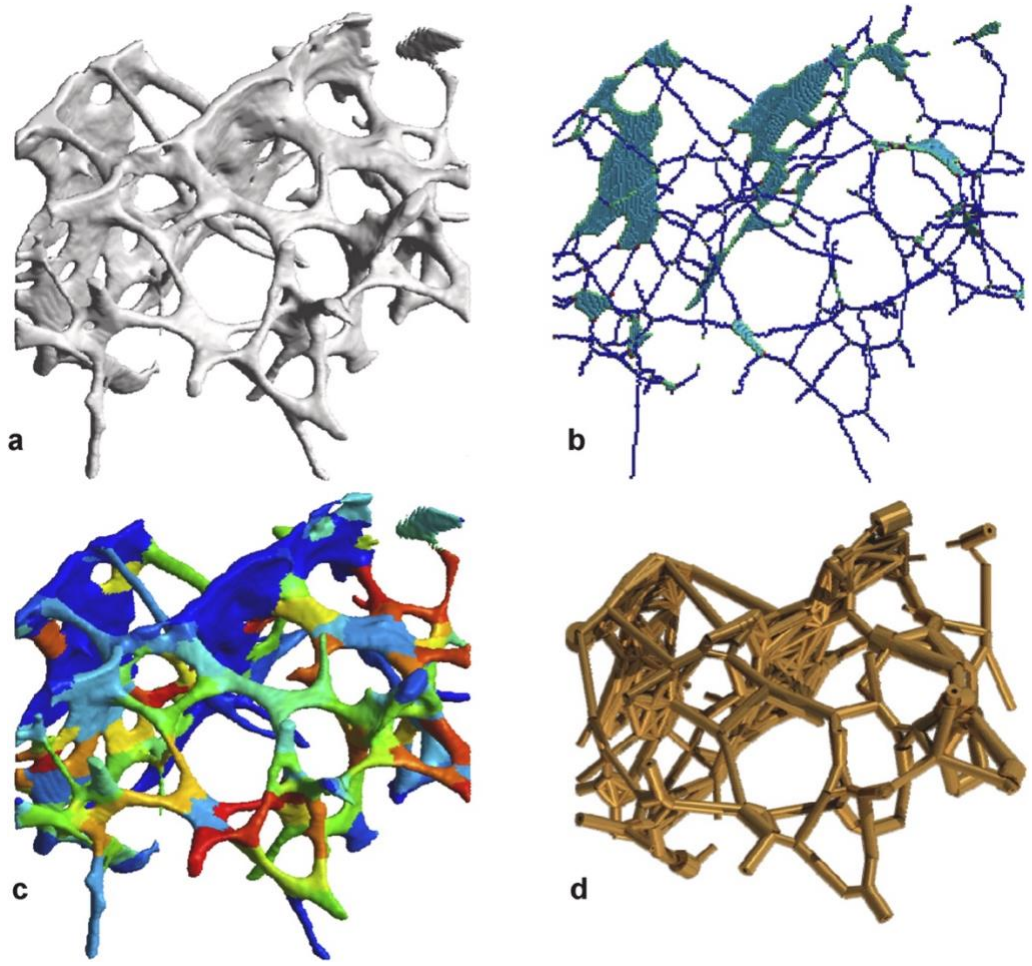


Figure 6.17 van Lenthe et al., used a micro computed tomographical (micro-CT) image of a human trabecular bone to develop a specimen-specific beam finite-element model. The process is shown above: (a) micro-CT reconstruction, (b) point cloud generation, (c) multi-colour dilation, and (d) assignment of element thickness and volume to finite element beams. Original figure obtained from (van Lenthe et al., 2006).

Callens et al. proposed a mathematical model for describing local and global trabecular micro-architecture which suggested that bone does not exhibit mean zero curvature, like those exhibited in TMPS structures Callens et al., 2020. Therefore, a stochastic surface-based lattice may

be the best selection for modelling trabecular bone. This has been successfully attempted by Kumar et al., 2020, and their work should be considered an emerging opportunity for the design of titanium lattice architectures for bone replacement and augmentation. Overall, surface lattices have shown success in replicating the mechanical properties of trabecular bone for titanium and titanium alloys and it is recommended that this avenue be pursued further Yadroitsava et al., 2019.

6.6 Conclusions

This review covers the breath of human bone geometry, mechanical properties of cortical and trabecular bone and the attempts made at replacing these tissues with additively manufactured titanium lattice structures. Human bone, particularly trabecular bone varies significantly with age, sex, disease state, skeletal location and region of the individual bones. Therefore, a site specific and function specific design approach should be considered when designing for human bone replacement, repair and augmentation. Titanium lattice structures generated through additive manufacturing have shown success in replicating cortical bone mechanical properties, promoting osseointegration for improved implant fixation and reduction of stress shielding at the bone-implant interface.

Overall, many studies were able to tune lattice parameters to obtain a Young's modulus and compressive stiffness within the range of human cortical bone, with challenges in addressing the porous network architecture concomitantly. Cortical bone is roughly 5–15% porous and titanium lattices with roughly 50–70% porosity were most successful in achieving comparable stiffness and compressive strength. Matching mechanical properties of trabecular bone was less achievable in the current literature. Trabecular thickness, or feature thickness, of human trabecular bone is on the cusp of what is attainable with existing metal additive manufacturing powder bed fusion technologies. Additionally, matching trabecular thickness to feature thickness in titanium-

based lattices does not account for the difference in bulk modulus. Therefore, matching feature thickness to trabecular bone thickness is not a recommended technique for matching the mechanical properties of titanium lattice structures to those of human trabecular bone. Control of pore size, porosity and lattice type may yield better results when attempting to replace trabecular bone with additively manufactured titanium lattices.

Young's modulus and compressive strength can be correlated to porosity of cellular latticed materials through the Gibson-Ashby model (Gibson, 2003). The Gibson-Ashby model has been used to predict compressive mechanical properties of Ti-6Al-4V lattice structures by adjusting lattice type, feature thickness and pore size to control porosity (Benedetti et al., 2019; Maconachie et al., 2019). Future efforts should build upon this work to develop a more robust transfer function that better relates the bulk moduli of titanium and Ti-6Al-4V to the anisotropic and variable lattice parameters required to generate structures that more seamlessly match the mechanical properties of site and patient specific cortical and trabecular bone. Future work should provide a comparison of the apparent density of dry and wet bone to better characterize human bone material. Due to the large variations in bone porosity and microstructure throughout the human skeleton and the increase of bone porosity with age and in females, patient specific design may yield the best outcome with respect matching mechanical properties of bone with additively manufactured lattices. Improved lattice design for bone replacement and augmentation will allow for improved orthopaedic implant design and may ultimately reduce the risk of stress shielding at the bone implant interface.

6.7 References

Aaron, J., Makins, N., & Sagreiya, K. (1987). The microanatomy of trabecular bone loss in normal aging men and women. Clinical orthopaedics and related research, 215, 260–271.

Abele, E., & Kniepkamp, M. (2015). Analysis and optimization of vertical surface roughness in micro-selective laser melting. Surface Topography: Metrology and Properties, 3 (3), 034007.620

Alabort, E., Barba, D., & Reed, R. C. (2019). Design of metallic bone by additive manufacturing. Scripta Materialia, 164, 110–114.

Al-Ketan, O., & Abu Al-Rub, R. K. (2019). Multifunctional mechanical metamaterials based on triply periodic minimal surface lattices. Advanced Engineering Materials, 21 (10), 1900524.

Al-Ketan, O., Rowshan, R., & Al-Rub, R. K. A. (2018). Topology-mechanical property relationship of 3d printed strut, skeletal, and sheet based periodic metallic cellular materials. Additive Manufacturing, 19, 167–183.

Andrew, J. J., Verma, P., & Kumar, S. (2021). Impact behavior of nanoengineered, 3d printed plate-lattices. Materials & Design, 202, 109516.

Arabnejad, S., Johnston, B., Tanzer, M., & Pasini, D. (2017). Fully porous 3d printed titanium femoral stem to reduce stress-shielding following total hip arthroplasty. Journal of Orthopaedic Research, 35 (8), 1774–1783.

Arabnejad, S., Johnston, R. B., Pura, J. A., Singh, B., Tanzer, M., & Pasini, D. (2016). High-strength porous biomaterials for bone replacement: A strategy to assess the interplay between cell morphology, mechanical properties, bone ingrowth and manufacturing constraints. Actabiomaterialia, 30, 345–356.

Arjunan, A., Demetriou, M., Baroutaji, A., & Wang, C. (2020). Mechanical performance of highly permeable laser melted Ti6Al4V bone scaffolds. journal of the mechanical behavior of biomedical materials, 102, 103517.

Asri, R., Harun, W., Samykano, M., Lah, N., Ghani, S., Tarlochan, F., & Raza, M. (2017). Corrosion and surface modification on biocompatible metals: A review. Materials Science and Engineering: C, 77, 1261–1274.

Balcı, A., Küçükaltun, F., Aycan, M. F., Usta, Y., & Demir, T. (2021). Reproducibility of replicated trabecular bone structures from ti6al4v extralow interstitials powder by selective laser melting. Arabian Journal for Science and Engineering, 46 (3), 2527–2541.

Barbas, A., Bonnet, A. -S., Lipinski, P., Pesci, R., & Dubois, G. (2012). Development and mechanical characterization of porous titanium bone substitutes. Journal of the mechanical behavior of biomedical materials, 9, 34–44.

Bari, K., & Arjunan, A. (2019). Extra low interstitial titanium based fully porous morphological bone scaffolds manufactured using selective laser melting. Journal of the mechanical behavior of biomedical materials, 95, 1–12.

Bartel, D. L., & Davy, D. T. (2006). Orthopaedic biomechanics: Mechanics and design in musculoskeletal systems. Prentice Hall.

Bartolomeu, F., Costa, M., Alves, N., Miranda, G., & Silva, F. (2021). Selective laser melting of Ti6Al4V sub-millimetric cellular structures: Prediction of dimensional deviations and mechanical performance. Journal of the Mechanical Behavior of Biomedical Materials, 113, 104123.

Bauer, J., Meza, L. R., Schaedler, T. A., Schwaiger, R., Zheng, X., & Valdevit, L. (2017). Nanolattices:An emerging class of mechanical metamaterials. Advanced Materials, 29 (40), 1701850.

Benedetti, M., Klarin, J., Johansson, F., Fontanari, V., Luchin, V., Zappini, G., & Molinari, A. (2019). Study of the compression behaviour of Ti6Al4V trabecular structures produced by additive laser manufacturing. Materials, 12 (9), 1471.

Berger, J., Wadley, H., & McMeeking, R. (2017). Mechanical metamaterials at the theoretical limit of isotropic elastic stiffness. Nature, 543 (7646), 533–537.

Biemond, J., Hannink, G., Verdonschot, N., & Buma, P. (2013). Bone ingrowth potential of electron beam and selective laser melting produced trabecular-like implant surfaces with and without a biomimetic coating. Journal of Materials Science: Materials in Medicine, 24 (3), 745–753.

Boonen, S., Cheng, X., Nijs, J., Nicholson, P., Verbeke, G., Lesaffre, E., Aerssens, J., & Dequeker, J. (1997). Factors associated with cortical and trabecular bone loss as quantified by peripheral computed tomography (pqct) at the ultradistal radius in aging women. Calcified tissue international, 60 (2), 164–170.

Burstein, A. H., Reilly, D. T., & Martens, M. (1976). Aging of bone tissue: Mechanical properties. The Journal of bone and joint surgery. American volume, 58 (1), 82–86.

Burton, H. E., Peel, S., & Eggbeer, D. (2018). Reporting fidelity in the literature for computer aided design and additive manufacture of implants and guides. Additive Manufacturing, 23, 362–373.

Calignano, F. (2018). Investigation of the accuracy and roughness in the laser powder bed fusion process Virtual and Physical Prototyping, 13 (2), 97–104.

Callens, S. J., Tourolle, D. C., Müller, R., & Zadpoor, A. A. (2020). The local and global geometry of trabecular bone. bioRxiv.

Casadei, A., Broda, R. et al. (2007). Impact of vehicle weight reduction on fuel economy for various vehicle architectures. Copy obtained from https://www.h3xed.com/blogmedia/RicardoF EM P GS tudy.pdf.

Charles, A., Elkaseer, A., Thijs, L., & Scholz, S. G. (2020). Dimensional errors due to overhanging features in laser powder bed fusion parts made of ti-6al-4v. Applied Sciences, 10 (7), 2416.

Chen, H., Zhou, X., Fujita, H., Onozuka, M., & Kubo, K.-Y. (2013). Age-related changes in trabecular and cortical bone microstructure. International journal of endocrinology, 2013.

Chen, Z., Wu, X., Tomus, D., & Davies, C. H. (2018). Surface roughness of selective laser melted Ti6Al4V alloy components. Additive Manufacturing, 21, 91–103.

Chougrani, L., Pernot, J. -P., Véron, P., & Abed, S. (2017). Lattice structure lightweight triangulation for additive manufacturing. Computer-Aided Design, 90, 95–104.

Chouirfa, H., Bouloussa, H., Migonney, V., & Falentin-Daudré, C. (2019). Review of titanium surface modification techniques and coatings for antibacterial applications. Acta biomaterialia, 83,690–54.

Choy, W. J., Mobbs, R. J., Wilcox, B., Phan, S., Phan, K., & Sutterlin III, C. E. (2017). Reconstruction of thoracic spine using a personalized 3d-printed vertebral body in adolescent with t9 primary bone tumor. World Neurosurgery, 105, 1032–e13.

Cooper, K., Steele, P., Cheng, B., & Chou, K. (2018). Contact-free support structures for part overhangs in powder-bed metal additive manufacturing. Inventions, 3 (1), 2.

Crook, C., Bauer, J., Izard, A. G., de Oliveira, C. S., e Silva, J. M. d. S., Berger, J. B., & Valdevit, L. (2020). Plate-nanolattices at the theoretical limit of stiffness and strength. Nature communications, 11 (1), 1–11.

Cuadrado, A., Yánez, A., Martel, O., Deviaene, S., & Monopoli, D. (2017). Influence of load orientation and of types of loads on the mechanical properties of porous Ti6Al4V biomaterials. Materials & Design, 135, 309–318.

Dallago, M., Raghavendra, S., Luchin, V., Zappini, G., Pasini, D., & Benedetti, M. (2021). The role of node fillet, unit-cell size and strut orientation on the fatigue strength of ti-6al-4v lattice

materials additively manufactured via laser powder bed fusion. International Journal of Fatigue,142, 105946.

Deering, J., Clifford, A., D'Elia, A., Zhitomirsky, I., & Grandfield, K. (2020). Composite dip coating improves biocompatibility of porous metallic scaffolds. Materials Letters, 274, 128057.

Deering, J., & Grandfield, K. (2021). Current interpretations on the in vivo response of bone to additively manufactured metallic porous scaffolds: A review. Biomaterials and Biosystems, 100013.

de Wild, M., Schumacher, R., Mayer, K., Schkommodau, E., Thoma, D., Bredell, M., Kruse Gujer, A., Grätz, K. W., & Weber, F. E. (2013). Bone regeneration by the osteoconductivity of porous titanium implants manufactured by selective laser melting: A histological and micro computed tomography study in the rabbit. Tissue Engineering Part A, 19 (23-24), 2645–2654.

Dong, G., Tang, Y., & Zhao, Y. F. (2017). A survey of modeling of lattice structures fabricated by additive manufacturing. Journal of Mechanical Design, 139 (10).

Druzgalski, C., Ashby, A., Guss, G., King, W., Roehling, T., & Matthews, M. (2020). Process optimization of complex geometries using feed forward control for laser powder bed fusion additive manufacturing. Additive Manufacturing, 34, 101169.

Du Plessis, A., Razavi, S. M. J., & Berto, F. (2020). The effects of microporosity in struts of gyroid lattice structures produced by laser powder bed fusion. Materials & Design, 194, 108899.

Du Plessis, A., Yadroitsev, I., Yadroitsava, I., & Le Roux, S. G. (2018). X-ray microcomputed tomography in additive manufacturing: A review of the current technology and applications. 3D Printing and Additive Manufacturing, 5 (3), 227–247.

du Plessis, A., Broeckhoven, C., Yadroitsava, I., Yadroitsev, I., Hands, C. H., Kunju, R., & Bhate, D. (2019). Beautiful and functional: A review of biomimetic design in additive manufacturing. Additive Manufacturing, 27, 408–427.

du Plessis, A., Yadroitsava, I., & Yadroitsev, I. (2018). Ti6Al4V lightweight lattice structures manufactured by laser powder bed fusion for load-bearing applications. Optics & Laser Technology, 108, 521–528.

Echeta, I., Feng, X., Dutton, B., Leach, R., & Piano, S. (2020). Review of defects in lattice structures manufactured by powder bed fusion. The International Journal of Advanced Manufacturing Technology, 106 (5), 2649–2668.

El-Sayed, M. A., Essa, K., Ghazy, M., & Hassanin, H. (2020). Design optimization of additively manufactured titanium lattice structures for biomedical implants. The International Journal of Advanced Manufacturing Technology, 110 (9), 2257–2268.

Emmelmann, C., Sander, P., Kranz, J., & Wycisk, E. (2011). Laser additive manufacturing and bionics: Redefining lightweight design. Physics Procedia, 12, 364–368.

Fousová, M., Vojtěch, D., Kubásek, J., Jablonská, E., & Fojt, J. (2017). Promising characteristics of gradient porosity ti-6al-4v alloy prepared by slm process. Journal of the mechanical behavior of biomedical materials, 69, 368–376.

Gauthier, R., Follet, H., Olivier, C., Mitton, D., & Peyrin, F. (2019). 3d analysis of the osteonal and interstitial tissue in human radii cortical bone. Bone, 127, 526–536.

Ge, J., Huang, J., Lei, Y., O'Reilly, P., Ahmed, M., Zhang, C., Yan, X., & Yin, S. (2020). Microstructural features and compressive properties of slm ti6al4v lattice structures. Surface and CoatingsTechnology, 403, 126419.

Ghouse, S., Reznikov, N., Boughton, O. R., Babu, S., Ng, K. G., Blunn, G., Cobb, J. P., Stevens, M. M., & Jeffers, J. R. (2019). The design and in vivo testing of a locally stiffness-matched porous scaffold. Applied materials today, 15, 377–388.

Gibson, I., Rosen, D., Stucker, B., & Khorasani, M. (2014). Additive manufacturing technologies (Vol. 17). Springer.

Gibson, L. J. (2003). Cellular solids. Mrs Bulletin, 28 (4), 270–274.

Gong, X., Anderson, T., & Chou, K. (2012). Review on powder-based electron beam additive manufacturing technology. International Symposium on Flexible Automation, 45110, 507–515.

Gui, N., Xu, W., Myers, D., Shukla, R., Tang, H., & Qian, M. (2018). The effect of ordered and partially ordered surface topography on bone cell responses: A review. Biomaterials science, 6 (2), 250–264.

Gümrük, R., Mines, R., & Karadeniz, S. (2013). Static mechanical behaviours of stainless steel microlattice structures under different loading conditions. Materials Science and Engineering: A, 586, 392–406.

Harrysson, O. L., Cansizoglu, O., Marcellin-Little, D. J., Cormier, D. R., & West II, H. A. (2008). Direct metal fabrication of titanium implants with tailored materials and mechanical properties using electron beam melting technology. Materials Science and Engineering: C, 28 (3), 366–373.

Heinl, P., Müller, L., Körner, C., Singer, R. F., & Müller, F. A. (2008). Cellular ti–6al–4v structures with interconnected macro porosity for bone implants fabricated by selective electron beam melting. Acta biomaterialia, 4 (5), 1536–1544.

Hildebrand, T., Laib, A., Müller, R., Dequeker, J., & Rüegsegger, P. (1999). Direct three-dimensional morphometric analysis of human cancellous bone: Microstructural data from spine, femur, iliac crest, and calcaneus. Journal of bone and mineral research, 14 (7), 1167–1174.

Hilton, T., Campbell, N., & Hosking, K. (2017). Additive manufacturing in orthopaedics: Clinical implications. SA Orthopaedic Journal, 16 (2), 63–67.

Hollander, D. A., Von Walter, M., Wirtz, T., Sellei, R., Schmidt-Rohlfing, B., Paar, O., & Erli, H.-J. (2006). Structural, mechanical and in vitro characterization of individually structured Ti6Al4V produced by direct laser forming. Biomaterials, 27 (7), 955–963.

Hrabe, N. W., Heinl, P., Flinn, B., Körner, C., & Bordia, R. K. (2011). Compression-compression fatigue of selective electron beam melted cellular titanium (Ti6Al4V). Journal of Biomedical Materials Research Part B: Applied Biomaterials, 99 (2), 313–320.

ISO 7206-4. (2010). Implants for surgery — partial and total hip joint prostheses — part 4: Determination of endurance properties and performance of stemmed femoral components (tech. rep.).International Organization for Standardization (ISO).

Khosla, S., Riggs, B. L., Atkinson, E. J., Oberg, A. L., McDaniel, L. J., Holets, M., Peterson, J. M., &Melton III, L. J. (2006). Effects of sex and age on bone microstructure at the ultradistal radius: A population-based noninvasive in vivo assessment. Journal of Bone and Mineral Research, 21 (1), 124–131.

Kim, D., Lim, J. -Y., Shim, K. -W., Han, J. W., Yi, S., Yoon, D. H., Kim, K. N., Ha, Y., Ji, G. Y., & Shin, D. A. (2017). Sacral reconstruction with a 3d-printed implant after hemisacrectomy in a patient with sacral osteosarcoma: 1-year follow-up result. Yonsei medical journal, 58 (2), 453.

Kumar, S., Tan, S., Zheng, L., & Kochmann, D. M. (2020). Inverse-designed spinodoid metamaterials. Computational Materials, 6 (1), 1–10.

Küpper, D., Heising, W., Corman, G., Wolfgang, M., Knizek, C., & Lukic, V. (2017). Get ready for industrialized additive manufacturing (tech. rep.). Boston Consulting Group.

Leary, M., Mazur, M., Elambasseril, J., McMillan, M., Chirent, T., Sun, Y., Qian, M., Easton, M., & Brandt, M. (2016). Selective laser melting (slm) of alsi12mg lattice structures. Materials & Design, 98, 344–357.

Lee, H., Lim, C. H. J., Low, M. J., Tham, N., Murukeshan, V. M., & Kim, Y. - J. (2017). Lasers in additive manufacturing: A review. International Journal of Precision Engineering and Manufacturing-Green Technology, 4 (3), 307–322.

Li, S., Hassanin, H., Attallah, M. M., Adkins, N. J., & Essa, K. (2016). The development of tini-based negative poisson's ratio structure using selective laser melting. Acta Materialia, 105, 75–83.

Lin, W.-S., Starr, T. L., Harris, B. T., Zandinejad, A., & Morton, D. (2013). Additive manufacturing technology (direct metal laser sintering) as a novel approach to fabricate functionally graded titanium implants: Preliminary investigation of fabrication parameters. The International journal of oral & maxillofacial implants, 28 (6), 1490–1495.

Liu, F., Zhang, D. Z., Zhang, P., Zhao, M., & Jafar, S. (2018). Mechanical properties of optimized diamond lattice structure for bone scaffolds fabricated via selective laser melting. Materials, 11 (3), 374.

Liu, L., Kamm, P., Garcıa-Moreno, F., Banhart, J., & Pasini, D. (2017). Elastic and failure response of imperfect three-dimensional metallic lattices: The role of geometric defects induced by selective laser melting. Journal of the Mechanics and Physics of Solids, 107, 160–184.

Liu, X. S., Sajda, P., Saha, P. K., Wehrli, F. W., Bevill, G., Keaveny, T. M., & Guo, X. E. (2008). Complete volumetric decomposition of individual trabecular plates and rods and its morphological correlations with anisotropic elastic moduli in human trabecular bone. Journal of Bone and Mineral Research, 23 (2), 223–235.

Liu, X. S., Zhang, X. H., Rajapakse, C. S., Wald, M. J., Magland, J., Sekhon, K. K., Adam, M. F., Sajda, P., Wehrli, F. W., & Guo, X. E. (2010). Accuracy of high-resolution in vivo micro magnetic resonance imaging for measurements of microstructural and mechanical properties of human distal tibial bone. Journal of Bone and Mineral Research, 25 (9), 2039–2050.

Liu, X., Chu, P. K., & Ding, C. (2004). Surface modification of titanium, titanium alloys, and related materials for biomedical applications. Materials Science and Engineering: R: Reports, 47 (3-4), 49–121.

Liu, Y. (2021). Mechanical properties of a new type of plate–lattice structures. International Journal of Mechanical Sciences, 192, 106141.

Macdonald, H. M., Nishiyama, K. K., Kang, J., Hanley, D. A., & Boyd, S. K. (2011). Age-related patterns of trabecular and cortical bone loss differ between sexes and skeletal sites: A population-based hr-pqct study. Journal of Bone and Mineral Research, 26 (1), 50–62.

Maconachie, T., Leary, M., Lozanovski, B., Zhang, X., Qian, M., Faruque, O., & Brandt, M. (2019). SLM lattice structures: Properties, performance, applications and challenges. Materials & Design,183, 108137.

Majumdar, S., Genant, H., Grampp, S., Newitt, D., Truong, V.-H., Lin, J., & Mathur, A. (1997). Correlation of trabecular bone structure with age, bone mineral density, and osteoporotic status: In vivo studies in the distal radius using high resolution magnetic resonance imaging. Journal of Bone and Mineral Research, 12 (1), 111–118.

Maliaris, G., & Sarafis, E. (2017). Mechanical behavior of 3d printed stochastic lattice structures. Solid State Phenomena, 258, 225–228.835

Marin, E., Pressacco, M., Fusi, S., Lanzutti, A., Turchet, S., & Fedrizzi, L. (2013). Characterization of grade 2 commercially pure trabecular titanium structures. Materials Science and Engineering: C, 33 (5), 2648–2656.

McCalden, R. W., McGeough, J. A., Barker, M. B., et al. (1993). Age-related changes in the tensile properties of cortical bone. the relative importance of changes in porosity, mineralization, and microstructure. The Journal of bone and joint surgery. American volume, 75 (8), 1193–1205.

Melancon, D., Bagheri, Z., Johnston, R., Liu, L., Tanzer, M., & Pasini, D. (2017). Mechanical characterization of structurally porous biomaterials built via additive manufacturing: Experiments, predictive models, and design maps for load-bearing bone replacement implants. Acta biomaterialia, 63, 350–368.

Mines, R., Tsopanos, S., Shen, Y., Hasan, R., & McKown, S. (2013). Drop weight impact behaviour of sandwich panels with metallic micro lattice cores. International Journal of Impact Engineering,60, 120–132.

Mobbs, R. J., Coughlan, M., Thompson, R., Sutterlin, C. E., & Phan, K. (2017). The utility of 3d printing for surgical planning and patient-specific implant design for complex spinal pathologies:Case report. Journal of Neurosurgery: Spine, 26 (4), 513–518.

Moiduddin, K., Darwish, S., Al-Ahmari, A., ElWatidy, S., Mohammad, A., & Ameen, W. (2017). Structural and mechanical characterization of custom design cranial implant created using additive manufacturing. Electronic Journal of Biotechnology, 29, 22–31.

Morgan, E. F., Unnikrisnan, G. U., & Hussein, A. I. (2018). Bone mechanical properties in healthy and diseased states. Annual review of biomedical engineering, 20, 119–143.

Moylan, S. P., Slotwinski, J. A., Cooke, A., Jurrens, K., & Donmez, M. A. (2013). Lessons learned in establishing the nist metal additive manufacturing laboratory. NIST technical note.

Munford, M. J., Ng, K. G., & Jeffers, J. R. (2020). Mapping the multi-directional mechanical properties of bone in the proximal tibia. Advanced Functional Materials, 30 (46), 2004323.

Murr, L., Amato, K., Li, S., Tian, Y., Cheng, X., Gaytan, S., Martinez, E., Shindo, P., Medina, F., & Wicker, R. (2011). Microstructure and mechanical properties of open-cellular biomaterials prototypes for total knee replacement implants fabricated by electron beam melting. Journal of the mechanical behavior of biomedical materials, 4 (7), 1396–1411.

Newton, L., Senin, N., Chatzivagiannis, E., Smith, B., & Leach, R. (2020). Feature-based characterization of Ti6Al4V electron beam powder bed fusion surfaces fabricated at different surface orientations. Additive Manufacturing, 35, 101273.

Nicks, K. M., Amin, S., Atkinson, E. J., Riggs, B. L., Melton III, L. J., & Khosla, S. (2012). Relationship of age to bone microstructure independent of areal bone mineral density. Journal of Bone and Mineral Research, 27 (3), 637–644.

Ong, J., Appleford, M. R., & Mani, G. (2014). Introduction to biomaterials: Basic theory with engineering applications. Cambridge University Press.

Oshida, Y. (2010). Bioscience and bioengineering of titanium materials. Elsevier.

Otsuki, B., Takemoto, M., Fujibayashi, S., Neo, M., Kokubo, T., & Nakamura, T. (2006). Pore throat size and connectivity determine bone and tissue ingrowth into porous implants: Three-dimensional micro-ct based structural analyses of porous bioactive titanium implants. Biomaterials, 27 (35), 5892–5900.

Park, J., & Lakes, R. S. (2007). Biomaterials: An introduction. Springer Science & Business Media. Park, S. -J., Bae, S. -B., Kim, S. -K., Eom, T. -G., & Song, S. -I. (2011). Effect of implant surface microtopography by hydroxyapatite grit-blasting on adhesion, proliferation, and differentiation of osteoblast-like cell line, mg-63. Journal of the Korean Association of Oral and Maxillofacial Surgeons, 37 (3), 214–224.

Patel, S., Rogalsky, A., & Vlasea, M. (2020). Towards understanding side-skin surface characteristics in laser powder bed fusion. Journal of Materials Research, 35 (15), 2055–2064.

Patel, S., & Vlasea, M. (2020). Melting modes in laser powder bed fusion. Materialia, 9, 100591.

Peel, S., & Eggbeer, D. (2016). Additively manufactured maxillofacial implants and guides–achieving routine use. Rapid Prototyping Journal.

Phan, K., Sgro, A., Maharaj, M. M., D'Urso, P., & Mobbs, R. J. (2016). Application of a 3d custom printed patient specific spinal implant for c1/2 arthrodesis. Journal of Spine Surgery, 2 (4), 314.

Riggs, B. L., Melton III, L. J., Robb, R. A., Camp, J. J., Atkinson, E. J., Peterson, J. M., Rouleau, P. A., McCollough, C. H., Bouxsein, M. L., & Khosla, S. (2004). Population-based study of age and sex differences in bone volumetric density, size, geometry, and structure at different skeletal sites. Journal of Bone and Mineral Research, 19 (12), 1945–1954.

Sames, W. J., List, F., Pannala, S., Dehoff, R. R., & Babu, S. S. (2016). The metallurgy and processing science of metal additive manufacturing. International materials reviews, 61 (5), 315–360.

Schouman, T., Schmitt, M., Adam, C., Dubois, G., & Rouch, P. (2016). Influence of the overall stiffness of a load-bearing porous titanium implant on bone ingrowth in critical-size mandibular bone defects in sheep. Journal of the mechanical behavior of biomedical materials, 59, 484–496.

Seeman, E. (2002). Pathogenesis of bone fragility in women and men. The Lancet, 359 (9320), 1841–1850.

Shanbhag, G., & Vlasea, M. (2020). The effect of reuse cycles on Ti6Al4V powder properties processed by electron beam powder bed fusion. Manufacturing Letters, 25, 60–63.

Sing, S. L., An, J., Yeong, W. Y., & Wiria, F. E. (2016). Laser and electron-beam powder-bed additive manufacturing of metallic implants: A review on processes, materials and designs. Journal of Orthopaedic Research, 34 (3), 369–385.

Snyder, J. C., & Thole, K. A. (2020). Understanding laser powder bed fusion surface roughness. Journal of Manufacturing Science and Engineering, 142 (7).

Song, C., Wang, A., Wu, Z., Chen, Z., Yang, Y., & Wang, D. (2017). The design and manufacturing of a titanium alloy beak for grus japonensis using additive manufacturing. Materials & Design, 117, 410–416.

Soro, N., Attar, H., Wu, X., & Dargusch, M. S. (2019). Investigation of the structure and mechanical properties of additively manufactured ti-6al-4v biomedical scaffolds designed with a schwartz primitive unit-cell. Materials Science and Engineering: A, 745, 195–202.

Soro, N., Saintier, N., Merzeau, J., Veidt, M., & Dargusch, M. S. (2021). Quasi-static and fatigue properties of graded Ti6Al4V lattices produced by laser powder bed fusion (lpbf). Additive Manufacturing, 37, 101653.

Spadaro, J., Werner, F., Brenner, R., Fortino, M., Fay, L., & Edwards, W. (1994). Cortical and trabecular bone contribute strength to the osteopenic distal radius. Journal of orthopaedic research, 12 (2), 211–218.

Srivas, P. K., Kapat, K., Dadhich, P., Pal, P., Dutta, J., Datta, P., & Dhara, S. (2017). Osseointegration assessment of extrusion printed Ti6Al4V scaffold towards accelerated skeletal defect healing via tissue in-growth. Bioprinting, 6, 8–17.

Strano, G., Hao, L., Everson, R. M., & Evans, K. E. (2013). Surface roughness analysis, modelling and prediction in selective laser melting. Journal of Materials Processing Technology, 213 (4), 589–597.

Taheri Andani, M., Haberland, C., Walker, J. M., Karamooz, M., Sadi Turabi, A., Saedi, S., Rahmanian, R., Karaca, H., Dean, D., Kadkhodaei, M., et al. (2016). Achieving biocompatible stiffness in NiTi through additive manufacturing. Journal of Intelligent Material Systems and Structures, 27 (19), 2661–2671.

Tan, X., Tan, Y., Chow, C., Tor, S., & Yeong, W. (2017). Metallic powder-bed based 3d printing of cellular scaffolds for orthopaedic implants: A state-of-the-art review on manufacturing, topological design, mechanical properties and biocompatibility. Materials Science and Engineering: C, 76, 1328–1343.

Tancogne-Dejean, T., Diamantopoulou, M., Gorji, M. B., Bonatti, C., & Mohr, D. (2018). 3d plate- lattices: An emerging class of low-density metamaterial exhibiting optimal isotropic stiffness. Advanced Materials, 30 (45), 1803334.

Tancogne-Dejean, T., Li, X., Diamantopoulou, M., Roth, C., & Mohr, D. (2019). High strain rate response of additively manufactured plate-lattices: Experiments and modeling. Journal of Dynamic Behavior of Materials, 5 (3), 361–375.

Tancogne-Dejean, T., Spierings, A. B., & Mohr, D. (2016). Additively manufactured metallic micro-lattice materials for high specific energy absorption under static and dynamic loading. Acta Materialia, 116, 14–28.

Taniguchi, N., Fujibayashi, S., Takemoto, M., Sasaki, K., Otsuki, B., Nakamura, T., Matsushita, T.,Kokubo, T., & Matsuda, S. (2016). Effect of pore size on bone ingrowth into porous titanium implants fabricated by additive manufacturing: An in vivo experiment. Materials Science and Engineering: C, 59, 690–701.

Thomsen, J. S., Laib, A., Koller, B., Prohaska, S., Mosekilde, L., & Gowin, W. (2005). Stereological measures of trabecular bone structure: Comparison of 3d micro computed tomography with 2d histological sections in human proximal tibial bone biopsies. Journal of Microscopy, 218 (2), 171–179.

Tian, Y., Tomus, D., Huang, A., & Wu, X. (2019). Experimental and statistical analysis on process parameters and surface roughness relationship for selective laser melting of hastelloy x. Rapid Prototyping Journal.

Tian, Y., Tomus, D., Rometsch, P., & Wu, X. (2017). Influences of processing parameters on surface roughness of hastelloy x produced by selective laser melting. Additive Manufacturing, 13, 103–112.

Tonino, A., Davidson, C., Klopper, P., & Linclau, L. (1976). Protection from stress in bone and its effects. experiments with stainless steel and plastic plates in dogs. The Journal of bone and joint surgery. British volume, 58 (1), 107–113.

Townsend, A., Senin, N., Blunt, L., Leach, R., & Taylor, J. (2016). Surface texture metrology for metal additive manufacturing: A review. Precision Engineering, 46, 34–47.

Van Bael, S., Chai, Y. C., Truscello, S., Moesen, M., Kerckhofs, G., Van Oosterwyck, H., Kruth, J.-P., & Schrooten, J. (2012). The effect of pore geometry on the in vitro biological behavior of

human periosteum-derived cells seeded on selective laser-melted ti6al4v bone scaffolds. Acta biomaterialia, 8 (7), 2824–2834.

Van der Stok, J., Van der Jagt, O. P., Amin Yavari, S., De Haas, M. F., Waarsing, J. H., Jahr, H., Van Lieshout, E. M., Patka, P., Verhaar, J. A., Zadpoor, A. A., et al. (2013). Selective laser melting-produced porous titanium scaffolds regenerate bone in critical size cortical bone defects. Journal of Orthopaedic Research, 31 (5), 792–799.

van Lenthe, G. H., Stauber, M., & Müller, R. (2006). Specimen-specific beam models for fast and accurate prediction of human trabecular bone mechanical properties. Bone, 39 (6), 1182–1189.

Velasco, M. A., Narváez-Tovar, C. A., & Garzón-Alvarado, D. A. (2015). Design, materials, and mechanobiology of biodegradable scaffolds for bone tissue engineering. BioMed research international, 2015.

Vilardell, A. M., Takezawa, A., Du Plessis, A., Takata, N., Krakhmalev, P., Kobashi, M., & Yadroitsev, I. (2019). Topology optimization and characterization of Ti6Al4V cellular lattice structures by laser powder bed fusion for biomedical applications. Materials Science and Engineering: A, 766, 138330.

Wadley, H. N. (2006). Multifunctional periodic cellular metals. Philosophical Transactions of the Royal Society A: Mathematical, Physical and Engineering Sciences, 364 (1838), 31–68.

Wang, L., Kang, J., Sun, C., Li, D., Cao, Y., & Jin, Z. (2017). Mapping porous microstructures to yield desired mechanical properties for application in 3d printed bone scaffolds and orthopaedic implants. Materials & Design, 133, 62–68.

Wang, P., Li, X., Jiang, Y., Nai, M. L. S., Ding, J., & Wei, J. (2020). Electron beam melted heterogeneously porous microlattices for metallic bone applications: Design and investigations of boundary and edge effects. Additive Manufacturing, 36, 101566.

Wang, X., Xu, S., Zhou, S., Xu, W., Leary, M., Choong, P., Qian, M., Brandt, M., & Xie, Y. M. (2016). Topological design and additive manufacturing of porous metals for bone scaffolds and orthopaedic implants: A review. Biomaterials, 83, 127–141.

Wang, X., & Chou, K. (2018). Effect of support structures on Ti6Al4V overhang parts fabricated by powder bed fusion electron beam additive manufacturing. Journal of Materials Processing Technology, 257, 65–78.

Wang, X., Li, Y., Lin, J., Yamada, Y., Hodgson, P., & Wen, C. (2008). In vitro bioactivity evaluation of titanium and niobium metals with different surface morphologies. Acta biomaterialia, 4 (5), 1530–1535.

Wang, Y. M., Voisin, T., McKeown, J. T., Ye, J., Calta, N. P., Li, Z., Zeng, Z., Zhang, Y., Chen, W., Roehling, T. T., et al. (2018). Additively manufactured hierarchical stainless steels with high strength and ductility. Nature materials, 17 (1), 63–71.

Wang, Z., Wang, C., Li, C., Qin, Y., Zhong, L., Chen, B., Li, Z., Liu, H., Chang, F., & Wang, J. (2017). Analysis of factors influencing bone ingrowth into three-dimensional printed porous metal scaffolds: A review. Journal of Alloys and Compounds, 717, 271–285.

Webster, T. J., & Ejiofor, J. U. (2004). Increased osteoblast adhesion on nanophase metals: Ti, Ti6Al4V, and cocrmo. Biomaterials, 25 (19), 4731–4739.

Wieding, J., Lindner, T., Bergschmidt, P., & Bader, R. (2015). Biomechanical stability of novel mechanically adapted open-porous titanium scaffolds in metatarsal bone defects of sheep. Biomaterials, 46, 35–47.

Wieding, J., Wolf, A., & Bader, R. (2014). Numerical optimization of open-porous bone scaffold structures to match the elastic properties of human cortical bone. Journal of the mechanical behavior of biomedical materials, 37, 56–68.

Wong, K., Kumta, S., Geel, N., & Demol, J. (2015). One-step reconstruction with a 3d-printed, biomechanically evaluated custom implant after complex pelvic tumor resection. Computer Aided Surgery, 20 (1), 14–23.

Wu, S.-H., Li, Y., Zhang, Y. -Q., Li, X.-K., Yuan, C.- F., Hao, Y.- L., Zhang, Z.-Y., & Guo, Z. (2013). Porous titanium-6 aluminum-4 vanadium cage has better osseointegration and less micromotion than a poly-ether-ether-ketone cage in sheep vertebral fusion. Artificial organs, 37 (12), E191–E201.

Xiong, Y.-Z., Gao, R. -N., Zhang, H., Dong, L.-L., Li, J. -T., & Li, X. (2020). Rationally designed functionally graded porous Ti6Al4V scaffolds with high strength and toughness built via selective laser melting for load-bearing orthopedic applications. Journal of the mechanical behavior of biomedical materials, 104, 103673.

Xiu, P., Jia, Z., Lv, J., Yin, C., Cheng, Y., Zhang, K., Song, C., Leng, H., Zheng, Y., Cai, H., et al. (2016). Tailored surface treatment of 3d printed porous Ti6Al4V by microarc oxidation for enhanced osseointegration via optimized bone in-growth patterns and interlocked bone/implant interface. ACS applied materials & interfaces, 8 (28), 17964–17975.

Xu, N., Wei, F., Liu, X., Jiang, L., Cai, H., Li, Z., Yu, M., Wu, F., & Liu, Z. (2016). Reconstruction of the upper cervical spine using a personalized 3d-printed vertebral body in an adolescent with ewing sarcoma. Spine, 41 (1), E50–E54.

Xue, W., Krishna, B. V., Bandyopadhyay, A., & Bose, S. (2007). Processing and biocompatibility evaluation of laser processed porous titanium. Acta biomaterialia, 3 (6), 1007–1018.

Yadroitsava, I., du Plessis, A., & Yadroitsev, I. (2019). Bone regeneration on implants of titanium alloys produced by laser powder bed fusion: A review. Titanium for Consumer Applications, 197–233.

Yan, C., Hao, L., Hussein, A., & Young, P. (2015). Ti6Al4V triply periodic minimal surface structures for bone implants fabricated via selective laser melting. Journal of the mechanical behavior of biomedical materials, 51, 61–73.

Yan, W. -Q., Nakamura, T., Kobayashi, M., Kim, H. -M., Miyaji, F., & Kokubo, T. (1997). Bonding of chemically treated titanium implants to bone. Journal of Biomedical Materials Research: An Official Journal of The Society for Biomaterials and The Japanese Society for Biomaterials, 37 (2), 267–275.

Yasa, E., Deckers, J., Craeghs, T., Badrossamay, M., & Kruth, J. -P. (2009). Investigation on occurrence of elevated edges in selective laser melting. International Solid Freeform Fabrication Symposium,Austin, TX, USA, 673–85.

Yavari, S. A., van der Stok, J., Chai, Y. C., Wauthle, R., Birgani, Z. T., Habibovic, P., Mulier, M., Schrooten, J., Weinans, H., & Zadpoor, A. A. (2014). Bone regeneration performance of surface-treated porous titanium. Biomaterials, 35 (24), 6172–6181.

Zadpoor, A. A. (2019). Mechanical performance of additively manufactured meta-biomaterials. Acta biomaterialia, 85, 41–59.

Zargarian, A., Esfahanian, M., Kadkhodapour, J., & Ziaei-Rad, S. (2016). Numerical simulation of the fatigue behavior of additive manufactured titanium porous lattice structures. Materials Science and Engineering: C, 60, 339–347.

Zhang, B., Pei, X., Zhou, C., Fan, Y., Jiang, Q., Ronca, A., D'Amora, U., Chen, Y., Li, H., Sun, Y.,et al. (2018). The biomimetic design and 3d printing of customized mechanical properties porous ti6al4v scaffold for load-bearing bone reconstruction. Materials & Design, 152, 30–39.

Zhang, X. -Y., Yan, X.-C., Fang, G., & Liu, M. (2020). Biomechanical influence of structural variation strategies on functionally graded scaffolds constructed with triply periodic minimal surface. Additive Manufacturing, 32, 101015.

Zhang, Y., Andrukhov, O., Berner, S., Matejka, M., Wieland, M., Rausch-Fan, X., & Schedle, A. (2010). Osteogenic properties of hydrophilic and hydrophobic titanium surfaces evaluated with osteoblast-like cells (mg63) in coculture with human umbilical vein endothelial cells (huvec). dental materials, 26 (11), 1043–1051.

Zhao, D., Huang, Y., Ao, Y., Han, C., Wang, Q., Li, Y., Liu, J., Wei, Q., & Zhang, Z. (2018). Effect of pore geometry on the fatigue properties and cell affinity of porous titanium scaffolds fabricated by selective laser melting. Journal of the mechanical behavior of biomedical materials, 88, 478–487.

Zheng, X., Smith, W., Jackson, J., Moran, B., Cui, H., Chen, D., Ye, J., Fang, N., Rodriguez, N., Weisgraber, T., et al. (2016). Multiscale metallic metamaterials. Nature materials, 15 (10), 1100–1106.

Chapter 7– A manufacturability evaluation of complex architectures by laser powder bed fusion additive manufacturing [4]

Abstract

Additive manufacturing (AM) enables new possibilities for the design and manufacturing of complex metal architectures. Incorporating lattice structures into complex part geometries can enhance strength-to-weight and surface area-to-volume ratios for valuable components, particularly in industries such as medical devices and aerospace. However, lattice structures and their interconnections may result in unsupported down-skin surfaces, potentially limiting their manufacturability by metal AM technologies, such as laser powder bed fusion (LPBF). This study aimed to examine the correlation between down-skin surface area and the manufacturability of lattice structures fabricated using LPBF. Image processing algorithms were used to analyze down-skin surface areas of seven unique lattice designs and to devise quantitative metrics (such as down-skin surface area, discrete surface count, surface interconnectivity, down-skin ratio, over-print/under-print volumes, etc.) to evaluate LPBF manufacturability. The seven lattice designs were subsequently manufactured using maraging steel via LPBF and then examined using imaging using X-ray micro-computed tomography (XCT). The geometric accuracy of the lattice designs was compared with XCT scans of the manufactured lattices by employing a voxel-based image comparison technique. The results indicated a strong relationship between down-skin surface area, surface interconnectivity, and the manufacturability of a given lattice design. The digital manufacturability evaluation workflow was also applied to a medical device design, further affirming its potential industrial utility for complex geometries.

[4] A version of this chapter has been published in a peer-reviewed journal: McGregor, M; Patel, S; Zhang, K; Yu, A; McLachlin, S; Vlasea, M. (2024). A manufacturability evaluation of complex architectures by laser powder bed fusion additive manufacturing. Journal of Manufacturing Science and Engineering, 1-17.

7.1 Introduction

Metal additive manufacturing (AM) facilitates new possibilities for complex part geometry design and fabrication (Gardan, 2019; Rosen, 2014). Within metal AM, laser powder bed fusion (LPBF) is commonly used for industrial part production due to superior part resolution (Sames et al., 2016) and adaptability to different material types (Sing et al., 2016). Despite these advantages of LPBF, limitations remain with respect to support structure requirements resulting in surface roughness, post-processing requirements, and material waste. Support structures are typically required on downward-facing (down-skin) surfaces having angles with respect to the build plate between 0 deg and 45 deg (McGregor et al., 2021). These down-skin surfaces, present in almost all parts designed for metal AM, require support structures for part anchoring and for thermal dissipation to mitigate the risk of excessive material vaporization and distortion due to residual stresses (Mercelis et al., 2006). Unsupported down-skin may lead to increased surface roughness, deviations in part geometry, porous flaws, print failures, and reduced mechanical performance (Ashby et al., 2022). Design considerations for down-skin surfaces, such as refinement and reduction of down-skin features with respect to part orientation to the build plate, need to be addressed prior to fabrication via LPBF. It can be challenging to completely minimize the occurrence of down-skin surfaces from components with complex architectures such as interconnected lattice structures with repeating down-skin surfaces (McGregor et al., 2021).

Many complex parts in AM incorporate lattice architectures, a form of hierarchical design structures, to improve strength-to-weight and surface area-to-volume ratios through fine-tuning design parameters. Lattice structures vary widely in design and may be homogeneous or heterogeneous, surface or strut-based, and/or periodic or stochastic (Dong et al., 2017; McGregor et a;., 2021; Wadley, 2006). Lattices can be further classified as homogeneous or heterogeneous.

Homogeneity (constant) versus heterogeneity (changing) in lattices refers to the thickness of unit cell features such as struts and/or walls (McGregor et al., 2021). Surface-based lattices, such as triply periodic minimal surface (TPMS) lattices, have a greater surface area-volume ratio than strut-based lattices, making them more suited for applications related to heat exchange, filtration, and biomedical devices wherein osseointegration is important. Strut-based lattices allow for higher strength and stiffness for structural components or load-bearing applications (du Plessis et al., 2021). Periodic lattices are comprised of a series of repeating unit cells, whereas stochastic lattices are random in nature. For high-value components like medical devices, the benefits of utilizing lattice structures within complex part geometries include lightweighting parts through topology optimization, controlling fluid flow, and tailoring biomimetic performance requirements for the human body (Boccini et al., 2019; McGregor et al, 2021; Patel et al., 2021; Zhang et al., 2020). Such lattice structures are challenging to manufacture through traditional manufacturing methods due to their geometric complexity (du Plessis et al., 2021). AM offers the adaptability required to produce these valuable metamaterials, independently or integrated as part of larger part geometries. However, lattice structures often have down-skin regions that cannot be supported adequately in LPBF due to the interconnectivity of the design features, making removal of support structures nonviable.

For the present study, the angle between a given polygonal cell element of a surface mesh and the build plate is referred to as the surface angle. Polygonal cell elements were then defined as features with a surface angle between 0 and 90 deg, where 0-deg features are parallel to the build plate and 90-deg surfaces are perpendicular to the build plate. Polygonal cell elements with a surface angle below 45 deg, termed down-skin surfaces, are of particular interest to the AM community due to well-recognized manufacturability challenges. Side-skin surfaces and up-skin

surfaces are polygonal cell elements with a surface angle between 90 deg and 180 deg and are generally considered manufacturable with LPBF technologies and were excluded from analysis in this study.

The quality of down-skin surfaces in LPBF components has been previously examined in literature. It is well established that surfaces between 0 deg and 45 deg to the build plate are prone to poor geometric fidelity and dross, or over-printing, the phenomenon in which partially sintered powder fuses to solid surfaces resulting in increased surface roughness (Calignano, 2014; Triantaphyllou et al., 2015; Fox et al., 2016; Chen et al., 2017). Meanwhile under-printing, the absence of material with respect to computer-aided design (CAD) parts, can be caused in LPBF parts by the porous powder melting and then rapidly solidifying (Mulhi et al., 2022; Echeta et al., 2020). Print parameters have been found to affect the manufacturability of down-skin surfaces through experiments examining surface angle, scanning speed, laser power, accumulated residual stress, and scanning vector length (Wang et al., 2013; Charles et al., 2021; Viale et al., 2022). Laser scanning strategies can also be controlled through tailored algorithms to improve surface roughness and reduce geometric variation on down-skin surfaces (Yeung et al., 2019). Down-skin surfaces have also been shown to increase near-surface porous defects in LPBF parts (Shange et al., 2021; Cabanettes et al., 2018). In an intensive experimental investigation, Shange et al., 2021, reported an inversely proportional relationship between down-skin surface angle and near-surface porosity and surface roughness, with a lower down-skin angle being associated with greater near-surface porosity and surface roughness. Design for additive manufacturing tools for the design of lattice structures has been established in efforts to optimize strut element shape and orientation (Almalki et al., 2023). These studies show that there is an overall interplay between process

parameters and design that often require significant optimization efforts to ensure manufacturability and geometric fidelity.

Measuring part tolerance and geometric accuracy is an important aspect of understanding part quality and evaluating manufacturability. Historically, the geometric accuracy of parts has been measured from two-dimensional (2D) cross sections at features of interest; this technique has been successfully used to complete complex part geometry investigations (Meyer et al., 2022). Through 2D measurement of part geometry, information concerning over-printing and under-printing of specific regions can be obtained. This is often how dross, or over-printing of down-skin surfaces, is measured. Over-printing and under-printing can also be measured volumetrically through analysis of the total part by weight, volume displacement, or X-ray computed tomography (XCT) images (Klingaa et al., 2019; Puttonen et al., 2020; Tanlak et al., 2017). While these techniques provide insight into the overall success of the manufactured part, there are few tools that include evaluation of localized over- and/or under-printing (Lozanovski et al., 2021).

Down-skin surfaces remain a difficult challenge for AM using LPBF, especially for complex interconnected lattice geometries where down-skin support is typically not feasible. The primary goal of this work is to develop digital evaluation tools to identify how and where down-skin surfaces are likely to fail within lattice structures produced through LPBF. This was completed by evaluating the angle, the degree of interconnectivity, and the surface area of down-skin surfaces within a lattice structure against outcomes from manufactured parts. To achieve this task, digital tools were developed to quantitatively assess manufacturability outcomes for different lattice types. Evaluation was done relative to down-skin characteristics by examining pore flaws and 3D geometric part divergence between ideal CAD and manufactured parts digitally reconstructed via XCT. It was hypothesized that down-skin characteristics such as surface area

and interconnectivity would correlate to geometric deviations in lattice structures produced through LPBF.

Following the evaluation of the maraging steel lattice structures, the manufacturability evaluation workflow was then applied to an example orthopaedic implant design featuring lattice structures. The orthopaedic implant was manufactured in Ti6Al4V in order to highlight the adaptability and applicability of the developed tool. The aim of the present work is to provide a new digital tool to better quantify the three-dimensional (3D) geometric fidelity of complex parts produced using AM at the design stage.

7.2 Methodology

7.2.1 Design and Evaluation of Lattice Structures

Seven unique homogeneous periodic lattices were designed to evaluate the effect of down-skin surface characteristics on manufacturability: face-centered cubic (FCC), body-centered cubic (BCC), graphical diamond, octet, TPMS gyroid, TPMS Schwarz, and TPMS diamond. The seven periodic lattice structures were designed using the nTopology software (nTopology Inc., New York, NY). Lattice geometries were used to fill a 20 × 20 × 20 mm cubic design space, with a homogeneous lattice. The wall thicknesses or strut thicknesses of CAD lattices were designed to be 1 mm thick, as shown in Fig. 7.1. For the seven periodic lattices, a unit cell size of 10 × 10 × 10 mm was used.

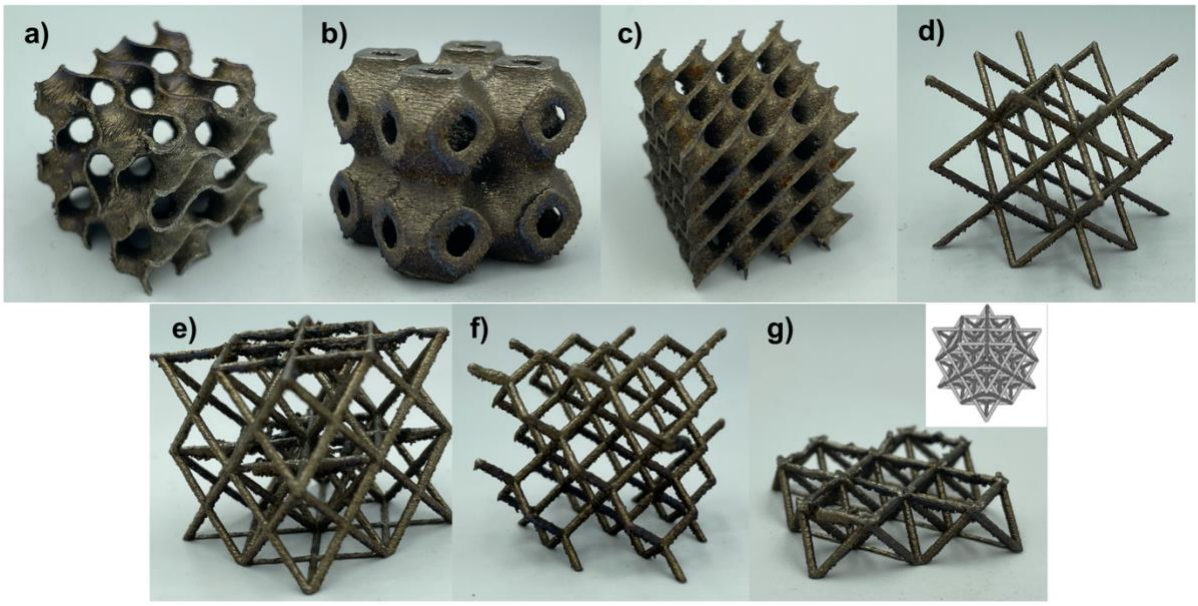


Figure 7.1 Seven unique homogenous lattice structures were printed using maraging steel through laser powder bed fusion (M290, EOS, Germany): (a) TPMS gyroid, (b) TPMS Schwarz, (c) TPMS diamond, (d) body-centered cubic, (e) face-centered cubic, (f) graphical diamond, and (g) octet (failed).

7.2.2 Evaluation of Down-skin

To further understand the impact of surface angle on the geometric fidelity of final parts, a custom Python software tool was developed using 3D Slicer (v.4.11) to determine localized surface angles from the CAD models of the different lattice types. 3D Slicer uses the open-source Visualization Toolkit (VTK) for polygonal representation of CAD models from STL files. Two VTK classes, namely vtkPolyDataNormals and vtkMath, were leveraged in the custom python script to determine the surface angle of individual polygon cell elements relative to a set normal plane (Flowchart in Appendix C). The normal plane in this case was set to match the LPBF build plate plane to determine the relative surface angle of polygon cells within the lattice structures. The calculated surface angles were then applied to each polygonal cell element as an associated scalar value.

With this approach, the normal plane, or build plate, has a unit normal of [0, 0, 1] in Cartesian coordinates. The angle between the auto-oriented (outward-facing) unit normal of each polygon cell and the build plate normal was calculated to obtain the surface angle of each triangular mesh element. To better visualize surface angles within the lattice structures, down-skin surfaces were discretized into 15-deg surface angle increments and assigned a color. The 15-deg discretization value was selected based on a balance between discretization of down-skin regions for visualization and analysis, prior manufacturability, and surface quality challenges reported in literature (Alrbaey et al., 2014; Covarrubias and Eshraghi et al., 2018; Tarakci et al., 2022; Zhang et al., 2019) and observed by the authors through experience. Within each 15-deg increment bin, up to 90-deg orientation, the total down-skin surface area and percentage of total down-skin surface per increment bin were calculated. Down-skin surfaces in contact with the build plate were excluded from surface area calculations, as these surfaces are supported during the LPBF manufacturing process and therefore do not pose the same challenges as unsupported down-skin surfaces.

7.2.3 Manufacturing and Evaluation of Manufacturability

The seven homogeneous lattice structures were manufactured with 18Ni-300 maraging steel (Böhler, Germany) using metal AM via LPBF (M290, EOS, Germany). The beam spot diameter of the EOS M290 LPBF system used was 90 μm, which was kept constant for the study. A hard recoater was utilized in this study. The maraging steel powders were gas atomized with a nominal particle size range of 15–43 μm. All the lattice structures were part of the same print. The LPBF print parameters were tailored for complex parts and thereby included different process parameters for the core, contour/border, down-skin, and up-skin based on a previously developed recipe for maraging steel and are summarized in Table 7.1. One contour was used for printing all

the lattice structures. If a given lattice was protruding above the powder bed before recoating the next layer of powder, this posed a potential risk of damage to the recoater and therefore raised edges on the build plate were used as visual inspection criteria.

Table 7.1 Summary of the LPBF print parameters for the nine lattice structures using 18Ni-300 maraging steel on EOS M290 that include core, contour, down-skin, and up-skin parameters.

Parameter	**Core**	**Contour[a]**	**Down-skin: core & contour[a]**	**Up-skin: core and contour[a]**
Power	370 W	321 W	100 W	325 W
Velocity	0.92 m/s	0.74 m/s	1 m/s	1 m/s
Hatch distance	0.1 mm	N/A	0.1 mm	0.1 mm
Beam offset	0.05 mm	0.05 mm	N/A	N/A
Hatch rotation	67 deg	N/A	90 deg	90 deg
Overlap with core	N/A	N/A	0.08 mm	0.08 mm
Strategy	Meander	N/A	Meander	Meander
Layer thickness	0.04 mm	N/A	4 Layers	2 Layers

[a] Note that contour is printed first and then the core.

7.2.3.1 Evaluation of part porosity

Following manufacturing, the nine lattice structures were removed from the LPBF build plate using electrodischarge machining (EDM) and were then imaged using an XCT scanner (ZEISS Xradia 520 Versa) for non-destructive evaluation of manufacturing outcomes. A voxel size of 30 μm was used for scanning each lattice structure, captured in a single field of view. An image processing software was used to complete porous flaw and geometric fidelity detection and visualization (Dragonfly 3.0, Object Research Systems Inc., Montreal, QC) and MATLAB (version 9.1). Lattice structures were imported into the imaging software and subjected to a greyscale threshold allowing for segmentation between the solid material and porous flaws. Segmentation results were then binarized, and resulting images were used to characterize porous flaws based on aspect ratio. Porous flaws with an aspect ratio greater than or equal to 0.7 were

considered rounded (spherical) flaws and porous flaws with an aspect ratio lesser than 0.7 were considered irregularly shaped flaws. The porous flaws within the XCT data volume were then highlighted through manual adjustment of brightness, contrast, and opacity. Boolean operators were used to compare the porous flaw to solid material ratio to determine overall print porosity.

7.2.3.2 Measurement of geometric accuracy

A voxel-based comparison method was used to assess the geometric fidelity of the printed parts compared to the original CAD models. The CAD design file for each lattice structure was segmented into a stack of black and white images, with a 30 μm voxel size to match the voxel size resolution from the XCT characterization. This allowed for the data to be represented as arrays of Boolean values, with the presence of material being denoted 1/white and material not present being denoted 0/black. A custom python script was then developed and employed to compare the CAD and XCT datasets voxel by voxel. Two measures of print inaccuracy were used: over-print and under-print. The over-print percentage was defined by the total number of voxels in which the XCT data returned material present, and the CAD geometry returned no material present, normalized by the total number of CAD voxels. Conversely, the under-print percentage was the number of voxels in which the CAD returned material present, but the XCT data did not, again normalized by total CAD volume. The under-print percentage includes the presence of pores, which are a contributing factor in assessing printability criteria. These metrics were evaluated both as a total value across the entire part and on a slice-by-slice basis (corresponding roughly to each print layer), in order to produce a more specific understanding of volumetric and local accuracy for the lattice structures. To obtain the layer-by-layer metrics, the over- and under-print values were normalized by the CAD volume for each layer.

7.2.3.3 Workflow adaptability for end-use product design

In addition to the maraging steel cubic lattice structures, two Ti6Al4V orthopaedic implant designs were manufactured on the same EOS M290 LPBF system using a set of previously optimized processing parameters (Patel et al., 2020). The two implants were also evaluated with the digital evaluation workflow to assess the adaptability of the workflow for industry applications. Additionally, the use of another material and a stochastic lattice design for these products helps determine the material and design independence of this workflow for LPBF. Both orthopaedic implants had the same outer geometry. However, the internal part was lightweighted with two different lattice structures: TPMS gyroid and Voronoi. The TPMS gyroid lattice was selected as it was successfully manufactured in the first stages of the study. The Voronoi lattice was selected for its novelty and ability to assess further potential of the digital evaluation workflow. Final implant designs are visualized in Fig. 7.8 in Sec. 7.3.2.1. Evaluation of the down-skin distribution, measurement of part porosity, and geometric accuracy were then performed for the orthopaedic implants to evaluate the adaptability and applicability of the digital evaluation workflow for end-use products.

7.3 Results

Only five of the seven lattice structures were considered to be successfully manufactured in maraging steel through LPBF. The BCC, graphical diamond, TPMS gyroid, TPMS Schwarz, and TPMS diamond all were successfully printed and were available for further evaluation. The FCC lattice was printed in full and was XCT imaged for analysis; however, it had significant part defects and was considered a print failure by visual inspection. The octet lattice structure suffered major print failures and was canceled during the LPBF printing process (Fig. 7.1). Therefore, it was omitted from the porous flaw and geometric accuracy analyses.

7.3.1.1 Evaluation of downskin surfaces

Further, the porosity fraction and actual mass to CAD mass estimation ratio for the six successfully manufactured homogeneous periodic lattice structures were determined. Porosity fraction was obtained through μCT imaging. The actual part mass of the final parts was measured with a micro resolution scale and compared to the estimation given by the nTopology software. The down-skin spatial distribution for the seven unique lattice structures was determined using the custom pipeline developed in Sec. 7.2.1. The down-skin angle for the surface of each lattice structure was discretized into 15-deg increments; the results of this discretization are shown in Fig. 7.2. The FCC and octet lattices had the highest percentage of down-skin surfaces with a surface angle below 30 deg with 11.07% and 11.47%, respectively, as visualized in Fig. 7.3.

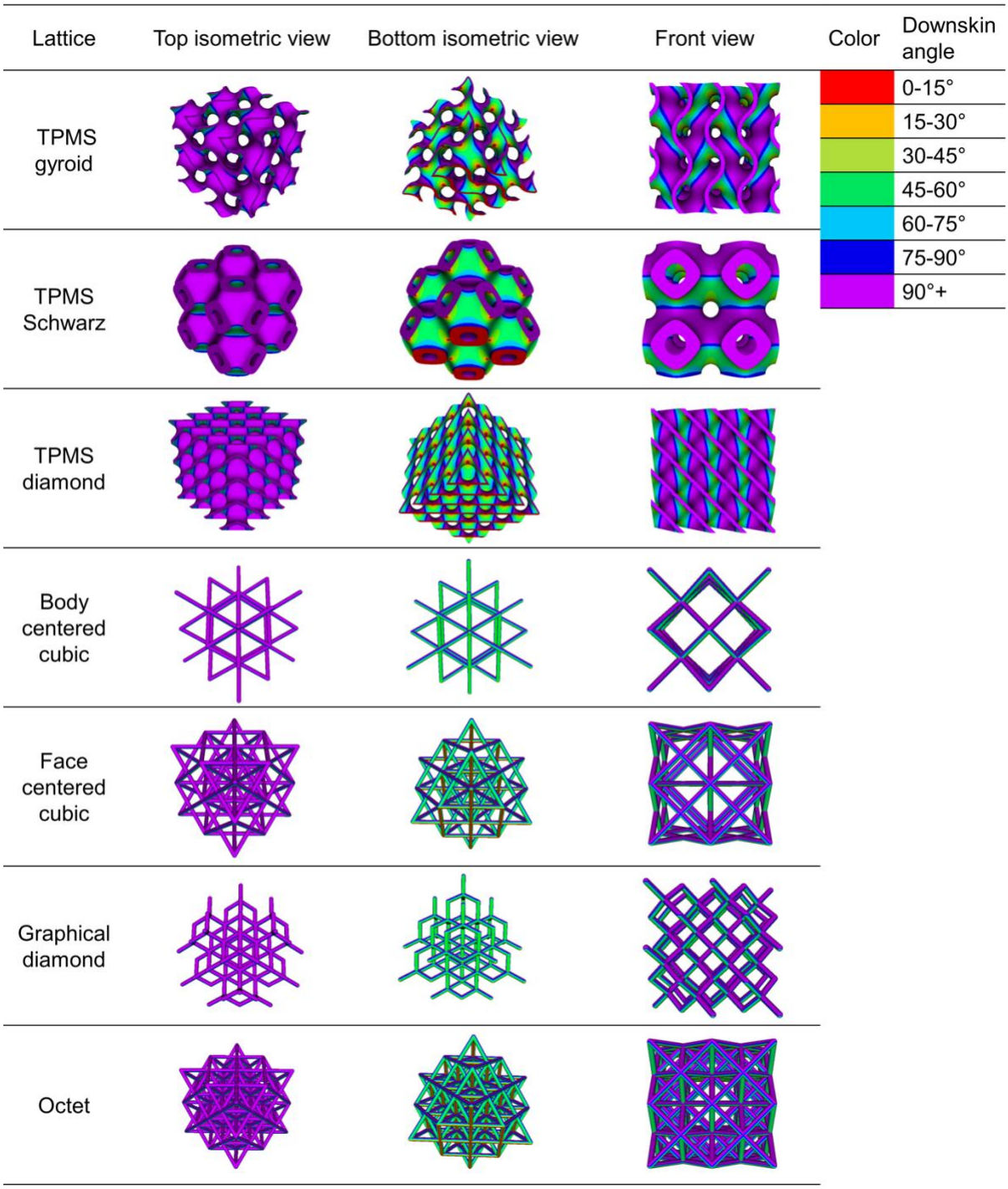


Figure 7.2 Seven unique homogeneous lattice structures were evaluated for down-skin regions ranging from 0 deg to 90 deg of down-skin in 15-deg increments: TPMS gyroid, TPMS Schwarz, TPMS diamond, body-centered cubic, face-centered cubic (partially failed), graphical diamond, and octet (failed).

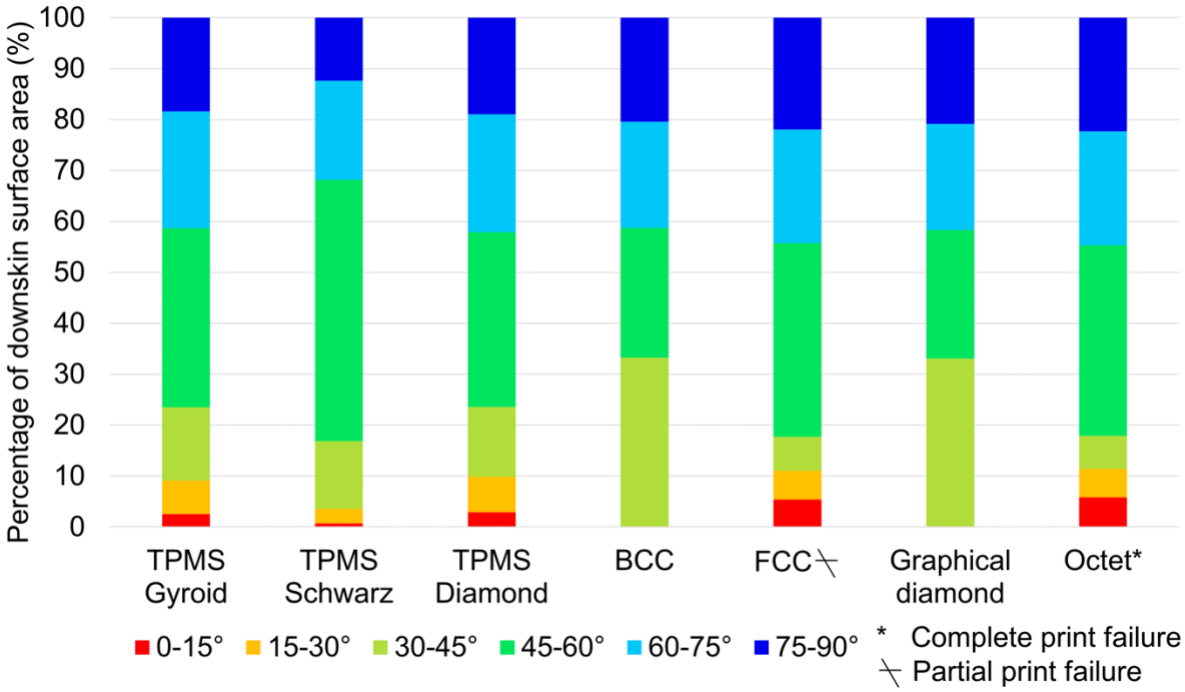


Figure 7.3 Down-skin distribution as determined using the custom 3D Slicer algorithm and discretized into 15o increments. Amongst the seven homogeneous lattice structures, FCC and octet lattices have the highest percentage of down-skin surfaces with an angle <30o at 11.07% and 11.47% respectively.

In addition, the interconnectivity of down-skin regions was examined to determine the number of discrete down-skin features with a surface angle between 0–15 deg. From this discrete down-skin feature calculation step, a down-skin ratio was defined in Eq. (7.1), which is given by the total surface area with a 0–15 deg surface angle divided by the number of discrete down-skin features with a surface angle of 0–15 deg to the build plate.

$$Down - skin\ ratio = \frac{Surface\ area\ with\ 0{-}15\ \mathrm{deg}\ surface\ angle}{Number\ of\ discrete\ down{-}skin\ features\ with\ 0{-}15\ deg} \quad (7.1)$$

The interconnectivity of down-skin surfaces with a down-skin angle between 0 deg and 15 deg was quantified by the down-skin ratio method. The down-skin ratio was calculated for all the lattice structures in Table 7.2. It was found that the lattice structures that printed successfully had a down-skin ratio of less than (<) 1, whereas lattice structures that failed to print had a down-skin

ratio greater than (>) 1. An illustration of the interconnectivity of such 0–15-deg down-skin surfaces is illustrated for select lattices as shown in Fig. 7.4.

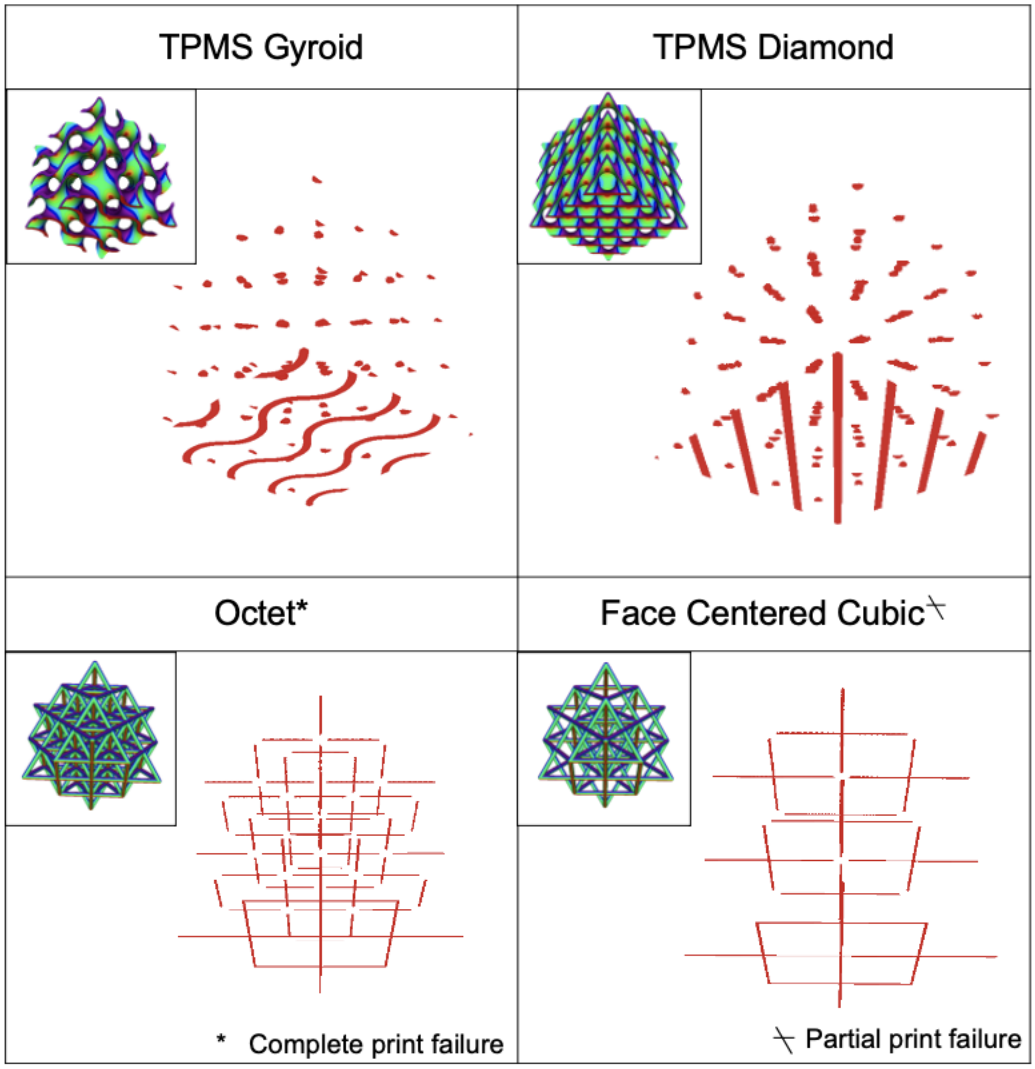


Figure 7.4 A bottom isometric view of the lattice down-skin is provided. Enlarged (1:3), discrete down-skin regions with an angle of 15 deg or less to the build plate (red) were isolated with the aim of better understanding the effect of down-skin area and interconnectivity of discrete down-skin features on printability challenges. Complete lattice structures with down-skin visualization were included for each lattice to provide context for the discrete down-skin regions. The discrete down-skin features for the TPMS gyroid (top left), TPMS diamond (top right), octet (bottom left), and face-centered cubic (bottom right) lattice structures are visualized above.

Table 7.2 Calculated values of the surface area of down-skin features, number of discrete down-skin features, and down-skin ratio for the seven homogeneous periodic lattice structures manufactured using LPBF in this study.

Lattice Structure	**Surface area of down-skin features <15 deg (mm^2)**	**Number of discrete down-skin features <15 deg**	**Down-skin ratio (mm^2/no of features)**
TPMS gyroid	64.2	80	0.78
TPMS Schwarz	12.1	48	0.25
TPMS diamond	89.5	128	0.70
BCC	0.54	9	0.06
FCC	82.1	65	1.26
Graphical diamond	0.78	13	0.06
Octet	119.0	9	13.22

7.3.2 Evaluation of Manufacturability

Porous flaw types, irregular or round, were also visualized. Few porous flaws were visible within the lattice structures, which may be attributed to the coarse resolution of the XCT. As an illustration, the XCT of the TPMS Schwarz lattice can be seen in Fig. 7.5, where irregular porous flaws are in blue and round porous flaws are in red. Those porous flaws present were clustered along the down-skin regions of the parts as previously shown by Shange et al. 2021. The qualitative pore visualization is further confirmation that porous flaws are closely related to the interplay between process parameters and the design in the down-skin region.

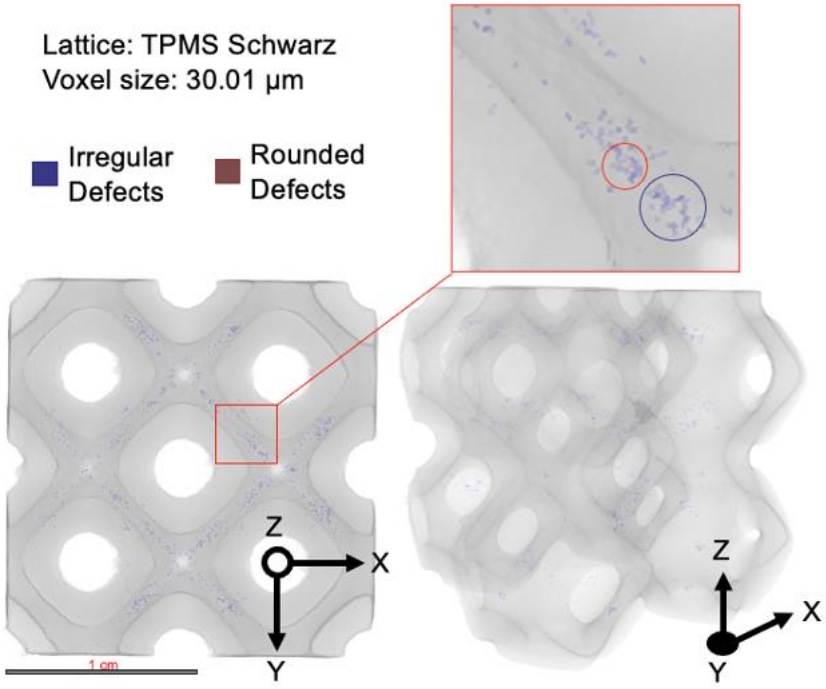


Figure 7.5 An X-ray computed tomography image of a maraging steel TPMS Schwarz lattice structure produced with laser powder bed fusion is visualized in frontal (left) and isometric (bottom right) views. An enlarged section (upper right) allows for visualization of irregular (blue) and round (red) porous defects to depict the prevalence and location.

The seven lattice structures that were printed to completion were analyzed based on the over-print and under-print metrics described in Sec. 7.2.3.2. The TPMS lattice structures printed more accurately to the design CAD than the strut-based lattices did, for both over-print volume and under-print volume, as captured in Table 7.3. In order to illustrate the relationship between surface angle and geometric print fidelity, the slice-by-slice over- and under-print data were aligned and compared. The TPMS gyroid and the FCC were used as examples from the surface-based and strut-based categories, respectively. Figure 7.6 shows that a small down-skin angle aligns with a peak in over-printing, while up-skin surfaces align with a peak in under-printing. These phenomena are more pronounced for the FCC lattice structure where large unsupported down-skin regions are present. The FCC lattice analysis shows two large spikes in layer over-print, which correspond to the areas of zero-deg down-skin angle. Significant dross formation is visible

on the superimposed XCT/CAD data, as seen in Fig. 7.6 and for the FCC lattice in particular. Layer-by-layer comparisons of the XCT and CAD data for the remaining four successfully printed homogeneous periodic lattice structures are provided in Appendix C.

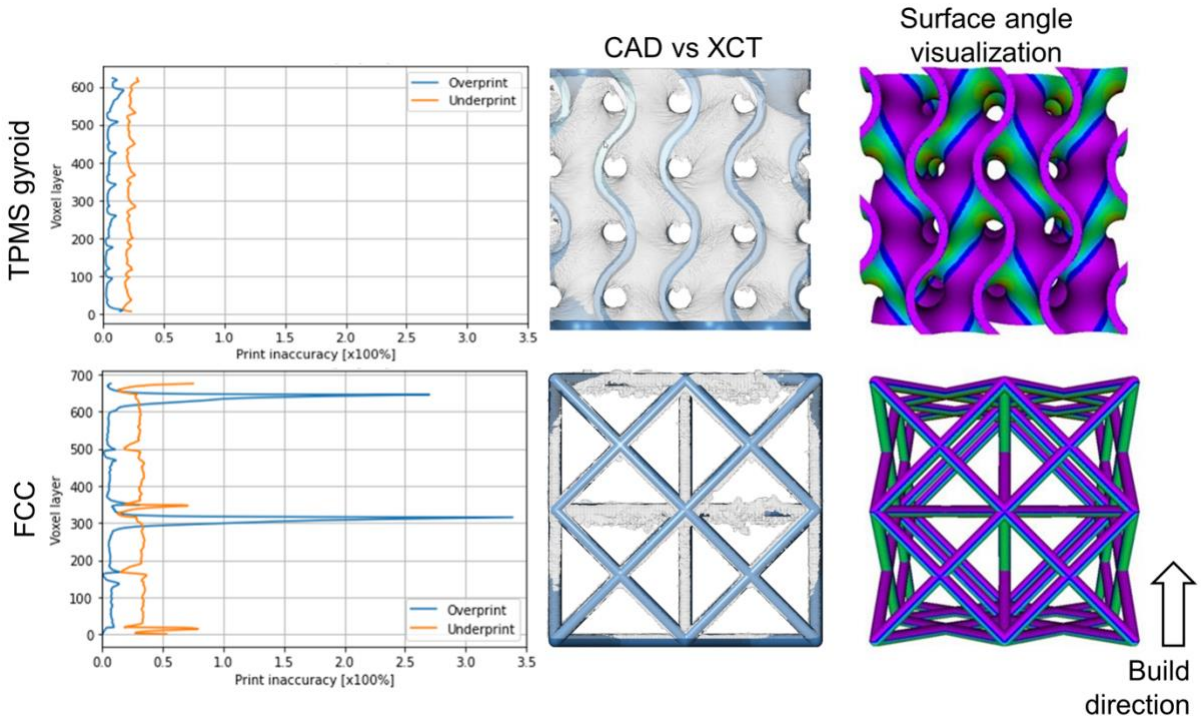


Figure 7.6 Surface-based lattices TPMS gyroid (top), were found to be more printable than strut-based lattices, FCC (bottom). The TPMS gyroid had 5.3% and 21.6% volumetric over- and under-print respectively, while the FCC had 16.0% and 31.3% (left). When aligning quantitative values for over-print and under-print to X-ray computed tomography (XCT; middle) and surface angle (right), a clear association between down-skin surfaces and poor print quality becomes apparent.

Table 7.3 Total volumetric over-print and under-print evaluation using the CAD and XCT data of the eight successfully manufactured structures

Lattice structure	**Percent volume over-print (%)**	**Percent volume under-print (%)**
TPMS Gyroid	5.3	21.6
TPMS Schwarz	2.7	11.3
TPMS Diamond	5.2	21.7
BCC	7.5	32.4
FCC	16.0	31.3
Graphical Diamond	8.9	32.6
Interbody cage: gyroid	21.3	8.5
Interbody cage: Voronoi	30.2	13.0

To further understand the effect of the down-skin ratio on the manufacturability of the various lattice structures, Table 7.4 and Fig. 7.7 provide a comparison of the average over-print and under-print between the CAD and XCT for all the eight successfully manufactured structures, with standard deviations provided for the slice-by-slice comparisons.

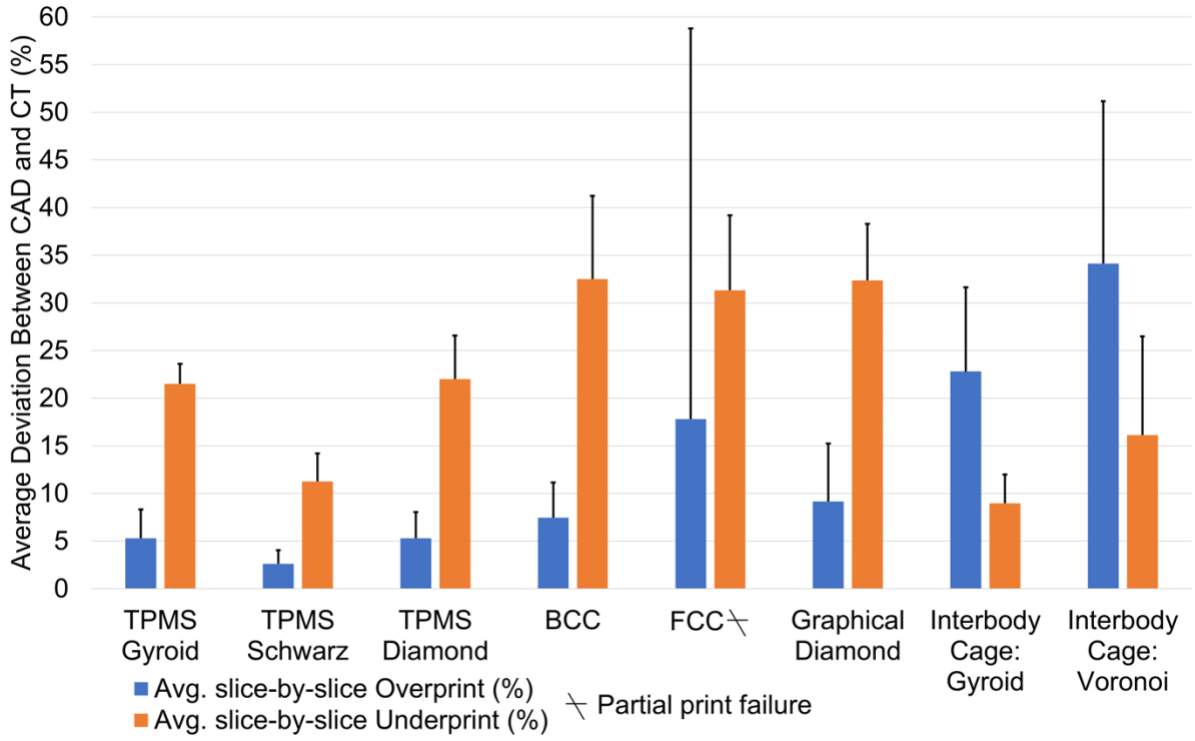


Figure 7.7 Average and standard deviations for volumetric over-print and under-print from slice-by-slice comparisons of the CAD and XCT data of the eight successfully manufactured structures

Table 7.4 Porosity fraction (of the CAD designs) and mass ratio (actual mass/CAD mass) for the six homogeneous periodic lattice structures manufactured to completion

Lattice Structure	**Porosity fraction of CAD (%)**	**Ratio of actual mass (from XCT) over CAD mass (%)**
TPMS Gyroid	80.66	83.76
TPMS Schwarz	65.7	91.35
TPMS Diamond	76.82	83.51
BCC	94.89	75.23
FCC	90.81	84.62
Graphical diamond	94.88	76.27

7.3.2.1 Example applicability to an industrial application

The two orthopaedic implant designs had a greater percentage of total down-skin surface area under 15 deg with respect to the build plate orientation when compared to most of the cubic lattice structures previously examined (as seen in Fig. 7.8 (left)); however, they were considered manufacturable due to the large distribution of small discrete down-skin regions throughout the part, as indicated by a down-skin ratio of less than one (<1) and illustrated in Fig. 7.8 (right). Layer-by-layer comparisons of the XCT and CAD data for the two implant structures are provided in (Appendix C) which shows the successful manufacturing of the two implant designs. From this, it was seen that the down-skin ratio may help evaluate manufacturability in the design phase. However, it remains important to take other design considerations into account such as the shape of discrete down-skin regions, wall or strut thickness, and aspect ratios to further ensure part manufacturability.

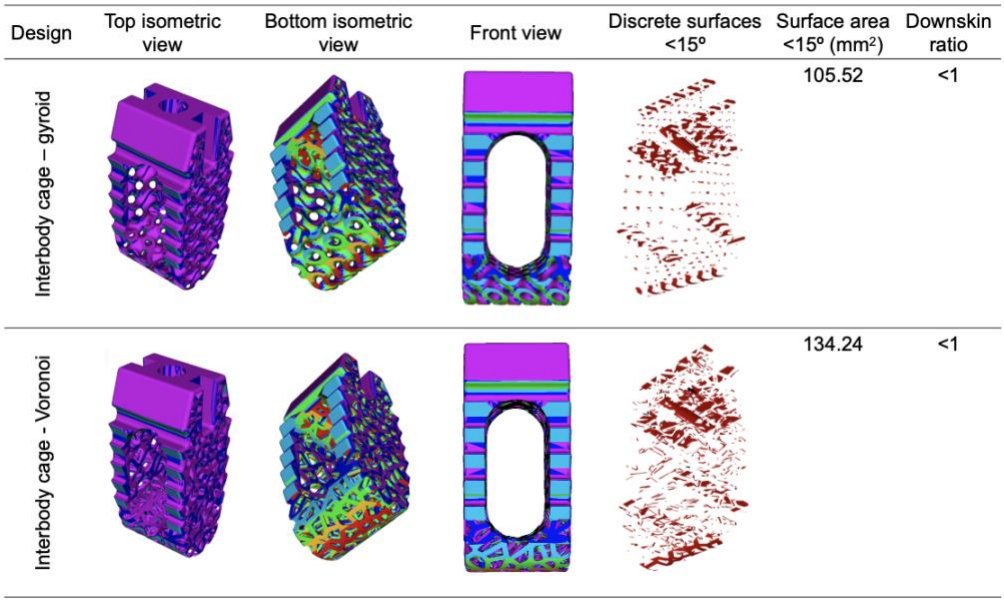


Figure 7.8 Down-skin distribution within the complete orthopaedic implant parts was determined using a custom algorithm and discretized into 15-deg increments. Distribution for the TMPS gyroid and Voronoi cubic designs were included for comparison. The two lightweighted orthopaedic implants were then evaluated for down-skin regions ranging from 0 deg to 90 deg of down-skin in 15-deg increments

7.4 Discussion

Lattice type was the first factor taken into consideration when examining the overall manufacturability of complex lattice architectures with respect to the down-skin surface areas. Comparing the strut-based lattices, the FCC and octet strut-based lattices have long struts whose central axis runs parallel to the build plate, unlike BCC and graphical diamond lattices, where strut elements are at a minimum of 45 deg to the build plate. This leads to a significant amount of challenging down-skin surfaces with a surface angle below 15 deg in the FCC and octet as evident in Fig. 7.4. Surface features that were parallel to and touching the build plate were excluded from the analysis. Excluding the failed FCC and octet lattices, the TPMS diamond and TPMS gyroid have the highest percentage of down-skin between 0 and 30 deg, as shown in Fig. 7.3. However, TPMS lattices (gyroid, diamond, and Schwarz) also have a significant amount of surface area touching the build plate and are all successfully manufactured using LPBF. This could be associated with the improved heat transfer to the solid metal on the LPBF build plate, when compared to printing on a powder bed which is known to have significantly lower thermal conductivity (Wei et al., 2018) and density (Wischeropp et al., 2019).

The distribution of down-skin features (unsupported down-skin surfaces between 0 deg and 15 deg) was also found to have an effect on the manufacturability of complex architectures. The TPMS gyroid lattice structure had 80 discrete features with a consistent surface angle between 0 deg and 15 deg. Similarly, the TPMS diamond had 128 discrete features with a consistent surface angle between 0 deg and 15 deg. However, the overall surface area for these discrete down-skin features was relatively small for these lattice types, leading to a down-skin ratio of 0.78 and 0.70 for the TPMS gyroid and TPMS diamond, respectively. The regions of interest in both lattices exhibit saddle-like geometry which has been shown to be suitable for additive manufacturing

(Adam et al., 2014; Jones et al., 2021). The FCC and octet lattices had fewer but larger discrete down-skin features between 0 deg and 15 deg leading to a down-skin ratio of 13.22 and 1.26, respectively. These regions are not saddle-shaped and are located at the underside of struts, which are parallel to the build plate. A large surface area of unsupported down-skin features (0–15 deg) likely contributes to manufacturability challenges for the FCC and octet lattice structures. It is known that stress accumulation occurs as the surface area of a given discrete region increases, thereby increasing the risk of defects (Yeung et al., 2019). Therefore, the down-skin ratio term proposed in this work may be a useful tool in digitally evaluating part manufacturability using AM as it provides a more comprehensive characterization of down-skin surfaces. A known limitation of this workflow is the lack of consideration for "knife edge" features. These features would be captured as one discrete down-skin feature, thereby lowering the down-skin ratio. However, the small surface area associated with knife edge features would act to decrease the down-skin ratio. This relationship between low surface area for singular down-skin features with respect to the performance of the down-skin ratio is unknown and should be considered in future work.

As expected, among the homogeneous periodic lattice structures that printed, the FCC lattice structure exhibits the highest average as well as the highest standard deviation in terms of over-printing when the CAD and XCT data are compared. The high standard deviation, in particular, is related to the two large down-skin (0–15 deg) features of the lattice structure that are shown to have a volumetric over-print of ~330% in the printed part as shown in Fig. 7.6. These down-skin features within the FCC lattice structure are effectively parallel to the LPBF build plate which would typically require support structures for improving thermal conductivity (Zhang et al., 2020), reducing part deformation (Khobzi et al., 2022), and preventing dross formation (Charles et al., 2021) in LPBF.

A relatively large volumetric under-print is observed in all of the homogeneous periodic lattice structures (Table 7.3 and Fig. 7.7). For the TPMS lattices, the total volumetric under-print is between 11.3% and 21.7% as shown in Table 7.3. For the strut-based lattices, the total volumetric under-print is significantly higher when compared to the TPMS lattices (31.3–32.6%, as shown in Table 3). Overall, all lattices did under-print when compared to the designed CAD (75–91%), as shown by the ratio of the actual mass from XCT data to the CAD mass in Table 7.4. The under-printing observed in all lattices can be partly explained by shrinkage caused by the melting of porous powder followed by rapid solidification in LPBF and has been reported for TPMS lattices in literature (Echeta et al., 2020; Mulhi et al., 2022). Additionally, laser power, scanning speed, layer thickness (Liu et al., 2017), and build plate location of a given part (Veetil et al., 2021) are other factors that could have effects on shrinkage (Liu et al., 2017).

Layer-by-layer specimen geometry is known to have significant effects on shrinkage as well (Chahal et al., 2020) since it would directly influence the boundary conditions for the following layer, in the sense of whether or not a given feature in the current layer is supported by solidified metal or the powder bed, both of which have significantly different thermal conductivity values (Wei et al., 2018). Porosity fraction for the surface-based (TPMS) and strut-based lattice designs in Table 7.4 can help understand the expected differences in layer-by-layer geometry. In Table 7.4, the porosity fraction of a given lattice structure design is calculated as 1—Volume fraction, wherein volume fraction denotes the volume of the lattice structure CAD divided by the volume of the solid cube model ($20 \times 20 \times 20$ mm^3). The porosity fractions of all strut-based lattice designs are >90% whereas the porosity fractions of all surface-based (TPMS) lattice designs are between 65–80%. The higher porosity fraction in strut-based lattice designs would mean that there is a higher probability that for a given feature in a given layer, the underlying boundary conditions

are more likely to be driven by the poor thermal conductivity powder bed for strut-based lattices when compared to the surface-based lattices. A powder bed-driven boundary condition would mean that for strut-based lattices, the melted portions of a given layer would also be on a relatively low-density powder bed. This would lead to a higher volumetric over-print due to dross formation, as well as under-print due to shrinkage and potential distortion of the down-skin features due to poor thermal conductivity of the powder bed (Zhang et al., 2022). A higher porosity fraction in strut-based lattice designs, as shown in Table 7.4 is thereby expected to cause the high volumetric under-print and over-print observed in Fig. 7.7 and Table 7.3, as also reported by Taib et al. 2016. It must be noted that imperfect alignment of the XCT and CAD datasets during analysis could also lead to some of the under-print and over-print values observed in this study.

An additional two orthopaedic implant designs were evaluated to assess the adaptability of the proposed digital workflow for biomedical applications. Two orthopaedic implant designs were light- weighted with either a periodic TPMS lattice structure (gyroid) or a stochastic Voronoi lattice structure and manufactured in Ti6Al4V. Both the implant designs have a down-skin ratio <1 as shown in Fig. 8, and both implants did print successfully. Both implants, however, have a higher volumetric over-print when compared to the successfully printed homogeneous lattice structures (except the FCC, which is considered a partial failure, and has the highest volumetric over-print when the standard deviation is considered, as shown in Fig. 7.7). The higher over-print for the implant designs is partly related to the use of support structures at the bottom of the implants during prints, which could not be completely removed during the XCT versus CAD analysis. Additionally, an exact alignment of the highly complex implant designs to the XCT dataset is challenging, which could add to inaccuracies in the reported under-print and over-print values for the two designs. Regardless, the trend of the surface-based (TPMS) lattice design is seen to again

outperform a strut-based stochastic Voronoi lattice design, in terms of both volumetric under-printing and over-printing.

While existing AM software, like Magics by Materialise (Belgium), has features to identify and calculate down-skin surfaces, the algorithms used in these commercial software packages are often a black box with few details available. The present digital workflow acts to liberate this information through a stand-alone python script that can apply metadata to individual mesh elements of STL files. This approach to harvesting and assigning metadata opens for future applications including utilizing data for machine learning and topology optimization pathways. The current down-skin ratio may act as a rule of thumb for the manufacturability of lattices and complex parts. Further, the present study is an important step toward developing predictive machine learning models that allow for accurate estimations of final manufactured parts from preliminary CAD.

The current study thereby presents a novel approach to quantify and validate the relationship between down-skin surfaces for a given design and manufacturability of the designs manufactured using LPBF. The down-skin surface of multiple lattice types was evaluated using an image processing workflow to develop the down-skin ratio term as a means to quantify the printability of a given design. In this work, designs with down-skin ratios lesser than one are expected to print successfully with high dimensional fidelity between the CAD and printed coupons. This approach would help reduce the transition from design ideas to successful prints in LPBF.

7.5 Conclusions

The current study presents a novel digital evaluation workflow to determine the surface area and nature of down-skin regions on complex interconnected parts as well as a new approach

for evaluating geometric fidelity as a function of volumetric over- and under-printing. Seven unique lattice structures were generated for down-skin evaluation. Six lattice structures were successfully manufactured in maraging steel and evaluated for the relationship between down-skin and geometric fidelity. A higher percentage of down-skin surface area with a surface angle of 15 deg or less and a down-skin ratio greater than one were indicators of poor geometric fidelity in the final parts. While down-skin evaluation is known to improve final part geometries, by characterizing the complex 3D interconnectivity of lattice structures, the robustness of the digital workflow was exhibited. The workflow was successfully applied to orthopaedic designs manufactured in Ti6Al4V to validate the adaptability to complex part geometries outside of individual unit cells. The use of multiple materials, marging steel and Ti–6Al–4V, strengthens the adaptability of the digital evaluation workflow by exhibiting that the down-skin ratio parameter is material agnostic, assuming pre-established print parameters for a given material. A known limitation exists with respect to evaluating the manufacturability of knife edge features and future work should look to address this challenge. These tools aim to assist in the evaluation of designs for manufacturability as well as serve to evaluate the success of final 3D printed parts using LPBF.

7.6 References

Adam, G.A., Zimmer, D. 2014. Design for additive manufacturing—element transitions and aggregated structures. *CIRP Journal of Manufacturing Science and Technology*, 7(1), 20-28.

Almalki, A., Downing, D., Noronha, J., Dash, J., Lozanovski, B., Tino, R., Alghamdi, A., Khorasani, M., Qian, M., Brandt, M. et al. 2023. The effect of geometric design and materials on section properties of additively manufactured lattice elements. *The International Journal of Advanced Manufacturing Technology*, 126(7-8), 3555-3577.

Ashby, A., Guss, G., Ganeriwala, R.K., Martin, A.A., DePond, P.J., Deane, D.J., Matthews, M.J., Druzgalski, C.L. 2022. Thermal history and high-speed optical imaging of overhang structures during laser powder bed fusion: A computational and experimental analysis. *Additive Manufacturing*, 53, 102669.

Boccini, E., Furferi, R., Governi, L., Meli, E., Ridolfi, A., Rindi, A., Volpe, Y. 2019. Toward the integration of lattice structure-based topology optimization and additive manufacturing for the design of turbomachinery components. *Advances in Mechanical Engineering*, 11(8), 1687814019859789.

Cabanettes, F., Joubert, A., Chardon, G., Dumas, V., Rech, J., Grosjean, C., Dimkovski, Z. 2018. Topography of as-built surfaces generated in metal additive manufacturing: A multi-scale analysis from form to roughness. *Precision Engineering*, 52, 249-265.

Calignano, F. 2014. Design optimization of supports for overhanging structures in aluminum and titanium alloys by selective laser melting. *Materials & Design*, 64, 203-213.

Charles, A., Elkaseer, A., Paggi, U., Thijs, L., Hagenmeyer, V., Scholz, S. 2021. Down-facing surfaces in laser powder bed fusion of Ti6Al4V: Effect of dross formation on dimensional accuracy and surface texture. *Additive Manufacturing*, 46, 102148.

Chahal, V., Taylor, R.M. 2020. A review of geometric sensitivities in laser metal 3D printing. *Virtual and Physical Prototyping*, 15(2), 227-241.

Chen, H., Gu, D., Xiong, J., Xia, M. 2017. Improving additive manufacturing processability of hard-to-process overhanging structures by selective laser melting. *Journal of Materials Processing Technology*, 250, 99-108.

Covarrubias, E.E., Eshraghi, M. 2018. Effect of build angle on surface properties of nickel superalloys processed by selective laser melting. *JOM*, 70, 336-342.

Dong, G., Tang, Y., Zhao, Y.F. 2017. A survey of modeling of lattice structures fabricated by additive manufacturing. *Journal of Mechanical Design*, 139(10), 100906.

du Plessis, A., Razavi, S.M.J., Benedetti, M., Murchio, S., Leary, M., Watson, M., Bhate, D., Berto, F. 2021. Properties and applications of additively manufactured metallic cellular materials: A review. *Progress in Materials Science*, 100918.

Echeta, I., Feng, X., Dutton, B., Leach, R., Piano, S. 2020. Review of defects in lattice structures manufactured by powder bed fusion. *The International Journal of Advanced Manufacturing Technology*, 106, 2649-2668.

Fox, J.C., Moylan, S.P., Lane, B.M. 2016. Effect of process parameters on the surface roughness of overhanging structures in laser powder bed fusion additive manufacturing. *Procedia CIRP*, 45, 131-134.

Gardan, J. 2019. Smart materials in additive manufacturing: State of the art and trends. *Virtual and Physical Prototyping*, 14(1), 1-18.

Jones, A., Leary, M., Bateman, S., Easton, M. 2021. Effect of surface geometry on laser powder bed fusion defects. *Journal of Materials Processing Technology*, 296, 117179.

Khobzi, A., Mehr, F.F., Cockcroft, S., Maijer, D., Sing, S.L., Yeong, W.Y. 2022. The role of block-type support structure design on the thermal field and deformation in components fabricated by laser powder bed fusion. *Additive Manufacturing*, 51, 102644.

Klingaa, C.G., Bjerre, M.K., Baier, S., De Chiffre, L., Mohanty, S., Hattel, J.H. 2019. Roughness investigation of SLM manufactured conformal cooling channels using X-ray computed tomography. *Proceedings of the 9th Conference on Industrial Computed Tomography (ICT 2019), Padova, Italy*, 13-15.

Liu, Y., Yang, Y., Wang, D. 2017. Investigation into the shrinkage in Z-direction of components manufactured by selective laser melting (SLM). *The International Journal of Advanced Manufacturing Technology*, 90, 2913-2923.

Lozanovski, B., Downing, D., Tino, R., Tran, P., Shidid, D., Emmelmann, C., Qian, M., Choong, P., Brandt, M., Leary, M. 2021. Image-based geometrical characterization of nodes in additively manufactured lattice structures. *3D Printing and Additive Manufacturing*, 8(1), 51-68.

McGregor, M., Patel, S., McLachlin, S., Vlasea, M. 2021. Architectural bone parameters and the relationship to titanium lattice design for powder bed fusion additive manufacturing. *Additive Manufacturing*, 47, 102273.

Mercelis, P., Kruth, J.-P. 2006. Residual stresses in selective laser sintering and selective laser melting. *Rapid Prototyping Journal*.

Meyer, G., Musekamp, J., Göbel, F., Gardian, F., Mittelstedt, C. 2022. Manufacturability investigation of inclined AlSi10Mg lattice struts by means of selective laser melting. *Manufacturing Letters*, 31, 101-105.

Mulhi, A., Dehgahi, S., Waghmare, P., Qureshi, A. 2022. Dimensional assessment of uniformly periodic porosity primitive TPMS lattices using additive manufacturing laser powder bed fusion technique. *The International Journal of Advanced Manufacturing Technology*, 1-22.

Patel, S., McGregor, M., McLachlin, S., Vlasea, M. 2021. Digital manufacturing challenge: Rapid deployment of patient-specific prosthesis in emergency medicine enabled by additive manufacturing. *Manufacturing Engineering*, 116(12), 9-11.

Patel, S., Rogalsky, A., Vlasea, M. 2020. Towards understanding side-skin surface characteristics in laser powder bed fusion. *Journal of Materials Research*, 35(15), 2055-2064.

Puttonen, T. 2020. Evaluation of metal lattice structures with X-ray micro-computed tomography: Dimensional accuracy and manufacturability. *ASME International Mechanical Engineering Congress and Exposition*, 84539, V006T06A015.

Rosen, D.W. 2014. Research supporting principles for design for additive manufacturing: A comprehensive review on current design principles and strategies for AM. *Virtual and Physical Prototyping*, 9(4), 225-232.

Sames, W.J., List, F., Pannala, S., Dehoff, R.R., Babu, S.S. 2016. The metallurgy and processing science of metal additive manufacturing. *International Materials Reviews*, 61(5), 315-360.

Shange, M., Yadroitsava, I., du Plessis, A., Yadroitsev, I. 2021. Roughness and near-surface porosity of unsupported overhangs produced by high-speed laser powder bed fusion. *3D Printing and Additive Manufacturing*.

Sing, S.L., An, J., Yeong, W.Y., Wiria, F.E. 2016. Laser and electron-beam powder-bed additive manufacturing of metallic implants: A review on processes, materials and designs. *Journal of Orthopaedic Research*, 34(3), 369-385.

Taib, Z.M., Harun, W.S.W., Ghani, S.A.C., Rashid, M., Omar, M.A., Ramli, H. 2016. Dimensional accuracy study of open cellular structure CoCrMo alloy fabricated by selective laser melting process. *Advanced Materials Research*, 1133, 280.

Tanlak, N., de Lange, D.F., Van Paepegem, W. 2017. Numerical prediction of the printable density range of lattice structures for additive manufacturing. *Materials & Design*, 133, 549-558.

Tarakçı, G., Khan, H.M., Yılmaz, M.S., Özer, G. 2022. Effect of building orientations and heat treatments on AlSi10Mg alloy fabricated by selective laser melting: Microstructure evolution, mechanical properties, fracture mechanism, and corrosion behavior. *Rapid Prototyping Journal*, 28(8), 1609-1621.

Triantaphyllou, A., Giusca, C.L., Macaulay, G.D., Roerig, F., Hoebel, M., Leach, R.K., Tomita, B., Milne, K.A. 2015. Surface texture measurement for additive manufacturing. *Surface Topography: Metrology and Properties*, 3(2), 024002.

Veetil, J.K., Khorasani, M., Ghasemi, A., Rolfe, B., Vrooijink, I., Van Beurden, K., Moes, S., Gibson, I. 2021. Build position-based dimensional deviations of laser powder-bed fusion of stainless steel 316L. *Precision Engineering*, 67, 58-68.

Viale, V., Stavridis, J., Salmi, A., Bondioli, F., Saboori, A. 2022. Optimisation of downskin parameters to produce metallic parts via laser powder bed fusion process: An overview. *The International Journal of Advanced Manufacturing Technology*, 1-24.

Wadley, H.N. 2006. Multifunctional periodic cellular metals. *Philosophical Transactions of the Royal Society A: Mathematical, Physical and Engineering Sciences*, 364(1838), 31-68.

Wang, D., Yang, Y., Yi, Z., Su, X. 2013. Research on the fabricating quality optimization of the overhanging surface in SLM process. *The International Journal of Advanced Manufacturing Technology*, 65(9), 1471-1484.

Wei, L.C., Ehrlich, L.E., Powell-Palm, M.J., Montgomery, C., Beuth, J., Malen, J.A. 2018. Thermal conductivity of metal powders for powder bed additive manufacturing. *Additive Manufacturing*, 21, 201-208.

Wischeropp, T.M., Emmelmann, C., Brandt, M., Pateras, A. 2019. Measurement of actual powder layer height and packing density in a single layer in selective laser melting. *Additive Manufacturing*, 28, 176-183.

Yeung, H., Lane, B., Fox, J. 2019. Part geometry and conduction-based laser power control for powder bed fusion additive manufacturing. *Additive Manufacturing*, 30, 100844.

Zhang, C., Wang, S., Li, J., Zhu, Y., Yang, H. 2020. Additive manufacturing of products with functional fluid channels: A review. *Additive Manufacturing*, 36, 101490.

Zhang, J., Chaudhari, A., Wang, H. 2019. Surface quality and material removal in magnetic abrasive finishing of selective laser melted 316L stainless steel. *Journal of Manufacturing Processes*, 45, 710-719.

Zhang, L., Li, Y., Zhu, H. 2022. Prediction and optimization of dimensional accuracy of inclined structures fabricated by laser powder bed fusion. *Journal of Manufacturing Processes*, 81, 281-289.

Zhang, Z.-D., Ibhadode, O., Ali, U., Dibia, C.F., Rahnama, P., Bonakdar, A., Toyserkani, E. 2020. Topology optimization parallel-computing framework based on the inherent strain method for support structure design in laser powder-bed fusion additive manufacturing. *International Journal of Mechanics and Materials in Design*, 16, 897-923.

Chapter 8- Design and Manufacturability of Anatomically-Optimized Spinal Implants using Laser Powder Bed Fusion Additive Manufacturing [5]

8.1 Background Rationale for Design

Laser powder bed fusion (LPBF) is a metal additive manufacturing (AM) technology which enables the realization of latticed or porous structures, valuable in improving osseointegration and compliance in orthopaedic implants (Arabnejad et al., 2017; Choy et al., 2017; Kim et al., 2017; Mobbs et al., 2017; Phan et al., 2016). The introduction of increased implant compliance through design for additive manufacturing (DfAM) methods like light-weighting has been previously shown to decrease risk of interbody cage subsidence in spinal implant testing (Kumar et al., 2022; Liu et al., 2018; Moolman et al., 2023). Additionally, patient-specific cages have shown promise in decreasing stress concentrations at the bone-cage interface and subsequently reducing subsidence risk (Fernandes et al., 2024, 2022). Previous work described in Chapters 6 established the relationship between lattice AM design parameters such as pore size, feature thickness, lattice type, and lattice porosity relative to the compressive mechanical properties of human bone tissues (McGregor et al., 2021). Further, Chapter 7 aimed at investigating the manufacturability of various lattice structures which can be leveraged for design in orthopaedic applications (McGregor et al., 2024). While this data provides helpful guidance for implant design, it has not yet been translated into design for optimized compliance, anatomical fit and manufacturability of latticed spinal implant designs. The goal of this investigation was to: (1) design and manufacture multiple lumbar interbody cages that incorporate tailored lattice structures

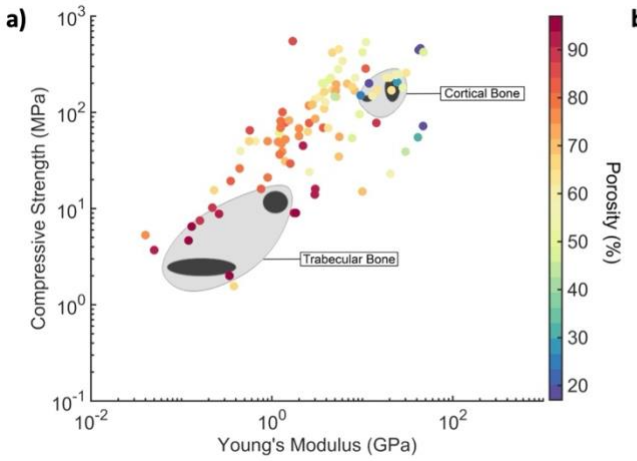
[5] A version of this chapter was published in conference proceedings as: McGregor ME; Vlasea ML; McLachlin SD; Design and Manufacturability of Compliant and Anatomically Optimized Spinal Implants. *High scoring abstract. Proceedings of the 2024 meeting of the International Society for Technology in Arthroplasty

to improve compliance and anatomical fit, and (2) evaluate manufacturability of the custom interbody cage designs.

8.2 Decisions for Interbody Cage Design

The initial geometry for a lumbar interbody cage implant was reverse engineered using computer assisted design (CAD) software. Data for lumbar endplate geometries was attained from literature, and the implant geometry was tailored for better sagittal endplate conformance (Lakshmanan et al., 2012). Further, ultimate compressive strength of human lumbar endplates was attained from literature and a pre-established design tool was used to determine the appropriate corresponding titanium lattice porosities (Lowe et al., 2004; McGregor et al., 2021), Figure 8.1.

Three cage geometries were generated; two different tapers were added to the implant height, a smaller 7 to 9 mm taper and a second, larger 9 to 11 mm taper to account for variation in the sagittal curvature of the endplate, as well as a third design based on a traditional straight cage, Figure 8.2. Lattice structures were applied to the medial, lateral, anterior and posterior regions of the implant geometry based on the endplate ultimate compressive strength using nTopology software (nTop, New York, NY, USA), Figure 8.3. Designed lattice porosity ranged from 40% (posterior), 50% (medial), 60% (anterior) and 70% (lateral). Implants had one of two lattice types: triply periodic minimal surface (TPMS) gyroid, superior for osseointegration, or stochastic Voronoi, for increased compliance, Figure 8.4. Voronoi lattices have known manufacturability challenges in LPBF AM due to the unpredictable down-skin surfaces presented. Final lumbar cage designs were manufactured in a Ti6Al4V alloy through LPBF. Print parameters for manufacturing can be found in Appendix X. Manufacturability was evaluated through slice-by-slice comparison of the original CAD and post-manufacture micro-computed tomography (mCT) scans (Xradia 520 Versa, Zeiss), as established in Chapter 7 (McGregor et al., 2024).



b)

Endplate Region	Correlating Porosity
Posterolateral (PL)	40%
Anterolateral (AL)	60%
Lateral (L)	50%
Central (C)	70%
Posterocentral (PC)	65%
Anterocetral (AC)	60%

Figure 8.1. (a) A pre-established design tool was leveraged to determine which titanium lattice porosities would best match endplate compressive properties would best match endplate compressive properties while maintain manufacturability (McGregor et al., 2021). (b) Titanium lattice porosity for lumbar cage designs varied from 40% at the posterior endplate to 70% at the central endplate.

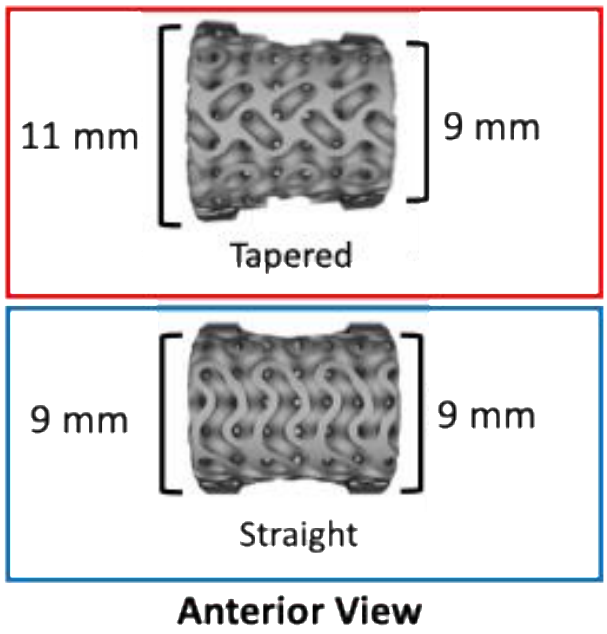


Figure 8.2. Three different cage geometries were designed, including two variations (small and large) of tapered cages (top) and a straight cage design (bottom).

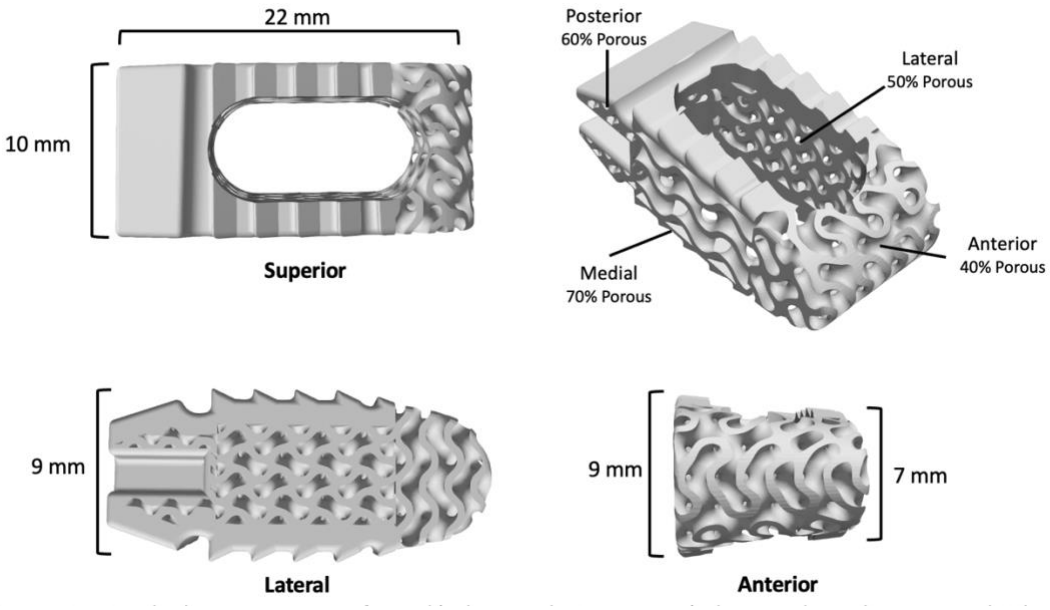


Figure 8.3. Six unique lumbar cages were manufactured (3 shapes x 2 lattice structures). The tapered cages have a greater height medially than laterally to account for the sagittal curvature of the endplate. The 9 mm to 7 mm tapered cage design with gyroid lattice structure is depicted in detail above.

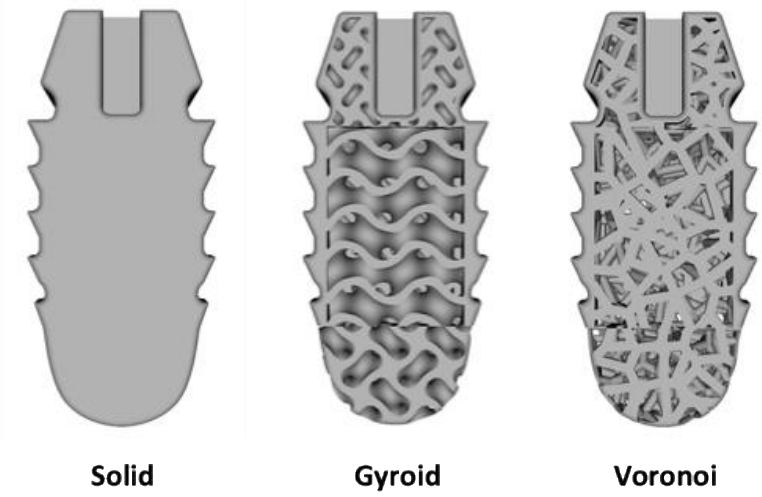


Figure 8.4. Solid cages, as well as cages light-weighted with either a triply periodic minimal surface gyroid, or stochastic Voronoi lattice structures were manufactured in Ti6Al4V alloy through laser powder bed fusion additive manufacturing.

8.3 Results of Manufacturability Investigation

Six unique lumbar cages were manufactured and all six lumbar cage designs were considered manufacturable. The total percentage of downskin distribution was measured in 15 degree increments, where parallel to build plate was 0 degrees and perpendicular to build plate was 90 degrees, Figure 8.5, left. Down-skin distribution was compared to unit cell designs of the same lattice type from Chapter 7(McGregor et al., 2024). Down-skin ratio was <1 for both TPMS gyroid cages and Voronoi cages, Figure 8.6, right. Analysis of post-manufacture mCT images showed under-printing not exceeding 0.5% for both lattice types, and over-printing not exceeding 1% and 2% for the TPMS gyroid and Voronoi lattice structures, respectively, Figure 8.6.

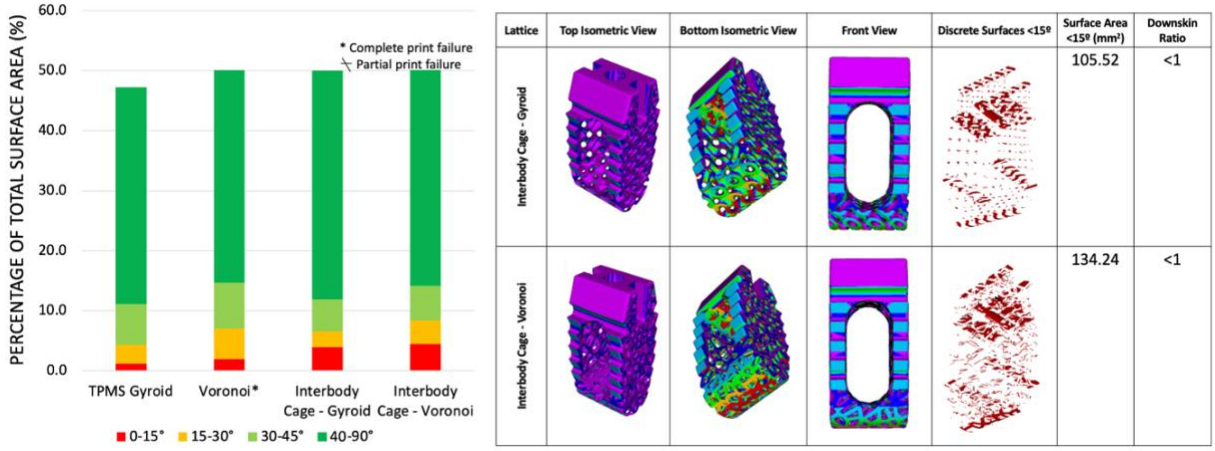


Figure 8.5. Down-skin distribution was measured in 15 degree increments for TPMS gyroid and Voronoi unit cells and interbody cages. Down-skin distribution ratio was determined for both cages, and they were considered manufacturable (down-skin ratio < 1).

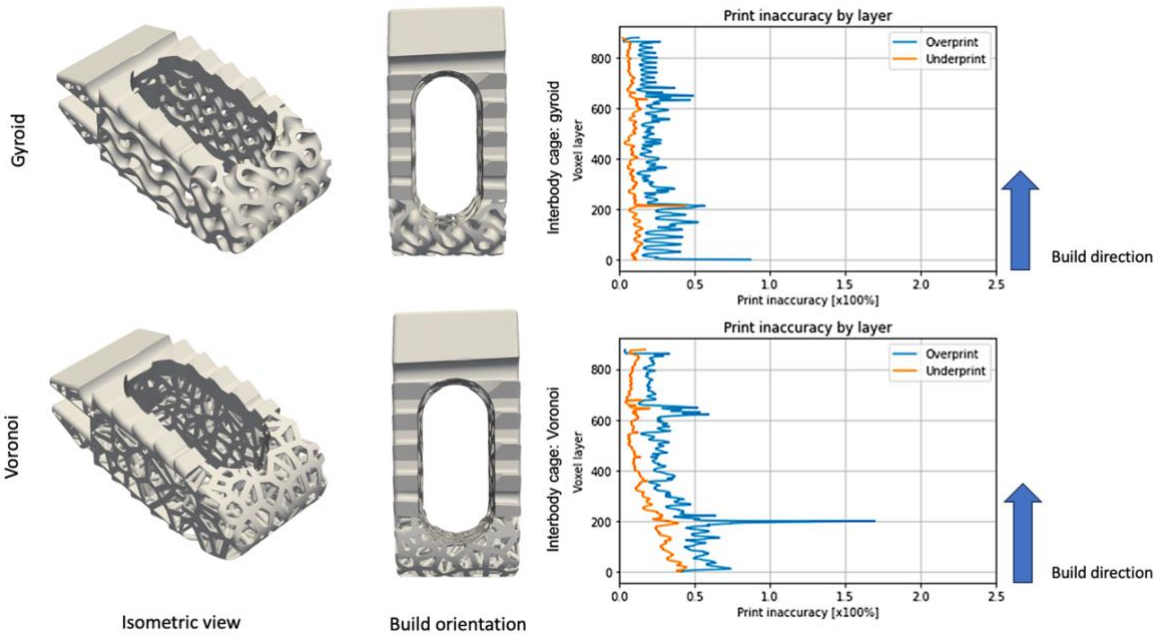


Figure 8.6. Manufacturability of the anatomically-optimized lumbar spinal cages was evaluated using X-ray micro-computed tomography (mCT). mCT images were collected post-manufacture and final cage geometries were compared to CAD designs to quantify over- and under-printing.

8.4 Methodology for the Bench-Top Investigation for Implant Evaluation

Two of the six cages cage designs, straight TPMS gyroid and large tapered TPMS, were compared for cage subsidence and migration. Sawbones were machined at a 5° angle to better represent the profile of the endplate in the medial-lateral direction. Six of each lumbar cage designs (straight: n=6, tapered n=6) were compressed into Solid Foam, 20 pounds per cubic foot (20 PCF), (Sawbones) up to 3.5 kN at 25 N/sec in load control with all off-axes maintaining zero load (0 N, 0 Nm), Figure 8.7. To maintain zero off-axis loading, actuators were able rotate freely. Implant motion was measured through actuator displacement and subsidence was considered to have occurred at 2 mm of displacement in the superior-inferior direction. Tests were continued past initial subsidence to ensure post-yield subsidence had occurred. A paired t-test was used to

determine differences in performance between the two cage designs and $p < 0.05$ was considered significant.

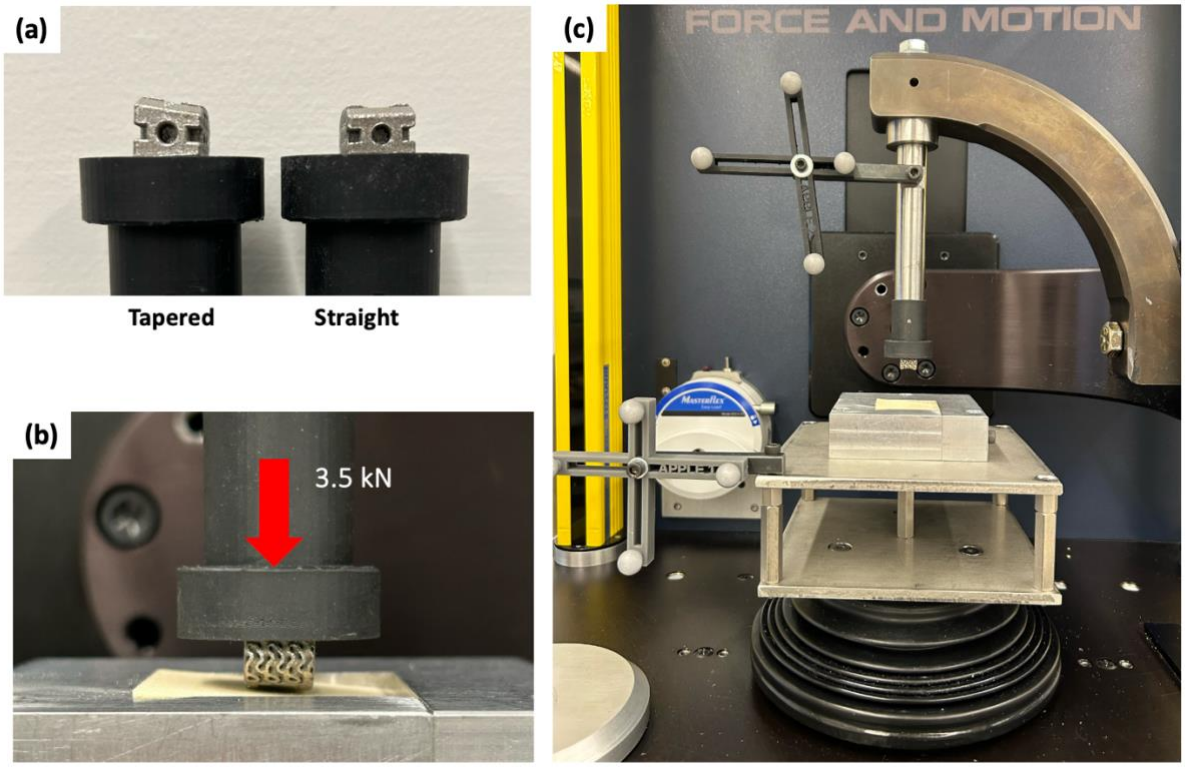


Figure 8.7. (a) Two lumbar cages were tested: an endplate conforming cage and a traditional cage. (b) Implants were held in a fully constrained fixture and compressed into an engineered foam at 25 N/sec to 3.5 kN. (c) A force control joint motion simulator was used to apply unconstrained force with all off-axis actuators held at 0 N load.

8.5 Results of Bench-Top Investigation for Implant Evaluation

The axial force required to reach 2 mm of cage subsidence was -643.4 ± 354.4 N and -900.8 ± 214.8 N for straight cage and tapered cage designs, respectively (p=0.188), Figures 8.8 and 8.9. At 2mm of subsidence, rotational displacement was significantly different between the two cages (p=0.000), -1.86 ± 1.34 deg for straight cages and 1.88 ± 0.55 deg for tapered cages, Figure 8.10. The preliminary medial rotation resulted in the straight cage conforming to the saw bone. For the tapered cages, actuators exhibited anterior-posterior rotation gradually in the lateral

direction throughout the duration of the test. Lateral rotation was thought to be seen post-subsidence in both cages due to the densification of the Sawbones foam from compression, resulting in implant rotation into less dense regions (Benais, 2024).

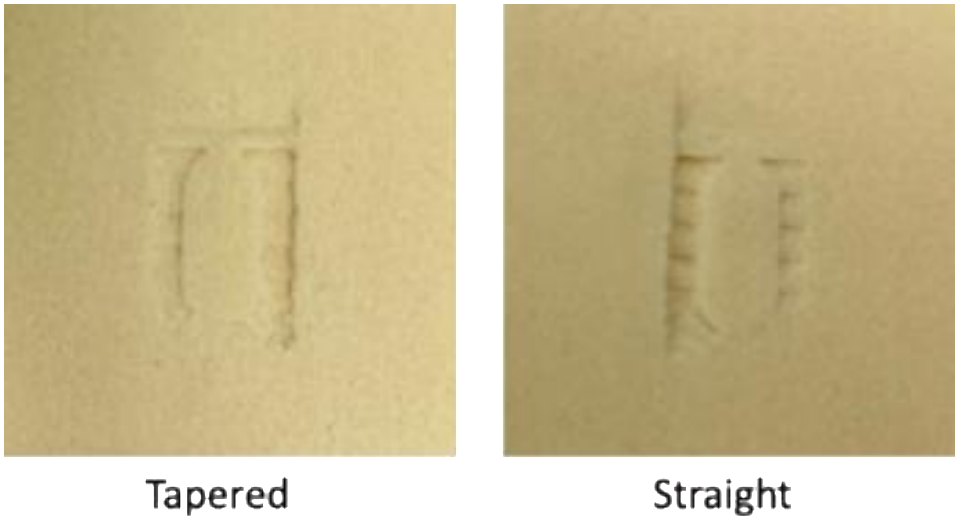


Figure 8.8 An example (n=1) of the compression pattern in the Sawbones test substrate for the tapered (left) and straight (right) cage designs following compression testing to 3.5 kN at 25 N/sec.

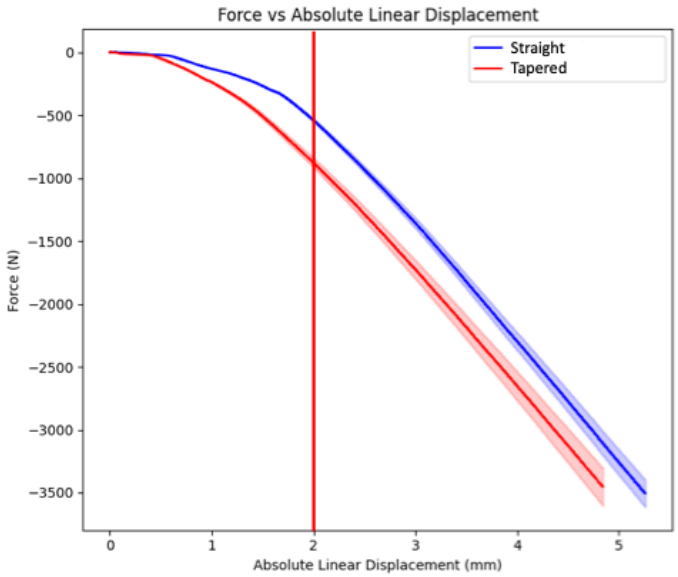


Figure 8.9 Vertical cage subsidence was considered to have occurred at 2 mm of vertical displacement. Subsidence occurred for both the traditional (blue, shaded ± standard deviation) and endplate conforming implants (red ± standard deviation) at -643.4 ± 354.4 N and -900.8 ± 214.8 N.

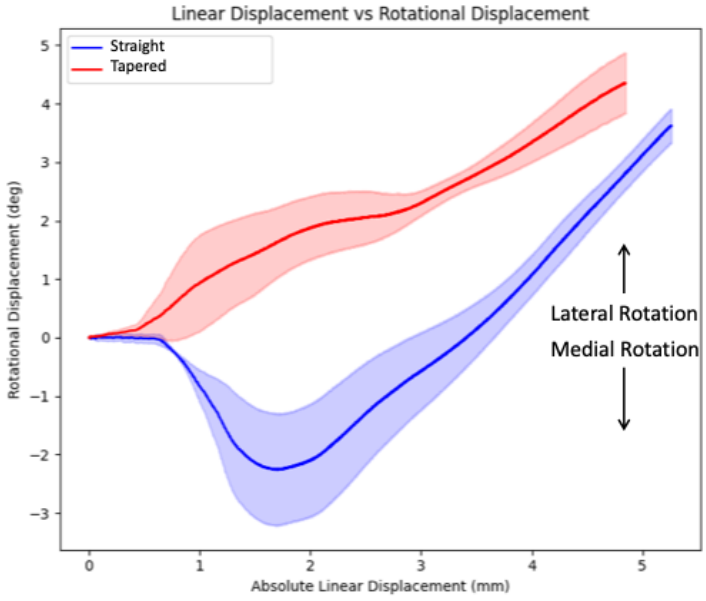


Figure 8.10 Both lumbar cages rotated about the anterior-posterior axis throughout the unconstrained cage subsidence testing. Straight cages (blue, shaded ± standard deviation) rotated medially during the initial subsidence as they conformed to the sawbones and then rotated similarly to the tapered cages (red, shaded ± standard deviation) during post-yield subsidence.

8.6 Conclusions on Interbody Cage Design Manufacturability and Preliminary Performance

Current LPBF AM technologies allow for the successful manufacturing of anatomically-optimized lattice implants. This technique has the potential to be adapted for other orthopaedic implant applications to improve implant compliance and generate implant shapes unattainable by traditional manufacturing processes. Further evaluation of post-manufacture mCT was beneficial to evaluate print performance and comment on manufacturability of anatomically-optimized orthopaedic implants produced through LPBF. Unconstrained force control testing was employed to evaluate novel tapered implants against current straight cage designs. Tapered cages exhibited less migration than straight cages ($p=0.000$) during unconstrained compression testing; however, subsidence performance was similar between the two designs ($p=0.188$). Future work will aim to validate our findings with an i*n vitro* cadaveric investigation in Chapter 9.

8.7 References

Arabnejad, S., Johnston, B., Tanzer, M., Pasini, D., 2017. Fully porous 3D printed titanium femoral stem to reduce stress-shielding following total hip arthroplasty. Journal of Orthopaedic Research 35, 1774–1783.

Benais, R., 2024. Computational modeling of trabecular bone indentation and development of a new test method to perform unconstrained load-induced subsidence of an intervertebral body fusion device. University of Waterloo.

Choy, W.J., Mobbs, R.J., Wilcox, B., Phan, S., Phan, K., Sutterlin III, C.E., 2017. Reconstruction of thoracic spine using a personalized 3D-printed vertebral body in adolescent with T9 primary bone tumor. World Neurosurg 105, 1032--e13.

Fernandes, R.J.R., Gee, A., Kanawati, A.J., Siddiqi, F., Rasoulinejad, P., Zdero, R., Bailey, C.S., 2024. Biomechanical Comparison of Subsidence Between Patient-Specific and Non-Patient-Specific Lumbar Interbody Fusion Cages. Global Spine J 14, 1155–1163. https://doi.org/10.1177/21925682221134913

Fernandes, R.J.R., Gee, A., Kanawati, A.J., Siddiqi, F., Rasoulinejad, P., Zdero, R., Bailey, C.S., 2022. Evaluation of the contact surface between vertebral endplate and 3D printed patient-specific cage vs commercial cage. Sci Rep 12. https://doi.org/10.1038/s41598-022-16895-9

Kim, D., Lim, J.-Y., Shim, K.-W., Han, J.W., Yi, S., Yoon, D.H., Kim, K.N., Ha, Y., Ji, G.Y., Shin, D.A., 2017. Sacral reconstruction with a 3D-printed implant after hemisacrectomy in a patient with sacral osteosarcoma: 1-year follow-up result. Yonsei Med J 58, 453.

Kumar, M., Meena, V.K., Singh, S., 2022. Static and Fatigue Load Bearing Investigation on Porous Structure Titanium Additively Manufactured Anterior Cervical Cages. Biomed Res Int 2022. https://doi.org/10.1155/2022/6534749

Lakshmanan, P., Purushothaman, B., Dvorak, V., Schratt, W., Thambiraj, S., Boszczyk, B.M., 2012. Sagittal endplate morphology of the lower lumbar spine. European Spine Journal 21. https://doi.org/10.1007/s00586-012-2168-4

Liu, F., Zhang, D.Z., Zhang, P., Zhao, M., Jafar, S., 2018. Mechanical properties of optimized diamond lattice structure for bone scaffolds fabricated via selective laser melting. Materials 11, 374.

Lowe, T.G., Hashim, S., Wilson, L.A., O, M.F., Smith, D.A., Diekmann, M.J., Trommeter, J., 2004. A Biomechanical Study of Regional Endplate Strength and Cage Morphology as It Relates to Structural Interbody Support. Spine (Phila Pa 1976) 29, 2389–2394.

McGregor, M., Patel, S., McLachlin, S., Vlasea, M., 2021. Architectural bone parameters and the relationship to titanium lattice design for powder bed fusion additive manufacturing. Addit Manuf 47, 102273.

McGregor, M., Patel, S., Zhang, K., Yu, A., Vlasea, M., McLachlin, S., 2024. A Manufacturability Evaluation of Complex Architectures by Laser Powder Bed Fusion Additive Manufacturing. J Manuf Sci Eng 146. https://doi.org/10.1115/1.4065315

Mobbs, R.J., Coughlan, M., Thompson, R., Sutterlin, C.E., Phan, K., 2017. The utility of 3D printing for surgical planning and patient-specific implant design for complex spinal pathologies: case report. J Neurosurg Spine 26, 513–518.

Moolman, F., kat, C.-J., Du Plessis, A., Khodja, M., 2023. Comparative analysis of the subsidence of solid polyetheretherketone (PEEK) and 3D printed lattice titanium interbody fusion cages. MATEC Web of Conferences 388, 01001. https://doi.org/10.1051/matecconf/202338801001

Phan, K., Sgro, A., Maharaj, M.M., D'Urso, P., Mobbs, R.J., 2016. Application of a 3D custom printed patient specific spinal implant for C1/2 arthrodesis. Journal of Spine Surgery 2, 314.

Chapter 9- An *in vitro* investigation of lumbar interbody cage migration under physiologically-derived loading conditions [6]

Abstract:

Posterior lumbar interbody fusion (PLIF) is a common surgical technique for treating degenerative disc disease and spinal deformities. Complications such as interbody cage migration and subsidence are common and can negatively impact surgical outcomes, potentially leading to revision surgery. Cage migration and subsidence are exacerbated by various factors, including poor bone quality, cage design, and spinal movements, but little is known about how early post-operative spinal movements contribute to these risks. This study aimed to investigate the biomechanical effects of different spinal movements on the migration and subsidence of two custom lattice titanium alloy interbody cage designs—straight and tapered—in lumbar spine segments. We hypothesized that movements such as flexion-extension would increase the risk of cage migration and subsidence. Eight lumbar spinal segments from cadavers were tested using a six-degree of freedom motion simulator. The specimens were subjected to flexion-extension (FE), lateral bending (LB), and axial rotation (AR) forces under pure moment loading conditions. A gait simulation protocol was applied for 3,000 steps, and cage migration was measured at 500-step intervals. Two interbody cage designs were tested: a straight and a tapered cage, both manufactured in Ti6Al4V alloy using laser powder bed fusion additive manufacturing. Range of motion (ROM) and cage migration were assessed using digital image correlation tracking. Cage instrumentation restored stability in FE ($p=0.05$) but did not fully correct rotational instability in AR ($p=0.04$). Posterior cage migration occurred primarily during FE ($p=0.02$), while cage subsidence into the adjacent vertebrae occurred most often during gait loading ($p=0.01$). No significant difference in migration or subsidence was observed between straight and tapered designs ($p > 0.05$). These findings suggest that spinal movements play a significant role in early cage migration, particularly in the absence of posterior fixation. Gait, rather than high-load movements, was the primary driver of subsidence due to repetitive smaller loads.

[6] A version of this chapter has is under peer-review: McGregor, M; Thompson, C; Fernandes, R; Rasoulinejad, P; McLachlin, S. (2024) An *in vitro* investigation of lumbar interbody cage migration under physiologic loading conditions Under review for The Spine Journal (SPINEE-D-24-01054)

9.1 Introduction

Lumbar fusion is a common surgical procedure for the treatment of low back pain in cases of degenerative disc disease, spondylolisthesis, or spinal deformities (Goh et al., 2000; Park et al., 2019; Polikeit et al., 2003). With the posterior lumbar interbody fusion (PLIF) or transforaminal lumbar interbody fusion (TLIF) approach, interbody "cage" devices are inserted bilaterally through the posterior disc space to re-establish intervertebral disc height for three potential goals: (1) restore radiographic spinal alignment to correct focal deformities, (2) provide structural support and potentially improve fusion rates, and (3) indirectly decompress neural elements (Mcafee, 1999). Yet, complications such as cage migration within the intervertebral disc space and subsidence into adjacent vertebrae remain a significant concern.

Cage migration refers to the unintended movement of the interbody cage from its original insertion location in the disc space, while subsidence describes the penetration of the cage into the adjacent vertebral bone (Corniola et al., 2015). In literature, cage migration and subsidence are typically defined as 2 mm or more of implant translation (Oh et al., 2017). Both complications can compromise the success of the surgery, with potential to lead to persistent pain and the need for revision surgery (Parisien et al., 2022). Studies suggest that cage migration occurs in approximately 2-5% of cases, while subsidence is more common, affecting up to 32% of patients within the first three months postoperatively (Marchi et al., 2013; Mi et al., 2017; Park et al., 2019; Tokuhashi et al., 2009). These complications are particularly problematic because they can destabilize the spine, facilitate a loss of disc height, and hinder bone fusion, leading to poor clinical outcomes (Choi and Sung, 2006; Polikeit et al., 2003).

Several risk factors contribute to cage migration and subsidence following lumbar fusion procedures. One of the primary factors is bone quality, with patients suffering from osteoporosis

or low bone mineral density being at higher risk due to the reduced capacity of their vertebrae to support the interbody cage (Formby et al., 2016; Mi et al., 2017). The size and design of the cage also play critical roles, with smaller or poorly positioned cages being more prone to migration and subsidence (Tokuhashi et al., 2009). The surgical technique, including the accuracy of cage placement and the use of additional fixation methods, such as pedicle screw and rod constructs, further influences the stability of the interbody cage (Grant et al., 2001; Polikeit et al., 2003). Additionally, multi-level fusions and excessive resection of the vertebral endplate can exacerbate the risk of cage instability (Marchi et al., 2013; Park et al., 2019).

While biomechanical investigations have previously examined how cage design and bone quality affects cage migration and subsidence (Fernandes et al., 2024, 2022; Jones et al., 2014; Oh et al., 2017; Tokuhashi et al., 2009), there is a relative lack of knowledge about how different spinal movements associated with activities of daily living in the early post-operative period affect the risk of cage migration. Movements of the low back such as flexion, extension, and lateral bending exert varying forces on the interbody cage (Wang et al., 2020; Yang et al., 2024), potentially influencing its stability within the disc space, depending on the contact between the cage and bony endplates. However, the relationship between these dynamic forces and cage behavior remains underexplored. Studies using finite element analysis have highlighted that certain movements, such as flexion, may increase the risk of cage migration, but more data is needed to quantify how each movement contributes to subsidence or migration over time (Gonzalez-Blohm et al., 2014; Labrom et al., 2005; Polikeit et al., 2003; Yang et al., 2024).

Latticed interbody cage designs, created using computer-aided design tools and metal additive manufacturing techniques, have shown promise in reducing the risk of cage subsidence (Kumar et al., 2022; Liu et al., 2018; Moolman et al., 2023). These architected implants aim to optimize fit,

enhance load distribution, and improve the overall stability of the vertebral fusion construct. By better contouring to a patient's endplate geometry, these interbody cages can achieve a larger surface contact area, which significantly reduces the stress concentration at the bone-cage interface—a known contributor to subsidence (Burnard et al., 2020; Calignano, 2014; Fernandes et al., 2024, 2022; Smit et al., 2024). Additionally, the use of metal additive manufacturing allows for precise customization of cage dimensions and porous structures that can mimic the mechanical properties of natural bone, enhance bony integration with the implant and promote fusion (Van Bael et al., 2012). Studies have demonstrated that customized 3D printed cages not only reduce subsidence rates but may also lead to better clinical outcomes, such as improved pain relief and spinal stability, compared to standard, commercially available cages (Burnard et al., 2020; Fernandes et al., 2024; Smit et al., 2024).

The goal of this *in vitro* investigation was to examine how loading conditions associated with different spinal movements impact lumbar interbody cage migration and subsidence. Two custom lattice titanium alloy (Ti6Al4V) cage designs, one straight and one tapered to better conform to endplate, were used for comparison of cage migration under the examined loading conditions. It was hypothesized that spinal movement, particularly flexion-extension, would exacerbate cage migration and subsidence when compared to other spinal movements.

9.2 Methods

9.2.1 Specimen Preparation

Institutional ethics approval was granted for the use of eight lumbar spinal segments (four L2-L3 and four L4-L5), sectioned from four fresh frozen cadavers (average age 69 ± 4.7 years, 3 female and 1 male) (Science Care, Phoenix, AZ, USA). Whole spine specimens were imaged with a 0.182 g/cm^3 phantom using clinical resolution computed tomography (CT) scanning before

sectioning to rule out bone defects and quantify bone mineral density (82.7 ± 3.8 mg/cm^3). Specimens were then sectioned and stored at -40°C until biomechanical testing. Lumbar spinal segments were thawed overnight at a room temperature of 20-22°C and further dissected while maintaining intact intervertebral discs and spinal ligaments. Specimens were then fixed to custom 3D printed clamps and mounted on a six degree-of-freedom (6DOF) joint motion simulator (AMTI VIVO, AMTI, USA).

9.2.2 Interbody Cage Design and Additive Manufacturing

The initial geometry (height: 9 mm, width: 10 mm, and length 22 mm) for a flat lumbar interbody cage implant was reverse engineered from the literature using computer-aided design (CAD) software (SolidWorks, Dassault Systèmes). A second cage design was then created by adding a 2 mm taper in the coronal plane for better sagittal endplate conformance (Figure 9.1a) based on (Lakshmanan et al., 2012), which reported an approximate 2 mm height difference between the mid-line disc height and disc height towards the periphery. Further, the ultimate compressive strength of human lumbar endplates was attained from literature and a pre-established design tool was used to determine corresponding titanium lattice porosities (McGregor et al., 2021). Custom porous gyroid lattice structures were then added to the interbody cage geometry using CAD software (nTop, NY, USA) to four regions (medial, lateral, anterior and posterior) of the implant geometry based on previously reported ultimate compressive strength of the lumbar vertebral endplate (Lowe et al., 2004). The titanium lattice porosity required to best match literature endplate compressive strengths were 40%, 50%, 60% and 70% porous for the posterior, lateral, anterior, and medial implant regions respectively (Figure 9.1b). Final lumbar cage designs were manufactured in Ti6Al4V alloy through laser powder bed fusion (EOS M290 LPBF) using

established print parameters (Patel and Vlasea, 2020) and were subsequently evaluated for manufacturability (McGregor et al., 2024).

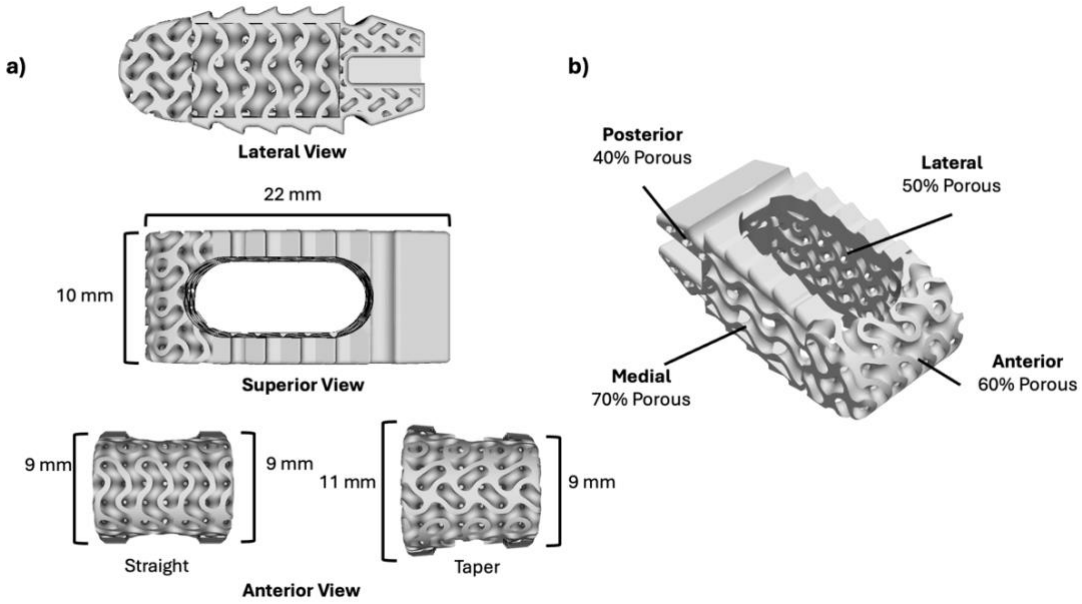


Figure 9.1. (a) Two posterior lumbar interbody fusion cage designs were developed for (1) a straight endplate, and (2) a 2mm tapered endplate. (b) Gyroid lattice structures were incorporated to reduce the mechanical modulus of the Ti6Al4V implants to better match previously reported values for the lumbar vertebral endplate.

9.2.3 Experimental Protocol and Biomechanical Testing

Biomechanical testing was conducted on the 6DOF joint motion simulator (Figure 9.2). Lumbar spinal segments were first tested under pure moment loading in 6DOF force control following established spine testing recommendations (Costi et al., 2021; Wilke et al., 1998). The superior vertebra was fixed to the upper actuators and the inferior vertebra was fixed to the lower actuators. Applied loads were resolved about the center of the superior vertebrae. A 250 N axial compressive pre-load was applied and five cycles of pure moment (±4 Nm, 0.5 N/s) were applied to generate flexion-extension, left-right lateral bending, and left-right axial rotation, in that order. The first three cycles were applied as pre-conditioning, the fourth was used for data collection and the fifth cycle allowed the joint to return to neutral loaded position.

The pure moment loading protocol for each of the three movements was applied to each specimen in three states: (1) intact with all bony, disc and ligamentous tissues retained, (2) a disrupted condition following posterior element resection, and (3) two instrumented conditions following bilateral insertion of straight or tapered cages. The cage testing order was randomized. The instrumented conditions did not include any posterior instrumentation (interbody cages only). Range of motion (ROM) and cage migration (left cage only) were measured using an optical 3D motion tracking system (ARAMIS Adjustable 12M, GOM Metrology, Braunschweig, Germany).

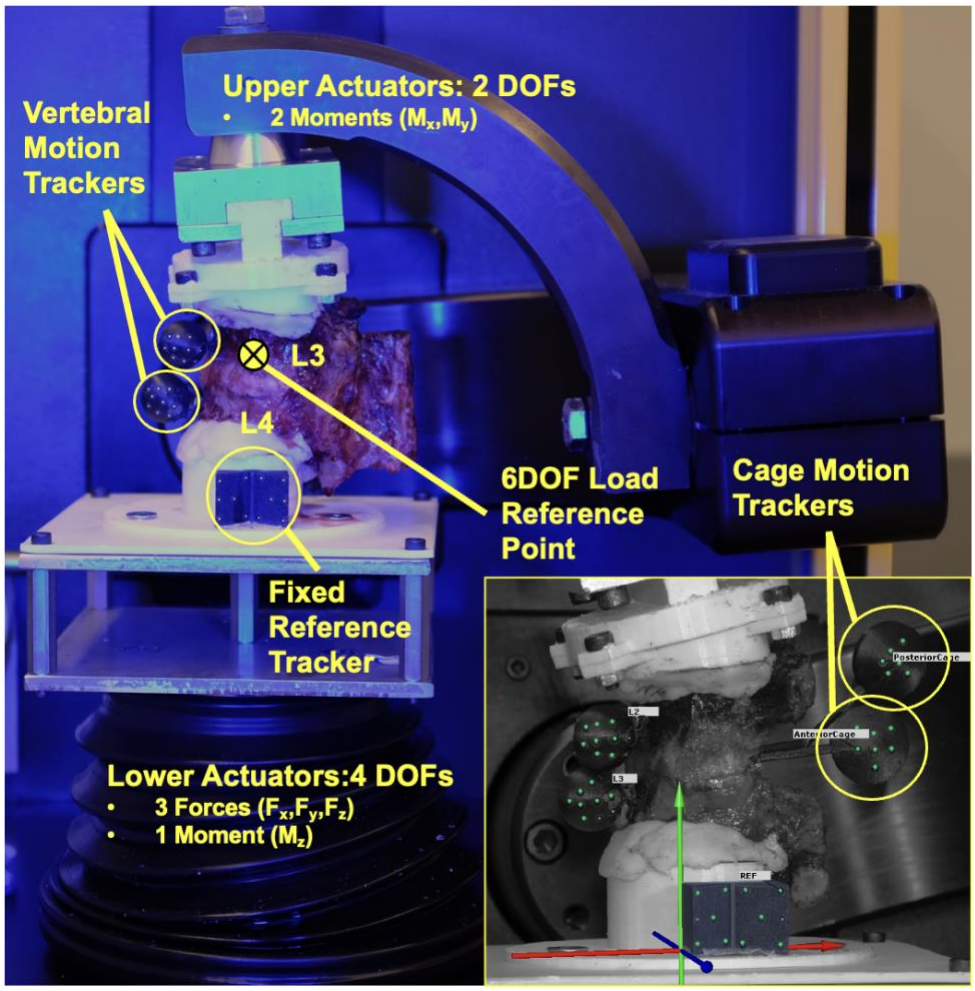


Figure 9.2. Lumbar motion segments were mounted to a six-degree of freedom joint motion simulator. Actuators worked together in force control to apply the translational and rotational displacements required to simulate spinal flexion-extension (My), lateral bedning (Mx), axial rotation (Mz) and a six-degree of freedom gait loading protocol.

Following ROM testing, a 6DOF force control loading scenario was applied to simulate human gait motion (Figure 9.3). 6DOF load data was obtained from an open-source repository consisting of load data collected from five human participants with instrumented vertebral body replacements (www.orthoload.org). Gait data was sectioned for two steps (right heel strike to right heel strike) from five participants and averaged using a dynamic time warping with a peak matching approach. The averaged 6DOF gait load waveform was applied at 2 Hz (two steps per second) for 3000 steps and cage migration was measured at 500 step increments. The iterative learning control function of the employed joint motion simulator was used to ensure force targets were met at the physiologic walking rate.

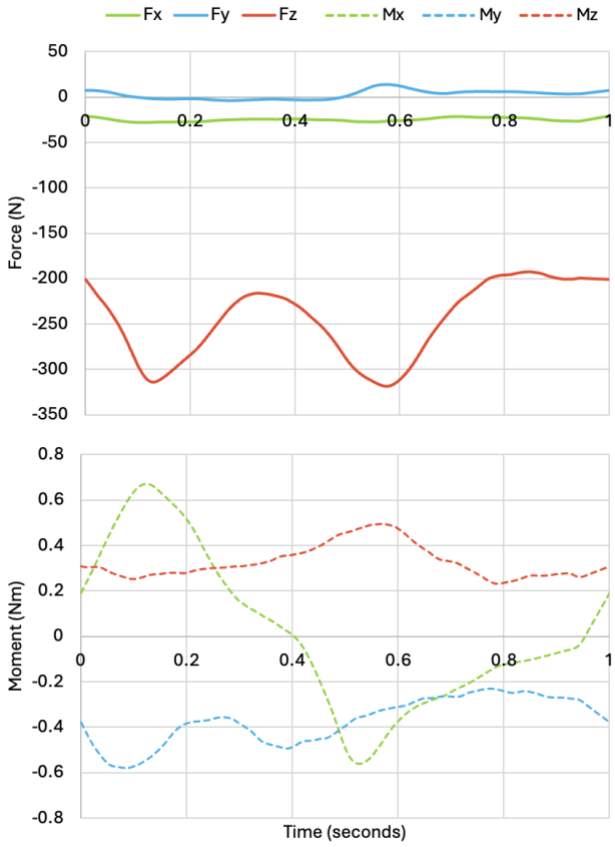


Figure 9.3. The averaged six-degree of freedom (Fx, Fy, Fz, Mx, My, Mz) gait loading waveform was developed from five instrumented vertebral body replacement patient datasets (www.orthoload.org) using a dynamic time warping with peak matching approach for normalization to a 1s time period.

9.2.4 Posterior Element Resection and Cage Insertion

Following intact ROM testing, the posterior elements of the motion segment were removed for cage insertion. This included removal of the spinous process of the superior vertebra along with the supraspinous and interspinous ligaments. Bi-lateral lamenectomy and facetectomy were also performed at this stage to gain posterior access to both sides of the intervertebral disc space, but the disc was left intact. Specimens were re-mounted on the joint motion simulator and pure moment ROM testing was reconducted of the injured segment prior to cage insertion.

After biomechanical testing of the posterior element deficient segments, interbody cages were placed. An incision was made in the posterior annulus fibrosus, the nucleus pulposus was removed and rongeurs were used to clear the disc space with attention to preserving the endplates. Initial cage selection, straight or tapered, was assigned randomly through a coin flip. Pairs of the selected interbody cage type were inserted bi-laterally, parallel to one another and as anterior and lateral as possible. Cage positioning was confirmed with X-ray imaging before biomechanical testing proceeded (inCiTe micro-CT, KA Imaging, Canada). Lumbar segments were then tested biomechanically and the initial cages (straight or tapered) were exchanged for the alternate design with the testing protocol repeated.

9.2.5 Simulated Cyclic Gait Loading

Following ROM testing under pure moment loading, a 6DOF force control loading scenario was applied to each of the instrumented cage conditions (straight and tapered) to simulate cyclic loading associated with human gait motion (Figure 3). 6DOF load data was obtained from an open-source repository consisting of load data collected from five human participants with instrumented vertebral body replacements (www.orthoload.org) (Rohlmann et al., 2014). Gait data

was sectioned for two steps (right heel strike to right heel strike) from five participants and averaged using a dynamic time warping with a peak matching approach.

The averaged 6DOF gait load waveform was applied at 2 Hz (two steps per second) for 3000 steps. The iterative learning control function of the employed joint motion simulator was used to ensure force targets were met at the physiologic walking rate. 6DOF cage migration was measured in 500 step increments relative to the cage starting position.

9.2.6 Statistical Analysis

Total lumbar segment ROM for simulated flexion-extension, lateral bending and axial rotation movements were compared to draw conclusions towards overall joint stability between the states (parameters: intact, posterior element resected, straight cage, and tapered cage). Cage migration between the two cage designs was compared (parameters: straight cage and tapered cage). Lastly, to better understand the contributions of spinal movements, cage migration and subsidence were compared in each translational and rotational direction between the four movement loading conditions (parameters: flexion-extension, lateral bending, axial rotation, and simulated gait).

A Bartlett's test for homogeneity of variance was used to determine if variance between parameters were equal. If they were, a one-way analysis of variance was used to test the differences between values between parameters. If not, a Welch's F-Test was used for comparison. A Holm's step-down post-hoc test was conducted to account for family-wise error rate and provide a more conservative assessment of significance. For all parameters, significance was considered to be $p<0.05$.

9.3 Results

9.3.1 Cage Design Decisions

Based on the preoperative CT scans, the specimens in the present study had an average mid-line disc height of 10.8 ± 3.2 mm and a disc height of 7.2 ± 2.5 mm and 7.9 ± 2.8 mm at the right and left peripheries, with an average difference between the mid-line and peripheral disc height of 3.2 ± 2.1 mm.

9.3.2 Lumbar Segment Range of Motion

Lumbar segment stability was impacted by posterior element resection and interbody instrumentation differently in each of the spine movements tested. Detailed ROM data can be found in Table 1 and illustrated in Figure *9.*4.

With simulated flexion-extension, posterior element resection significantly increased medial-lateral joint translation when compared to intact range of motion (p=0.01) (Figure 4a). Medial-lateral joint translation was not reduced to the intact level with interbody cage instrumentation for either the straight (p=0.01) or tapered (p=0.02) cages. However, the addition of the tapered cage did result in a significant decrease in medial-lateral range of motion when compared to the posterior element resected state (p=0.03). Rotational flexion-extension range of motion was significantly increased following posterior element resection (p=0.05), and there was no significant difference between the FE ROM in intact and interbody cage instrumented states (p>0.05).

With the simulated axial rotation movement, posterior element resection significantly increased anterior-posterior translation (p=0.00) when compared to intact ROM. Anterior-posterior translation was not reduced to the intact level with interbody cage instrumentation for

either the straight ($p=0.04$) or tapered ($p=0.04$) cages. Rotation in the transverse plane significantly increased following cage instrumentation with both straight ($p=0.02$) and tapered ($p=0.01$) cage designs, likely as a result of the posterior disc disruption for cage insertion.

With simulated lateral bending loading, lumbar segment stability was not significantly impacted by posterior element resection nor interbody cage instrumentation ($p>0.05$).

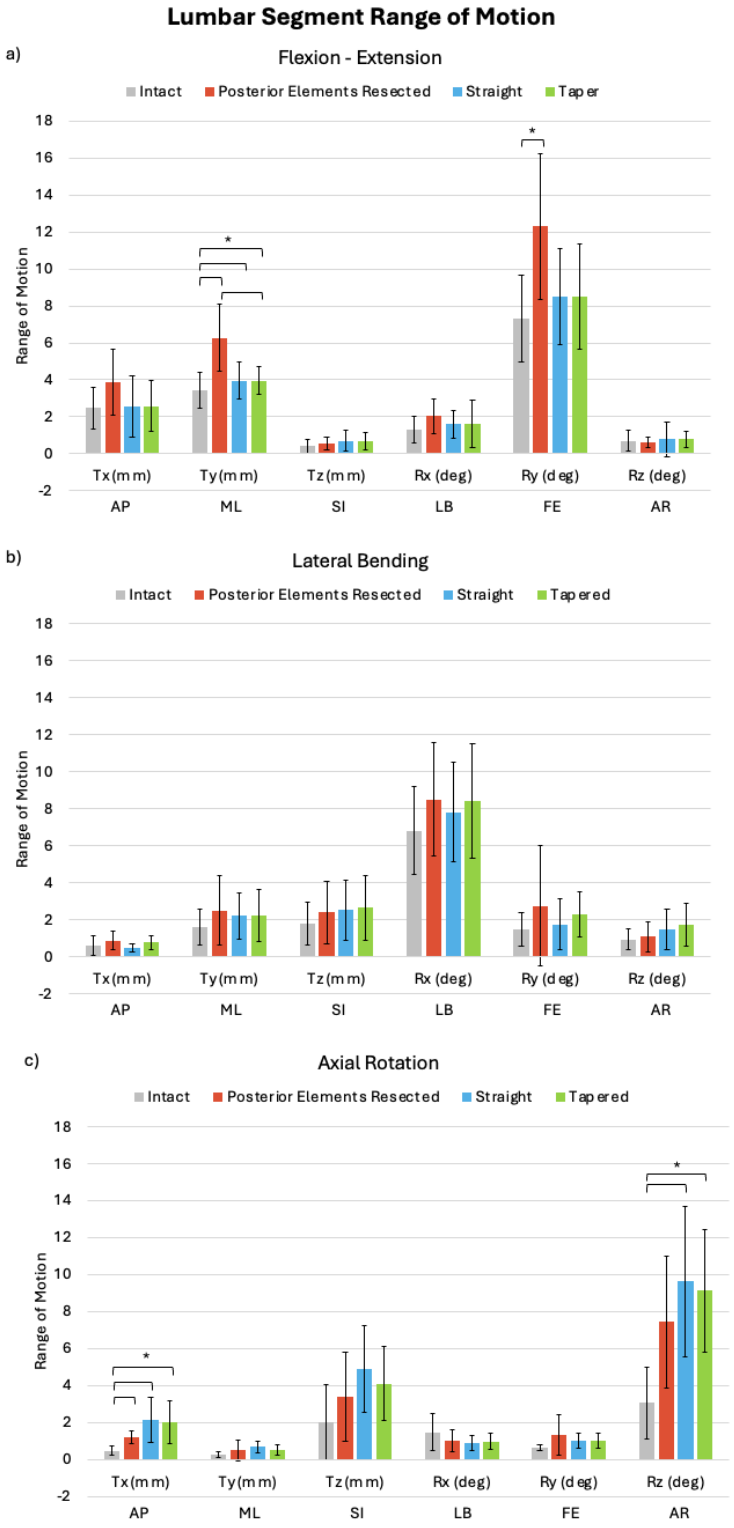


Figure 9.4. The average lumbar motion segment range of motion during simulated pure moment flexion-extension, lateral bending and axial rotation is shown with error bar representing standard deviations. Significant differences between intact, injured and repair states are shown with a * and $p < 0.05$ considered significant.

9.3.3 Cage Migration and Subsidence

There were no difference in the magnitude of cage migration between the straight and tapered cage designs throughout flexion-extension, lateral bending, axial rotation or simulated gait movements ($p>0.05$) (Figure 9.5). Four of the eight straight cages tested and five of eight tapered cages subsided (Tz translation > 2mm) into the adjacent vertebra following the range of motion and gait testing. Of the four straight cages that subsided, two subsided into the superior vertebra during axial rotation and two subsided into the inferior vertebra during gait. Of the five tapered cages that subsided, four subsided into the inferior vertebra during flexion-extension (1) and gait (3) and one subsided into the superior vertebra during gait. Translation of the cage into the inferior (±Tz) vertebra occurred most during the gait loading protocol ($p=0.01$).

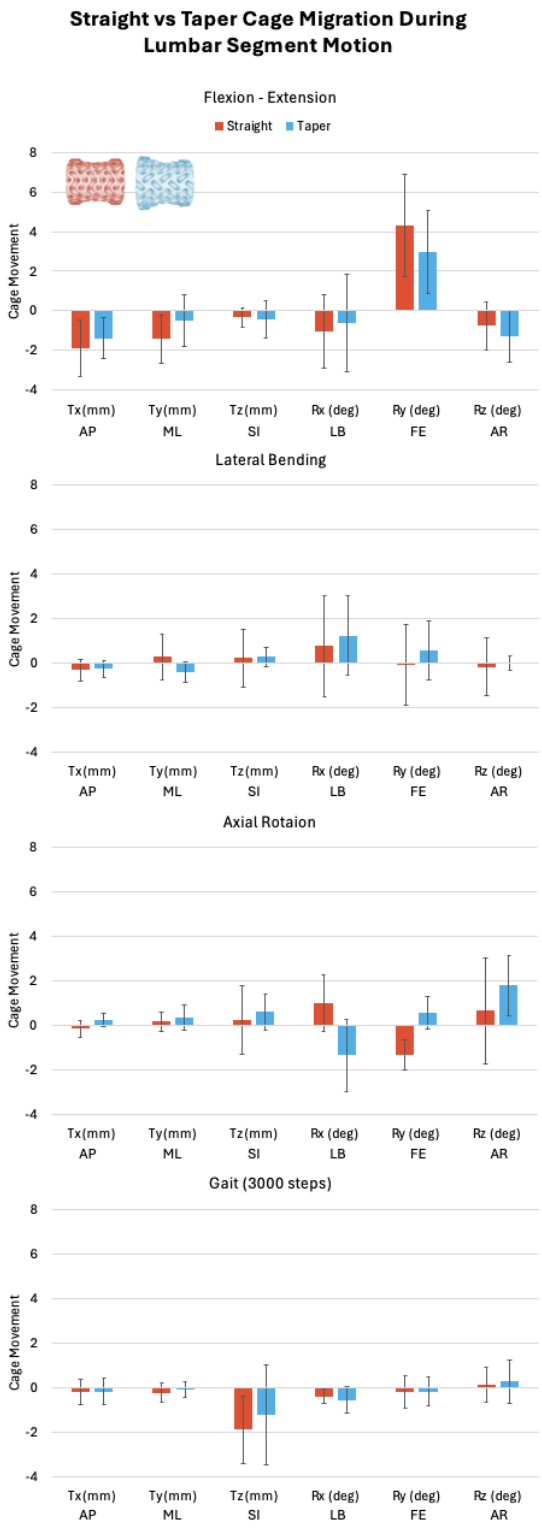


Figure 9.5. The average cage migration for straight and taper cage designs during simulated pure moment flexion-extension, lateral bending, axial rotation and six degree of freedom gait is shown with error bar representing ± standard deviations. There were no significant differences between cage designs, with $p > 0.05$.

The interbody cages migrated throughout lumbar segment range of motion testing and the 3000 steps under 6DOF gait loading (Figure 9.6). Two straight cages and two tapered cages had posterior migration larger than 2mm (-Tx) towards the spinal canal. The majority of anterior-posterior (±Tx) translation occurred in the posterior direction during flexion-extension (±Ry) ($p=0.02$). Medial-lateral (± Ty) cage migrations were primarily in the medial direction and occurred most often during flexion-extension (± Ry) ($p=0.03$). Rotation of the cages followed the loading direction of the pure moment bending, with cage rotation being greatest in the direction of lumbar segment movement ($p<0.05$).

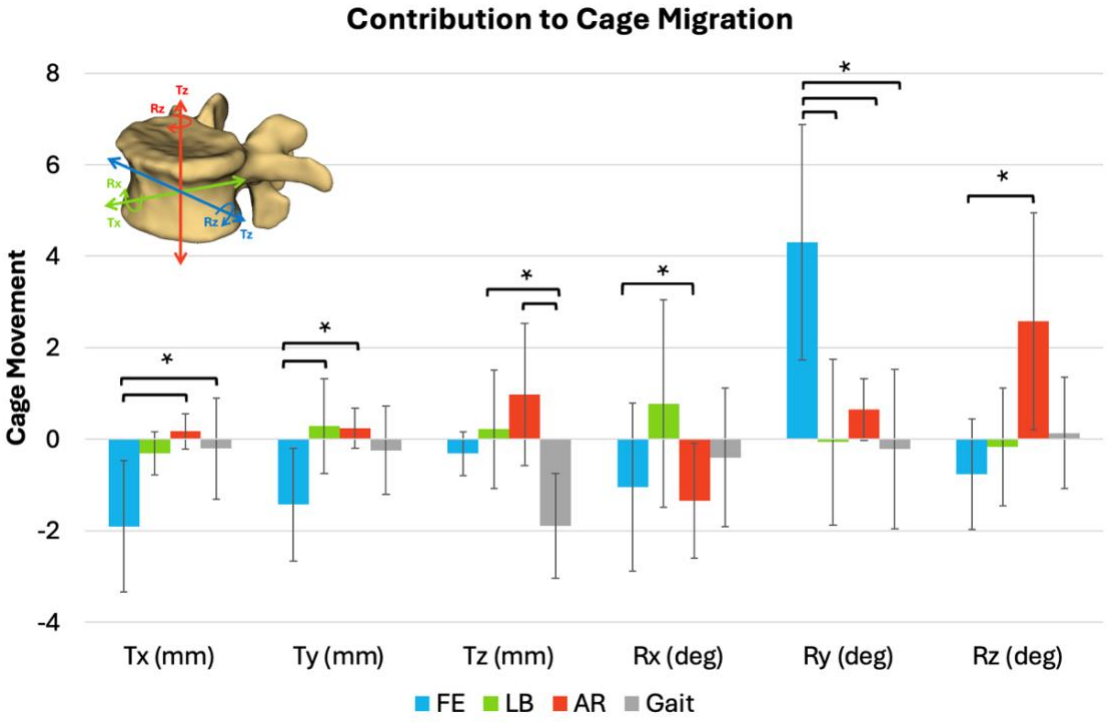


Figure 9.6. Contributions towards cage migration differed between the simulated spinal motions. Significant differences between spinal flexion-extension, lateral bending, axial rotation and gait loading for 3000 steps are shown with a * and $p < 0.05$ considered significant.

9.4 Discussion

9.4.1 Lumbar Segment Range of Motion

The present study investigated the biomechanics of interbody cage movement following simulated loading associated with flexion-extension, lateral bending, axial rotation, and gait movements. Interbody cage instrumentation restored lumbar segment ROM to levels comparable to an intact spine with simulated flexion-extension, but did not significantly alter the ROM when compared between injured and instrumented states for the other movements. Rotational ROM in the axial direction increased with both posterior element resection and cage instrumentation, suggesting the incision of the posterior disc for cage insertion may increase rotational instability under these conditions. Our results are consistent with prior studies showing that interbody cages can restore segmental stability during flexion-extension but may be less effective in stabilizing axial rotation, a challenge often noted in biomechanical analyses (Polikeit et al., 2003). Therefore, the findings of this study are consistent with others that have encouraged additional posterior fixation, through pedicle screw and rod constructs, for effective lumbar spine stabilization following anterior column reconstruction (Ames et al., 2005).

9.4.2 Cage Migration and Subsidence

The present study did not find significant differences in migration rates between traditional (straight) and endplate-conforming (tapered) cages, suggesting that the shape of the cage alone does not adequately mitigate migration risk. Previous studies have reported the benefits of anatomy conforming and patient-specific cage designs towards limiting implant subsidence due to reduced stress concentrations at the implant-endplate interface (Burnard et al., 2020; Fernandes et al., 2024; Smit et al., 2024). However, these studies have traditionally employed a uniaxial compression test

to evaluate cage designs against one another (Fernandes et al., 2022). Results from the current study, simulating 6DOF loading associated with various spinal movements, indicated potential nuances in lumbar interbody cage performance under different loading protocols.

Superior-inferior interbody cage subsidence was prevalent, occurring in 4 out of 8 straight cages (50%) and 5 out of 8 tapered cages (62.5%), with the majority of subsidence events occurring during simulated gait loading. This observation is consistent with existing literature suggesting that the bone-implant interface between the cage and endplate is susceptible to early-onset subsidence in the immediate post-operative period with activities of daily living (Malham et al., 2015; Marchi et al., 2013). Interbody cage subsidence occurred at a higher rate than published in clinical literature, which is thought to upwards of 32% incidence (Le et al., 2012; Malham et al., 2015; Marchi et al., 2013). This may be due to the osteopenic-osteoporotic nature of the specimens used (82.7 ± 3.8 mg/cm^3), as low bone mineral density has been linked to increased subsidence rates clinically (Formby et al., 2016; Mi et al., 2017). Further, the titanium lattice porosities, 40-70% porous, were selected from literature to best mimic adjacent bone mechanical properties. Based on this study, it may have been beneficial to further push the titanium lattice porosity closer to 80-90% to match the mechanical properties of osteoporotic human lumbar vertebrae, though this level of porosity is challenging to obtain with current metal additive manufacturing techniques. Further, the difference between mid-line and periphery intervertebral disc height was found to be greater in the specimens used for the present study then reported in literature. Therefore, the full stress distribution advantages of anatomy conforming cage designs may not have been realized with the cage designs employed in the present study.

Cage migration and rotation largely followed the patterns of spinal segment movement, with flexion-extension playing a dominant role in driving both posterior and medial cage

migration. This supports the hypothesis that spinal movements directly influence interbody cage behavior, particularly when posterior elements are compromised. Interbody cage migration (translation > 2 mm) occurred in 4 out of 8 (50%) of straight cages and 5 out of 8 (62.5%) of tapered cages. This is much greater than the 2-5% incidence seen clinically (Kobayashi et al., 2018; Park et al., 2019; Tokuhashi et al., 2009). There was no posterior fixation used in the present study and therefore, the lumbar motion segments were subjected to larger ranges of motion than would be expected with both anterior and posterior column reconstruction (Ames et al., 2005). This may be what contributed to the larger cage migration rate seen in the present study. Further, cage migration is only measured clinically when part of an investigational study or there is a symptomatic relapse requiring additional 3D medical imaging (Parisien et al., 2022). As such, the true incidence of cage migration may be higher than previously thought.

9.4.3 Study Limitations

The present study is not without limitations. There are known limitations of cadaveric implant testing, primarily inter-specimen variability and small sample sizes. A repeated measures study design was selected for this reason and the order of cage instrumentation between the straight and tapered cages designs was randomized. While cage type was randomized, the pure moment loading protocol was not, with a common sequential movement order. This may explain why there was a larger amount of cage migration in the initial movement (flexion-extension), where the cage may have been settling into its desired position under load. Gait movement accounted for the large amount of cage subsidence, but this was the only movement tested for thousands of cycles. This simulated gait loading protocol was novel and therefore it is difficult to directly compare to existing literature on cage migration and subsidence. Specimens used were predominantly female. The higher prevalence of subsidence in women observed in some studies is often attributed to

below average BMD rather than sex-specific biomechanical differences in spinal anatomy (Formby et al., 2016). Therefore, bone mineral density was both measured and reported to account for the disproportionate number of female specimens used. Finally, posterior instrumentation was not used, and its effects were not examined. PLIF procedures are commonly accompanied by posterior fixation through pedicle screw and rod constructs to limit spinal motion segment motion during the initial fusion process. The benefits of posterior fixation for spinal stabilization are well established for PLIF procedures. Cage subsidence testing however is often done with isolated anterior reconstruction. Therefore, posterior fixation was not used in the present study as to better characterize the isolated performance of the selected interbody cages designs

9.4.4 Clinical Significance

Cage subsidence and migration remain clinically significant complications following PLIF procedures with anterior reconstruction using interbody cages. The results of this study highlight that different spinal movements impact these complications in distinct ways, with gait as the major driver of subsidence. Notably, failure did not occur during high-load movements such as flexion-extension, but rather after prolonged, repetitive, lower loads seen in gait, underscoring the role of cumulative fatigue on cage stability. Current test standards primarily focus on assessing subsidence risk under maximum compression testing. However, this study suggests that a more comprehensive pre-clinical evaluation of interbody cages should include longitudinal fatigue testing under physiologically relevant loading conditions. For clinicians, these findings emphasize the importance of considering not only the cage design but also post-operative movement patterns, as migration and subsidence risks are particularly high in the immediate post-operative period. These insights can guide surgical decision-making and improve patient outcomes by minimizing the likelihood of early cage failure.

9.5 Conclusions

To the best of our knowledge this study includes the first examination of cage migration and subsidence under physiologically derived longitudinal gait loading. The present study provides critical insights towards how spinal movements influence the acute biomechanical stability of interbody cages, offering valuable information for surgeons to optimize cage design as well as postoperative care recommendations. Incorporating fatigue testing under physiologically relevant loads could enhance pre-clinical evaluation and improve understanding of patient outcomes.

9.6 References

Ames, C.P., Acosta, F.L., Chi, J., Iyengar, J., Muiru, W., Acaroglu, E., Puttlitz, C.M., 2005. Biomechanical Comparison of Posterior Lumbar Interbody Fusion and Transforaminal Lumbar Interbody Fusion Performed at 1 and 2 Levels. Spine (Phila Pa 1976) 30, 562–566.

Burnard, J.L., Parr, W.C.H., Choy, W.J., Walsh, W.R., Mobbs, R.J., 2020. 3D-printed spine surgery implants: a systematic review of the efficacy and clinical safety profile of patient-specific and off-the-shelf devices. European Spine Journal. https://doi.org/10.1007/s00586-019-06236-2

Calignano, F., 2014. Design optimization of supports for overhanging structures in aluminum and titanium alloys by selective laser melting. Mater Des 64, 203–213.

Choi, J.Y., Sung, K.H., 2006. Subsidence after anterior lumbar interbody fusion using paired stand-alone rectangular cages. European Spine Journal 15, 16–22. https://doi.org/10.1007/s00586-004-0817-y

Corniola, M. V., Jägersberg, M., Stienen, M.N., Gautschi, O.P., 2015. Complete cage migration/subsidence into the adjacent vertebral body after posterior lumbar interbody fusion. Journal of Clinical Neuroscience 22, 597–598. https://doi.org/10.1016/j.jocn.2014.08.017

Costi, J.J., Ledet, E.H., O'Connell, G.D., 2021. Spine biomechanical testing methodologies: The controversy of consensus vs scientific evidence. JOR Spine. https://doi.org/10.1002/jsp2.1138

Fernandes, R.J.R., Gee, A., Kanawati, A.J., Siddiqi, F., Rasoulinejad, P., Zdero, R., Bailey, C.S., 2024. Biomechanical Comparison of Subsidence Between Patient-Specific and Non-Patient-Specific Lumbar Interbody Fusion Cages. Global Spine J 14, 1155–1163. https://doi.org/10.1177/21925682221134913

Fernandes, R.J.R., Gee, A., Kanawati, A.J., Siddiqi, F., Rasoulinejad, P., Zdero, R., Bailey, C.S., 2022. Evaluation of the contact surface between vertebral endplate and 3D printed patient-specific cage vs commercial cage. Sci Rep 12. https://doi.org/10.1038/s41598-022-16895-9

Formby, P.M., Kang, D.G., Helgeson, M.D., Wagner, S.C., 2016. Clinical and Radiographic Outcomes of Transforaminal Lumbar Interbody Fusion in Patients with Osteoporosis. Global Spine J 6, 660–664. https://doi.org/10.1055/s-0036-1578804

Goh, J.C.H., Wong, H.-K., Thambyah, A., Yu, C.-S., 2000. Influence of PLIF Cage Size on Lumbar Spine Stability. Spine (Phila Pa 1976) 25, 35–40.

Gonzalez-Blohm, S.A., Doulgeris, J.J., Aghayev, K., Lee, W.E., Volkov, A., Vrionis, F.D., 2014. Biomechanical analysis of an interspinous fusion device as a stand-alone and as supplemental fixation to posterior expandable interbody cages in the lumbar spine. Spine (Phila Pa 1976) 20, 209–219.

Grant, J.P., Sc, M., Oxland, T.R., Dvorak, M.F., 2001. Mapping the Structural Properties of the Lumbosacral Vertebral Endplates. Spine (Phila Pa 1976) 26, 889–896.

Jones, C.W., Hons, M., Lawson, R.D., Ortho, F., 2014. One Size Does Not Fit All : Distal Radioulnar Joint Dysfunction after Volar Locking Plate Fixation. J Wrist Surg 3, 42–45.

Kobayashi, K., Ando, K., Kato, F., Kanemura, T., Sato, K., Hachiya, Y., Matsubara, Y., Kamiya, M., Sakai, Y., Yagi, H., others, 2018. Reoperation within 2 years after lumbar interbody fusion: a multicenter study. European Spine Journal 27, 1972–1980.

Kumar, M., Meena, V.K., Singh, S., 2022. Static and Fatigue Load Bearing Investigation on Porous Structure Titanium Additively Manufactured Anterior Cervical Cages. Biomed Res Int 2022. https://doi.org/10.1155/2022/6534749

Labrom, R.D., Tan, J.-S., Reilly, C.W., Tredwell, S.J., Fisher, C.G., Oxland, T.R., 2005. The Effect of Interbody Cage Positioning on Lumbosacral Vertebral Endplate Failure in Compression. Spine (Phila Pa 1976) 30, 556–561.

Lakshmanan, P., Purushothaman, B., Dvorak, V., Schratt, W., Thambiraj, S., Boszczyk, B.M., 2012. Sagittal endplate morphology of the lower lumbar spine. European Spine Journal 21. https://doi.org/10.1007/s00586-012-2168-4

Le, T. V., Baaj, A.A., Dakwar, E., Burkett, C.J., Murray, G., Smith, D.A., Uribe, J.S., 2012. Subsidence of polyetheretherketone intervertebral cages in minimally invasive lateral retroperitoneal transpsoas lumbar interbody fusion. Spine (Phila Pa 1976) 37, 1268–1273. https://doi.org/10.1097/brs.0b013e3182458b2f

Liu, F., Zhang, D.Z., Zhang, P., Zhao, M., Jafar, S., 2018. Mechanical properties of optimized diamond lattice structure for bone scaffolds fabricated via selective laser melting. Materials 11, 374.

Lowe, T.G., Hashim, S., Wilson, L.A., O, M.F., Smith, D.A., Diekmann, M.J., Trommeter, J., 2004. A Biomechanical Study of Regional Endplate Strength and Cage Morphology as It Relates to Structural Interbody Support. Spine (Phila Pa 1976) 29, 2389–2394.

Malham, G.M., Parker, R.M., Blecher, C.M., Seex, K.A., 2015. Assessment and classification of subsidence after lateral interbody fusion using serial computed tomography. J Neurosurg Spine 23, 589–597.

Marchi, L., Abdala, N., Oliveira, L., Amaral, R., Coutinho, E., Pimenta, L., 2013. Radiographic and clinical evaluation of cage subsidence after stand-alone lateral interbody fusion. J Neurosurg Spine 19, 110–118.

McGregor, M., Patel, S., McLachlin, S., Vlasea, M., 2021. Architectural bone parameters and the relationship to titanium lattice design for powder bed fusion additive manufacturing. Addit Manuf 47, 102273.

McGregor, M., Patel, S., Zhang, K., Yu, A., Vlasea, M., McLachlin, S., 2024. A Manufacturability Evaluation of Complex Architectures by Laser Powder Bed Fusion Additive Manufacturing. J Manuf Sci Eng 146. https://doi.org/10.1115/1.4065315

Mi, J., Li, K., Zhao, X., Zhao, C.Q., Zhao, J., 2017. Vertebral body Hounsfield units are associated with cage subsidence after transforaminal lumbar interbody fusion with unilateral pedicle screw fixation. Clin Spine Surg 30, 1130–1136.

Moolman, F., kat, C.-J., Du Plessis, A., Khodja, M., 2023. Comparative analysis of the subsidence of solid polyetheretherketone (PEEK) and 3D printed lattice titanium interbody fusion cages. MATEC Web of Conferences 388, 01001. https://doi.org/10.1051/matecconf/202338801001

Oh, K.W., Lee, J.H., Lee, D.Y., Shim, H.J., 2017. The correlation between cage subsidence, bone mineral density, and clinical results in posterior lumbar interbody fusion. Clin Spine Surg 30, 683–689.

Parisien, A., Wai, E.K., Elsayed, M.S.A., Frei, H., 2022. Subsidence of Spinal Fusion Cages: A Systematic Review. Int J Spine Surg 16, 1103–1118. https://doi.org/10.14444/8363

Park, M.K., Park, S.A., Son, S.K., Park, W.W., Choi, S.H., 2019. Clinical and radiological outcomes of unilateral biportal endoscopic lumbar interbody fusion (ULIF) compared with conventional posterior lumbar interbody fusion (PLIF): 1-year follow-up. Neurosurg Rev 42, 753–761. https://doi.org/10.1007/s10143-019-01114-3

Patel, S., Vlasea, M., 2020. Melting modes in laser powder bed fusion. Materialia (Oxf) 9, 100591.

Paul Mcafee, B.C., 1999. Current Concepts Review Interbody Fusion Cages in Reconstructive Operations on the Spine *.

Polikeit, A., Ferguson, S.J., Nolte, L.P., Orr, T.E., 2003. The importance of the endplate for interbody cages in the lumbar spine. European Spine Journal 12, 556–561. https://doi.org/10.1007/s00586-003-0556-5

Rohlmann, A., Dreischarf, M., Zander, T., Graichen, F., Bergmann, G., 2014. Loads on a vertebral body replacement during locomotion measured in vivo. Gait Posture 39, 750–755. https://doi.org/10.1016/j.gaitpost.2013.10.010

Smit, T., Aage, N., Haschtmann, D., Ferguson, S.J., Helgason, B., 2024. Anatomically and mechanically conforming patient-specific spinal fusion cages designed by full-scale topology optimization. J Mech Behav Biomed Mater 159. https://doi.org/10.1016/j.jmbbm.2024.106695

Tokuhashi, Y., Ajiro, Y., Umezawa, N., 2009. Subsidence of metal interbody cage after posterior lumbar interbody fusion with pedicle screw fixation. Orthopedics 32, 259–264.

Van Bael, S., Chai, Y.C., Truscello, S., Moesen, M., Kerckhofs, G., Van Oosterwyck, H., Kruth, J.-P., Schrooten, J., 2012. The effect of pore geometry on the in vitro biological behavior of human periosteum-derived cells seeded on selective laser-melted Ti6Al4V bone scaffolds. Acta Biomater 8, 2824–2834.

Wang, H., Wan, Y., Li, Q., Xia, Y., Liu, X., Liu, Z., Li, X., 2020. Porous fusion cage design via integrated global-local topology optimization and biomechanical analysis of performance. J Mech Behav Biomed Mater 112. https://doi.org/10.1016/j.jmbbm.2020.103982

Wilke, H.-J., Wenger, K., Claes, L., 1998. Testing criteria for spinal implants: recommendations for the standardization of in vitro stability testing of spinal implants. European spine journal 7, 148–154.

Yang, S.-C., Wu, C.-L., Tu, Y.-K., Liu, P.-H., 2024. Dislodgment Effects of Different Cage Arrangements in Posterior Lumbar Interbody Fusion: A Finite Element Study. Bioengineering 11, 558. https://doi.org/10.3390/bioengineering11060558

Chapter 10– General Discussion and Conclusions

10.1 Summary and Global Research Contributions

The overall goals of this thesis were to: (1) to better understand mechanisms of clinical implant failures by improving pre-clinical spinal implant testing methodologies through the adoption of physiologically-derived loading conditions; and (2) to develop new tools to better understand how emergent LPBF AM technologies should be tailored for spinal implant designs. To achieve these goals, three distinct themes of the thesis were defined: (1) multiaxial spinal loading, (2) spinal implant evaluation and (3) metal additive manufacturing. Ultimately, the overall thesis objectives were met through a series of integrated *in vitro* biomechanical studies and DfAM investigations across these three research themes (Figure 10.1).

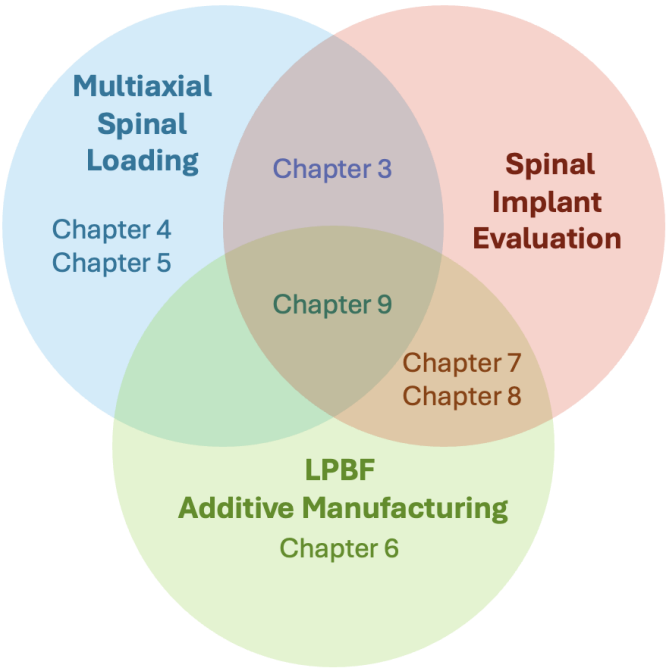


Figure 10.1. A Venn diagram describing the interconnectivity of the thesis chapters across three distinct research themes: (1) multiaxial spinal load simulation, (2) spinal implant evaluation, and (3) metal additive manufacturing.

Chapter 3: A Biomechanical Investigation of Multiaxial Pedicle Screw Loosening in Osteoporotic Human Vertebral Bone

Hypothesis H3: multiaxial loading will accelerate pedicle screw loosening, resulting in decreased screw fixation and increased volumetric bone deformation – **ACCEPTED**

Chapter 3 included both (1) multiaxial spinal loading and (2) spinal implant evaluation to address the first overall thesis goal to better understand mechanisms of spinal implant failure. Through an *in vitro* biomechanical human cadaver investigation, a novel test method was developed to evaluate pedicle screw loosening caused by multiaxial loading of lumbar pedicle screw fixation (SO3a). Further, relative screw loosening outcomes from traditional uniaxial toggle testing and multiaxial loading were assessed through a repeated-measures study design (SO3b). This investigation was the first to provide a side-by-side comparison, confirming accelerated implant loosening and increased volumetric bone deformation under multi-axial loading protocols when directly compared to uniaxial test methods.

Chapter 4: An experimental evaluation of *in vitro* lumbar motion segments under traditional pure moment and physiologically derived multiaxial joint motion simulation

Hypothesis (H4): By comparing outlined parameters, this study will provide new data as steps towards validation of a six degree-of-freedom spine motion simulator - **ACCEPTED**. It was hypothesized lumbar segment ROM would be smaller under dynamic test rates than quasi-static test rates (H4a) - **REJECTED**, ROM would not differ between force and displacement (H4b) – ACCEPTED, and ROM would be smaller under physiologically-derived loads than pure moment loading (H5c) - **ACCEPTED**.

Chapter 4 focused on the multiaxial spinal loading theme towards the first overall thesis goal. Through an *in vitro* biomechanical human cadaver investigation, complex physiologically-derived lumbar spine loads were accurately replicated through the use of a commercially available joint motion simulator. This study further examined the influence of quasi-static vs dynamic loading rates (SO4a), load vs displacement control method (SO4b), and the impact of pure moment testing compared to physiologically derived surrogates on lumbar segment range of motion (SO4c). Lumbar segment range of motion and neutral zone were largely unaffected by changes to loading rate and simulator control. Conversely, this study showed significant differences in lumbar segment kinematics between pure moment and physiologically derived loading protocols. Ultimately, this study provided a validation of a commercially available 6DOF joint motion simulator for *in vitro* spine investigations and proposed a new pathway to applying more physiologically relevant loading protocols.

Chapter 5: The *in vitro* simulation of physiologically derived gait and sit-to-stand loading on the lumbar spine

Hypothesis (H5a): by employing general PID controller tuning sit-to-stand and gait loading can be reliably simulated at quasi-static and dynamic rates - **ACCEPTED** and, Hypothesis (H5b): by employing iterative learning control, a 6DOF complex loading protocol can be applied in force control at a physiologic rate with minimal error over longitudinal cyclic testing - **ACCEPTED**.

Chapter 5 continued the focus on the multiaxial spinal loading these and first overall thesis goal. This study developed a novel *in vitro* testing method to apply cyclic 6DOF loading waveforms associated with sit-to-stand and gait activities (SO5a) and compared lumbar spine kinematics before and after simulation of 10,000 cycles of gait loading (SO5b). The iterative

learning control capabilities of a commercially available joint motion simulator were able to simulate lumbar loads experienced by human gait at a physiologic frequency (2 Hz) for 10,000 steps in load control with minimal error between the input and output loading waveforms. To the best of the author's knowledge, this is first successful simulation of complex 6DOF waveforms for load control, longitudinal lumbar spine testing at a physiologic-like loading rate. The establishment of this protocol has potential for improving *in vitro* fatigue protocols for pre-clinical evaluations of lumbar spine instrumentation.

Chapter 6: Architectural bone parameters and the relationship to titanium lattice design for powder bed fusion additive manufacturing

Hypothesis (H6): Recommendations will be made on how to best use this information towards the design and additive manufacturing of improved titanium and Ti6Al4V lattice structures for bone replacement and repair – **ACCEPTED**.

Chapter 6 was interested in better defining the links between LPBF additive manufacturing and bone properties as part of the second overall thesis goal. A comprehensive literature review of existing additive manufacturing literature to determine which titanium lattice parameters have been examined for bone replacement and repair implants was completed (SO6). This study was successful in culminating a large number of studies and examining the impact of lattice design decisions (e.g. porosity, feature thickness, lattice type, pore size) on compressive and elastic moduli. Recommendations are made towards design decisions for fatigue performance, osseointegration, and implant compliance. The data collected during the review process was synthesized into new design tools aimed at improving lattice selection in DfAM.

Chapter 7: A manufacturability evaluation of complex architectures by laser powder bed fusion additive manufacturing

Hypothesis (H7): Surface based lattices such as gyroid and Schwarz lattices will prove to be the most manufacturable based on the known challenges of printing down-skin surfaces with an angle of less than 45 degrees to build plate - **ACCEPTED**.

Chapter 7 was conducted between the intersection of two research themes: spinal implant evaluation and LPBF additive manufacturing. This chapter included the development of a digital workflow for to examine the manufacturability of common lattice structures using laser powder bed fusion based on geometric and defect analysis. (SO7). Manufacturability evaluation showed that homogeneous surface based lattices are largely manufacturable (e.g. TPMS gyroid) and successful manufacture of stochastic and strut-based lattices is highly dependent on down-skin surface distribution. The manufacturability evaluation digital workflow was validated on two latticed lumbar interbody fusion cage designs described in Chapter 8.

Chapter 8: Design and Manufacturability of Compliant and Anatomically Optimized Spinal Implants using Laser Powder Bed Fusion Additive Manufacturing

Hypothesis: none

Chapter 8 leveraged two thesis themes: spinal implant evaluation and LPBF additive manufacturing to address the second overall thesis goal. This chapter acted as a bridge to utilize the design tools developed in Chapters 6 and 7 to design a lumbar interbody cage and assess manufacturability (SO8). The lumbar interbody cage developed was then evaluated through the study conducted in the final investigation (Chapter 9). Novel spinal interbody implant designs were successfully manufactured in Ti6Al4V alloy through LPBF AM. A brief bench top investigation

was undertaken to better understand the impact of incorporating a taper on the implant surface to improve implant conformance to the shape of the lumbar vertebral endplate. The initial findings of the bench top investigation were promising, and further *in vitro* cadaveric investigations were subsequently completed in Chapter 9.

Chapter 9: An *in vitro* investigation of lumbar interbody cage migration under physiologically-derived loading conditions

Hypothesis: Spinal movement, particularly flexion-extension, would exacerbate cage migration and subsidence when compared to other spinal movements – **ACCEPTED**.

Chapter 9 is located at the center of the Venn diagram in Figure 10.1 as the culminating investigation of this thesis. Chapter 9 brings together all three research themes: (1) multiaxial spinal loading, (2) spinal implant evaluation, and (3) LPBF additive manufacturing to address both overall thesis goals. Through an *in vitro* biomechanical human cadaver investigation, the pure moment and complex physiologically-derived lumbar spine loading protocols developed in Chapter 4 and Chapter 5 were applied to intact and anterior-column reconstructed lumbar spine segments. The impact of loading conditions associated with different spinal movements impact lumbar interbody cage migration and subsidence (SO9). It was discovered that cyclic, low load gait movements were most influential for cage subsidence, while pure moment flexion-extension was the largest contributor towards posterior cage migration.

10.2 Future Directions

The validation of a commercially available joint motion simulator for simulating complex spinal movements and implant testing sets the groundwork for many future investigations. Examining implant performance under pure moment and physiologically derived loads in multi-

segment spine specimens is the logical next step of this work. Next, there is an exciting opportunity to leverage the waveform building algorithms and spinal load simulation learnings improve complex loading waveforms to better represent true *in vivo* loads through additional live participant experiments or through use of more detailed computational spine models.

Damage at the bone implant interface was examined in Chapter 3; however, this was completed post-implant removal and at clinical CT resolution. Advances in medical imaging modalities and metal artifact reconstruction have the potential to improve this characterization by examining bone-implant interface throughout testing to better characterize when tissue failure has occurred. Comparison of patient images following *in vivo* implant failure and images captured following bench top *in vitro* tests in human cadaveric specimens can then be compared to validate if simulating physiologically representative 6DOF spinal loads leads to more clinically relevant implant failure modes.

The work presented in Chapters 6 and 7 aimed to bridge the knowledge gap between AM expertise and orthopaedic implant DfAM. However, findings were applied to a single test case and implants generated were not evaluated against existing test standards. In future works, the findings of Chapter 6 can be integrated into a more advanced topology optimization design approach. This has potential of yielding a more thorough design able to better meet biomechanical performance requirements. Further, LPBF process parameter optimization for improving fatigue performance in latticed orthopaedic implants is an important step in translating these findings into clinical practice.

10.3 Significance

In conclusion, this thesis provides valuable insights to the engineering and clinical spine communities on the themes of multiaxial spinal loading, spinal implant fixation, and the use of DfAM to improve spinal implants, and eventually outcomes following surgery. New test protocols outlined in this work can potentially improve pre-clinical implant evaluation methods and further advanced both the engineering and clinical understanding of implant failure modes under physiologically-derived loading. Contributions to the additive manufacturing field were made through the development of new DfAM tools in the areas of lattice selection and manufacturability for orthopaedic implant designs. Ultimately, these contributions help to address the clinical and socioeconomic burden and improve future outcomes of lumbar spine surgeries.

References

Amirouche, F., Solitro, G.F., Magnan, B.P., 2016. Stability and spine pedicle screws fixation strength—a comparative study of bone density and insertion angle. Spine Deform 4, 261–267.

Andriamifidy, H.F., Rohde, M., Swami, P., Liang, H., Grande, D., Virk, S., 2024. Influence of Placement of Lumbar Interbody Cage on Subsidence Risk: Biomechanical Study. World Neurosurg 183, e440–e446. https://doi.org/10.1016/j.wneu.2023.12.118

Arami, A., Delaloye, J.-R., Rouhani, H., Jolles, B.M., Aminian, K., 2018. Knee implant loosening detection: a vibration analysis investigation. Ann Biomed Eng 46, 97–107.

Arjmand, N., Shirazi-Adl, A., 2006. Model and in vivo studies on human trunk load partitioning and stability in isometric forward flexions. J Biomech 39, 510–521.

Aycan, F., Demir, T., 2020. Toggling effect on pullout performance of pedicle screws: Review. International Advanced Researches and Engineering Journal 04, 161–172. https://doi.org/10.35860/iarej.722229

Aycan, M.F., Tolunay, T., Demir, T., Yaman, M.E., Usta, Y., 2017. Pullout performance comparison of novel expandable pedicle screw with expandable poly-ether-ether-ketone shells and cement-augmented pedicle screws. Proc Inst Mech Eng H 231, 169–175.

Aycan, M.F., Yaman, M.E., Usta, Y., Demir, T., Tolunay, T., 2018. Investigation of toggling effect on pullout performance of pedicle screws. Proc Inst Mech Eng H 232, 395–402.

Bari, K., Arjunan, A., 2019. Extra low interstitial titanium based fully porous morphological bone scaffolds manufactured using selective laser melting. J Mech Behav Biomed Mater 95, 1–12.

Bohl, M.A., Hlubek, R.J., Kakarla, U.K., Chang, S.W., 2018. Divergent Bilateral Posterior Lumbar Interbody Fusion with Cortical Screw Fixation: Description of New Trajectory for Interbody Technique from Midline Exposure. World Neurosurg 113, e480–e485. https://doi.org/10.1016/j.wneu.2018.02.060

Boos, N., Webb, J.K., 1997. Pedicle screw fixation in spinal disorders: a European view. European Spine Journal 6, 2–18.

Borkowski, S. L., Sangiorgio, S. N., Bowen, R. E., Scaduto, A. A., Kwak, J., & Ebramzadeh, E. (2017). Flexibility of thoracic spines under simultaneous multi-planar loading. European Spine Journal, 26, 173-180.

Bredow, J., Boese, C.K., Werner, C.M.L., Siewe, J., Löhrer, L., Zarghooni, K., Eysel, P., Scheyerer, M.J., 2016. Predictive validity of preoperative CT scans and the risk of pedicle screw loosening in spinal surgery. Arch Orthop Trauma Surg 136, 1063–1067.

Briski, D.C., Goel, V.K., Waddell, B.S., Serhan, H., Kodigudla, M.K., Palepu, V., Agarwal, A.K., Zavatsky, J.M., 2017. Does Spanning a Lateral Lumbar Interbody Cage Across the Vertebral Ring Apophysis Increase Loads Required for Failure and Mitigate Endplate Violation. Spine (Phila Pa 1976) 42, E1158–E1164. https://doi.org/10.1097/BRS.0000000000002158

Burstein, A.H., Reilly, D.T., Martens, M., 1976. Aging of bone tissue: mechanical properties. J Bone Joint Surg Am 58, 82–86.

Cadieux, C., Brzozowski, P., Fernandes, R.J.R., McGregor, M.E., Zdero, R., Bailey, C.S., McLachlin, S.D., Rasoulinejad, P., 2024. Topping-Off a Long Thoracic Stabilization With Semi-Rigid Constructs May Have Favorable Biomechanical Effects to Prevent Proximal Junctional Kyphosis: A Biomechanical Comparison. Global Spine J. https://doi.org/10.1177/21925682241259695

Callens, S.J.P., Tourolle, D.C., Müller, R., Amir, A., 2020. The local and global geometry of trabecular bone.

Chen, Y.-L., Chen, W.-C., Chou, C.-W., Chen, J.-W., Chang, C.-M., Lai, Y.-S., Cheng, C.-K., Wang, S.-T., 2014. Biomechanical study of expandable pedicle screw fixation in severe osteoporotic bone comparing with conventional and cement-augmented pedicle screws. Med Eng Phys 36, 1416–1420.

Cho, W., Shimer, A.L., Shen, F.H., 2011. Complications Associated with Posterior Lumbar Surgery. Semin Spine Surg 23, 101–113. https://doi.org/10.1053/j.semss.2010.12.013

Christophy, M., Senan, N.A.F., Lotz, J.C., O'Reilly, O.M., 2012. A musculoskeletal model for the lumbar spine. Biomech Model Mechanobiol 11, 19–34.

Cornaz, F., Widmer, J., Farshad-Amacker, N.A., Spirig, J.M., Snedeker, J.G., Farshad, M., 2021. Biomechanical Contributions of Spinal Structures with Different Degrees of Disc Degeneration. Spine (Phila Pa 1976).

Cunningham, B.W., Gordon, J.D., Dmitriev, A.E., Hu, N., Mcafee, P.C., 2003. Biomechanical Evaluation of Total Disc Replacement Arthroplasty: An In Vitro Human Cadaveric Model. Number 20S 28, 110–117.

Demir, T., Örmeci, M.F., 2014. New pedicle screw design with expandable shell for low bone quality. J Med Device 8.

Denis, F., 1983. The three column spine and its significance in the classification of acute thoracolumbar spinal injuries. Spine (Phila Pa 1976) 8, 817–831.

Deviren, V., Tang, J.A., Scheer, J.K., Buckley, J.M., Pekmezci, M., McClellan, R.T., Ames, C.P., 2012. Construct Rigidity after Fatigue Loading in Pedicle Subtraction Osteotomy with or without Adjacent Interbody Structural Cages. Global Spine J 2, 213–220. https://doi.org/10.1055/s-0032-1331460

Dreischarf, M., Albiol, L., Zander, T., Arshad, R., Graichen, F., Bergmann, G., Schmidt, H., Rohlmann, A., 2015. In vivo implant forces acting on a vertebral body replacement during upper body flexion. J Biomech 48, 560–565.

du Plessis, A., Yadroitsava, I., Yadroitsev, I., 2018. Ti6Al4V lightweight lattice structures manufactured by laser powder bed fusion for load-bearing applications. Opt Laser Technol 108, 521–528.

Dunlop, R.B., Adams, M.A., Hutton, W.C., 1984. Disc space narrowing and the lumbar facet joints. J Bone Joint Surg Br 66, 706–710.

Ebisch, I., Lazaro-Pacheco, D., Farris, D.J., Holsgrove, T.P., 2024. Replicating spine loading during functional and daily activities: An in vivo, in silico, in vitro research pipeline. J Biomech 163. https://doi.org/10.1016/j.jbiomech.2023.111916

El-Sayed, M.A., Essa, K., Ghazy, M., Hassanin, H., 2020. Design optimization of additively manufactured titanium lattice structures for biomedical implants. The International Journal of Advanced Manufacturing Technology 110, 2257–2268.

Ekman, P., Möller, H., Shalabi, A., Yu, Y.X., Hedlund, R., 2009. A prospective randomised study on the long-term effect of lumbar fusion on adjacent disc degeneration. European spine journal 18, 1175–1186.

Emmelmann, C., Sander, P., Kranz, J., Wycisk, E., 2011. Laser additive manufacturing and bionics: redefining lightweight design. Phys Procedia 12, 364–368.

Engh, C. A., O'connor, D., Jasty, M., McGovern, T. F., Bobyn, J. D., & Harris, W. H. (1992). Quantification of implant micromotion, strain shielding, and bone resorption with porous-coated anatomic medullary locking femoral prostheses. Clinical Orthopaedics and Related Research (1976-2007), 285, 13-29.

Esses, S.I., Sachs, B.L., Dreyzin, V., 1993. Complications associated with the technique of pedicle screw fixation. A selected survey of ABS members. Spine (Phila Pa 1976) 18, 2231–2238.

Fernandes, R.J.R., Gee, A., Kanawati, A.J., Siddiqi, F., Rasoulinejad, P., Zdero, R., Bailey, C.S., 2024. Biomechanical Comparison of Subsidence Between Patient-Specific and Non-Patient-Specific Lumbar Interbody Fusion Cages. Global Spine J 14, 1155–1163. https://doi.org/10.1177/21925682221134913

Fölsch, C., Goost, H., Figiel, J., Paletta, J.R.J., Schultz, W., Lakemeier, S., 2012. Correlation of pull-out strength of cement-augmented pedicle screws with CT-volumetric measurement of cement. Biomedical Engineering/Biomedizinische Technik 57, 473–480.

Formby, P.M., Kang, D.G., Helgeson, M.D., Wagner, S.C., 2016. Clinical and Radiographic Outcomes of Transforaminal Lumbar Interbody Fusion in Patients with Osteoporosis. Global Spine J 6, 660–664. https://doi.org/10.1055/s-0036-1578804

Freeman, A.L., Camisa, W.J., Buttermann, G.R., Malcom, J.R., 2016. Flexibility and fatigue evaluation of oblique as compared with anterior lumbar interbody cages with integrated endplate fixation. J Neurosurg 24, 54–59.

Galbusera, F., Volkheimer, D., Reitmaier, S., Berger-Roscher, N., Kienle, A., Wilke, H.J., 2015. Pedicle screw loosening: a clinically relevant complication? European Spine Journal 24, 1005–1016. https://doi.org/10.1007/s00586-015-3768-6

Gay, R.E., Ilharreborde, B., Zhao, K., Boumediene, E., An, K.N., 2008. The effect of loading rate and degeneration on neutral region motion in human cadaveric lumbar motion segments. Clinical Biomechanics 23, 1–7. https://doi.org/10.1016/j.clinbiomech.2007.08.006

Ghiselli, G., Wang, J.C., Bhatia, N.N., Hsu, W.K., Dawson, E.G., 2004. Adjacent segment degeneration in the lumbar spine. JBJS 86, 1497–1503.

Grant, J.P., Sc, M., Oxland, T.R., Dvorak, M.F., 2001. Mapping the Structural Properties of the Lumbosacral Vertebral Endplates. Spine (Phila Pa 1976) 26, 889–896.

Hansson, T.H., Keller, T.S., Spengler, D.M., 1987. Mechanical behavior of the human lumbar spine. II. Fatigue strength during dynamic compressive loading. Journal of Orthopaedic Research 5, 479–487.

Hashemi, A., Bednar, D., Ziada, S., 2009. Pullout strength of pedicle screws augmented with particulate calcium phosphate: an experimental study. The spine journal 9, 404–410.

Hawes, M.C., O'brien, J.P., 2006. The transformation of spinal curvature into spinal deformity: pathological processes and implications for treatment. Scoliosis 1, 1–9.

Hildebrand, T., Laib, A., Müller, R., Dequeker, J., Rüegsegger, P., 1999. Direct three-dimensional morphometric analysis of human cancellous bone: microstructural data from spine, femur, iliac crest, and calcaneus. Journal of bone and mineral research 14, 1167–1174.

Holsgrove, T.P., Gheduzzi, S., Gill, H.S., Miles, A.W., 2014. The development of a dynamic, six-axis spine simulator. Spine Journal 14, 1308–1317. https://doi.org/10.1016/j.spinee.2013.11.045

Holsgrove, T.P., Nayak, N.R., Welch, W.C., Winkelstein, B.A., 2015. Advanced multi-axis spine testing: Clinical relevance and research recommendations. Int J Spine Surg 9, 1–21. https://doi.org/10.14444/2034

Hosein, Yara K., King, G.J.W., Dunning, C.E., 2014. The effect of stem material and surface treatment on the torsional stability at the metal-cement interface of upper limb joint replacement systems. J Biomed Mater Res B Appl Biomater 102, 1217–1222. https://doi.org/10.1002/jbm.b.33105

Hosein, Yara K, King, G.J.W., Dunning, C.E., 2014. The effect of stem circumferential grooves on the stability at the implant-cement interface. J Med Device 8.

Jasty, M., Bragdon, C., Burke, D., O'Connor, D.., Lowenstein, J., & Harris, W. H. (1997). In vivo skeletal responses to porous-surfaced implants subjected to small induced motions. JBJS, 79(5), 707-14.

Jost, B., Cripton, P.A., Lund, T., Oxland, T.R., Lippuner, K., Jaeger, P., Nolte, L.-P., 1998. Compressive strength of interbody cages in the lumbar spine: the effect of cage shape, posterior instrumentation and bone density. European Spine Journal 7, 132–141.

Kaplan, F.S., Hayes, W.C., Keaveny, T.M., Boskey, A., Einhorn, T.A., Iannotti, J.P., 1994. Form and function of bone. Orthopaedic basic science 4, 131–133.

Khalid, S.I., Nunna, R.S., Maasarani, S., Belmont, E., Deme, P., Chilakapati, S., Eldridge, C., Singh, R., Bagley, C.A., Adogwa, O., 2020. Association of osteopenia and osteoporosis with higher rates of pseudarthrosis and revision surgery in adult patients undergoing single-level lumbar fusion. Neurosurg Focus 49, E6.

Kiapour, A., Massaad, E., Joukar, A., Hadzipasic, M., Shankar, G.M., Goel, V.K., Shin, J.H., 2022. Biomechanical analysis of stand-alone lumbar interbody cages versus 360° constructs: an in vitro and finite element investigation. J Neurosurg Spine 36, 928–936. https://doi.org/10.3171/2021.9.SPINE21558

Kim, Y.J., Bridwell, K.H., Lenke, L.G., Rhim, S., Cheh, G., 2006. Pseudarthrosis in long adult spinal deformity instrumentation and fusion to the sacrum: prevalence and risk factor analysis of 144 cases. Spine (Phila Pa 1976) 31, 2329–2336.

Kobayashi, K., Ando, K., Kato, F., Kanemura, T., Sato, K., Hachiya, Y., Matsubara, Y., Kamiya, M., Sakai, Y., Yagi, H., others, 2018. Reoperation within 2 years after lumbar interbody fusion: a multicenter study. European Spine Journal 27, 1972–1980.

Kumar, M., Meena, V.K., Singh, S., 2022. Static and Fatigue Load Bearing Investigation on Porous Structure Titanium Additively Manufactured Anterior Cervical Cages. Biomed Res Int 2022. https://doi.org/10.1155/2022/6534749

Kwon, J., Ha, M.H., Lee, M.G., 2020. Alternative pedicle screw design via biomechanical evaluation. Applied Sciences 10, 4746.

Law, M., Tencer, A.F., Anderson, P.A., 1993. Caudo-cephalad loading of pedicle screws: mechanisms of loosening and methods of augmentation. Spine (Phila Pa 1976) 18, 2438–2443.

Lazaro-Pacheco, D., Ebisch, I., Holsgrove, T.P., 2024. The physiological, in-vitro simulation of daily activities in the intervertebral disc using a load Informed kinematic evaluation (LIKE) protocol. J Biomech 163. https://doi.org/10.1016/j.jbiomech.2023.111919

Le, T. V, Baaj, A.A., Dakwar, E., Burkett, C.J., Murray, G., Smith, D.A., Uribe, J.S., 2012. Subsidence of polyetheretherketone intervertebral cages in minimally invasive lateral retroperitoneal transpsoas lumbar interbody fusion. Spine (Phila Pa 1976) 37, 1268–1273.

Lee, T.C., O'Brien, F.J., Taylor, D., 2000. The nature of fatigue damage in bone. Int J Fatigue 22, 847–853.

Liebsch, C., Zimmermann, J., Graf, N., Schilling, C., Wilke, H.J., Kienle, A., 2018. In vitro validation of a novel mechanical model for testing the anchorage capacity of pedicle screws using physiological load application. J Mech Behav Biomed Mater. https://doi.org/10.1016/j.jmbbm.2017.10.030

Liu, F., Zhang, D.Z., Zhang, P., Zhao, M., Jafar, S., 2018. Mechanical properties of optimized diamond lattice structure for bone scaffolds fabricated via selective laser melting. Materials 11, 374.

Long, J.P., Bartel, D.L., 2006. Surgical variables affect the mechanics of a hip resurfacing system. Clin Orthop Relat Res 453, 115–122.

Lotz, J.C., Hu, S.S., Chiu, D.F.M., Yu, M., Colliou, O., Poser, R.D., 1997. Carbonated apatite cement augmentation of pedicle screw fixation in the lumbar spine. Spine (Phila Pa 1976) 22, 2716–2723.

Lysack, J.T., Dickey, J.P., Dumas, G.A., Yen, D., 2000. A continuous pure moment loading apparatus for biomechanical testing of multi-segment spine specimens, Journal of Biomechanics.

Majumdar, S., Genant, H.K., Grampp, S., Newitt, D.C., Truong, V.-H., Lin, J.C., Mathur, A., 1997. Correlation of trabecular bone structure with age, bone mineral density, and osteoporotic status: in vivo studies in the distal radius using high resolution magnetic resonance imaging. Journal of Bone and Mineral Research 12, 111–118.

Malham, G.M., Parker, R.M., Blecher, C.M., Seex, K.A., 2015. Assessment and classification of subsidence after lateral interbody fusion using serial computed tomography. J Neurosurg Spine 23, 589–597.

Marchi, L., Abdala, N., Oliveira, L., Amaral, R., Coutinho, E., Pimenta, L., 2013. Radiographic and clinical evaluation of cage subsidence after stand-alone lateral interbody fusion. J Neurosurg Spine 19, 110–118.

Martin, B.I., Deyo, R.A., Mirza, S.K., Turner, J.A., Comstock, B.A., Hollingworth, W., Sullivan, S.D., 2008. Expenditures and health status among adults with back and neck problems. JAMA - Journal of the American Medical Association 299, 656–664. https://doi.org/10.1001/jama.299.6.656

McLachlin, S., 2011. Comparative assessment of sacral screw loosening augmented with PMMA versus a calcium triglyceride bone cement.pdf.

McLachlin, S., 2008a. Design and Development of in vitro Tools to Assess Fixation and Motion in the Spine. UWO Thesis Reponsitory.

McLachlin, S., 2008b. Comparing the Fixation of a Novel Hollow Screw Versus a Conventional Solid Screw in Human Sacra Under Cyclic L.pdf.

Mi, J., Li, K., Zhao, X., Zhao, C.Q., Zhao, J., 2017. Vertebral body Hounsfield units are associated with cage subsidence after transforaminal lumbar interbody fusion with unilateral pedicle screw fixation. Clin Spine Surg 30, 1130–1136.

Moolman, F., kat, C.-J., Du Plessis, A., Khodja, M., 2023. Comparative analysis of the subsidence of solid polyetheretherketone (PEEK) and 3D printed lattice titanium interbody fusion cages. MATEC Web of Conferences 388, 01001. https://doi.org/10.1051/matecconf/202338801001

Morosato, F., Traina, F., Cristofolini, L., 2019. A reliable in vitro approach to assess the stability of acetabular implants using digital image correlation. Strain 55. https://doi.org/10.1111/str.12318

Murr, L.E., Amato, K.N., Li, S.J., Tian, Y.X., Cheng, X.Y., Gaytan, S.M., Martinez, E., Shindo, P.W., Medina, F., Wicker, R.B., 2011. Microstructure and mechanical properties of open-cellular biomaterials prototypes for total knee replacement implants fabricated by electron beam melting. J Mech Behav Biomed Mater 4, 1396–1411.

Myers, E.R., Wilson, S.E., 1997. Biomechanics of osteoporosis and vertebral fracture. Spine (Phila Pa 1976) 22, 25S--31S.

Nowak, B., 2019. Experimental study on the loosening of pedicle screws implanted to synthetic bone vertebra models and under non-pull-out mechanical loads. J Mech Behav Biomed Mater 98, 200–204.

Okuyama, K., Abe, E., Suzuki, T., Tamura, Y., Chiba, M., Sato, K., 2000. Can insertional torque predict screw loosening and related failures?: an in vivo study of pedicle screw fixation augmenting posterior lumbar interbody fusion. Spine (Phila Pa 1976) 25, 858–864.

Orías, A.A.E., Sheha, E., Zavras, A., John, P., Fitch, A.A., An, H.S., Inoue, N., Colman, M., 2023. CT Osteoabsorptiometry Assessment of Subchondral Bone Density Predicts Intervertebral Implant Subsidence in a Human ACDF Cadaver Model. Global Spine J 13, 1374–1383. https://doi.org/10.1177/21925682211034845

Park, J., Lakes, R.S., 2007. Biomaterials: an introduction. Springer Science & Business Media.

Park, M.K., Park, S.A., Son, S.K., Park, W.W., Choi, S.H., 2019. Clinical and radiological outcomes of unilateral biportal endoscopic lumbar interbody fusion (ULIF) compared with conventional posterior lumbar interbody fusion (PLIF): 1-year follow-up. Neurosurg Rev 42, 753–761. https://doi.org/10.1007/s10143-019-01114-3

Pearson, H.B., Dobbs, C.J., Grantham, E., Niebur, G.L., Chappuis, J.L., Boerckel, J.D., 2017. Intraoperative biomechanics of lumbar pedicle screw loosening following successful arthrodesis. Journal of Orthopaedic Research 35, 2673–2681.

Pilliar, R. M., Lee, J. M., & Maniatopoulos, C. D. D. S. (1986). Observations on the effect of movement on bone ingrowth into porous-surfaced implants. Clinical Orthopaedics and Related Research (1976-2007), 208, 108-113.

Polikeit, A., Ferguson, S.J., Nolte, L.P., Orr, T.E., 2003. The importance of the endplate for interbody cages in the lumbar spine. European Spine Journal 12, 556–561. https://doi.org/10.1007/s00586-003-0556-5

Ponnusamy, K.E., Iyer, S., Gupta, G., Khanna, A.J., 2011. Instrumentation of the osteoporotic spine: biomechanical and clinical considerations. The Spine Journal 11, 54–63.

Puleo, D.A., Nanci, A., 1999. Understanding and controlling the bone--implant interface. Biomaterials 20, 2311–2321.

Rohlmann A, Graichen F, Weber U, & B.G., 2000. Monitoring in vivo implant loads with a telemeterized internal spinal fixation device. Spine (Phila Pa 1976) 25, 1005–16.

Rohlmann, A., Pohl, D., Bender, A., Graichen, F., Dymke, J., Schmidt, H., Bergmann, G., 2014. Activities of everyday life with high spinal loads. PLoS One 9, 1–9. https://doi.org/10.1371/journal.pone.0098510

Rohlmann, A., Bergmann, G., Graichen, F., 1999. Loads on internal spinal fixators measured in different body positions. European Spine Journal 8, 354–359.

Rohlmann, A., Consmüller, T., Dreischarf, M., Bashkuev, M., Disch, A., Pries, E., Duda, G.N., Schmidt, H., 2014. Measurement of the number of lumbar spinal movements in the sagittal plane in a 24-hour period. European Spine Journal 23, 2375–2384.

Schmidt, J., Berg, D.R., Ploeg, H.-L., Ploeg, L., 2009. Precision, repeatability and accuracy of Optotrak®optical motion tracking systems. Int J Exp Comput Biomech 1, 114–127.

Schultz, A., Andersson, G., Ortengren, R., Haderspeck, K., Nachemson, A., 1982. Loads on the lumbar spine. Validation of a biomechanical analysis by measurements of intradiscal pressures and myoelectric signals. J Bone Joint Surg Am 64, 713–720.

Seth, A., Hicks, J.L., Uchida, T.K., Habib, A., Dembia, C.L., Dunne, J.J., Ong, C.F., DeMers, M.S., Rajagopal, A., Millard, M., others, 2018. OpenSim: Simulating musculoskeletal dynamics and neuromuscular control to study human and animal movement. PLoS Comput Biol 14, e1006223.

Shibasaki, Y., Tsutsui, S., Yamamoto, E., Murakami, K., Yoshida, M., Yamada, H., 2020. A bicortical pedicle screw in the caudad trajectory is the best option for the fixation of an osteoporotic vertebra: An in-vitro experimental study using synthetic lumbar osteoporotic bone models. Clinical Biomechanics 72, 150–154.

Shirazi-Adl, A., El-Rich, M., Pop, D.G., Parnianpour, M., 2005. Spinal muscle forces, internal loads and stability in standing under various postures and loads—application of kinematics-based algorithm. European spine journal 14, 381–392.

Stemper, B.D., Pintar, F.A., Baisden, J.L., 2015. Lumbar spine injury biomechanics, in: Accidental Injury. Springer, pp. 451–470.

Stokes, I.A., Gardner-Morse, M., Churchill, D., Laible, J.P., 2002. Measurement of a spinal motion segment stiffness matrix, Journal of Biomechanics.

Suh, P.B., Puttlitz, C., Lewis, C., Bal, B.S., McGilvray, K., 2017. The effect of cervical interbody cage morphology, material composition, and substrate density on cage subsidence. Journal of the American Academy of Orthopaedic Surgeons 25, 160–168. https://doi.org/10.5435/JAAOS-D-16-00390

Sumiya, S., Fukushima, K., Kurosa, Y., Hirai, T., Inose, H., Yoshii, T., Okawa, A., 2021. Comparative analysis of clinical factors associated with pedicle screw pull-out during or immediately after surgery between intraoperative cone-beam computed tomography and postoperative computed tomography. BMC Musculoskelet Disord 22, 1–10.

Tan, J.-S., Bailey, C.S., Dvorak, M.F., Fisher, C.G., Oxland, T.R., 2005. Interbody device shape and size are important to strengthen the vertebra--implant interface. Spine (Phila Pa 1976) 30, 638–644.

Tan, X.P., Tan, Y.J., Chow, C.S.L., Tor, S.B., Yeong, W.Y., 2017. Metallic powder-bed based 3D printing of cellular scaffolds for orthopaedic implants: A state-of-the-art review on manufacturing, topological design, mechanical properties and biocompatibility. Materials Science and Engineering: C 76, 1328–1343.

Tokuhashi, Y., Ajiro, Y., Umezawa, N., 2009. Subsidence of metal interbody cage after posterior lumbar interbody fusion with pedicle screw fixation. Orthopedics 32, 259–264.

Tonino, A.J., Davidson, C.L., Klopper, P.J., Linclau, L.A., 1976. Protection from stress in bone and its effects. Experiments with stainless steel and plastic plates in dogs. J Bone Joint Surg Br 58, 107–113.

van Lenthe, G.H., Stauber, M., Müller, R., 2006. Specimen-specific beam models for fast and accurate prediction of human trabecular bone mechanical properties. Bone 39, 1182–1189.

Varghese, V., Saravana Kumar, G., Krishnan, V., 2017. Effect of various factors on pull out strength of pedicle screw in normal and osteoporotic cancellous bone models. Med Eng Phys 40, 28–38. https://doi.org/10.1016/j.medengphy.2016.11.012

Velasco, M.A., Narváez-Tovar, C.A., Garzón-Alvarado, D.A., 2015. Design, materials, and mechanobiology of biodegradable scaffolds for bone tissue engineering. Biomed Res Int 2015.

Wang, L., Kang, J., Sun, C., Li, D., Cao, Y., Jin, Z., 2017. Mapping porous microstructures to yield desired mechanical properties for application in 3D printed bone scaffolds and orthopaedic implants. Mater Des 133, 62–68.

Weinstein, J.N., Rydevik, B.L., Rauschning, W., 1992. Anatomic and technical considerations of pedicle screw fixation. Clin Orthop Relat Res 284, 34–46.

Weiss, A.J., Elixhauser, A., Andrews, R.M., 2014. Characteristics of operating room procedures in US hospitals, 2011: statistical brief\# 170.

Weistroffer, J.K., Perra, J.H., Lonstein, J.E., Schwender, J.D., Garvey, T.A., Transfeldt, E.E., Ogilvie, J.W., Denis, F., Winter, R.B., Wroblewski, J.M., 2008. Complications in long fusions to the sacrum for adult scoliosis: minimum five-year analysis of fifty patients. Spine (Phila Pa 1976) 33, 1478–1483.

Wilke, H.-J., Claes, L., Schmitt, H., Wolf, S., 1994. A universal spine tester for in vitro experiments with muscle force simulation. Eur Spine J 3, 91–97.

Wilke, H.J., Rohlmann, A., Neller, S., Schultheiss, M., Bergmann, G., Graichen, F., Claes, L.E., 2001. Is it possible to simulate physiologic loading conditions by applying pure moments? A comparison of in vivo and in vitro load components in an internal fixator. Spine (Phila Pa 1976) 26, 636–42.

Wilke, H.-J., Wenger, K., Claes, L., 1998. Testing criteria for spinal implants: recommendations for the standardization of in vitro stability testing of spinal implants. European spine journal 7, 148–154.

Xu, Y., Yen, D., Whitehead, M., Xu, J., Johnson, A.P., 2019. Use of instrumented lumbar spinal surgery for degenerative conditions: trends and costs over time in Ontario, Canada. Canadian Journal of Surgery 62, 393.

Yang, H., Bayoglu, R., Renani, M.S., Behnam, Y., Navacchia, A., Clary, C., Rullkoetter, P.J., 2020. Validation and sensitivity of model-predicted proximal tibial displacement and tray micromotion in cementless total knee arthroplasty under physiological loading conditions. J Mech Behav Biomed Mater 109. https://doi.org/10.1016/j.jmbbm.2020.103793

Yuan, W., Kaliya-Perumal, A.-K., Chou, S.M., Oh, J.Y.-L., 2020. Does lumbar interbody cage size influence subsidence? A biomechanical study. Spine (Phila Pa 1976) 45, 88–95.

Zehr, J.D., Callaghan, J.P., 2022. Reaction Forces and Flexion-Extension Moments Imposed on Functional Spinal Units With Constrained and Unconstrained In Vitro Testing Systems. J Biomech Eng 144. https://doi.org/10.1115/1.4053208

Zindrick, M.R., Wiltse, L.L., Widell, E.H., Thomas, J.C., Holland, W.R., Field, B.T., Spencer, C.W., 1986. A biomechanical study of intrapeduncular screw fixation in the lumbosacral spine. Clin Orthop Relat Res 203, 2.

Appendix A - Data related to architectural bone parameters and the relationship to Ti lattice design for powder bed fusion additive manufacturing[7]

Abstract

The data included in this article provides additional supporting information on our publication (McGregor et al. 2021) on the review of the natural lattice architecture in human bone and its implication towards titanium (Ti) lattice design for laser powder bed fusion and electron beam powder bed fusion. For this work, X-ray computed tomography was deployed to understand and visualize a Ti-6Al-4V lattice structure manufactured by laser powder bed fusion. This manuscript includes details about the manufacturing of the lattice structure using laser powder bed fusion and computed tomography methods used for analyzing the lattice structure. Additionally, a comprehensive literature review was conducted to understand how lattice parameters are controlled in additively manufactured Ti and Ti-alloy parts aimed at replacing or augmenting human bone. From this literature review, lattice design information was collected and is summarized in tabular form in this manuscript.

[7] A version of this chapter has been published in peer-reviewed journal: McGregor, M; Patel, S; McLachlin, S; Vlasea, M. (2021). Data related to architectural bone parameters and the relationship to Ti lattice design for powder bed fusion additive manufacturing. Data in Brief, 39: 107633.

Table A0. Specifications Table

Subject	Engineering, Materials science, Health, and medical sciences
Specific subject area	Additive Manufacturing, Bone Replacement, Metamaterials, Lattice structures, Orthopaedic design, Bone micro-architecture
Type of data	Table
How data were acquired	Instruments: Laser powder bed fusion (L-PBF) machine, X-ray computed tomography (CT), analytics on CT datasets Make and model of the instruments used: Renishaw AM 400 (L-PBF machine), ZEISS Xradia 520 Versa (CT hardware), Dragonfly 3.0, Object Research Systems Inc. (CT software)
Data format	Raw Analyzed
Parameters for data collection	The sample was manufactured laser powder bed fusion additive manufacturing and analyzed using X-ray computed tomography.
Description of data collection	The lattice structure was manufactured using Ti-6Al-4V powder using laser powder bed fusion (L-PBF) additive manufacturing. The lattice structure was then analyzed in a 3D X-ray computed tomography (XCT) scanner. The analysis of the XCT results was performed using an image processing software. Additionally, the lattice design information presented in tabular form was collected by reviewing 49 journal articles that deployed either laser powder bed fusion (L-PBF) or electron beam powder bed fusion (E-PBF) for lattice manufacturing with the objective of replacing, repairing, or augmenting human bone.
Data source location	Multi-Scale Additive Manufacturing Laboratory, University of Waterloo, Waterloo, ON, Canada
Data accessibility	The analyzed data is available with this article. The raw data is available upon request.
Related research article	(McGregor et al., 2021)

Value of the Data

- The data included in Table A3 provides a comprehensive overview at attempts made at replacing and repairing human bone through Ti and Ti-6Al-4V lattice structures manufactured with powder bed fusion technologies.
- The richness of this dataset in Table A3 creates value for future reference when selecting of lattice design parameters to tailor structures for compressive strength, yield strength and Young's modulus in aims of matching the mechanical properties of human bone.
- The design and laser powder bed fusion (L-PBF) manufacturing data provided about the Voronoi lattice, a stochastic lattice structure, is important to help additive manufacturing readers reproduce the lattice structure showcased in Figures 15 and 16 in McGregor et al. (McGregor et al., 2021) using any L-PBF system. The design of the lattice structure in particular can help a reader better visualize the various surface types described in Figure 15 in McGregor et al. (McGregor et al., 2021).
- The data provided about the the X-ray computed tomography (XCT) measurements and analysis provides additive manufacturing and bone replacement readers with sufficient information to examine a similar lattice structure using XCT and recreate results shown in McGregor et al. (McGregor et al., 2021).

Data Description

The Ti-6Al-4V Voronoi lattice structure manufactured by laser powder bed fusion (L-PBF) was analyzed in a 3D X-ray computed tomography (XCT) scanner (ZEISS Xradia 520 Versa). Voronoi lattices structures have numerous down-skin and overhanging features which cannot be controlled due to the stochastic nature of the lattice and therefore make an excellent showcase for manufacturability challenges with powder bed fusion AM. The original publication, McGregor et

al, 2021, brings into question the manufacturability limits powder bed fusion technology for the Ti and Ti-alloy lattice structures for bone replacement and repair. Therefore, the Voronoi lattice structure was selected as the test object for exhibiting these challenges. Voronoi lattice structures are also relatively new to the AM community and not well-studied, further justifying the use of a Voronoi lattice structure for comparison of manufacturability in this work. The design file for the Voronoi lattice structure is attached as supplementary material to this article. The Voronoi lattice designed for manufacturability comparison had a strut thickness of 500 μm and a random point spacing of 50 points at 1000 μm and was 5x10x10 mm in size. The important processing parameters used to obtain the XCT results for the entire lattice structure (left of Figure 15 in McGregor et al., 2021) are shown in Table 1, and the parameters used for the high resolution scan (center and right of Figure 15 in McGregor et al., 2021 are shown in Table A2. To visualize the defect space within the sample, the XCT scanned file was then analyzed using an image processing software (Dragonfly 3.0, Object Research Systems Inc., Montreal, QC) ("Dragonfly | 3D Visualization and Analysis Solutions for Scientific and Industrial Data,"). The brightness, contrast, and opacity of the data volume was adjusted to highlight the features of interest within the XCT data volume.

The lattice design parameters provided in Table A3 was collected by reviewing 49 journal articles that deployed either laser powder bed fusion or electron beam powder bed fusion for Ti or Ti-6Al-4V lattice manufacturing with the objective of replacing, repairing, or augmenting human bone. The review methodology followed is depicted in the flowchart in Figure 1. Details about the manufacturing technology used (L-PBF or E-PBF), lattice type, lattice porosity (%), lattice pore size (μm), lattice feature thickness (μm), material (Ti or Ti-6Al-4V), Young's modulus (E, GPa), compressive yield strength (σ_y), and ultimate compressive strength (σ_u, MPa) are provided in Table

A3. The values reported in Table A3 represent those reported in each individual study, which differ from individual lattice properties to average compressive mechanical properties from multiple tests. Individual values were included whenever available, averages from large data sets are denoted with a "*" and data not reported in a given study was denoted "---". The addition of these characters is aimed at improving data interpretation and allowing readers to use the table to appropriately design Ti lattice for bone replacement and repair in the future. Findings from Table A3 were used to create Figures 10, 11, 12, 13, and 14 in McGregor et al., 2021.

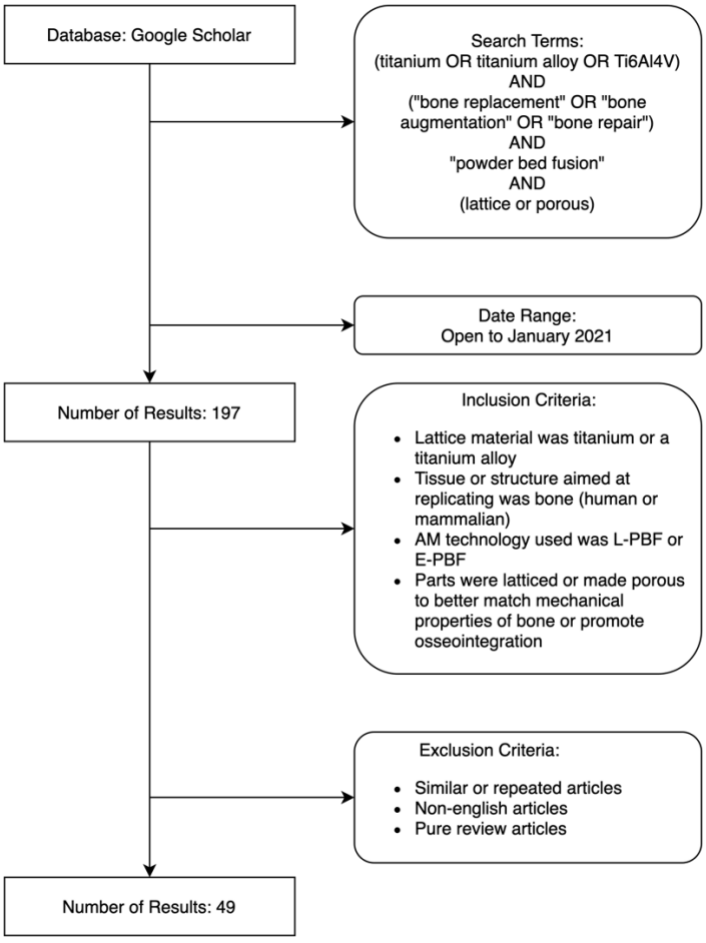


Figure A1: A flowchart has been utilized to describe the review methodology with the search terms, inclusion and exclusion criteria outlined.

Table A1. X-ray computed tomography (XCT) parameters used for scanning the entire Ti-6Al-4V Voronoi lattice structure.

Parameter	Unit	Value
Voxel size	[μm]	12.54
Source power	[W]	7
Source voltage	[kV]	80
Filter	-	LE6
X-ray optic	-	0.4x lens
Source-to-sample position	[mm]	23.019
Detector-to-sample position	[mm]	103.00
Exposure time	[s]	1.5
Number of projections	-	2401
Binning level	-	2

Table A2. X-ray computed tomography (XCT) parameters used for scanning the high-resolution scan of a portion of the Ti-6Al-4V Voronoi lattice structure.

Parameter	Unit	Value
Voxel size	[μm]	2.0029
Source power	[W]	7
Source voltage	[kV]	80
Filter	-	LE6
X-ray optic	-	4x lens
Source-to-sample position	[mm]	14.0390156
Detector-to-sample position	[mm]	103.0033
Exposure time	[s]	4
Number of projections	-	3001
Binning level	-	2

Table A3. Literature reporting the use of Ti lattices for the purpose of human bone replacement and/or augmentation is summarized. Lattice design parameters, lattice type, AM technology (laser powder bed fusion (L-PBF) and electron beam powder bed fusion (E-PBF)) and compressive mechanical properties were recorded as available. Blank entries reflect data not included in the original publication. Findings from Table A3 were used to create Figures 10, 11, 12, 13, and 14 in McGregor et al., 2021.

Reference	**Porosity (%)**	**Pore Size (µm)**	**Feature Thickness (µm)**	**Lattice Type**	**Unit Cell Size (mm^3)**	**AM Technology**	**Material**	**E (GPa)**	**σ_c (MPa)**	**σ_y (MPa)**
(Mobbs et al., 2017)	---	---	---	FCC	---	---	Ti	---	---	---
(Kim et al., 2017)	---	---	---	FCC	---	E-PBF	Ti-6Al-4V	---	---	---
(Choy et al., 2017)	---	---	---	---	---	---	Ti	---	---	---
(Phan et al., 2016)	---	---	---	Simple Cubic	---	---	Ti-6Al-4V	---	---	---
(Xu et al., 2016)	---	---	---	---	---	E-PBF	---	---	---	---
(Taniguchi et al., 2016)	61.6*	309*	220.0*	Diamond	---	L-PBF	Ti	0.66*	50.0*	---
	66.4*	632*	416.0*	Diamond	---	L-PBF	Ti	0.56*	50.0*	---
	64.0*	956*	577.0*	Diamond	---	L-PBF	Ti	0.76*	16.0*	---
(de Wild et al., 2013)	83.0	550*	200.0	Simple Cubic	---	L-PBF	Ti	0.76*	16.0*	---
(Hilton et al., 2017)	---	---	---	---	---	E-PBF	Ti-6Al-4V	---	---	---
(Schouman et al., 2016)	53.0	800-1500	---	---	---	L-PBF	Ti	37.90	---	---
(Arabnejad et al., 2017)	70.0	500	200.0	Tetrahedron	---	L-PBF	Ti-6Al-4V	---	---	---
(Wu et al., 2013)	68.0	710	---	---	---	E-PBF	Ti-6Al-4V	2.50	63.0	---
(Biemond et al., 2013)	63.0	250–800	---	---	---	L-PBF	Ti	---	---	---

	49.0	350–1400	---	---	---	E-PBF	Ti	---	---	---
(Xue et al., 2007)	17.0	100	---	---	---	L-PBF	Ti	44.00	463.0	---
	20.0	300	---	---	---	L-PBF	Ti	42.00	444.0	---
	27.0	450	---	---	---	L-PBF	Ti	24.30	205.0	---
	48.0	550	---	---	---	L-PBF	Ti	7.70	54.0	---
	58.0	800	---	---	---	L-PBF	Ti	2.60	24.0	---
(der Stok et al., 2013)	88.0	---	120.0	Dodecahedron	---	L-PBF	Ti-230	14.30	77.7	---
	68.0	---	230.0	Dodecahedron	---	L-PBF	Ti-120	0.38	1.6	---
(Srivas et al., 2017)	58.0	500	348.0	Simple Cubic	---	FDM	Ti-6Al-4V	0.45	39.6	---
(Wieding et al., 2015)	70.0	700	400.0	Simple Cubic	1.33	L-PBF	Ti-6Al-4V	8.22	168.2	---
(Van Bael et al., 2012)	---	500-1000	200.0	Triangular Honeycomb	---	L-PBF	Ti-6Al-4V	---	---	---
	---	500-1000	200.0	Hexagonal Honeycomb	---	---	Ti-6Al-4V	---	---	---
	---	500-1000	200.0	Rectangular honeycomb	---	---	Ti-6Al-4V	---	---	---
(Otsuki et al., 2006)	48.0	233*	---	Porous foam	---	---	Ti	---	---	---
	50.0	303*	---	Porous foam	---	---	Ti	---	---	---
	69.0	268*	---	Porous foam	---	---	Ti	---	---	---

	70.0	333*	---	Porous foam		---	Ti	---	---	---
(Ghouse et al., 2019)	87.3	830	210.0	Stochastic	---	L-PBF	Ti	1.70	550.0	---
(Zhao et al., 2018)	67.0	500	---	Tetrahedron	---	L-PBF	Ti	4.66	417.7	135.6
	84.0	1000	---	Tetrahedron	---	L-PBF	Ti	1.31	100.7	31.8
	63.0	500	---	Octahedron	---	L-PBF	Ti	5.51	453.0	228.4
	77.0	1000	---	Octahedron	---	L-PBF	Ti	2.57	117.3	81.2
(Fousová et al., 2017)	48.4	---	300.0	Rhombic Dodecahedron	2	L-PBF	Ti-6Al-4V	47.60	422.0	---
	62.1	---	300.0	Rhombic Dodecahedron	2	L-PBF	Ti-6Al-4V	30.50	257.0	---
	79.2	---	300.0	Rhombic Dodecahedron	2	L-PBF	Ti-6Al-4V		19.0	---
(Arabnejad et al., 2016)	50.0	500	390.0	Tetrahedron	1.52	L-PBF	Ti	4.30	219.0	---
	60.0	500	310.0	Tetrahedron	1.39	L-PBF	Ti	3.00	136.0	---
	70.0	500	240.0	Tetrahedron	1.27	L-PBF	Ti	2.80	120.0	---
	75.0	500	200.0	Tetrahedron	1.2	L-PBF	Ti	2.00	68.0	---
	50.0	770	400.0	Octahedron	1.66	L-PBF	Ti	4.50	228.0	---
	60.0	770	320.0	Octahedron	1.54	L-PBF	Ti	3.40	145.0	---

	70.0	770	250.0	Octahedron	1.44	L-PBF	Ti	1.40	31.0	---
	75.0	770	200.0	Octahedron	1.37	L-PBF	Ti	1.30	39.0	---
(Moiduddin et al., 2017)	49.8	700	800.0	BCC	2	E-PBF	Ti-6Al-4V	1.20	62.0	---
(Harrysson et al., 2008)	59.0	---	---	Rhombic Dodecahedron	3	E-PBF	Ti-6Al-4V	---	91.7	---
	59.0	---	---	Rhombic Dodecahedron	3	E-PBF	Ti-6Al-4V	---	94.1	---
	59.0	---	---	Rhombic Dodecahedron	3	E-PBF	Ti-6Al-4V	---	94.9	---
	92.0	---	---	Rhombic Dodecahedron	8	E-PBF	Ti-6Al-4V	---	2.9	---
	92.0	---	---	Rhombic Dodecahedron	8	E-PBF	Ti-6Al-4V	---	3.1	---
	95.0	---	---	---	10	---	---	---	0.8	---
(Wong et al., 2015)	70.0	720	350.0	---	---	L-PBF	Ti-6Al-4V	---	---	---
(Taheri et al., 2016)	20.0	---	800.0	---	2	L-PBF	NiTi	47.00	72.0	---
	32.0	---	700.0	---	2	L-PBF	NiTi	41.20	55.0	---
	45.0	---	600.0	---	2	L-PBF	NiTi	30.00	39.0	---
	58.0	---	500.0	---	2	L-PBF	NiTi	20.50	23.0	---
	71.0	---	400.0	---	2	L-PBF	NiTi	10.00	15.0	---
(Wang et al., 2017)	72.3	---	400.0	BCC	2	L-PBF	Ti-6Al-4V	3.40	---	184.4

	56.3	---	600.0	BCC	2	L-PBF	Ti-6Al-4V	4.80	---	333.0
	29.3	---	900.0	BCC	2	L-PBF	Ti-6Al-4V	10.40	---	842.6
(Marin et al., 2013)	66.3*	660*	---	Hexagonal Honeycomb	2	E-PBF	Ti	0.23*	15.5*	---
	75.5*	1370*	---	Hexagonal Honeycomb	2	E-PBF	Ti	0.04*	5.3*	---
(Lin et al., 2013)	---	---	---	---	---	L-PBF	Ti-6Al-4V	35.00	---	---
(Barbas et al., 2012)	53.0	1180	---	Custom	---	L-PBF	Ti	28.00	180.0	---
(Wieding et al., 2014)	---	799	416.0	Simple Cubic	1.215	L-PBF	Ti-6Al-4V	15.00	---	---
	---	797	1448.0	FCC	4.024	L-PBF	Ti-6Al-4V	15.00	---	---
	---	789	393.0	Custom	1.182	L-PBF	Ti-6Al-4V	15.00	---	---
(du Plessis et al., 2018)	50.0	---	1317.0	Flourite	5	L-PBF	Ti-6Al-4V	3.80	200.0	---
	50.0	---	1669.0	BCC	5	L-PBF	Ti-6Al-4V	3.60	200.0	---
(Arjunan et al., 2020)	71.0	---	---	Custom	---	L-PBF	Ti-6Al-4V	6.81	198.5	125.9
	74.3	---	---	Custom	---	L-PBF	Ti-6Al-4V	5.14	195.0	79.5
	81.2	---	---	Custom	---	L-PBF	Ti-6Al-4V	2.58	77.4	67.1
	83.0	---	---	Custom	---	L-PBF	Ti-6Al-4V	10.90	284.5	236.3

	83.1	---	---	Custom	---	L-PBF	Ti-6Al-4V	3.69	69.1	59.0
	91.4	---	---	Custom	---	L-PBF	Ti-6Al-4V	2.21	45.0	39.5
(Murr et al., 2011)	---	---	200.0	Dodecahedron	---	E-PBF	Ti-6Al-4V	---	---	---
	---	---	---	Stochastic	---	E-PBF	Ti-6Al-4V	---	---	---
(Soro et al., 2019)	25*	138*	768*	Schwarz TPMS	---	L-PBF	Ti-6Al-4V	58*	---	520*
	42*	282*	635*	Schwarz TPMS	---	L-PBF	Ti-6Al-4V	44*		325*
	64*	596	552*	Schwarz TPMS	---	L-PBF	Ti-6Al-4V	22.3*		160*
(Alabort et al., 2019)	85.0	500	---	Diamond TPMS	1	L-PBF	Ti-6Al-4V	0.57	65.0	---
	85.0	350	---	Neovious TPMS	1	L-PBF	Ti-6Al-4V	0.90	50.0	---
	85.0	200	---	Gyroid TPMS	1	L-PBF	Ti-6Al-4V	1.30	55.0	---
(Zhang et al., 2018)	79.5	650	200.0	Diamond	---	L-PBF	Ti-6Al-4V	1.22	36.5	---
	76.3	650	250.0	Diamond	---	L-PBF	Ti-6Al-4V	2.00	56.6	---
	72.6	650	300.0	Diamond	---	L-PBF	Ti-6Al-4V	3.02	85.8	---
	67.9	650	350.0	Diamond	---	L-PBF	Ti-6Al-4V	3.79	109.2	---
	66.1	650	400.0	Diamond	---	L-PBF	Ti-6Al-4V	5.15	144.9	---
(Bartolomeu et al., 2021)	64.2	500	300.0	Simple Cubic	0.8	L-PBF	Ti-6Al-4V	42.00	---	---

	70.3	600	300.0	Simple Cubic	0.9	L-PBF	Ti-6Al-4V	28.60	---	---
	84.0	500	150.0	Simple Cubic	0.65	L-PBF	Ti-6Al-4V	22.60	---	---
	87.6	600	150.0	Simple Cubic	0.75	L-PBF	Ti-6Al-4V	16.10	---	---
	93.3	600	100.0	Simple Cubic	0.7	L-PBF	Ti-6Al-4V	12.40	---	---
(Balci et al., 2021)	54.5	540	0.3	Custom	---	L-PBF	Ti-6Al-4V	---	---	---
	54.1	890	0.4	Custom	---	L-PBF	Ti-6Al-4V	---	---	---
	61.0	130	0.6	Custom	---	L-PBF	Ti-6Al-4V	---	---	---
	39.3	390	0.2	Custom	---	L-PBF	Ti-6Al-4V	---	---	---
	48.9	620	0.3	Custom	---	L-PBF	Ti-6Al-4V	---	---	---
	60.6	650	0.3	Custom	---	L-PBF	Ti-6Al-4V	---	---	---
(Xiong et al., 2020)	65.8	631	283.0	Diamond	---	L-PBF	Ti-6Al-4V	4.72	170.5	126.8
	67.1	643	285.0	Hexagonal Honeycomb	---	L-PBF	Ti-6Al-4V	3.79	163.0	110.9
	51.4	636	283.0	Diamond	---	L-PBF	Ti-6Al-4V	10.07	419.8	350.1
	52.7	643	285.0	Hexagonal Honeycomb	---	L-PBF	Ti-6Al-4V	10.99	536.9	423.8
(Dallago et al., 2021)	92.7	---	670.0	Simple Cubic	4	L-PBF	Ti-6Al-4V	3.02	16.0	16.0

	92.7	---	670.0	Simple Cubic	4	L-PBF	Ti-6Al-4V	1.75	9.0	9.0
	94.1	---	670.0	Simple Cubic	4	L-PBF	Ti-6Al-4V	1.84	9.0	9.0
	92.7	---	500.0	Simple Cubic	3	L-PBF	Ti-6Al-4V	2.98	14.0	15.0
(Bari and Arjunan, 2019)	63.6	---	---	Custom	---	L-PBF	Ti-6Al-4V	13.87	---	---
	56.9	---	---	Custom	---	L-PBF	Ti-6Al-4V	19.52	---	---
	68.0	---	---	Custom	---	L-PBF	Ti-6Al-4V	10.74	---	---
	74.0	---	100.0	Custom	---	L-PBF	Ti-6Al-4V	5.09	169.0	---
	61.0	---	500.0	Custom	---	L-PBF	Ti-6Al-4V	6.07	342.0	---
	55.0	---	900.0	Custom	---	L-PBF	Ti-6Al-4V	5.42	280.0	---
(Heinl et al., 2008)	81.1	1230	---	Diamond	---	E-PBF	Ti-6Al-4V	1.60	29.3	22.0
	80.8	1230	---	Diamond	---	E-PBF	Ti-6Al-4V	0.90	21.0	16.1
	59.5	450	---	Simple Cubic	---	E-PBF	Ti-6Al-4V	12.90	148.4	107.5
	59.5	450	---	Simple Cubic	---	E-PBF	Ti-6Al-4V	3.90	127.1	49.6
(Liu et al., 2018)	97.0	---	---	Diamond	5.5	L-PBF	Ti-6Al-4V	0.34	2.0	---
	81.0	---	---	Diamond	5.5	L-PBF	Ti-6Al-4V	1.40	78.0	---
(Yan et al., 2015)	80.0	1600*	---	Gyroid TPMS	---	L-PBF	Ti-6Al-4V	1.25*	81.3*	---

	95.0	560*	---	Gyroid TPMS	---	L-PBF	Ti-6Al-4V	0.13*	6.5*	---
	80.0	1450*	---	Diamond TPMS	---	L-PBF	Ti-6Al-4V	1.25*	69.2*	---
	95.0	480*	---	Diamond TPMS	---	L-PBF	Ti-6Al-4V	0.12*	4.7*	---
(Ge et al., 2020)	72.6	550	---	Trabecular	---	L-PBF	Ti-6Al-4V	5.58	55.7	---
	70.0	550	---	Gyroid TPMS	---	L-PBF	Ti-6Al-4V	5.51	34.6	---
(El-Sayed et al., 2020)	82.4	---	840.0	Diamond	---	L-PBF	Ti-6Al-4V	0.35	19.3	---
	78.1	---	600.0	Diamond	---	L-PBF	Ti-6Al-4V	0.44	26.1	---
	26.4	---	360.0	Diamond	---	L-PBF	Ti-6Al-4V	9.59	150.0	---
	93.2	---	360.0	Diamond	---	L-PBF	Ti-6Al-4V	0.05	3.7	---
	65.5	---	600.0	Diamond	---	L-PBF	Ti-6Al-4V	7.73	184.5	---
	73.1	---	840.0	Diamond	---	L-PBF	Ti-6Al-4V	1.55	82.4	---
	75.0	---	600.0	Diamond	---	L-PBF	Ti-6Al-4V	1.28	47.3	---
	89.4	---	200.0	Diamond	---	L-PBF	Ti-6Al-4V	0.22	10.2	---
	43.9	---	360.0	Diamond	---	L-PBF	Ti-6Al-4V	4.95	145.8	---
	64.5	---	840.0	Diamond	---	L-PBF	Ti-6Al-4V	4.19	68.7	---
	90.3	---	600.0	Diamond	---	L-PBF	Ti-6Al-4V	0.16	7.5	---

	90.8	---	360.0	Diamond	---	L-PBF	Ti-6Al-4V	0.26	8.8	---
	20.0	---	600.0	Diamond	---	L-PBF	Ti-6Al-4V	11.83	200.0	---
	51.4	---	840.0	Diamond	---	L-PBF	Ti-6Al-4V	9.31	95.5	---
	55.5	---	1000.0	Diamond	---	L-PBF	Ti-6Al-4V	8.34	228.4	---
	74.8	---	600.0	Diamond	---	L-PBF	Ti-6Al-4V	1.41	52.2	---
	76.0	---	600.0	Diamond	---	L-PBF	Ti-6Al-4V	1.17	49.3	---
(Wang et al., 2020)	64.4	---	670.0	---	3	E-PBF	Ti-6Al-4V	14.70	169.7	---
	62.4	---	500.0	---	4	E-PBF	Ti-6Al-4V	21.00	169.5	---
	59.7	---	400.0	---	5	E-PBF	Ti-6Al-4V	20.00	229.0	---
	59.9	---	670.0	---	3	E-PBF	Ti-6Al-4V	18.30	229.1	---
	58.2	--	500.0	--	4	E-PBF	Ti-6Al-4V	23.30	243.9	--
	58.3	--	400.0	--	5	E-PBF	Ti-6Al-4V	25.30	250.7	--
(Zhang et al., 2020)	---	---	---	Gyroid TPMS	Graded	L-PBF	Ti-6Al-4V	---	---	---

Table A4: A glossary of the lattice types described in Table A3 has been included. The unit cells are 10x10x10 mm with a feature thickness of 1mm. An isometric and frontal view of each unit cell are included.

Lattice Name	Isometric View	Front View	Associated Table Entries
Body Centered Cubic (BCC)			[3], [4],
Face Centered Cubic (FCC)			
Simple Cubic			[5], [9], [17], [18]
Diamond			[8]
Flourite			
Hexagonal Honeycomb			
Triangular Honeycomb			[19]
Rectangular Honeycomb			
Tetrahedron			[12]
Octahedron			
Dodecahedron			[16]
Schwarz TPMS			
Gyroid TPMS			
Diamond TPMS			
Neovious TPMS			
Porous Foam			
Stochastic (e.g., Voronoi)			
Custom	Varies	Varies	

Experimental Design, Materials and Methods

The Voronoi lattice structure was manufactured using Ti-6Al-4V powder on the reduced build volume (RBV) of a modulated laser powder bed fusion (L-PBF) system (AM 400, Renishaw, UK). The design (STL) file for the Voronoi lattice structure is attached as supplementary material to this article. The powder used was plasma atomized, grade 23 with a size distribution of 15-45 μm (d10 of 20 μm, d50 of 34 μm, and d90 of 44 μm), provided by AP&C (Quebec, Canada). A powder layer thickness value of 30 μm and a hatching distance of 100 μm. The laser power and velocity settings were selected as per the L-PBF system manufacturers recommendation for Ti-6Al-4V which are predicted to lie in the transition melting mode from previous work (Patel and Vlasea, 2020). For the AM 400 system, the beam spot radius at the focal point is given by rB = 35 μm, which was kept constant for this study. The scan strategy followed this order: scanning of the core using the meander scanning strategy, followed by a single border scan that involves melting of the edge of each contour within a layer specified by the CAD of the lattice structure.

References:

See Chapter 6.7 Reference List

Appendix B – Standard Operating Procedures

Pedicle Screw Loosening Standard Operating Procedure

SPECIMEN PREPARATION

- ☐ Thaw specimen at 5 degrees C (fridge temp) overnight
- ☐ Place wood screws in transverse processes and posterior elements
- ☐ Cut 1-2'' black PVC pot
- ☐ Pot specimen (vertebral body) in Denstone Dental cement
    - Ensuring sufficient coverage of screw surfaces
    - Using yogurt container technique to fill through spinal canal

VIVO SET-UP

- ☐ Mount lower fixture with rod rigidly fixed
- ☐ Mount upper fixture and specimen
- ☐ Ensure no contact between actuators and zero load cell
- ☐ Set reference pose to defaults
- ☐ Using alignment tool and laser level, align screw extension with vertical by:
    - Rotating fixture in the FE direction
    - Rotating specimen in Ab/Ad direction
- ☐ Using digitization probe take landmark locations of L Screw, R Screw, and Screw Tail
- ☐ Using digitization probe take landmark locations of Vivo FE arm and lower fixture
- ☐ Using force control guide rod into tulip
- ☐ Change to displacement control for all axes excluding VL, which should have -25 N applied
- ☐ Fix set screw in place rigidly!
- ☐ Adjust pose to 0, 0, 0, N/m 0, 0, 0 N, GoTo pose
- ☐ Redefine reference pose to resolve forces about the screw using digitization measurements and Ab/Ad rotational offset
- ☐ Put Vivo in Mode: Displacement
- ☐ Load control parameters and waveform files
- ☐ Prepare test protocol file [waveform(s) variable for step increases every 2000 cycles]
- ☐ Ensure Data Acquisition Parameters (every 50 cycles, 500 Hz, etc)
- ☐ Set start and stop conditions
- ☐ Set event monitoring to trigger message at "failure" scenario (6 mm of displacement in any direction considered failure (Liebsch et al., 2018)
- ☐ Run test protocol (step increase waveforms)
- ☐ Add additional bottom plate and fix rod on both ends with chuck and set screws
- ☐ Adjust pose to 0, 0, 0, N/m 0, 0, 0 N, GoTo pose (OR GoTo Park Pose)
- ☐ Load Displacement, No ILC Control Parameters

☐ Make displacement control waveform that maintains specimen in current position while translating 2 cm downwards
☐ Change Data Acquisition parameters to pull-out settings

DATA COLLECTION (What data are we collecting)

- VIVO
    - Load cell and actuators with respect to reference pose origin:
        - Mx, My, Mz, Fx, Fy, Fz, x, y, z, pitch, yaw, roll
- Post-test imaging
    - Confirmation of bone deformation envelope

SINGLE FSU TESTING

SPECIMEN PREPARATION

- ☐ Thaw specimen at 20-22 degrees C (fridge temp) overnight
- ☐ Remove any unnecessary soft tissues that may obstruct line of sight for tracking
- ☐ Fix specimen to endplate cap fixtures with wood screws and PMMA cement
- ☐ Wrap specimen in saline soaked gauze

VIVO SET-UP

- ☐ Ensure VIVO is in specimen set up, default reference pose, and neutral position
- ☐ Mount specimen to AB/AD arm with upper fixture
- ☐ Mount specimen to lower fixture by moving actuators until there is fixture alignment
- ☐ Ensure no contact between actuators and zero load cell
- ☐ Finish specimen fixation to the VIVO by aligning bottom fixtures, adding -20N compression, placing and tightening screws on upper and lower fixtures
- ☐ Set up Aramis testing camera
- ☐ Add tracker mounts to upper and lower vertebrae
- ☐ Using digitization probe to determine endplate cap to spine landmark CS
- ☐ Adjust pose to 0, 0, -250, N/m 0, 0, 0 N, GoTo pose
- ☐ Set new reference pose as 0, 0, [distance to center of upper vert mm], 0, 0 ,0
- ☐ Put Vivo in Mode: Load

PURE MOMENT TESTING

- ☐ Load control parameters and pure flexion waveform file
- ☐ Ensure Data Acquisition Parameters (continuous, 50 Hz, etc)
- ☐ Check set start and stop conditions
- ☐ Run Flexion waveform (0 to 4 Nm) for 25 cycles and check PID control adjust as required
- ☐ Run pure flexion/extension wave form for 5 cycles (+/- 4 Nm)
    - Quasistatic
    - Dynamic
- ☐ Run pure lateral bending waveform for 5 cycles (+/- 4 Nm)
    - Quasistatic
    - Dynamic
- ☐ Run pure axial rotation waveform for 5 cycles (+/- 4 Nm)
    - Quasistatic
    - Dynamic

6 DOF PHYSIOLOGICALLY DERIVED LOAD TESTING

- ☐ Load control parameters and 6DOF flexion waveform file
- ☐ Ensure Data Acquisition Parameters (continuous, 50 Hz, etc)
- ☐ Check set start and stop conditions
- ☐ Run Flexion waveform for 25 cycles and check PID control adjust as required
- ☐ Run flexion wave form for 5 cycles
    - Quasistatic
    - Dynamic
- ☐ Run extension wave form for 5 cycles
    - Quasistatic
    - Dynamic
- ☐ Run lateral bending waveform for 5 cycles
    - Quasistatic
    - Dynamic
- ☐ Run pure axial rotation waveform for 5 cycles
    - Quasistatic
    - Dynamic

PURE MOMENT DISPLACEMENT CONTROL TESTING

- ☐ Determine specimen specific ROM from pure moment load control testing
- ☐ Generate sinusoidal displacement waveform
- ☐ Displacement control parameters and pure flexion waveform file
- ☐ Ensure Data Acquisition Parameters (continuous, 50 Hz, etc)
- ☐ Check set start and stop conditions
- ☐ Run pure flexion/extension wave form for 5 cycles (ROM deg)
    - Quasistatic
- ☐ Run pure lateral bending waveform for 5 cycles (ROM deg)
    - Quasistatic
- ☐ Run pure axial rotation waveform for 5 cycles (ROM deg)
    - Quasistatic

DATA COLLECTION (What data are we collecting)

- VIVO
    - Load cell and actuators with respect to reference pose origin:
        - Mx, My, Mz, Fx, Fy, Fz, x, y, z, pitch, yaw, roll
- FSU Kinematics from digital 3D optical tracking system
    - Measurement of vertebral body kinematics

Appendix C –Supplementary Material for Chapter 6

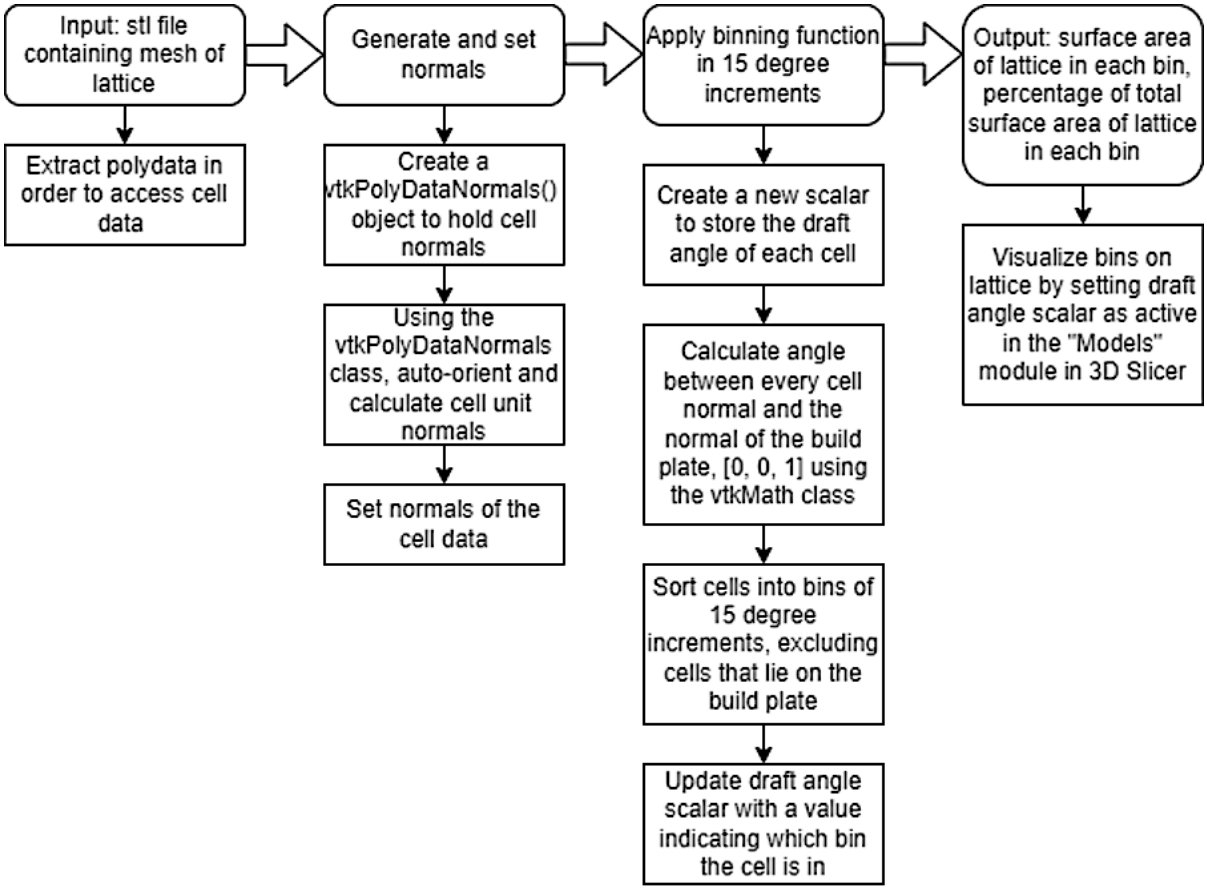


Figure C.1. A flowchart was developed to describe the process by which a custom python script was used to assign surface angle values to .stl files and visualize down-skin angle using 3D Slicer (v.4.11).

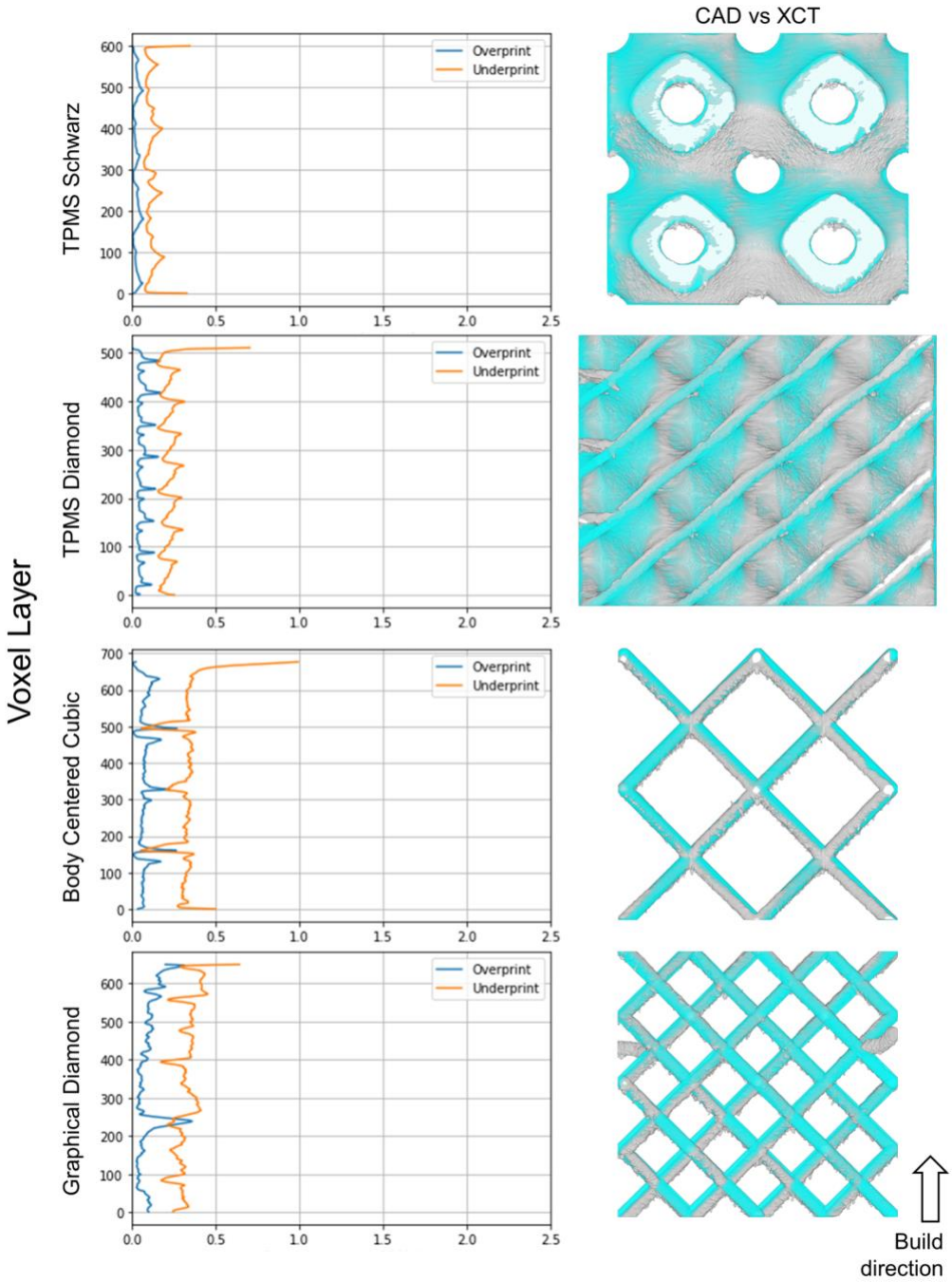


Figure C.2. Quantitative comparisons of the X-ray computed tomography and CAD datasets to understand slice-by-slice underprint and overprint of TPMS Schwarz, TPMS diamond, BCC and graphical diamond lattice structures. In the visualization on the right, grey is XCT and blue is the original CAD.

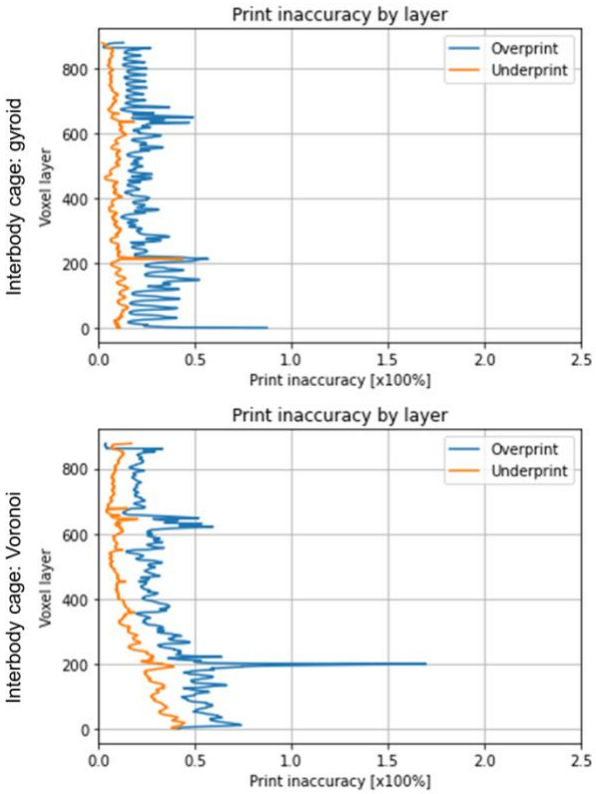


Figure C3. Quantitative comparisons of the X-ray computed tomography and CAD datasets to understand slice-by-slice underprint and overprint of the interbody cages with gyroid and Voronoi lattice structures.